SLAC-R-911

MEASUREMENTS OF CP-VIOLATING ASYMMETRIES IN NEUTRAL B MESON DECAYS INTO THREE KAONS

A DISSERTATION
SUBMITTED TO THE DEPARTMENT OF PHYSICS
AND THE COMMITTEE ON GRADUATE STUDIES
OF STANFORD UNIVERSITY
IN PARTIAL FULFILLMENT OF THE REQUIREMENTS
FOR THE DEGREE OF
DOCTOR OF PHILOSOPHY

Joshua M. Thompson
November 2008

SLAC-Report-911
Work supported by U. S. Department of Energy contract DE-AC02-76SF00515

SLAC National Accelerator Center, 2575 Sand Hill Road, Menlo Park, CA 94309

I certify that I have read this dissertation and that, in my opinion, it is fully adequate in scope and quality as a dissertation for the degree of Doctor of Philosophy.

(Aaron Roodman) Principal Adviser

I certify that I have read this dissertation and that, in my opinion, it is fully adequate in scope and quality as a dissertation for the degree of Doctor of Philosophy.

(David Leith)

I certify that I have read this dissertation and that, in my opinion, it is fully adequate in scope and quality as a dissertation for the degree of Doctor of Philosophy.

(Patricia Burchat)

I certify that I have read this dissertation and that, in my opinion, it is fully adequate in scope and quality as a dissertation for the degree of Doctor of Philosophy.

(JoAnne Hewett)

Approved for the University Committee on Graduate Studies.

Abstract

The Standard Model (SM) of particle physics successfully describes all of the observed interactions of the fundamental particles (with the exception of non-zero neutrino mass). Despite this enormous success, the SM is widely viewed as an incomplete theory. For example, the size of the asymmetry between matter and antimatter is not nearly large enough to account for the abundance of matter observed throughout the universe. It is thus believed that as-yet-unknown physical phenomena must exist that introduce new asymmetries between matter and antimatter. In this thesis, by studying decays that happen only rarely in the SM, we make measurements of asymmetries between matter and antimatter that are potentially sensitive to the existence of processes beyond the SM.

At the PEP-II asymmetric-energy B Factory at SLAC, electrons and positrons are collided at the $\Upsilon(4S)$ resonance to create pairs of B mesons. The *BABAR* detector is used to measure the subsequent decay products. Using 383 million $\Upsilon(4S) \to B\overline{B}$ decays, we study the decay $B^0 \to K^+K^-K^0$. In the SM, this decay is dominated by loop amplitudes. Asymmetries between matter and antimatter (CP asymmetries) are extracted by measuring the time-dependence of the complex amplitudes describing the B^0 and $\overline{B}^0$ decays as functions of their kinematics. The interference between decays with and without the mixing of neutral B mesons allows for the measurement of the angle β_{eff}, which is a measure of CP violation. We also measure the direct CP asymmetry A_{CP}.

Data samples reconstructed from three K^0 modes ($K^0_S \to \pi^+\pi^-$, $K^0_S \to \pi^0\pi^0$, and K^0_L) are fit simultaneously. We find $A_{CP} = -0.015 \pm 0.077 \pm 0.053$ and $\beta_{\mathit{eff}} = 0.352 \pm 0.076 \pm 0.026$ rad, corresponding to a CP violation significance of 4.8σ. A

second solution near $\pi/2-\beta_{\mathit{eff}}$ is disfavored with a significance of 4.5σ. In a subsequent fit to the region with $m_{K^+K^-} > 1.1\,\mathrm{GeV}/c^2$, we find $A_{CP} = -0.054 \pm 0.102 \pm 0.060$ and $\beta_{\mathit{eff}} = 0.436 \pm 0.087\,^{+0.055}_{-0.031}$ rad, excluding the possibility that $\beta_{\mathit{eff}} = 0$ at 5.1σ. We use the data with $m_{K^+K^-} < 1.1\,\mathrm{GeV}/c^2$ to extract CP asymmetries separately for B^0 decays to $\phi(1020)K^0$ and $f_0(980)K^0$, finding $\beta_{\mathit{eff},\phi} = 0.11 \pm 0.14 \pm 0.06$ and $\beta_{\mathit{eff},f_0} = 0.14 \pm 0.15 \pm 0.05$.

Acknowledgments

First and foremost, thanks go to my parents, Paul and Paulette, who gave me the opportunity to do whatever I wanted in life, and have supported me at every turn; and to my brother Ben, for everything he has done. Also, I could never have reached this point without the companionship and support of Evonne, my wife and best friend. Thanks also to my friend Lena Troncoso, who has always been there for me. It has been wonderful to get to know Sarah and John Garcia, as well the Genetics people: Shawn, Jay, Jeff, Matt, Dan, Heather, and Nanibaa.

I will always be in debt to my advisor, Aaron Roodman, whose tenacity for knowledge and devotion to his students are the archetype of an excellent professor. I thank Denis Dujmic for his extensive mentorship; Bill Dunwoodie also deserves special recognition. Thanks also to Witold Kozanecki, Chris O'Grady, and Matt Weaver for their guidance and patience. Mark Allen was the best officemate I could have asked for — tolerant of my idiosyncrasies and always ready for an intellectual (or non-intellectual) discussion. Erkcan Özcan not only taught me `awk`, but also how to be a better human being. I thank my fellow *BABAR* graduate students: Brian Lindquist, Tetiana Hryn'ova, Nicolas Berger, Jörg Stelzer, Wells Wulsin, Andrew Wagner, Manuel Franco, Kyle Knoepfel, Amanda Weinstein, and Stephanie Majewski. Thanks also go to Vera Lüth, and to Mike Kelsey, Jim MacDonald, Karl Bouldin, Helmut Marsiske, Steve Wagner, Adam Boyarski, Rainer Bartoldus, Stephen Gowdy, Ingrid Ofte, Hojeong Kim, Jochen Dingfelder, Phillip Bechtle, Markus Cristinziani, Bernie Culver, Anna Pacheco, Barbara Valdez, Mika Stratton, and everyone else in Group C. Finally I would like to thank my reading committee for their efforts: David Leith, JoAnne Hewett, Patricia Burchat, and Brent Sockness.

Contents

List of Tables

List of Figures

Chapter 1

Introduction

Since becoming operational in 1999, the B Factory experiments *BABAR* and Belle have made enormous contributions to particle physics, publishing hundreds of papers each. Although both experiments have addressed a myriad of physics topics, both were constructed with the principle goal of studying CP violation in the decay of B mesons. This chapter gives a brief motivation for the construction of these experiments. It also provides an introduction to the nature and scope of the PEP-II accelerator and the *BABAR* experiment, which are the facilities whose operation provided the data for this research.

1.1 Motivation

In 1956, C. S. Wu discovered that when a sample of Cobalt 60 is prepared with the spins of its nuclei aligned, electrons from β decay are preferentially emitted along the direction of the nuclear spin. Because the mirror image of this process flips the apparent spin direction of the nuclei, but does not change the direction of the emitted electrons, this process violates parity symmetry ($\mathcal{P}$). This discovery was quickly followed by the awarding of the 1957 Nobel Prize in Physics to Yang and Lee, who had proposed the experiment to her [2]. Despite the strong violation of $\mathcal{P}$ symmetry observed by Wu, the combination of charge conjugation (C) with $\mathcal{P}$ appeared to yield a conserved quantity. In 1964, however, Fitch and Cronin observed

the decay $K_L^0 \to \pi^+\pi^-$, which violates *CP* symmetry [3]. In contrast to $\mathcal{P}$-symmetry violation alone, the observed *CP* violation was very small, at the level of $\mathcal{O}(10^{-3})$.

Although the violation of *CP* symmetry was a surprise at the time and considered by some to be aesthetically unpleasing, it is actually a requirement of living in a matter-dominated universe [6]. In a universe with perfect *CP* symmetry, the Big Bang would have created equal amounts of matter and antimatter, resulting in a sea of photons and little else. Astrophysicists tell us, however, that the observable universe is made entirely of matter. Therefore, the violation of *CP* symmetry is not unexpected. A puzzle remained since the amount of *CP* violation observed in the kaon system is not sufficient to explain the observed dominance of matter in the universe [7].

At the time of its discovery, *CP* violation lacked any theoretical explanation. In 1963, Cabbibo compared the decay rates of kaons and pions into identical final states ($\mu\nu$ and $\pi^0 e\nu$) and extracted the value of the mixing angle for strangeness-changing processes [8]. Kobayashi and Maskawa expanded on this framework in 1973, showing that to include *CP* violation required adding a third generation of quarks to the mixing matrix [9]. The discovery of the charm quark in 1974 and later the third generation of fundamental particles supported their proposed mechanism, but for conclusive evidence one needs to study *CP* violation in decays of the bottom quark. This is the key motivation for the construction of the *B* Factories. More detail on the theoretical formulation of *CP* violation in the Standard Model (SM) is given in Chapter 2.

1.2 The PEP-II Accelerator

The PEP-II collider consists of two storage rings, each 2.2 km in circumference. The low energy ring (LER) stores positrons with an energy of 3.1 GeV, while the high energy ring (HER) stores electrons with an energy of 9.0 GeV, yielding a center-of-mass (CM) energy equal to the mass of the $\Upsilon(4S)$ resonance (10.58 GeV). Due to the asymmetric beam energies, the CM system is boosted relative to the laboratory frame by $\beta\gamma = 0.56$. The $\Upsilon(4S)$ decays almost exclusively to pairs of *B* mesons, which are

produced nearly at rest in the CM frame. As will be discussed in Chapter 2, key *CP* violation measurements require measuring the difference in decay times between a pair of B^0 mesons. The boost of the CM system separates the decay vertices of the B mesons in the lab frame, allowing for the measurement of the decay time difference. Electrons and positrons are accelerated to their final energies by the SLAC linear accelerator, then injected into PEP-II. PEP-II has a design luminosity of $3 \times 10^{33}\,\mathrm{cm}^{-2}s^{-1}$ and has achieved a luminosity four times higher.

The design and operation of the accelerator complex are the fruits of the labors of a diverse group of accelerator physicists, accelerator operators, engineers, and technicians. Much of the success of the *BABAR* experiment can be attributed to the success of the PEP-II team.

1.3 The *BABAR* Experiment

The *BABAR* detector is a general purpose particle physics detector, optimized for the detection of B meson decays in the high-luminosity, asymmetric-energy environment provided by the PEP-II collider. The detector will be described in detail in Chapter 3.

The *BABAR* Experiment is an international collaboration of physicists, with roughly 500 members at any given time. The detector was designed and built in the 1990s with data collection beginning in 1999, all long before the author was a member of the project. Data collection and processing for such a complicated detector is necessarily a collaborative effort. The analysis presented in this dissertation would not have been possible without the efforts of hundreds of physicists, engineers, and technicians. Additionally, the specific analysis presented here was a collaborative effort of several physicists.

1.4 Outline

In Chapter 2, a theoretical introduction to *CP* violation in B mesons is presented. A detailed description of the *BABAR* detector is given in Chapter 3. The measurement procedure is given in Chapter 4, including details of the event selection and fit

procedures. Conclusions are presented in Chapter 5. Appendix C presents the author's contribution to an effort to study the luminous region of the accelerator with unprecedented precision.

Chapter 2

Theory

2.1 Introduction to the Standard Model

2.1.1 The Fundamental Particles

The Standard Model of particle physics is a comprehensive description of the fundamental interactions of matter, excluding gravity. The fundamental particles are characterized by their masses and various quantum numbers, and by how they interact with the other particles. The fundamental fermions, with spin $\frac{1}{2}$, are classified into quarks and leptons, where the former carry the color charge of the strong interaction while the latter do not. The fundamental bosons, with spin 1, mediate the interactions between the fermions. The fundamental quarks, leptons, and bosons are listed in Tables 2.1, 2.2, and 2.3, respectively.

Both the quarks and leptons are groups into three "generations," each consisting of a pair of particles. The generations are similar in their properties, except that each successive generation is more massive than the previous one.

2.1.2 Mesons

Quarks are not found in isolation in nature, but rather are bound into colorless objects consisting of three quarks (baryons) or of a quark and antiquark (mesons). All of the key particles discussed in this work are mesons, and are listed in Table 2.4.

Table 2.1: A summary of the quarks [4]. The masses of the light quarks (d, u, s) are approximate.

Name	Symbol	Charge	Mass (MeV/c^2)
down	d	$-1/3$	$3-7$
up	u	$2/3$	$1.5-3.0$
strange	s	$-1/3$	95 ± 25
charm	c	$2/3$	$(1.25 \pm 0.09) \times 10^3$
bottom	b	$-1/3$	$(4.20 \pm 0.07) \times 10^3$
top	t	$2/3$	$(174.2 \pm 3.3) \times 10^3$

Table 2.2: A summary of the leptons [4]. Although the absolute masses of the neutrinos are poorly known, it is well-established via the observation of neutrino flavor oscillations that the masses are non-zero [4].

Name	Symbol	Charge	Mass (MeV/c^2)
electron	e	-1	0.511
electron neutrino	ν_e	0	$< 2 \times 10^{-6}$
muon	μ	-1	106
muon neutrino	ν_μ	0	< 0.19
tau	τ	-1	1777
tau neutrino	ν_τ	0	< 18.2

Table 2.3: A summary of the fundamental bosons [4]. Although it is predicted to exist in the SM, the Higgs boson has not been observed experimentally and is thus not listed.

Name	Symbol	Charge	Mass (GeV/c^2)	Mediated Interaction
photon	γ	0	0	Electromagnetic
W	$W^\pm$	± 1	80.403 ± 0.029	Weak
Z	Z^0	0	91.1876 ± 0.0021	Weak
gluon	g	0	0	Strong

Table 2.4: A summary of mesons most relevant to this thesis [4]. The quantum number J is the total spin. The C and P quantum numbers are discussed in Section 2.1.3. For particles that are not eigenstates of C, J^P is given instead of J^{PC}; for K^0_S and K^0_L, the C eigenvalue is only valid when CP violation is neglected. The quark content of the $f_0(980)$ is not known conclusively. The last column lists the modes of experimental interest in the environment of the *BABAR* detector; a particle is listed as "Stable in *BABAR*" if it is detected directly instead of reconstructed from its decay products.

Symbol	Charge	Mass (MeV/c^2)	J^{PC}	Quark Content	Principle Decay Modes
$\pi^{\pm}$	±1	139.57	0^{-}	$u\overline{d}$	Stable in *BABAR*
π^0	0	134.98	0^{-+}	$u\overline{u} - d\overline{d}$	$\gamma\gamma$
$K^{\pm}$	±1	493.68	0^{-}	$u\overline{s}$	Stable in *BABAR*
K^0_S	0	497.65	0^{--}	$d\overline{s} + \overline{d}s$	$\pi^+\pi^-,\ \pi^0\pi^0$
K^0_L	0	497.65	0^{-+}	$d\overline{s} - \overline{d}s$	Stable in *BABAR*
$f_0(980)$	0	980 ± 10	0^{++}	See caption	$\pi^+\pi^-,\ K^+K^-$
ϕ	0	1019.460 ± 0.019	1^{--}	$s\overline{s}$	$K^+K^-,\ K^0_SK^0_L$
B^0	0	5279.4 ± 0.5	0^{-}	$d\overline{b}$	Many
$\Upsilon(4S)$	0	10579.4	1^{--}	$b\overline{b}$	$B^0\overline{B}^0,\ B^+B^-$

2.1.3 Symmetries

The invariance of physics under a transformation is known as a symmetry of nature, and the study of symmetries is extremely important in both classical and modern physics. Noether's theorem tells us that there is a direct relation between continuous symmetries and conservation laws [5]. A famous example is a translation in space, which corresponds to the conservation of momentum. We will focus our attention on three discrete symmetries: parity, charge conjugation, and time reversal.

Parity

The parity operator $\mathcal{P}$ causes the inversion of all three spatial coordinates; for a four-vector this can be written as

$$(t,\ x,\ y,\ z) \rightarrow (t,\ -x,\ -y,\ -z).$$

The eigenvalues of $\mathcal{P}$ are ± 1, and the operator is multiplicative, so $\mathcal{P}^2 = 1$. Parity is conserved in the strong and electromagnetic interactions, and is thus a useful quantum number for analyzing many interactions. The mesons are classified according to their parity: spin zero mesons with even parity such as the $f_0(980)$ are known as scalars, while those with odd parity such as the π^0 are known as pseudoscalars. Similarly, spin one mesons with odd parity such as the ϕ are called vector mesons, while those with even parity are called pseudovectors (or axial vectors). The parity of a meson is related to the orbital angular momentum l of its constituents by the relation $\mathcal{P} = (-1)^{l+1}$.

Charge conjugation

The charge conjugation operator C converts a particle to its antiparticle. Only particles that are their own antiparticles can be eigenstates of C. The eigenvalues are ± 1, and are multiplicative. As with parity, C is conserved in strong and electromagnetic interactions, but is not conserved in weak interactions.

Time reversal and *CP*

The time-reversal operator T inverts the time component of the four-vector:

$$(t,\ x,\ y,\ z) \rightarrow (-t,\ x,\ y,\ z).$$

T symmetry is more difficult to access experimentally than the symmetries discussed above because no particle is an eigenstate of the operator. However, T violation has been observed experimentally by comparing, as a function of time, the probability of a $K^0 \rightarrow \overline{K}^0$ transition to the probability of a $\overline{K}^0 \rightarrow K^0$ transition [10]. Also, it is well established that Lorentz-invariant quantum field theories must be invariant under the combination of all three of the discrete symmetries described here, CPT. With CPT conservation assumed, the violation of T symmetry implies the violation of the combination of C and $\mathcal{P}$ symmetries, and vice versa. As mentioned in the Introduction, CP violation was discovered in the kaon system in 1964, and the study of CP violation in B meson decays is the main purpose of the *BABAR* experiment.

2.2 The Weak Interaction and the CKM Matrix

The weak interaction contains two classes of interactions: the charged-current interaction mediated by the W boson, and the neutral-current interaction mediated by the Z^0 boson. The latter process has the important property that it cannot change the flavor of the quark (or lepton) involved. Therefore it will not play a role in the flavor-changing processes that we will discuss. In a charged-current process, a quark emits a W boson and changes flavor to another type of quark. This process has a vertex factor of $\frac{-ig_w}{2\sqrt{2}}\gamma^\mu\left(1-\gamma^5\right)V_{qq'}$, where g_w is the weak coupling constant, γ^μ are Dirac matrices, and $V_{qq'}$ is an element of the Cabbibo-Kobayashi-Maskawa (CKM) quark-mixing matrix. The CKM matrix is a unitary matrix that expresses the mixing of the up-type quarks with the down-type quarks:

$$V_{\mathrm{CKM}} \equiv \begin{pmatrix} V_{ud} & V_{us} & V_{ub} \\ V_{cd} & V_{cs} & V_{cb} \\ V_{td} & V_{ts} & V_{tb} \end{pmatrix}. \tag{2.1}$$

Any 3×3 unitary matrix can be expressed in terms of four parameters (neglecting unphysical phases). The standard exact parameterization, in terms of the sines and cosines of three mixing angles plus one complex phase, can be found in The Review of Particle Physics (RPP) [4]. For our purposes the most useful form is the Wolfenstein parameterization,

$$V_{\mathrm{CKM}} = \begin{pmatrix} 1-\lambda_{\mathrm{CKM}}^2/2 & \lambda_{\mathrm{CKM}} & A\lambda_{\mathrm{CKM}}^3(\rho-i\eta) \\ -\lambda_{\mathrm{CKM}} & 1-\lambda_{\mathrm{CKM}}^2/2 & A\lambda_{\mathrm{CKM}}^2 \\ A\lambda_{\mathrm{CKM}}^3(1-\rho-i\eta) & -A\lambda_{\mathrm{CKM}}^2 & 1 \end{pmatrix} + \mathcal{O}(\lambda_{\mathrm{CKM}}^4), \tag{2.2}$$

which has a form inspired by the empirical observation that the magnitudes of the matrix elements are neatly expressed in terms of powers of $\lambda_{\mathrm{CKM}} \approx 0.22$. The potential for *CP* violation is created by the imaginary terms in this matrix. We can exploit the unitarity requirement, ${V_{\mathrm{CKM}}}^\dagger V_{\mathrm{CKM}} = 1$, to form several relations between

the matrix elements, including

$$V_{ud}V_{ub}^* + V_{cd}V_{cb}^* + V_{td}V_{tb}^* = 0. \tag{2.3}$$

This equation is used to construct a "unitarity triangle" in the complex plane, shown in Fig. 2.1 with the sides normalized to the $V_{cd}V_{cb}^*$ term. When normalized this way, the base of the triangle has unit length and the apex is at $(\bar{\rho}, \bar{\eta})$, where $\bar{\rho}$ and $\bar{\eta}$ are given by

$$\begin{aligned} \bar{\rho} &\equiv (1 - \lambda_{\rm CKM}^2/2)\rho, \text{ and} \\ \bar{\eta} &\equiv (1 - \lambda_{\rm CKM}^2/2)\eta. \end{aligned}$$

The angles of the triangle are

$$\begin{aligned} \alpha &\equiv \arg\left(-\frac{V_{td}V_{tb}^*}{V_{ud}V_{ub}^*}\right), \\ \beta &\equiv \arg\left(-\frac{V_{cd}V_{cb}^*}{V_{td}V_{tb}^*}\right), \text{ and} \\ \gamma &\equiv \arg\left(-\frac{V_{ud}V_{ub}^*}{V_{cd}V_{cb}^*}\right). \end{aligned} \tag{2.4}$$

The values of the CKM matrix parameters are not predicted by the SM, but rather must be measured experimentally. One of the main goals of the B Factory programs is to redundantly measure the angles and sides of the unitarity triangle, overconstraining the triangle and thus testing the CKM model. We will focus on the measurement of the angle β.

2.2.1 Mixing of B^0 Mesons

Although flavor-changing neutral currents are forbidden at tree level, they are easily achieved through loop diagrams. One example, known as a box diagram, is shown in Fig. 2.2, where the exchange of a pair of W bosons allows a B^0 meson to transform into a $\overline{B}^0$ meson. (Note that there is an equally valid diagram obtained by swapping the W bosons and top quarks.) In this section we will study the details of this process,

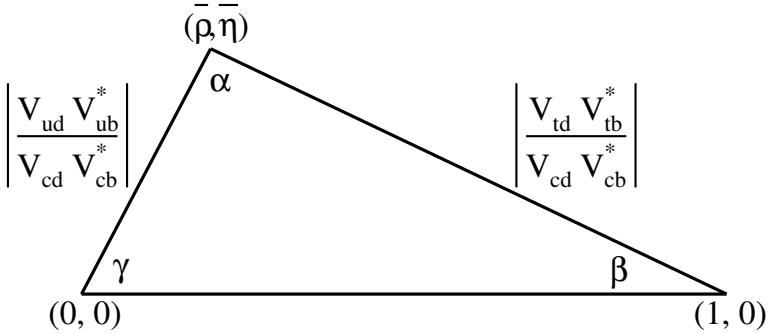

Figure 2.1: The unitarity triangle showing the CKM angles α, β, and γ.

known as B^0 mixing.

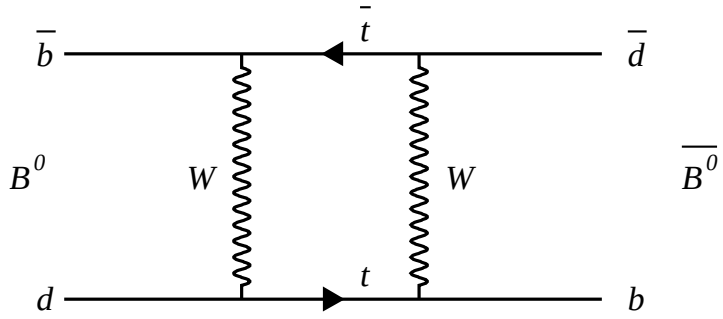

Figure 2.2: The Feynman diagram of the dominant amplitude for B^0-$\overline{B}^0$ mixing. Similar diagrams where u or c quarks replace the t quarks are suppressed by factors of $(m_q/m_W)^2$.

The B^0 and $\overline{B}^0$ mesons are flavor eigenstates with definite quark content, but are not the mass eigenstates that propagate through space. For a linear combination of flavor eigenstates $a|B^0\rangle + b|\overline{B}^0\rangle$, the time evolution is governed by a time-dependent Schrodinger equation,

$$i\frac{d}{dt}\begin{pmatrix} a \\ b \end{pmatrix} = \mathcal{H}\begin{pmatrix} a \\ b \end{pmatrix} = \left(M - \frac{i}{2}\Gamma\right)\begin{pmatrix} a \\ b \end{pmatrix}, \tag{2.5}$$

where M and Γ are 2×2 Hermitian matrices, and $\mathcal{H}_{11} = \mathcal{H}_{22}$ due to CPT symmetry.

Solving the eigenvalue problem, we can write the mass eigenstates in terms of linear combinations of the flavor eigenstates:

$$\begin{aligned} |B_L\rangle &= pB^0 + q\overline{B}^0, \\ |B_H\rangle &= pB^0 - q\overline{B}^0, \end{aligned} \tag{2.6}$$

where the subscripts L and H refer to the lighter and heavier eigenstates, respectively, and p and q are complex numbers, normalized so that $|q|^2 + |p|^2 = 1$. The mass and width splitting between the eigenstates can be written in terms of the real and imaginary parts of the difference between the eigenvalues:

$$\Delta m \equiv m_H - m_L = 2\mathcal{R}e\sqrt{(M_{12} - \frac{i}{2}\Gamma_{12})(M_{12}^* - \frac{i}{2}\Gamma_{12}^*)} \tag{2.7}$$

$$\Delta\Gamma \equiv \Gamma_H - \Gamma_L = -2\mathcal{I}m\sqrt{(M_{12} - \frac{i}{2}\Gamma_{12})(M_{12}^* - \frac{i}{2}\Gamma_{12}^*)}. \tag{2.8}$$

We can then derive the relations

$$(\Delta m)^2 - \frac{1}{4}(\Delta\Gamma)^2 = 4\left[|M_{12}|^2 - \frac{1}{4}|\Gamma_{12}|^2\right], \text{and} \tag{2.9}$$

$$\Delta m \Delta\Gamma = 4\mathcal{R}e M_{12}^* \Gamma_{12}, \tag{2.10}$$

as well as an expression for the ratio q/p:

$$\frac{q}{p} = -\frac{\Delta m - \frac{i}{2}\Delta\Gamma}{2(M_{12} - \frac{i}{2}\Gamma_{12})}. \tag{2.11}$$

We can simplify these relations by noting the current experimental values $\Delta\Gamma/\Gamma = 0.009 \pm 0.037$ and $\Delta m/\Gamma = 0.776 \pm 0.008$ [4], implying that $\Delta\Gamma \ll \Delta m$. Applying

this, we find that, to a good approximation,

$$\begin{aligned} \Delta m &= 2|M_{12}|, & (2.12)\\ \Delta\Gamma &= 2\mathcal{R}e(M_{12}\Gamma_{12}^{*})/|M_{12}|, \text{and} & (2.13)\\ q/p &= -|M_{12}|/M_{12}. & (2.14) \end{aligned}$$

The matrix element M_{12} can be calculated by evaluating the amplitude corresponding to the box diagram shown in Fig. 2.2, plus all the other subleading amplitudes that also contribute to the process. The dominant amplitude depends on the CKM matrix elements V_{td} and V_{tb}, as well as several factors that depend on the hadronic physics of the B^0 meson. Fortunately we will see that *CP* violation depends largely on q/p, with many of the hadronic quantities canceling in the ratio.

The mixing of a state that is purely B^0 at time $t = 0$, $|B^0_{\rm phys}\rangle$, and similarly for a state that begins as purely $\overline{B}^0$, $|\overline{B}^0_{\rm phys}\rangle$, proceeds according to

$$\begin{aligned} |B^0_{\rm phys}\rangle &= e^{-iM_Bt}e^{-\Gamma t/2}\left[\cos(\Delta mt/2)|B^0\rangle + i(q/p)\sin(\Delta mt/2)|\overline{B}^0\rangle\right],\\ |\overline{B}^0_{\rm phys}\rangle &= e^{-iM_Bt}e^{-\Gamma t/2}\left[i(p/q)\sin(\Delta mt/2)|B^0\rangle + \cos(\Delta mt/2)|\overline{B}^0\rangle\right], \quad (2.15) \end{aligned}$$

where $M_B = \frac{1}{2}(m_H + m_L)$.

A constraint is imposed on the flavor oscillations given in Eq. 2.15 by the fact that the B^0 and $\overline{B}^0$ mesons measured by *BABAR* are produced in decays of the $\Upsilon(4S)$ to a coherent $L = 1$ state. As the mesons evolve in time, the constraint implies that there is always exactly one B^0 and one $\overline{B}^0$ present. After one of the mesons decays, the other continues to evolve in time.

2.2.2 *CP* Violation in B Mesons

Violations of *CP* symmetry can manifest themselves in several ways:

1. *CP* violation in decay, where the total amplitude for a decay and its *CP* conjugate process have unequal magnitudes.

2. *CP* violation in mixing, where the neutral mass eigenstates are admixtures of

the *CP* eigenstates.

3. *CP* violation in the interference between decays with and without mixing, where both B^0 and $\overline{B}^0$ can decay into a common final state.

We define the decay amplitudes to a final state f as:

$$\mathcal{A}_f \equiv \langle f|\mathcal{H}|B^0\rangle,$$
$$\bar{\mathcal{A}}_{\bar{f}} \equiv \langle \bar{f}|\mathcal{H}|\overline{B}^0\rangle,$$

where the latter definition is for the *CP* conjugate process.

CP Violation in Decay

In the SM, the total decay amplitude $\mathcal{A}_f$ can be written in terms of a sum of amplitudes with magnitudes $\mathcal{A}_i$, strong phases δ_i, and weak phases φ_i. The magnitudes and strong phases are conserved under *CP* conjugation, while the weak phases change sign. The ratio in Eq. 2.17 is then given by

$$\left|\frac{\bar{\mathcal{A}}_{\bar{f}}}{\mathcal{A}_f}\right| = \left|\frac{\sum_i \mathcal{A}_i e^{i(\delta_i-\varphi_i)}}{\sum_i \mathcal{A}_i e^{i(\delta_i+\varphi_i)}}\right|. \tag{2.16}$$

If all the phases φ_i are equal, an overall factor of $\exp(-2i\varphi_i)$ factors out of the sums and the ratio is equal to one. However, if there are weak phase differences,

$$\left|\frac{\bar{\mathcal{A}}_{\bar{f}}}{\mathcal{A}_f}\right| \neq 1, \tag{2.17}$$

implying direct *CP* violation. The size of this deviation depends on the strong amplitudes as well as the weak phases, and so is difficult to predict theoretically.

CP Violation in Mixing

$$|q/p| \neq 1 \tag{2.18}$$

implies *CP* violation in mixing. The SM predicts $|q/p|$ to equal unity to a part in 10^3. Consistent with this prediction, the current experimental value is $|q/p| =$

1.0015 ± 0.0039 [4]. We will assume $|q/p| = 1$ in future calculations.

CP Violation in the Interference between Decays with and without Mixing

The final manifestation of *CP* violation is in the interference between decays without mixing, $B^0 \to f$, and those with mixing, $B^0 \to \overline{B}^0 \to f$, to a common final state f. Obviously, this effect is limited to final states f that are accessible to both B^0 and $\overline{B}^0$. This type of *CP* violation is defined by

$$\mathcal{I}m\left(\frac{q}{p}\frac{\bar{\mathcal{A}}_f}{\mathcal{A}_f}\right) \neq 0. \tag{2.19}$$

Continuing from the expressions for the mixing of the B^0 and $\overline{B}^0$ mesons (Eq. 2.15), we can write an expression for the total decay rate of a B^0-$\overline{B}^0$ pair. This expression can be simplified if we impose the condition that one meson has decayed to a final state that uniquely identifies, or "tags," its flavor. (An example is the decay $B^0 \to D^-\ell^+\nu_\ell$, where the charge of the lepton ℓ identifies the flavor of the B meson.) Given this condition, the decay rate as a function of the decay times $t_{\rm tag}$ and t_{CP} is

$$\begin{aligned} R \;\propto\; & e^{-\Gamma(t_{\rm tag}+t_{CP})} \times \\ & \left\{|\mathcal{A}_f|^2 + |\bar{\mathcal{A}}_f|^2 \mp 2\mathcal{I}m\left[\frac{q}{p}\mathcal{A}_f^*\bar{\mathcal{A}}_f\right]\sin\Delta m\Delta t \pm (|\mathcal{A}_f|^2 - |\bar{\mathcal{A}}_f|^2)\cos\Delta m\Delta t\right\}, \end{aligned} \tag{2.20}$$

where the upper (lower) signs correspond to the tagging meson decaying as a $\overline{B}^0$ (B^0), and $\Delta t \equiv t_{CP} - t_{\rm tag}$. Dependence on the individual decay times can be integrated out, giving an expression that depends only on the observable Δt.

The time-dependent rate asymmetry is defined as

$$a(\Delta t) \;\equiv\; \frac{R(\overline{B}^0 \to f) - R(B^0 \to f)}{R(\overline{B}^0 \to f) + R(B^0 \to f)} \tag{2.21}$$

$$= \frac{2\mathcal{I}m\left[\frac{q}{p}\mathcal{A}_f^*\bar{\mathcal{A}}_f\right]\sin\Delta m\Delta t - (|\mathcal{A}_f|^2 - |\bar{\mathcal{A}}_f|^2)\cos\Delta m\Delta t}{|\mathcal{A}_f|^2 + |\bar{\mathcal{A}}_f|^2}. \tag{2.22}$$

The term proportional to $\cos\Delta m\Delta t$ is non-zero only in the case of direct *CP* violation (*CP* violation in decay). The first term, proportional to $\sin\Delta m\Delta t$, is the result of *CP* violation caused by the interference of decays with and without mixing. For simplicity, the expression in Eq. 2.22 is often written as

$$a(\Delta t) = S\sin\Delta m\Delta t - C\cos\Delta m\Delta t, \tag{2.23}$$

where S and C are parameters to be measured experimentally.

Unlike *CP* violation in decay, the *CP* violation in the interference between decays with and without mixing can be reliably calculated in the SM. Looking at the diagram in Fig. 2.2 and using the expression in Eq. 2.14, we find that

$$\frac{q}{p} = \frac{V_{tb}^* V_{td}}{V_{tb} V_{td}^*}. \tag{2.24}$$

The evaluation of the decay amplitude $\mathcal{A}_f$ depends on the final state in question. For the decay $B^0 \to J/\psi\, K^0$, the dominant amplitude is given by the tree diagram shown in Fig. 2.3. From this diagram we see that the amplitude is proportional to $V_{cb}^* V_{cs}$. The mixing of the K^0 introduces another factor proportional to $V_{cd} V_{cs}^*$. Plugging these expressions into Eq. 2.19, we find

$$\begin{aligned}
\mathcal{I}m\left[\frac{q}{p}\frac{\bar{\mathcal{A}}_f}{\mathcal{A}_f}\right] &= \mathcal{I}m\left[\left(\frac{V_{tb}^* V_{td}}{V_{tb} V_{td}^*}\right)\left(\frac{V_{cb} V_{cs}^*}{V_{cb}^* V_{cs}}\right)\left(\frac{V_{cd}^* V_{cs}}{V_{cd} V_{cs}^*}\right)\right] \\
&= \mathcal{I}m\left[\left(\frac{V_{tb}^* V_{td}}{V_{tb} V_{td}^*}\right)\left(\frac{V_{cb} V_{cd}^*}{V_{cb}^* V_{cd}}\right)\right] \\
&= \mathcal{I}m\frac{V_{td}}{V_{td}^*},
\end{aligned} \tag{2.25}$$

where in the last step we have used the fact that most of the CKM matrix elements are real in the Wolfenstein parameterization (Eq. 2.2). This leads to the SM prediction that in $B^0 \to J/\psi\, K^0$,

$$-\eta_f S_{J/\psi\, K^0} = \sin 2\beta,\ C_{J/\psi\, K^0} = 0, \tag{2.26}$$

where η_f is the *CP* eigenvalue of the final state.

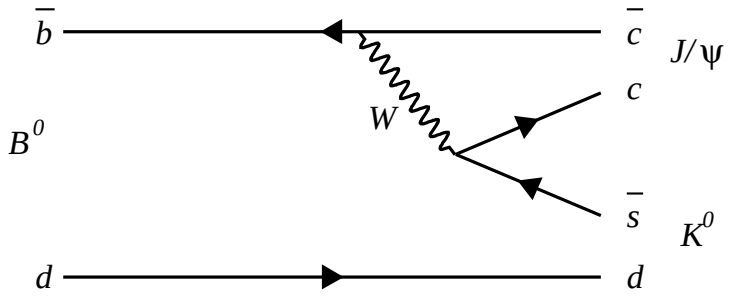

Figure 2.3: The dominant amplitude for the decay $B^0 \to J/\psi\, K^0$.

This prediction is accurate to better than 1% in the SM, since contributions from diagrams with a weak phase are highly suppressed compared to the dominant tree amplitude. Because of this low theoretical uncertainty, the decay $B^0 \to J/\psi\, K^0$ and related $b \to c\bar{c}s$ decays are known as the "Golden Mode," providing a clean environment for measuring the angle β in the SM. The current experimental value, $S_{J/\psi\, K} = 0.685 \pm 0.032$ [4, 11], agrees well with other measurements and supports the CKM explanation of *CP* violation in the SM.

2.3 *CP* Violation in $b \to s\bar{s}s$

With the SM value of $\sin 2\beta$ precisely measured using $b \to c\bar{c}s$ decays, one is interested in measurements that might show deviations from the SM that would be hidden in the tree-dominated decays. The dominant amplitude in $b \to s\bar{s}s$ decays is a loop diagram, also known as a "penguin" diagram. An example is shown in Fig. 2.4, illustrating the specific process $B^0 \to \phi K^0$. Other $b \to s$ processes have similar diagrams and the same short-distance physics.

The analysis of *CP* violation for this class of decays is the same as for the $B^0 \to J/\psi\, K^0$ decay shown in the previous section. The CKM matrix elements entering through the decay amplitude are real in the Wolfenstein parameterization, with a

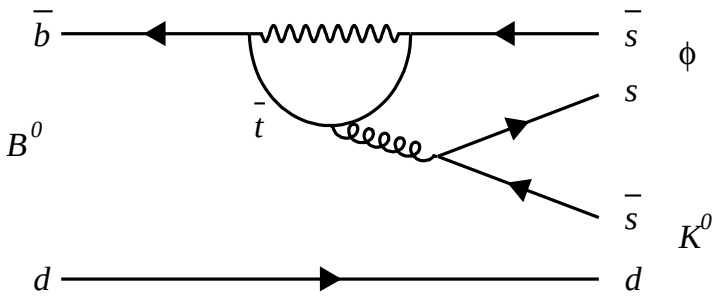

Figure 2.4: The dominant amplitude for the decay $B^0 \to \phi K^0$.

relative weak phase introduced by the q/p factor from B^0-$\overline{B}^0$ mixing. The SM predicts

$$-\eta_f S_{b\to s\overline{s}s} = \sin 2\beta_{\mathit{eff}},\ C_{b\to s\overline{s}s} = 0, \tag{2.27}$$

where $\beta_{\mathit{eff}} = \beta$ as long as we neglect hadronic uncertainties, which depend on the exact final state being considered. (We will use β_{eff} as the symbol for the effective value of β measured in penguin-dominated decays, while reserving the symbol β for the SM value measured in the Golden Mode.) The overall rate of the decay will be smaller in the SM than for the $b \to c\overline{c}s$ transitions, but the expected CP asymmetry is the same.

Loop diagrams offer the possibility that physics beyond the SM, sometimes called "New Physics" (NP), could contribute significantly. Just as the top quark and W boson enter the SM loop amplitude, a NP amplitude could have heavy non-SM particles in the loop. An example diagram of a NP process is shown in Fig. 2.5. If such a diagram exists, it would contribute at the same order as the dominant SM diagram, and the effects of NP could be observable [12].

To illustrate this effect, consider the case where the total decay amplitude $\mathcal{A}_f$ contains contributions from both the SM diagram (Fig. 2.4) and a NP diagram (Fig. 2.5).

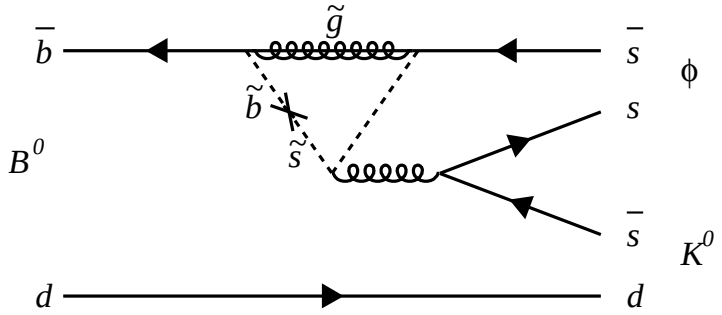

Figure 2.5: An example of a diagram for a flavor-changing neutral current process beyond the SM. Squarks and a gluino replace the top quark and W boson of the SM diagram.

Using similar notation to Eq. 2.16, we can write this as

$$\begin{aligned} \mathcal{A}_f &= \mathcal{A}_{SM} e^{i\delta_{SM}} + \mathcal{A}_{NP} e^{i(\delta_{NP}+\varphi_{NP})}, \\ \bar{\mathcal{A}}_f &= \mathcal{A}_{SM} e^{i\delta_{SM}} + \mathcal{A}_{NP} e^{i(\delta_{NP}-\varphi_{NP})}, \end{aligned} \tag{2.28}$$

where we have assumed that the relative weak phase between the SM and NP decay amplitudes is φ_{NP}. Defining $r_{NP} \equiv \mathcal{A}_{NP}/\mathcal{A}_{SM}$, to first order in r_{NP} the coefficients S and C are

$$S = \sin 2\beta - 2r_{NP} \cos 2\beta \sin \varphi_{NP} \cos \delta_{SM-NP}, \tag{2.29}$$

$$C = 2r_{NP} \sin \varphi_{NP} \sin \delta_{SM-NP}, \tag{2.30}$$

where $\delta_{SM-NP} = \delta_{SM} - \delta_{NP}$ [13]. As one would expect, these expressions reduce to the SM expectation given in Eq. 2.27 when either $r_{NP} = 0$ or $\varphi_{NP} = 0$.

Note that there is nothing preventing NP processes from contributing to the total decay amplitude in $b \to c\bar{c}s$ decays such as $B^0 \to J/\psi K^0$. However, the SM tree amplitude will have a much larger contribution than any NP loop amplitude, and the value of r_{NP} will be small. Because the dominant SM amplitude in $b \to s\bar{s}s$ decays is itself a loop, r_{NP} has the potential to be much larger. Also note that we have not

considered the possibility of NP contributions to the B^0-$\overline{B}^0$ mixing amplitude. Such contributions would change the measured *CP* asymmetry identically in both $b \to c\overline{c}s$ and $b \to s\overline{s}s$ decays, which is disfavored by the precision measurement of $S_{J/\psi K^0}$.

2.4 Analysis of $B^0 \to K^+K^-K^0$

The Feynman diagram shown in Fig. 2.4 illustrates the dominant amplitude for the decay $B^0 \to \phi K^0$. This is an ideal mode for the study of *CP* violation in $b \to s\overline{s}s$ transitions because ϕK^0_S and ϕK^0_L are *CP* eigenstates, and the ϕ resonance is easy to select experimentally because of its narrow width. Also, as will be discussed in Section 2.4.4, the hadronic uncertainties in this mode are relatively small. However, $B^0 \to \phi K^0$ decays account for only about 15% of the total $B^0 \to K^+K^-K^0$ rate. By measuring the *CP* asymmetries in all $B^0 \to K^+K^-K^0$ decays (an "inclusive" measurement), the sensitivity of the measurement can be increased significantly.

2.4.1 Quasi-Two Body Method

In order to measure the *CP* asymmetries in the inclusive decay, at the minimum we must split the sample into *CP*-odd and *CP*-even subsamples, and estimate the purity of the *CP* content of each subsample. This "quasi-two body" method is the original experimental approach used by both *BABAR* and Belle. As mentioned, the ϕK^0 subdecay is a *CP* eigenstate and can be analyzed without complication, although care must be taken to estimate the amount of *CP*-even contamination of the sample.[1] (Also, interference between decay amplitudes will be ignored.) Outside the ϕ region of phase space, the *CP* content is not known a priori. However, measurements using an isospin method, which relates the rate in $B^0 \to K^+K^-K^0$ to the rate in $B^+ \to K^+K^0_SK^0_S$, indicated that this region is largely *CP*-even. Measurements of the *CP* asymmetries in this region can then be made, using the measurement of the *CP*-even fraction to interpret the results. Again, any effects caused by interference between

[1] Throughout this work, I will refer to measurements of decays including a K^0 as shorthand for individual measurements of the K^0_S and K^0_L states.

decay amplitudes will be ignored, introducing a systematic error of a difficult to quantify size.

2.4.2 Parameterization of the Decay Amplitude

A more comprehensive approach to measuring the *CP* asymmetries in the inclusive three-body decay involves modeling the total decay amplitude over the entire phase space. This type of amplitude analysis, often called a "Dalitz plot analysis," is commonly used to understand the decay dynamics of three-body decays. The decay amplitudes $\mathcal{A}_f$ that enter into the decay rate for a B^0-$\overline{B}^0$ pair as shown in Eq. 2.20 are functions of the position of the decay in the allowed phase space. For the decay of a spin zero particle such as a B^0 to three pseudoscalar daughters (called a, b, and c in this section), the kinematics can be described completely by two kinematic variables. The most common choice is to use two invariant masses of daughter pairs, $m^2_{ab} \equiv (p_a + p_b)^2$ and $m^2_{ac} \equiv (p_a + p_c)^2$.

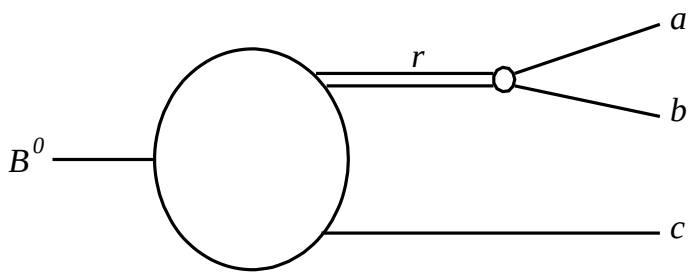

Figure 2.6: An illustration of the isobar model, where the decay of the B^0 is a two-body process followed by the subsequent decay of the resonance r.

Figure 2.6 illustrates the concept of the *isobar model* [14]. In this picture the decay of the B^0 is considered a two step process; first $B^0 \to rc$, then $r \to ab$. Here r is a resonance such as the $\phi(1020)$ or the $f_0(980)$. Each similar contribution is known as an *isobar*, and the total amplitudes are given by the sum over the amplitudes of the

isobars:

$$\begin{aligned} \mathcal{A}_f &= \sum_r C_r f_r, \\ \bar{\mathcal{A}}_f &= \sum_r \bar{C}_r \bar{f}_r, \end{aligned} \tag{2.31}$$

where C_r and $\bar{C}_r$ are complex numbers that must be determined in a fit to the data. The amplitudes f_r and $\bar{f}_r$ are described below. We parameterize these complex coefficients in terms of four real-valued variables as follows:

$$\begin{aligned} C_r &\equiv c_r(1+b_r)e^{i(\varphi_r+\delta_r)} \\ \bar{C}_r &\equiv c_r(1-b_r)e^{i(\varphi_r-\delta_r)}. \end{aligned} \tag{2.32}$$

We will refer to the average magnitude and phase c_r and φ_r as the *isobar coefficients*, while we will call the parameters b_r and δ_r the *CP asymmetry parameters*.

The amplitude f_r for the process shown in Fig. 2.6 is

$$\begin{aligned} f_r &= \sum_\lambda \langle ab|r_\lambda\rangle T_r(m_{ab}) \langle cr_\lambda|B^0\rangle \\ &= Z_L(\vec{p},\vec{q}) F_L^{B^0}(|\vec{p}|) F_L^r(|\vec{q}|) T_r(m_{ab}), \end{aligned} \tag{2.33}$$

where the sum is over the helicity states λ of r. L is the orbital angular momentum between r and c, and $\vec{p}$ and $\vec{q}$ are the momenta of c and a, respectively, in the rest frame of r. Z_L is a function that describes the angular distribution of the final-state particles, and F^{B^0} (F^r) is a barrier factor for the production of the rc (ab) system. Finally, $T_r(m_{ab})$ is a dynamical function describing the resonance r.

Angular Distributions

When the resonance r is a scalar, $L = 0$ and the angular distribution is isotropic: $Z_0 = 1$. For other spins, the angular distribution of the final-state particles is described using the Zemach formalism [15]. An alternative formalism, used by CLEO [16], is

derived as follows. For the case of a vector resonance,

$$\begin{aligned} Z_1 &= (p_{B^0} + p_c)_\mu \sum_\lambda \epsilon_\lambda^{*\mu} \epsilon_\lambda{}^\nu (p_a - p_b)_\nu & (2.34) \\ &= (p_{B^0} + p_c)_\mu \left[-g^{\mu\nu} + \frac{(p_a + p_b)^\mu (p_a + p_b)^\nu}{m_{ab}^2} \right] (p_a - p_b)_\nu \\ &= (m_{ac}^2 - m_{bc}^2) + (m_{B^0}^2 - m_c^2)(m_b^2 - m_a^2)/m_{ab}^2, & (2.35) \\ &= -4\vec{q} \cdot \vec{p}. & (2.36) \end{aligned}$$

In Eq. 2.34, ϵ_λ is the polarization vector and the sum is over all helicity states $\lambda = \{+, 0, -\}$. Note that the end result in Eq. 2.36 is identical to the Zemach form. CLEO takes the additional step of relaxing the transversality requirement, replacing m_{ab}^2 with m_r^2 in the denominator in Eq. 2.35, which also breaks the equality with Eq. 2.36. We do not do this, and use the simpler Zemach form.[2]

Table 2.5 summarizes the expressions for angular distributions, rewritten in terms of the helicity angle $\cos\theta_H = \vec{p} \cdot \vec{q}/(|\vec{p}||\vec{q}|)$. Expressions for spin 2 are listed for completeness, although they are not used in this analysis.

Barrier Factors

For angular momentum to be conserved in a resonance decay, the spin J of the resonance must be translated into orbital angular momentum L of the resonance daughters. This is modeled by a "centrifugal" potential that varies as a function of the radius ρ,

$$U_L(\rho) = \frac{\hbar^2 L(L+1)}{2m_r\rho^2} \quad (\text{for } \rho > R), \tag{2.37}$$

where R is the meson radius [17]. Higher angular momentum leads to a higher potential barrier to be overcome in the decay. Solving the Schrodinger equation for this potential gives the solutions listed in Table 2.5 as functions of $z = |\vec{q}|R$ and $z_0 = |\vec{q_0}|R$, where $|\vec{q_0}|$ is the value of $|\vec{q}|$ when $m_{ab} = m_r$. We choose a convention

[2]Note that our fitting code actually returns $4\vec{q} \cdot \vec{p}$ (no minus sign). This difference, like any difference in overall normalization, is accommodated in the isobar coefficients and does not change the shape of the resonance.

where the barrier factors are equal to one when $z = z_0$, and use $R = 1.5\,\mathrm{GeV}^{-1}$. The barrier factor for the decay of the B^0 can be neglected, so $F^{B^0} = 1$.

Table 2.5: The spin dependence of the Blatt-Weisskopf form factors and the angular distribution of resonance daughters.

Spin	$F_L(z)$	$Z_L(\cos\theta_H)$
0	1	1
1	$\sqrt{\frac{1+z_0^2}{1+z^2}}$	$-4\lvert\vec{q}\rvert\lvert\vec{p}\rvert\cos\theta_H$
2	$\sqrt{\frac{9+3z_0^2+z_0^4}{9+3z^2+z^4}}$	$\lvert\vec{q}\rvert^2\lvert\vec{p}\rvert^2(3\cos^2\theta_H - 1)$

Decay Dynamics

The dynamical function $T_r(m_{ab})$ describes the lineshape of the resonance r. For most resonances the relativistic Breit-Wigner form,

$$T_r(m_{ab}) = \frac{1}{m_r^2 - m_{ab}^2 - im_r\Gamma(|\vec{q}|)}, \tag{2.38}$$

is used. The mass-dependent width is given by

$$\Gamma(|\vec{q}|) = \Gamma_r \left(\frac{|\vec{q}|}{|\vec{q_0}|}\right)^{2L+1} \frac{m_r}{m_{ab}} {F_L}^2, \tag{2.39}$$

where F_L is the Blatt-Weisskopf barrier factor from Table 2.5.

The Breit-Wigner form is useful for modeling the lineshape of single-channel, single-pole resonances. The $f_0(980)$ is a two-channel decay to $\pi^+\pi^-$ and K^+K^-, and so is better modeled by a coupled-channel lineshape as proposed by Flatté [18]. In this case,

$$T_r(m_{ab}) = \frac{1}{m_r^2 - m_{ab}^2 - im_r\Gamma_{tot}}, \tag{2.40}$$

where

$$\begin{aligned}\Gamma_{tot} &= \Gamma_K + \Gamma_\pi \\ &= \frac{g_K}{m_{ab}}\sqrt{m_{ab}^2 - 4m_K^2} + \frac{g_\pi}{m_{ab}}\sqrt{m_{ab}^2 - 4m_\pi^2}. \end{aligned} \tag{2.41}$$

m_K and m_π are the masses of the charged kaon and pion, respectively. The constants $g_\pi = 0.165 \pm 0.010 \pm 0.015\,\mathrm{GeV}/c^2$ and $g_K/g_\pi = 4.21 \pm 0.25 \pm 0.21$ are taken from the BES experiment [19]. Note that the literature contains a number of parameterizations and parameters for the $f_0(980)$. The BES data are obtained from J/ψ decays to both $\phi\pi^+\pi^-$ and ϕK^+K^-. Other experiments obtain data on the $f_0(980)$ from $\phi(1020)$ decays where the available phase space is very limited [20], or from the decay $D_s^+ \to \pi^+\pi^-\pi^+$ where the K^+K^- channel is not measured [21]. We feel the BES data are most applicable to our measurements.

Definition of the Helicity Angle

We define the helicity angle θ_H as the angle between the K^+ and the K^0 in the rest frame of the K^+K^- system. Because of this definition, for vector resonances there is a sign flip between the amplitude for B^0 decay and the amplitude for $\overline{B}^0$ decay:

$$\bar{f}_{L=1} = -f_{L=1}. \tag{2.42}$$

For resonances with even L, $\bar{f} = f$.

Non-Resonant Amplitudes

Previous studies of Dalitz plot (DP) structures in three-body decays of D and B mesons have found that in order to describe the data, models must include "non-resonant" amplitudes in addition to resonant terms. In D decays, it has been sufficient to parameterize the non-resonant contribution as a constant complex number with no dependence on DP location. In B decays, however, the available phase space is much larger and more complicated models are necessary.

Theoretical studies of charmless three-body B decays include the use of heavy

meson chiral perturbation theory (HMChPT) to calculate inclusive branching fractions [22]. However, results obtained with this method have predicted rates much higher than the measured values, because HMChPT is only valid in a small amount of the three-body phase space (where two of the daughters are soft) [23]. Alternatively, HMChPT can be applied in a more limited fashion, using other methods to compute the relevant form factors [24]. This approach suffers from the opposite problem — the calculated non-resonant contribution is too small compared with the experimental results reported here and in the preliminary version of this analysis [25]. In the absence of strong theoretical guidance, we take an empirical approach to modeling the non-resonant contributions.

In $B^+ \to K^+K^-K^+$ decays, an exponential shape $f_{NR} = \exp(\alpha_{NR} m^2_{K^+K^-})$ has been used to fit the data, where $\alpha_{NR} = 0.14 \pm 0.02\,\mathrm{GeV}^{-2}c^4$ is a parameter determined in the fit [26, 27]. We generalize that form to include three non-resonant amplitudes:

$$\begin{aligned} f_{NR,K^+K^-} &= \exp(-\alpha_{NR} m^2_{K^+K^-}), \\ f_{NR,K^+K^0} &= \exp(-\alpha_{NR} m^2_{K^+K^0}), \text{ and} \\ f_{NR,K^-K^0} &= \exp(-\alpha_{NR} m^2_{K^-K^0}). \end{aligned} \tag{2.43}$$

2.4.3 Dalitz Plot Model

We construct a Dalitz plot model based on previous measurements made by *BABAR* and Belle. As noted in the preceding section, the similar decay $B^+ \to K^+K^-K^+$ has been studied using DP analyses. The $\phi(1020)$, $f_0(980)$, χ_{c0}, and non-resonant component (discussed in the previous section) were included in the model. In addition, a wide spin-zero resonance near $1500\,\mathrm{MeV}/c^2$, which we will call the $X_0(1550)$, was found to be necessary to fully describe the data. Other scalar resonances (for example, the $f_0(1710)$) were found not to be statistically significant.

In the $B^0 \to K^+K^-K^0_S$ mode, *BABAR* previously reported the results of an angular moments analysis, where the amplitude is analyzed as the sum of partial waves [28]. This analysis found that outside of the $\phi(1020)$ region, the decay is dominated by S-wave contributions, including an excess of events around $1500\,\mathrm{MeV}/c^2$. No evidence

was found of D-wave (or higher) contributions.

Based on known branching fractions [4], we expect to see some contribution from decays of charged D mesons. Because of the long lifetime of the D meson, these will not interfere with other amplitudes and so are incoherently added to the DP model.

Based on these experimental inputs, our nominal model for the decay amplitude consists of the components given in Table 2.6.

Table 2.6: Components of the Dalitz plot model. Parameters are from Ref. [4] unless otherwise noted. RBW stands for relativistic Breit-Wigner. Details of the parameterizations of the $f_0(980)$ and non-resonant components are given in the text.

Component	Lineshape	Mass (MeV/c^2)	Width (MeV/c^2)	Source
$f_0(980)$	Flatté	965 ± 10	See text	[19]
$\phi(1020)$	RBW	1019.456 ± 0.019	4.26 ± 0.05	
$X_0(1550)$	RBW	1539 ± 20	257 ± 33	[27]
NR K^+K^-	Eq. 2.43			[27]
NR K^+K^0	Eq. 2.43			[27]
NR K^-K^0	Eq. 2.43			[27]
χ_{c0}	RBW	3415.19 ± 0.35	10.1 ± 0.7	
D^-	Gaussian	1869.4 ± 0.4	6.7 ± 1.0	Width from MC
D_s^-	Gaussian	1968.3 ± 0.5	6.7 ± 1.0	Width from MC

2.4.4 Standard Model Uncertainties

If we observe a deviation of β_{eff} from the SM value of β, we must take into account possible SM effects on the value of β_{eff}.

Several theorists have made calculations of the possible deviations of β_{eff} from β within the SM. Decays through a resonance, such as ϕK^0, are easier to calculate than the non-resonant decays. Using QCD factorization, the value of $\Delta S_{SM} \equiv \sin 2\beta_{\mathit{eff}} - \sin 2\beta$ is estimated to be small ($\Delta S_{SM} = 0.02 \pm 0.01$) for ϕK^0 decays [29, 30].

The color-allowed (but CKM suppressed) tree diagram shown in Fig. 2.7 could cause ΔS_{SM} to be as large as $\mathcal{O}(10\%)$ for inclusive $K^+K^-K^0$. (It cannot contribute to ϕK^0.) However, with the aid of the Dalitz plot model from this analysis, Ref. [25] derives a value for $K^+K^-K^0$ of $\Delta S_{SM} = 0.047^{+0.028}_{-0.033}$.

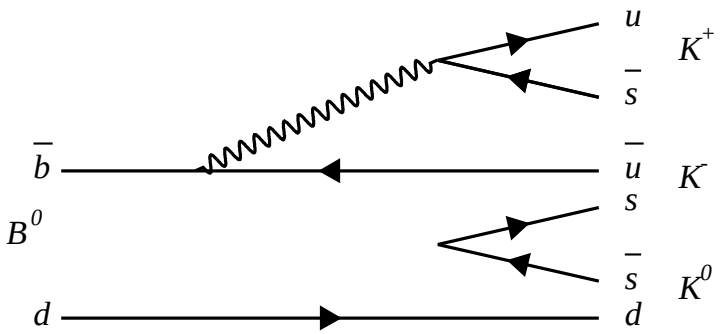

Figure 2.7: Subleading tree amplitude contributing to $B^0 \to K^+K^-K^0$.

Chapter 3

PEP-II and the *BABAR* Detector

As discussed in the Introduction, the PEP-II accelerator and *BABAR* detector were designed to create and detect a large number of B meson pairs in order to study CP violation. This section presents a more thorough introduction to the accelerator and its operation. The interested reader can find more detail on the accelerator, including some discussion of basic accelerator physics, in Appendix C. This section also presents a summary of the *BABAR* detector and its subsystems. Unless otherwise noted, the content of this section is derived from Ref. [31].

3.1 The PEP-II Accelerator

The B Factory complex consists of the SLAC linear accelerator (linac) and the PEP-II storage rings. Electrons from an electron gun are accelerated starting at the beginning of the linac, then extracted into a damping ring to reduce the emittance of the beam, and finally returned to the linac where they are further accelerated through Sector 8 (out of 30). At this point they are extracted at the full energy of 9.0 GeV into a bypass line. This bypass transports the electrons the rest of the length of the linac to the high energy ring (HER) of PEP-II. Some electrons are accelerated through 19 sectors of the linac, where they are extracted and collided with a tungsten target to create electron-positron pairs. The positrons are extracted from these collisions into a positron return line, which transports them back to the beginning of the linac.

Similarly to the electrons, the emittance of this beam is reduced by passing it through a dampling ring. The positrons are then accelerated to 3.1 GeV in the first four sectors of the linac, extracted into their own bypass line, and transported to the low energy ring (LER) of PEP-II [32].

The HER is stacked on top of the LER in the pre-existing 2.2- km PEP tunnel. The beams intersect at one interaction point (IP), which is surrounded by the *BABAR* detector. The beams collide head-on, brought together and subsequently separated by a pair of permanent dipole magnets. Operating parameters for PEP-II are given in Table 3.1. The RF frequency is 476 MHz, but to avoid parasitic crossings of the beams away from the IP only every other bucket can be filled, leading to a minimum time between bunch crossings of about 4 ns.

Table 3.1: Design beam parameters at the PEP-II IP. The numbers in parentheses are the best-achieved values (not necessarily simultaneously).

	LER (e^+)	**HER** (e^-)	Units
Energy	3.1	9.0	GeV
ϵ_x/ϵ_y	64/2.6	48/1.9	nm-rad
β_x^*/β_y^*	37.5/1.5	50/2.0	cm
σ_x^*/σ_y^*	155/6.2	155/6.2	μm
σ_x'/σ_y'	0.4/0.4	0.3/0.3	mrad
Current	2140 (3213)	990 (2069)	mA
$N_{\rm bunch}$	1658 (1722)		
$\mathcal{L}$	3 (12) $\times 10^{33}$		$\rm cm^{-2}s^{-1}$

The nominal energies of 9.0 GeV and 3.1 GeV give a collision energy in the CM frame of 10.58 GeV, the peak of the $\Upsilon(4S)$ resonance. Approximately 10% of the data is collected with the CM energy lowered to about 40 MeV below the $\Upsilon(4S)$ peak, below the threshold for production of B meson pairs, providing a control data sample free of B mesons. Data collected at this lower energy are known as *offpeak*, while data taken at the $\Upsilon(4S)$ are called *onpeak*.

For the first several years of operation, *BABAR* collected data continuously in blocks ("runs") of just under one hour. At the end of each run, the detector high-voltage was ramped down to a safe state and PEP-II was refilled to the nominal currents from

the linac. Subsequently, PEP-II was operated in a mode known as *trickle injection*, in which electrons and positrons were injected at a rate of up to 10 Hz each without interrupting data collection by *BABAR*. This mode of operation has several obvious advantages: there is no need to regularly stop data collection, and beam currents and thus luminosity are continuously maintained at peak values. Also, the non-changing accelerator configuration tends to lead to greater stability of accelerator operations, with fewer beam losses. Note that *BABAR* continued to break the data collection into runs of about 55 minutes, even after the implementation of trickle injection. However, the amount of time lost at each run transition is on the order of a second, rather than the roughly five minutes required to refill the accelerator.

3.2 The *BABAR* Detector

The *BABAR* detector is a general-purpose particle physics detector, optimized for the study of *CP* violation in B mesons in the asymmetric-energy environment of PEP-II. Key design requirements are described here.

- A large acceptance in the CM frame, implying that the detector must be asymmetric with more acceptance in the direction of the HER beam;
- good reconstruction efficiency down to low momenta, to allow the efficient reconstruction of rare B meson decay modes;
- good vertex resolution, for measurement of the distance between decays of B mesons;
- excellent particle identification, in particular identification of leptons and discrimination between pions and kaons for tagging the flavor of neutral B meson decays;
- the ability to operate and process data in a high-luminosity environment.

Schematic views of the detector are shown in Fig. 3.1 (end view) and Fig. 3.2 (side view). The key subdetectors, starting near the beam pipe and working outwards, are the following:

- Silicon Vertex Tracker (SVT), for tracking and precision vertex measurements;
- Drift Chamber (DCH), for tracking and momentum measurements;
- Detector of Internally Reflected Cherenkov light (DIRC), for particle identification (PID);
- Electromagnetic Calorimeter (EMC), for detection of neutral particles; and
- Instrumented Flux Return (IFR), consisting of resistive plate chambers (RPC) and limited streamer tubes (LST), for detection of long-lived particles.

All of the subdetectors are used in the analysis presented here, and are described in more detail below. Note that the center of the detector is offset from the IP by about 37 cm in the direction of the HER beam.

In addition to the subdetectors listed above, the superconducting solenoid magnet that surrounds the EMC is crucial for physics measurements. It provides a 1.5-Tesla magnetic field, approximately parallel to the direction of the HER beam, to allow momentum measurements of charged particles in the DCH. The field is quite uniform, with a maximum variation of 2.5% within the tracking volume. The azimuthal component of the magnetic field does not exceed 1 mT.

The *BABAR* coordinate system is defined with respect to the DCH because it is both the primary tracking detector and a stable frame of reference. The z-axis runs down the center of the DCH, with $+z$ (the "forward" direction) in the direction of the HER beam. The $+x$ direction points outward from the center of the PEP-II rings, and the $+y$ direction points vertically upward. This forms a right-handed coordinate system.

3.2.1 Silicon Vertex Tracker

The SVT makes precise measurements of charged particle trajectories very close to the IP. This is essential for reconstructing the decay vertices of B mesons, which are produced nearly at rest in the CM frame and thus decay near the IP. Precise measurement of B^0 decay vertices is essential for time-dependent CP asymmetry

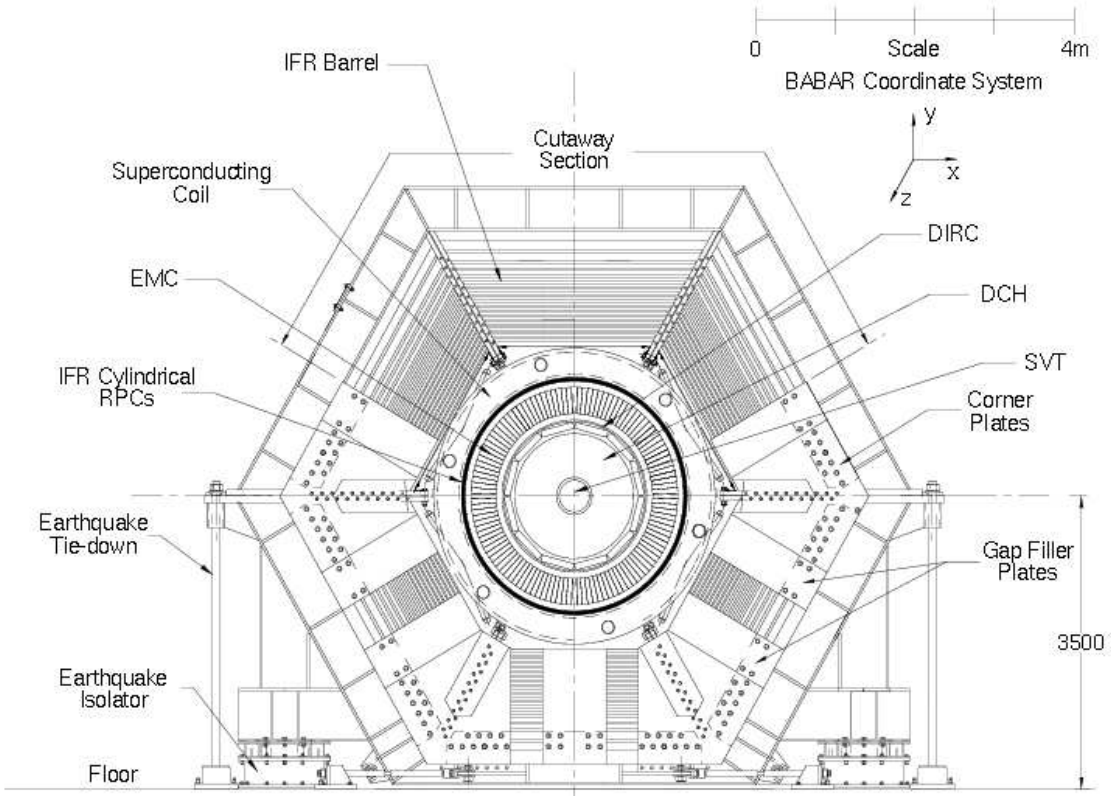

Figure 3.1: Schematic of the *BABAR* detector as viewed along the beam pipe. Dimensions are given in millimeters.

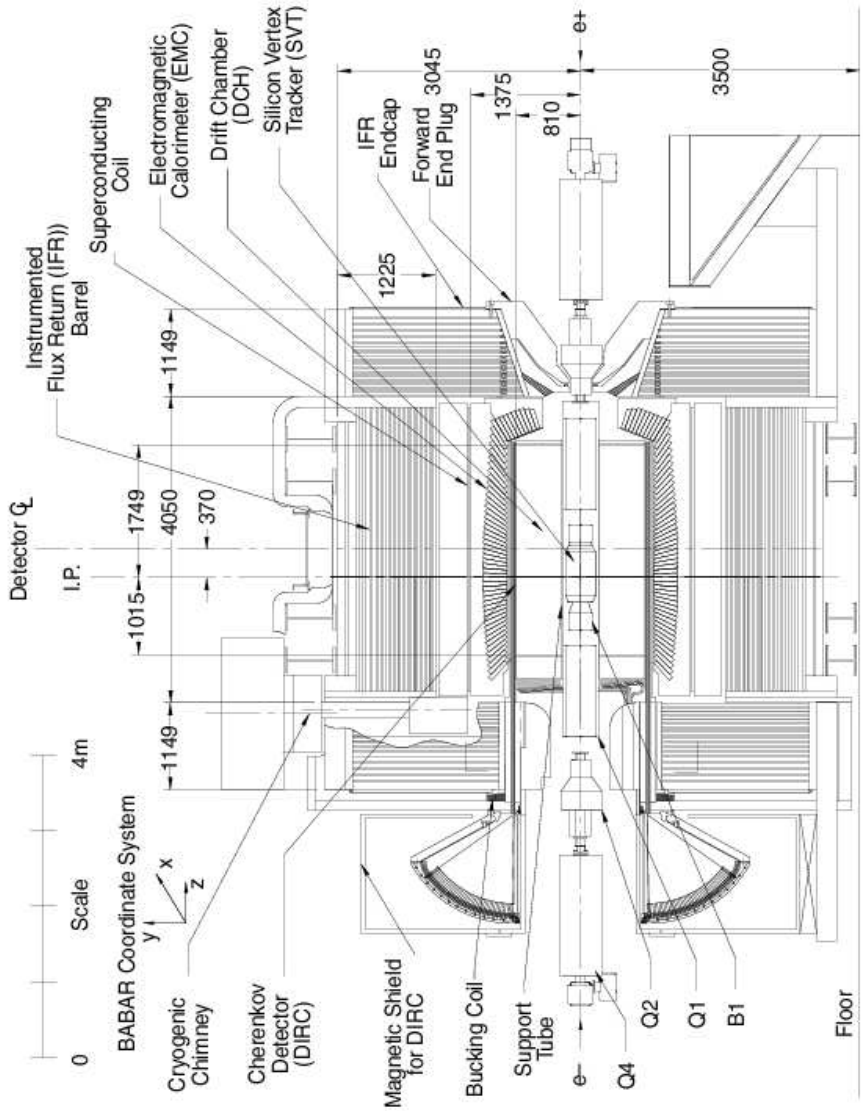

Figure 3.2: Schematic of the *BABAR* detector as viewed from the side. Dimensions are given in millimeters.

measurements. For these measurements, the vertex resolution along the z-axis for a fully reconstructed B decay must be better than $80\,\mu$m on average. The SVT must also provide standalone reconstruction of low-momentum tracks. Particles with transverse momentum $p_T < 120\,\mathrm{MeV}/c$ are not reliably measured by the DCH and so must be reconstructed solely with the SVT. Many B meson decays result in particles of low p_T, most notably the slow pion from the decay of the $D^{*\pm}$. The SVT also makes the most precise measurements of track angles, which for high-momentum tracks is particularly important as an input to measurements made by the DIRC. $\mathrm{d}E/\mathrm{d}x$ measurements made by the SVT are used directly for particle identification of low-momentum tracks.

The SVT consists of five layers of double-sided silicon strip sensors. Strips on one side of each sensor are oriented parallel to the beam and measure the azimuthal angle (ϕ strips), while the strips on the other side are transversely oriented and measure the z position (z strips). The inner three layers dominate the vertex measurement precision and are located just outside the beam pipe. They are mounted parallel to the beam in a hexagonal shape with a slight overlap between modules. The outer two layers are at a larger radius to allow for standalone tracking, and also play an important role in measuring charged pions from K^0_S decays. To minimize the amount of silicon required and make the angle of incidence closer to normal for particles near the edge of the acceptance, they are mounted in arch-shaped modules. Layers 4 and 5 consist of 16 and 18 modules, respectively. The geometry of the SVT layers is shown in Figures 3.3 and 3.4. Note that the forward acceptance angle of 350 mrad is limited by the magnets used to bring the beams into head-on collision. The backward acceptance angle is less critical because of the forward boost of the CM system. The geometric acceptance of the SVT in the CM system is 90%.

The SVT sensors are $300\,\mu$m thick, and the total area of the silicon is $0.96\,\mathrm{m}^2$. The sensors are reverse-biased and held at a voltage about 10 V above the depletion voltage. Typical depletion voltages are $25-35$ V. A charged particle passing through the silicon creates electron-hole pairs. The electrons and holes move in opposite directions in the electric field caused by the bias voltage. ϕ strips in each half-module are connected with wire bonds, forming a single readout strip. z strips are individually

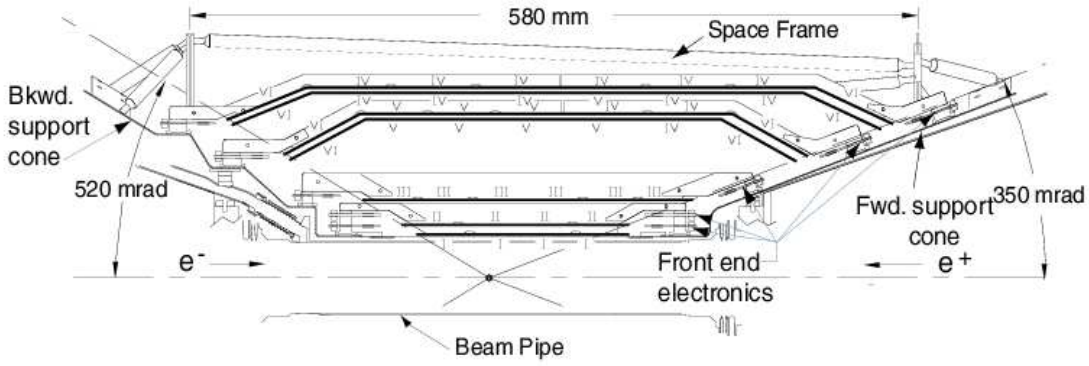

Figure 3.3: A cutaway side view of the SVT.

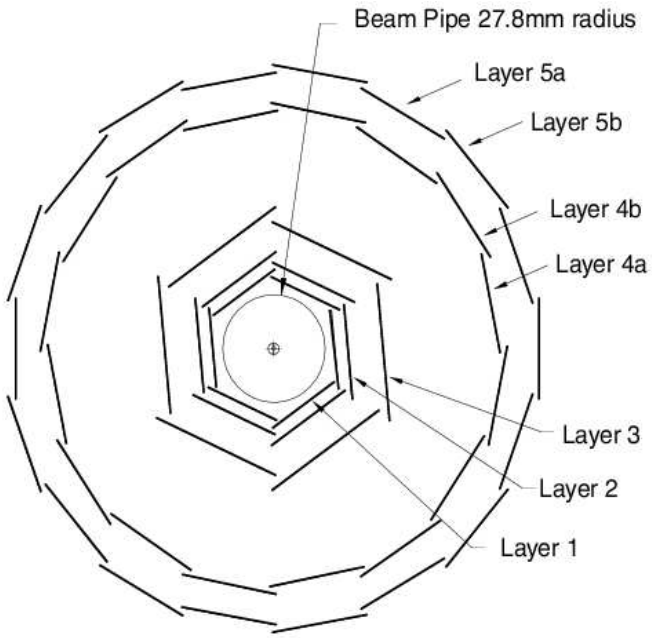

Figure 3.4: Schematic end-on view of the SVT sensor modules.

Table 3.2: Details of the SVT geometry.

Layer	Radius (mm)	Readout pitch (μm)	Floating strips	Strip length (mm)
$1z$	32	100	1	40
1ϕ	32	50 (100)	0 (1)	82
$2z$	40	100	1	48
2ϕ	40	55 (110)	0 (1)	88
$3z$	54	100	1	70
3ϕ	54	110	1	128
$4z$	91-127	210	1	104
4ϕ	91-127	100	1	224
$5z$	114-144	210	1	104
5ϕ	114-144	100	1	265

readout through fanout circuits in the inner three layers. In the outer layers pairs of z strips are ganged together for readout, introducing an ambiguity that is resolved during pattern recognition. To lower the number of readout channels necessary, most modules have a floating strip interleaved between strips that are readout. Details of the SVT geometry are given in Table 3.2.

The main component of the SVT front end electronics is a custom chip known as A Time-Over-Threshold Machine (ATOM). On the ATOM chip, signals are processed by a charge-sensitive preamplifier with a selectable gain. They are then passed to a shaper, followed by a programmable-threshold comparator. The output of the threshold comparator is sampled at 15 MHz and stored in a buffer. Upon receipt of a Level 1 (L1) trigger, the time and time-over-threshold are sparsified and stored in a second, smaller buffer. If the L1 trigger subsequently accepts the event, these data as well as the address of the SVT strip are delivered to the readout module.

The SVT occupancy is dominated by machine backgrounds and is highest in the horizontal plane of the innermost layer. After applying a time correction to account for the delay between the particle transversing the sensor and the signal passing over threshold, hits with times more than 200 ns from the event time as determined by the DCH are discarded. Remaining hits are grouped into clusters according to their geometry and timing.

SVT performance is benchmarked using two-prong events ($e^+e^- \to e^+e^-$ and $e^+e^- \to \mu^+\mu^-$). Hit resolution is calculated from distributions of residuals between reconstructed track trajectories and hit positions. For the inner three layers, the hit resolution varies from 15 to 35 μm. In Layers 4 and 5, the ϕ hit resolution is about 15 μm, while the z hit resolution ranges from 40 to 50 μm. Excluding defective sections, the average hit efficiency of the SVT is 97%.

Alignment of the SVT is an important issue. The local alignment, which consists of determining the relative positions of the 340 silicon sensors, is done first. Performed using dimuon, cosmic ray, and some hadronic events, the local alignment is a complex fit to all six degrees of freedom for each sensor. The sensors are relatively stable with respect to each other, so the local alignment is done relatively infrequently. The secondary alignment, known as the global alignment, corrects for movements of the SVT with respect to the rest of the detector. The SVT is attached to the inside of the 4.5 m-long beryllium support tube, which is attached to the accelerator and independent of the rest of *BABAR*. As a result, the SVT moves significantly with respect to the DCH on relatively short time scales due to factors such as temperature variations. The global alignment algorithm fits for rotations and translations of the SVT as a whole in order to minimize the differences between tracks fit using information from the SVT only and tracks fit using the DCH. Much simpler than the local alignment, the global alignment is updated once per run.

3.2.2 Drift Chamber

The drift chamber is the main tracking detector for charged particles. It is the main source of momentum measurements. It is also crucial for reconstruction of the K^0_S, which often decays outside or near the edge of the SVT. The DCH provides time measurements critical for triggering. Measurements of $\mathrm{d}E/\mathrm{d}x$ made by the DCH are used for PID for low-momentum tracks.

The DCH is a 3 m long cylinder with an outer radius of about 81 cm. Radially, the DCH extends from the outside of the support tube to the inside of the DIRC. Exact dimensions are shown in Fig. 3.5. As with the SVT, the detector is asymmetric

to account for the asymmetric beam energies. The electronics and high-voltage cards and cables are all mounted on the backward end.

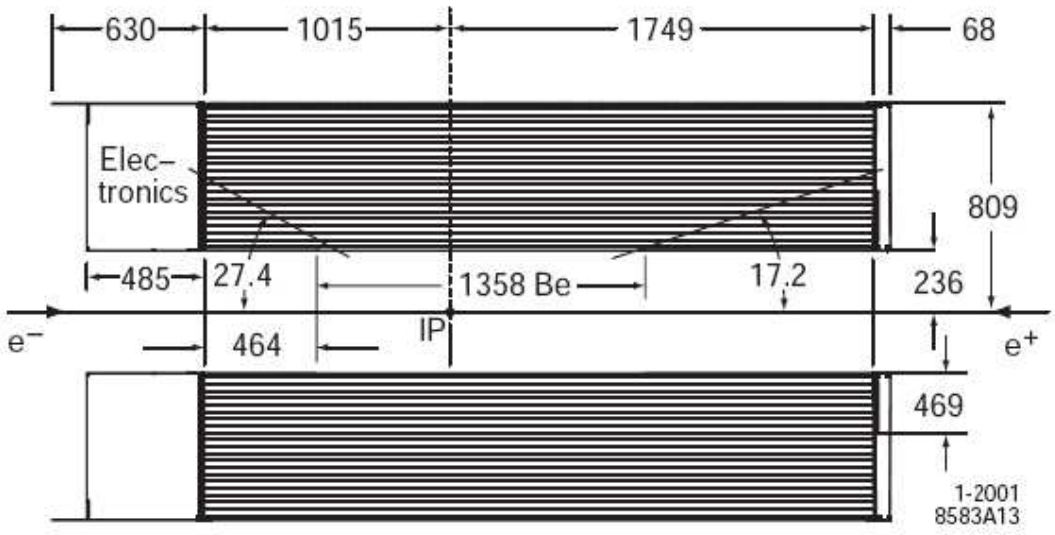

Figure 3.5: A schematic side view of the DCH. Lengths are given in millimeters; angles are given in degrees.

The inner cylindrical wall was kept as thin as possible to reduce multiple scattering and conversions, therefore improving momentum resolution, SVT to DCH track matching, and backgrounds in the EMC. To further reduce mass, the field wires are made of aluminum and the drift gas is an 80:20 mixture of helium:isobutane. At normal incidence, the DCH thickness is 1.08% of a radiation length (X_0), where $0.2\%X_0$ comes from the wires and gas. The outer wall was also made as thin as possible to avoid degrading the performance of the DIRC and EMC. The forward endcap wall is also kept to a thickness of 12 mm at a radius great than 46.9 cm (compared to 24 mm at lower radii) in order to reduce the material seen by particles entering the EMC.

The DCH wires are arranged in 40 cylindrical layers, grouped in 10 superlayers. The wires form small hexagonal cells (7104 in total), where each cell has one sense wire at the center surrounded by six field wires. This arrangement is shown in Fig. 3.6. Individual cells are 11.9 mm in the radial direction by 19.0 mm azimuthally. For tracks with $p_T > 180\,\mathrm{MeV}/c$, 40 measurements of position and energy loss are possible. The

wires in six of the superlayers are tilted with respect to the z-axis, allowing the DCH to provide longitudinal position information. Axial (A) superlayers, with wires parallel to the z-axis, are followed by a pair of stereo (U, V) superlayers, with tilted wires, to give an overall arrangement of AUVAUVAUVA. Further details on the superlayer geometry are given in Table 3.3.

Table 3.3: Geometry of the superlayer structure of the DCH. The radius listed is the radius of the innermost sense wire. The ranges of cell widths and angles are due to variation over the layers in a superlayer. Widths and radii are specified at the center of the chamber.

Superlayer number	Number of cells	Radius (mm)	Width (mm)	Angle (mrad)
1	96	260.4	17.0-19.4	0
2	112	312.4	17.5-19.5	45-50
3	128	363.4	17.8-19.6	-(53-57)
4	144	422.7	18.4-20.0	0
5	176	476.6	16.9-18.2	56-60
6	192	526.1	17.2-18.3	-(63-57)
7	208	585.4	17.7-18.8	0
8	224	636.7	17.8-18.8	65-69
9	240	688.0	18.0-18.9	-(72-76)
10	256	747.2	18.3-19.2	0

Passage of a charged particle through the drift chamber leaves a trail of ionization in the drift chamber gas. The rate of ionization is listed in Table 3.4. The sense wires are held at a positive high voltage, causing freed electrons to drift towards them. (Field wires are held at ground.) In the vicinity of the sense wire, the drifting electrons accelerate and cause an avalanche of secondary ionizations. The positive ions left behind by this process cause an image charge to form on the sense wire, which can be readout by the electronics connected to the wire. The sense wire voltage was 1930 V for most of *BABAR* operation, with brief periods at 1900 V and 1960 V in the first year of operation. These voltages yield an avalanche gain of about 5×10^4.

The DCH electronics are housed in front-end assemblies (FEAs), which are mounted directly onto the rear endplate. Each of the 16 azimuthally-symmetric sectors of the DCH has three FEAs. The sectors are separated by brass bars that

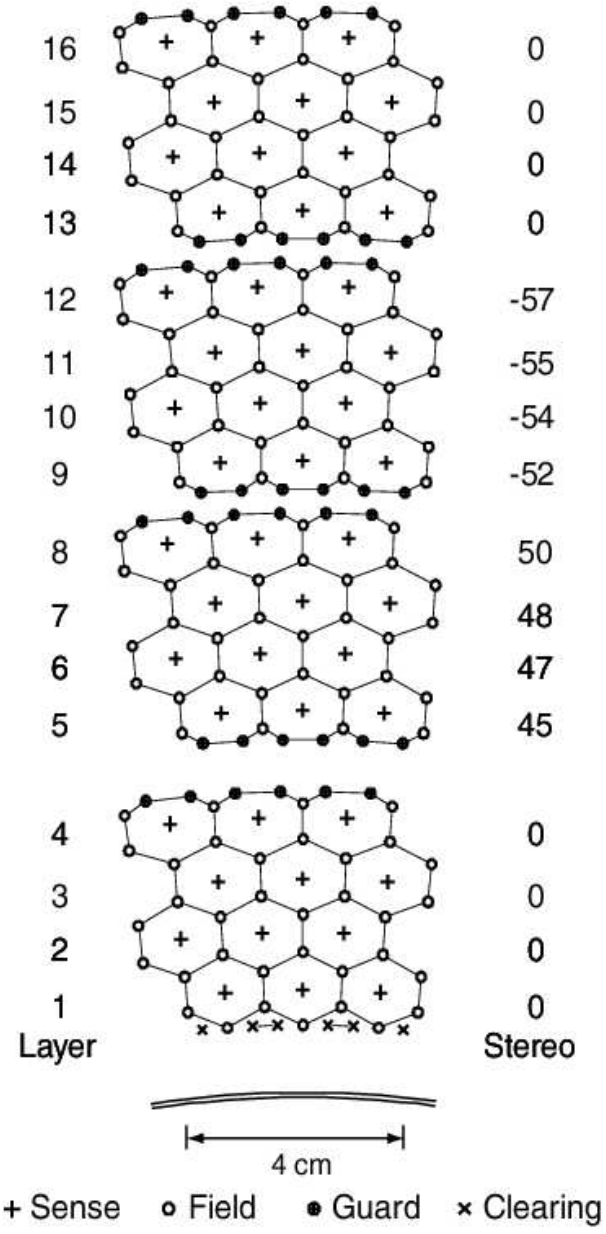

Figure 3.6: Schematic layout of the drift chamber cells for the four innermost superlayers. The stereo angles of the sense wires are given on the right in mrad. Lines are shown connecting the field wires to illustrate the cell boundaries. Guard wires are used to match the gain of boundary cells to that of inner cells. Clearing wires collect charge created by photon conversions in the DCH walls.

Table 3.4: Properties of the DCH gas mixture of 80% helium and 20% isobutane. The drift velocity is given for zero magnetic field, while the Lorentz angle is for the nominal 1.5 T field.

Parameter	Value
Radiation length	807 m
Primary ions	21.2/ cm
Drift velocity	22 μm/ ns
Lorentz angle	32°
dE/dx Resolution	6.9%

provide mechanical support and water cooling. Service boards connect the sense wires to the FEAs, where the signals are amplified and digitized. The custom amplifier circuit produces both a discriminator output signal for drift time measurement and a shaped analog signal for dE/dx measurement. Digitized signals are held in a buffer until receipt of an accept signal from the L1 trigger.

The leading edge of the amplified signal is used to determine the position of the primary ionization. The digitizer achieves 1 ns precision for leading edge timing. Samples of Bhabha and dimuon events are used to calibrate the conversion from drift time to drift distance. The position resolution of the DCH is best for tracks passing about 5 mm from the sense wire, where the resolution is 0.1 mm. Resolution degrades to about 0.25 mm at the center of the cell and up to 0.4 mm at the cell edges.

The specific energy loss, dE/dx, is measured for each drift cell as part of the feature extraction algorithm in the ROM. dE/dx for a track is computed as the truncated mean of the lowest 80% of the measurements for the individual cells contributing to the track. Various corrections are applied to correct for variations in pressure, temperature, and cell geometry. Global corrections are more important to the resolution than corrections to individual cells. A sample of dE/dx data from the DCH is shown in Fig. 3.7.

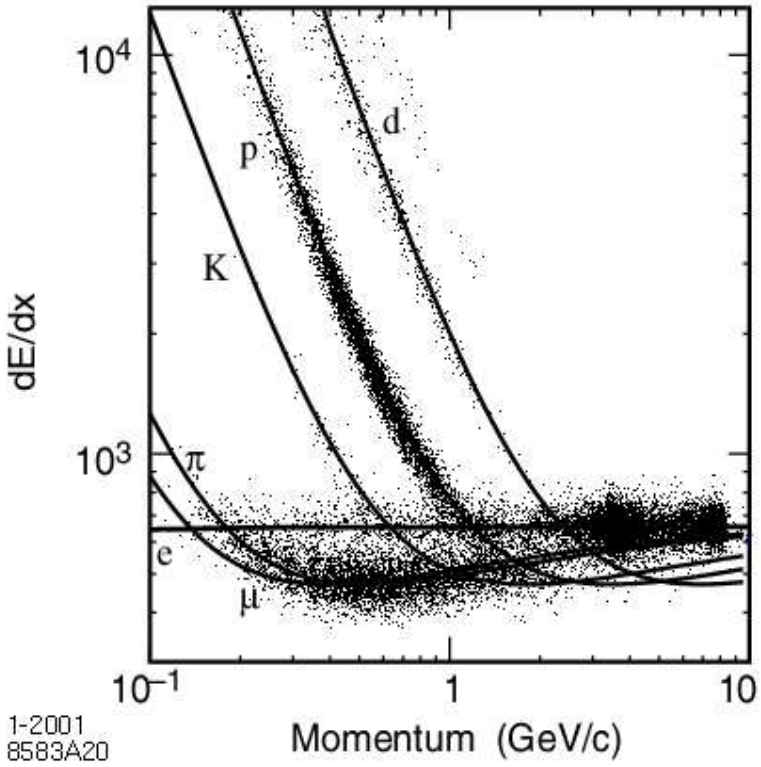

Figure 3.7: Measurement of $\mathrm{d}E/\mathrm{d}x$ in the DCH as a function of momentum for tracks recorded with beam background triggers. The curves are those predicted by the Bethe-Bloch formula.

3.2.3 Detector of Internally Reflected Cherenkov Light

Identification of particles, in particular the discrimination of kaons from pions, is important for *BABAR* in general and particularly important for the analysis presented here. One of the main methods of tagging the flavor of B^0 decays is to identify kaons from the common decay chain $b \to c \to s$. Also, because we reconstruct a final state with two charged kaons, efficient PID with a low fake rate is essential for separating the relatively rare signal from similar decays with pions in the final state. As shown in Fig. 3.7, the discrimination between pions and kaons provided by $\mathrm{d}E/\mathrm{d}x$ measurements is good only up to momenta of about $700\,\mathrm{MeV}/c$. For higher momentum tracks, *BABAR* relies on a novel detector of Cherenkov light known as the DIRC. Cherenkov light provides a measurement of the particle's velocity via the relation $\cos\theta_C = c/(nv)$, where θ_C is the angle of the Cherenkov light cone with respect to the particle's direction, c is the speed of light, n is the index of refraction of the detector material, and v is the particle velocity.

The DIRC needs to be as thin as possible, both geometrically and in terms of radiation lengths. Extra material and size would degrade the resolution of the EMC and make the EMC more expensive, respectively. To meet this challenge, the barrel of the DIRC consists of 144 radiator bars made of fused silica. The bars are only 17.25 mm thick, with a width of 35.00 mm. They are 4.9 m long to stretch the length of the barrel. At normal incidence, the DIRC is 80 mm in the radial extent including all supports, and has a thickness of $17\%X_0$. The bars have a geometrical acceptance of 94% azimuthally and 83% of the polar angle cosine.

Particles traversing the bars with $v/c \approx 1$ emit Cherenkov radiation that is internally reflected in the bar. The forward ends of the bars are covered with mirrors. At the backward end, photons pass through a wedge designed to reflect photons at large angles relative to the bar axis and photons that reflect off the silica-water boundary. The photons then emerge into a water-filled *standoff box*. The standoff box is outfitted with photomultiplier tubes (PMTs) to measure the position and timing of the Cherenkov photons. The DIRC is shown schematically in Fig. 3.8, and to scale in Fig. 3.9.

The radiator bars are housed in 12 hermetically-sealed aluminum *bar boxes*. The

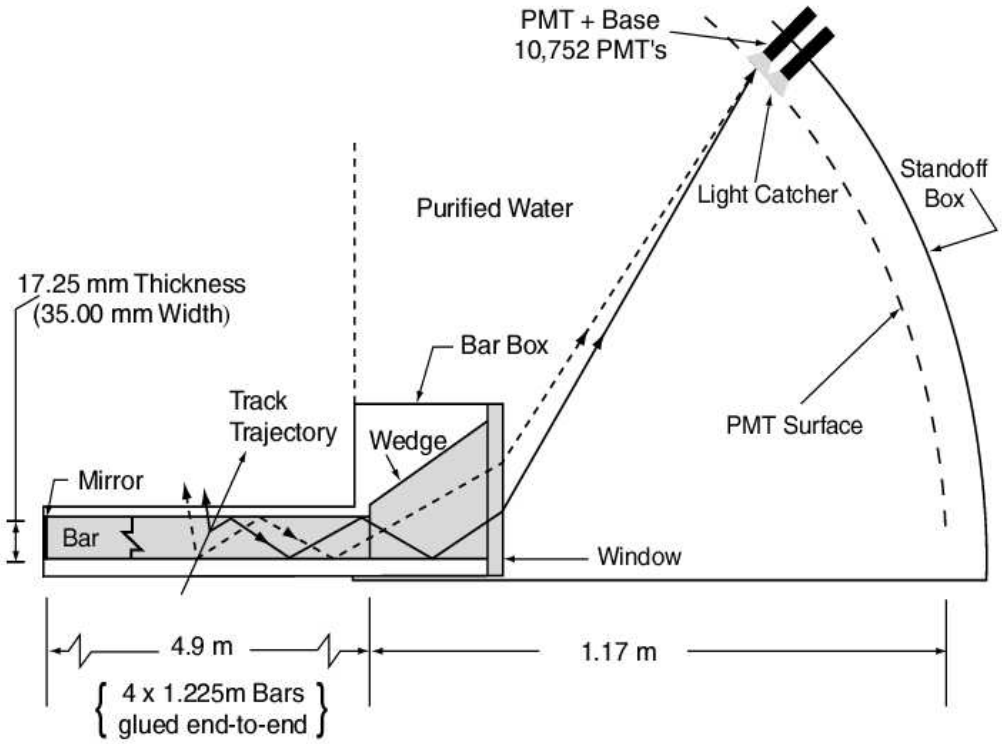

Figure 3.8: Schematic view of the propagation of photons from the DIRC radiator bars, through the wedge, and into the water-filled standoff box. The backward end of *BABAR* is to the right in the diagram.

bars are optically isolated from each other within each bar box. Fused silica is an ideal material for the radiator bars because of its radiation hardness, high light transmission, large index of refraction ($n = 1.473$), low chromatic dispersion, and the ability to achieve a good optical finish on the bar surfaces. Each bar has its own wedge at the forward end, made of the same material as the bar. The wedges in a bar box are glued to a common fused silica window with a thickness of 10 mm. The standoff box is made of stainless steel and holds about 6000 l of purified water. Water is used because it is inexpensive and has optical properties similar to fused silica. A steel shield surrounds the standoff box, which, in conjunction with the bucking coil, reduces the magnetic field in the PMT region to less than 1 G.

There are 12 sectors of 896 PMTs each, mounted at the rear of the standoff box about 1.2 m from the ends of the bars. The PMTs are 29 mm in diameter, and each has a hexagonal light-catching cone mounted around its photocathode. This yields an effective active surface area fraction of 90%. Due to an extremely high internal reflection coefficient in the radiator bars, about 80% of the initial Cherenkov light is maintained through multiple reflections. The efficiency of photon detection is thus dominated by the quantum efficiency of the PMTs. For a particle with $v/c = 1$ entering normal to the surface at the center of a bar, the expected number of photoelectrons is about 28.

The DIRC front-end electronics are mounted on the outside of the standoff box. Signals are processed by 168 front-end boards, each of which handles 64 PMTs. Each board has custom electronics which amplify and shape the signals, then pass them to custom time-to-digital converters (TDCs) with 0.5 ns binning. The electronics are designed to measure the arrival time of each photon with an accuracy limited by the intrinsic 1.5-ns time resolution of the PMTs.

The reconstruction algorithm associates candidate PMT signals with tracks measured by the tracking detectors. PMT signals generated within 300 ns of the trigger time are used to calculate a vector from the center of the radiator bar end to the center of each PMT. Using Snell's law, the vector is extrapolated into the bar. This determines the angle θ_C as well as an azimuthal angle around the track direction, up to a 16-fold ambiguity. This ambiguity comes from the combination of left/right,

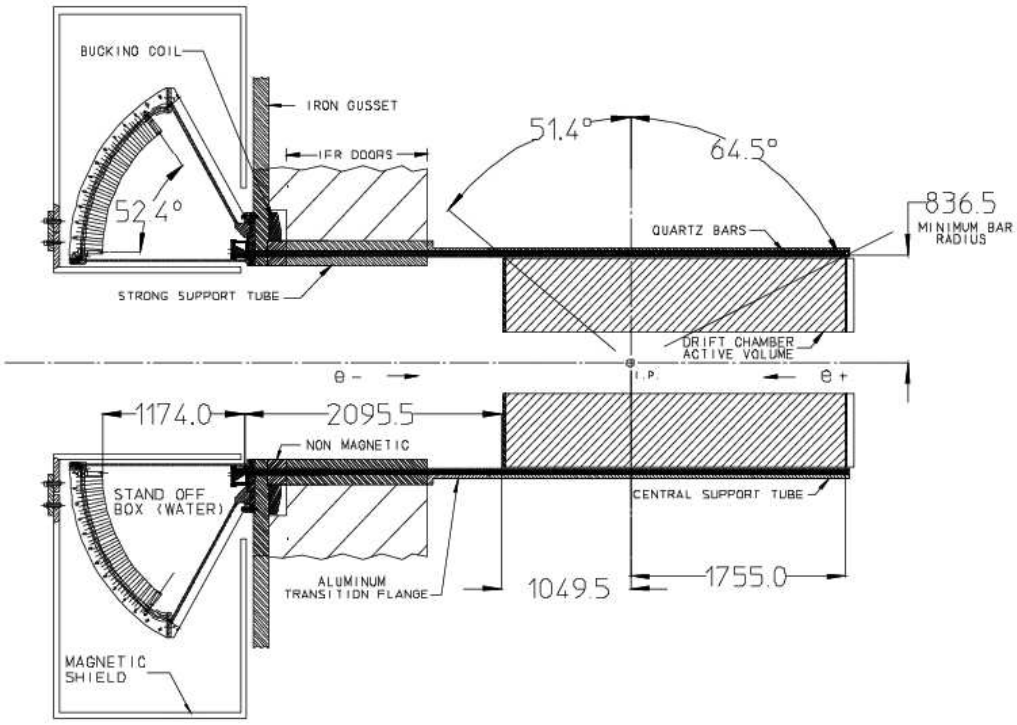

Figure 3.9: View of the DIRC geometry. Dimensions are given in millimeters.

top/bottom, and forward/backward ambiguities plus whether or not the photon was reflected by the wedge. The ambiguity is reduced using timing information and by requiring photons to take only physical paths. The algorithm uses a maximum likelihood technique to calculate a likelihood for each of the particle hypotheses (e, μ, π, K, p). If possible, a best fit value of θ_C and the number of signal photons is calculated for each track. Figure 3.10 shows the distribution of θ_C versus momentum for a large number of data tracks.

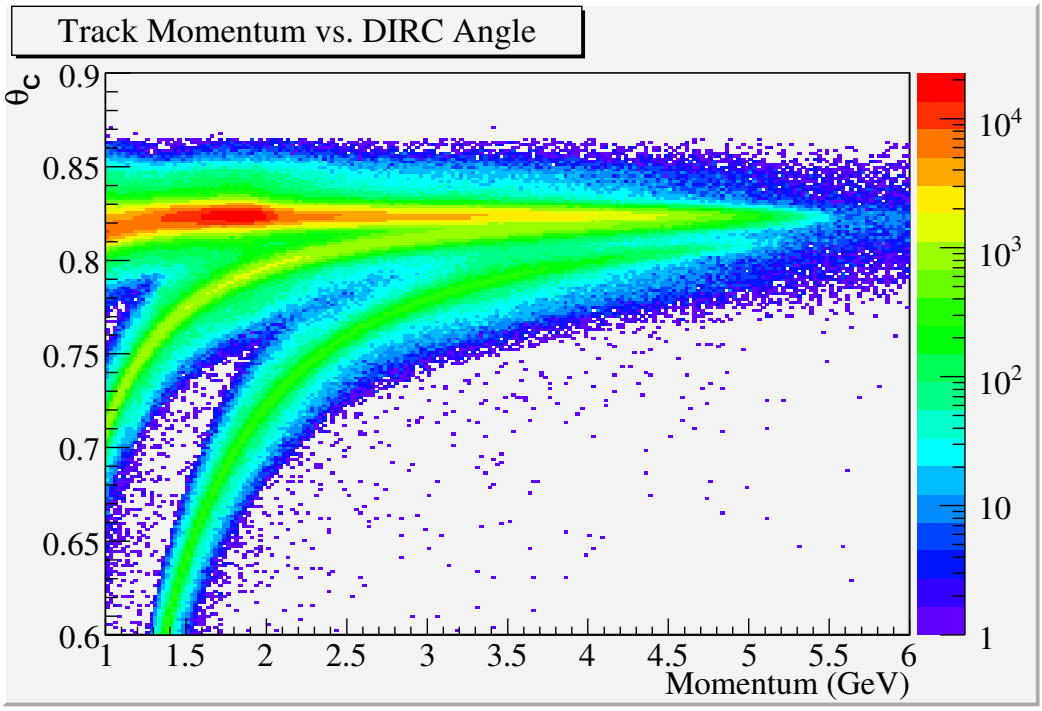

Figure 3.10: The distribution of Cherenkov angle θ_C versus momentum for a collection of tracks from the data [33]. The lowest band is protons, the middle band is kaons, and the upper band is mostly pions.

3.2.4 Electromagnetic Calorimeter

The EMC is the innermost subdetector capable of detecting neutral particles. It is designed to measure electromagnetic showers over the energy range from 20 MeV to 9 GeV. In this analysis, its main contributions are the detection of photons from the

decay chain $K^0 \to K^0_S \to \pi^0\pi^0 \to \gamma\gamma\gamma\gamma$ and the detection of K^0_L. It also contributes to B^0 flavor tagging by identifying electrons.

The EMC consists of 6580 thallium-doped cesium iodide (CsI(Tl)) crystals. As shown in Fig. 3.11, the crystals are arrange in a barrel section plus an endcap at the front end of the detector. This translates to solid-angle coverage of 90% in the CM system. The barrel consists of 48 rings with 120 identical crystals each. The remaining 820 crystals are arranged in eight rings in the endcap. The angle of the crystals changes as a function of z so that the crystals point towards the IP. The crystals are machined into tapered trapezoids, shown in Fig. 3.12, with a typical front face area of $4.7 \times 4.7\,\mathrm{cm}^2$ and back face area of $6.1 \times 6.0\,\mathrm{cm}^2$.

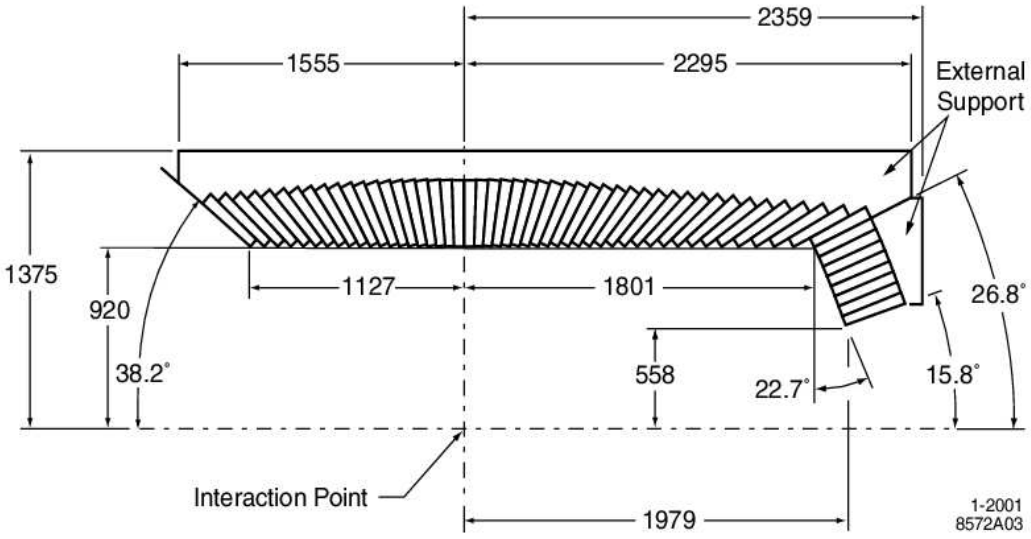

Figure 3.11: Cross section of the top half of the EMC. The EMC is symmetric about the z-axis. Linear dimensions are given in millimeters.

Thallium-doped CsI has a high light yield (50000 $\gamma/\,\mathrm{MeV}$) and small Moliére radius (3.8 cm), as well as a short radiation length (1.85 cm). These features allow for excellent energy and angular resolution, as well as good containment of showers in a compact design. The crystals range in length from 29.6 cm at the backward end

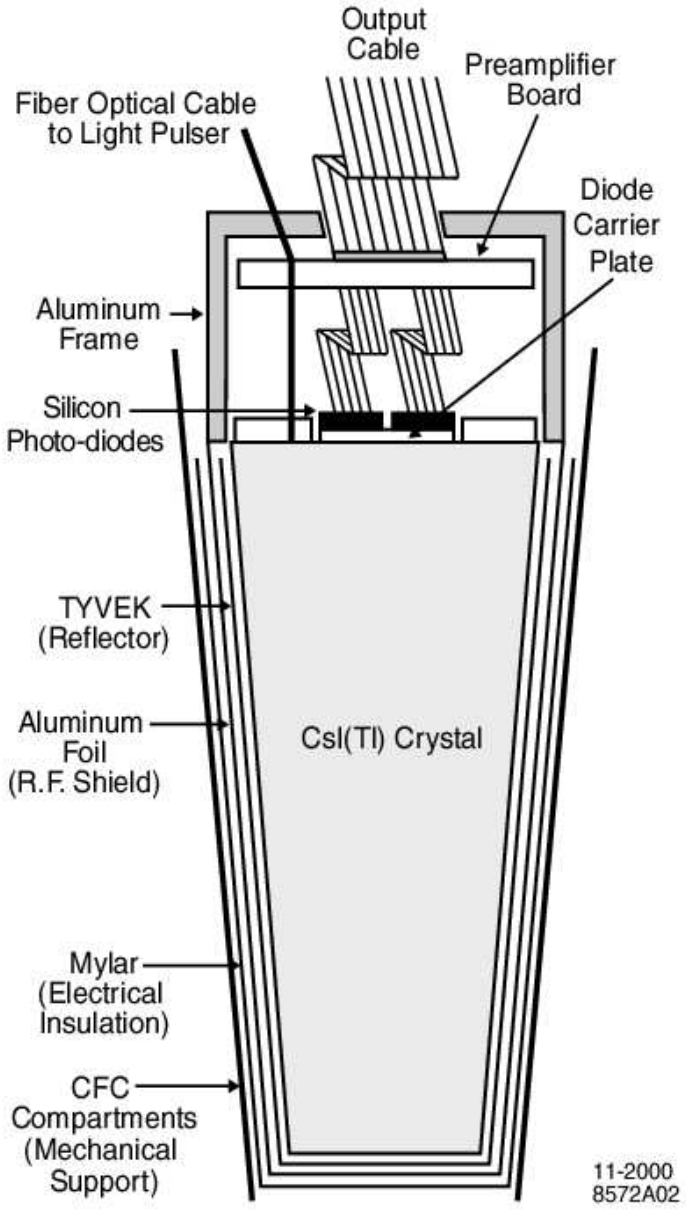

Figure 3.12: Schematic of an EMC crystal.

to 32.4 cm in the forward direction, corresponding to between 16.0 and 17.5 radiation lengths. The crystals act as both a scintillator and a light guide. Light is internally reflected at the polished surface of the crystals, with light retention aided by white reflector material used to wrap each crystal.

As discussed in previous sections, the tracking detectors and DIRC are all designed to keep the material inside of the EMC to a minimum. In keeping with this goal, the EMC crystals are supported from the outside, with only a thin seal of gas at their front. The barrel and outer five rings of the endcap have less than $0.3 - 0.6X_0$ of material in front of their crystal faces. The SVT support structure and electronics, as well as the innermost dipole magnet of the accelerator are in front of the inner three endcap rings, increasing the material thickness there to $3.0X_0$.

Photons are detected by silicon PIN diodes, which are glued to the back of the crystals with optical epoxy. A pair of the $2 \times 1\,\mathrm{cm}^2$ diodes is attached to each crystal, providing redundancy to improve operational reliability. These diodes, operated at 50 V, have a quantum efficiency of 85% for the crystal scintillation light. Each diode is directly connected to a low-noise charge-sensitive preamplifier. The signals are further amplified by a custom chip with four outputs, providing total gains of 256, 32, 4, and 1 corresponding to energy ranges of $0-50\,\mathrm{MeV}$, $50-400\,\mathrm{MeV}$, $0.4-3.2\,\mathrm{GeV}$, and $3.2 - 13.0\,\mathrm{GeV}$. The appropriate range is digitized by a 10-bit analog-to-digital converter. Upon receipt of an accept signal from the L1 trigger, samples within a $\pm 1\,\mu$s window are selected for feature extraction.

Signals measured in a given crystal must be translated to the deposited energy using a calibration. Individual crystals are calibrated at opposite ends of the energy scale. On the low-energy side, a neutron source is used to start a decay chain that generates single 6.13 MeV photons. Multi-GeV energies are calibrated using the well-defined kinematics of Bhabha events, collected at a high rate during normal data-taking. A `GEANT`-based Monte Carlo simulation is used to account for detector inefficiencies. The high energy showers generated in these events are spread over several crystals, but a set of linear equations can be used to determine the gain of each crystal individually. To reconstruct the total energy deposited in the EMC by a particle, the energy deposited in several crystals must be combined, accounting for

losses at the front, rear, and sides of the crystals. This correction is applied in bins of cluster energy and polar angle, and is derived from reconstruction of the π^0 mass and from $e^+e^- \to \mu^+\mu^-\gamma$ events.

Typical electromagnetic showers are spread over many crystals and often overlap, requiring the development of algorithms to separate them. Each cluster is divided into bumps defined by the local maxima of energy deposits in that cluster. The position of each bump is then refined using an iterative weighting procedure. The reconstruction algorithm then attempts to match each bump with a charged track. If no charged track is found, the bump is assumed to correspond to a neutral particle.

3.2.5 Instrumented Flux Return

The IFR is used for detection of long-lived particles. Efficient identification of muons is important for B^0 flavor tagging as well as reconstruction of particles such as the J/ψ. The IFR is also used to detect neutral hadrons, most notably the K_L^0. The steel flux return of the solenoid magnet acts as a muon filter and hadron absorber, and the detectors are placed in the gaps of the segmented steel. The IFR was initially instrumented entirely with single gap resistive plate chambers (RPCs). However, RPC performance quickly degraded during the first year of detector operation [34], leading to the eventual replacement of most of the RPCs with limited streamer tubes (LSTs) [35].

As shown in Fig. 3.13, the initial configuration of the IFR consisted of a barrel portion with 19 layers of RPCs and an endcap with 18 layers. The IFR detectors cover a total active area of about $2000\,\mathrm{m}^2$. The RPCs are constructed from two 2 mm-thick Bakelite sheets, separated by a 2 mm-thick gap filled with an argon-based gas mixture. The outer surfaces of the Bakelite sheets are coated with graphite. A high voltage of 8 kV is applied to one of the graphite surfaces, while the other is held at ground. The RPCs are operated in limited streamer mode. Signals are read out capacitively by strips located on the other side of an insulating layer from the graphite surfaces. A schematic cross section of an RPC is shown in Fig. 3.14.

Signals from the strips are digitized by front-end cards. Digitized signals are

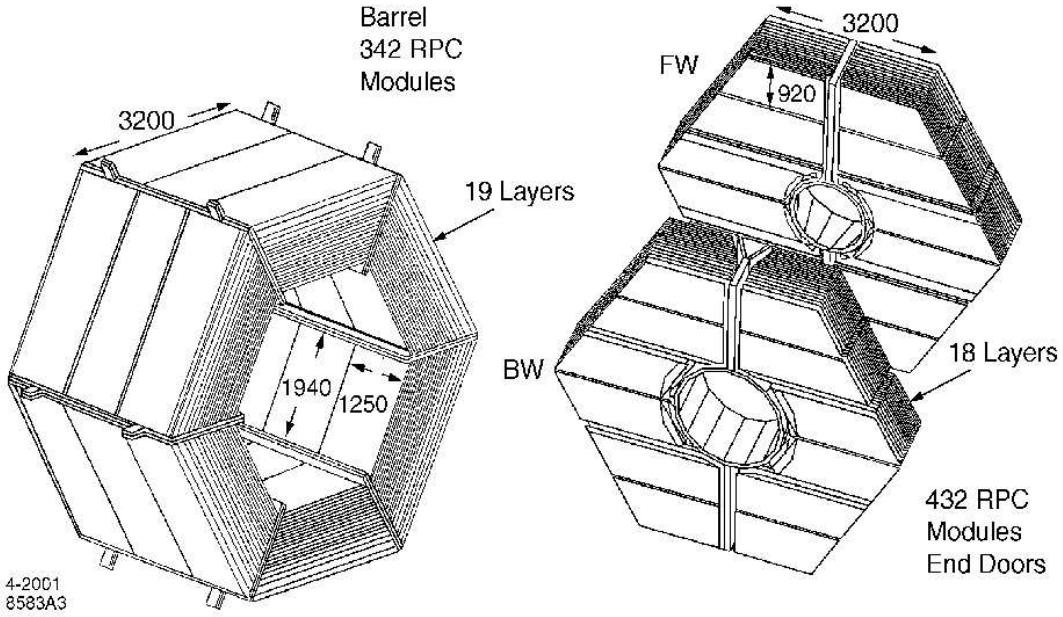

Figure 3.13: A schematic overview of the IFR geometry, with dimensions shown in millimeters.

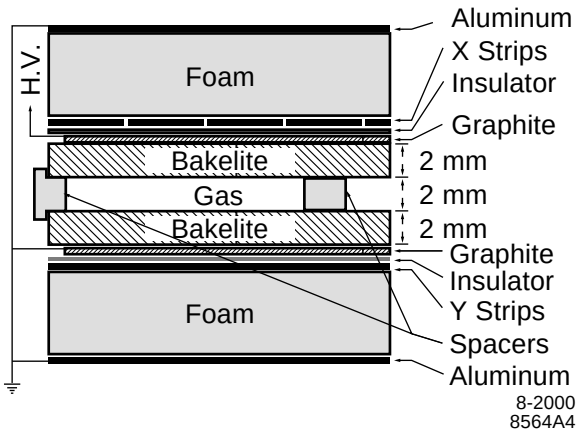

Figure 3.14: Schematic cross section of an RPC.

passed to boards that buffer strip hits, and to TDCs to measure hit timing. The custom TDCs are designed to preserve the excellent 1-2 ns time resolution of the RPCs.

Research and design of the LST system began in 2002, and the first LSTs were installed in the summer of 2004. Installation was completed in the fall of 2006. There are 1164 tubes in all, occupying the inner 18 layers of the IFR barrel previously filled by RPCs (6 layers are filled with brass to provide additional absorbing material, while 12 layers are filled with LSTs).

Each streamer tube in the LST system consists of 8 cells coated internally with graphite paint. At the center of each cell is a 100 μm anode wire. The tubes are filled with a gas mixture of argon, isobutane, and carbon dioxide in the ratio 3:8:89. This gas is ionized by a passing charged particle, causing a streamer discharge in the gas between the anode wire and the graphite coating. The potential difference between the coating and the wire is 5.5 kV. The streamer is detected by measuring the charge on the wire, and by detecting the induced charge on strips mounted below the tube that run perpendicular to the wire direction. This arrangement provides two-dimensional reconstruction of the hit position. Signals from the detector are amplified and discriminated into 1-bit digital signals in the front end electronics, then passed to the main *BABAR* data acquisition system.

3.2.6 Trigger

The trigger must quickly identify events of physics interest, while reducing spurious events caused by beam backgrounds. The system must be highly efficient for $B\overline{B}$ and continuum events (minimum goals are 99% and 95% efficiency, respectively), while reducing the event rate from a beam-background rate of 20 kHz to an output rate of several hundred Hz.

The *BABAR* trigger system has two levels. The Level 1 (L1) trigger executes in hardware, while the Level 3 (L3) trigger is based in software. The L1 trigger decision is primarily based on charged tracks in the DCH and showers in the EMC. These detectors' triggers are independent and largely redundant. There is also a trigger

based on the IFR, used primarily for diagnostic purposes. The L1 trigger operates in a continuous sampling mode, with three trigger processors sending summary data on the position and energy of particles every 134 ns. L1 trigger decisions are reached within 12 μs of the e^+e^- collision. Depending on background conditions and luminosity, the typical output rate of the L1 trigger is $1 - 5$ kHz.

The L1 DCH trigger (DCT) takes 1 bit from each of the 7104 DCH cells as input and passes this data to 24 Track Segment Finder (TSF) modules. The TSF modules search for hits in a contiguous set of cells that span all four layers of a DCH superlayer. These segments are passed to the Binary Link Tracker (BLT), which moves radially outward from the innermost superlayer, linking segments from the TSFs into complete tracks. Long tracks from the BLT are analyzed by a transverse momentum discriminator, which searches for tracks with $p_T > 800\,\mathrm{MeV}/c$. Tracks are thus classified by the DCT into three categories: short tracks, long tracks, and high p_T tracks. The L1 EMC trigger (EMT) treats the EMC barrel as divided into 7×40 $(\theta \times \phi)$ towers, each composed of 8×3 $(\theta \times \phi)$ crystals. The endcap is divided into 40 towers, each with about 20 crystals. The sum in each tower of all crystal energies above a threshold of 20 MeV is given as input to the EMT. The energy deposited in each ϕ-sector is compared to a preset threshold to make the trigger decision.

The L3 trigger has access to the complete event data, as well as the output of the L1 trigger processors. The L3 trigger operated in three phases. In the first phase, events are classified into any number of input lines based on the L1 trigger output. The second phase executes a number of classification tests, called *scripts*, that run code from the standard event data analysis framework. The code is written so that if a particular calculation is used by multiple scripts while processing one event, the calculation is done only once. The final phase assembles the output of the scripts into output lines. The output rate of the L3 trigger is roughly 300 Hz, depending on the instantaneous luminosity. Using simulated events, the combined efficiency of the L1 and L3 triggers for generic $B\overline{B}$ events is found to be $> 99.9\%$.

Table 3.5: Luminosity recorded over the history the *BABAR* detector. The analysis presented in this work uses the data from Runs 1-5. Offpeak data for Run 7 includes all data taken away from the $\Upsilon(4S)$.

Run	Date Range	Onpeak (fb^{-1})	Offpeak (fb^{-1})	$B\overline{B}$ pairs ($\times 10^6$)
1	Oct 1999-Oct 2000	20.02	2.62	21.98
2	Feb 2001-June 2002	61.08	6.92	67.39
3	Dec 2002-June 2003	31.85	2.47	35.10
4	Sep 2003-July 2004	100.28	10.12	110.45
5	Apr 2005-Aug 2006	133.26	14.49	147.19
1-5 Subtotal		346.49	36.62	382.11
6	Jan 2007-Sep 2007	78.78	7.88	86.88
7	Dec 2007-Apr 2008	0.78	53.21	0.86

3.3 Collected Data

The PEP-II B Factory collected data from 1999 until 2008, with data taking broken into seven Runs. The recorded luminosity is listed in Table 3.5. The total number of $B\overline{B}$ pairs produced is determined to a precision of 1.1%. The first six Runs were taken at or near the $\Upsilon(4S)$, while Run 7 was used to explore other Υ resonances. The analysis presented in this work is based on data collected during Runs 1-5. A plot of the luminosity delivered by PEP-II and the luminosity recorded by *BABAR* as functions of time is shown in Fig. 3.15.

3.4 Monte Carlo Simulation

We make extensive use of several samples of simulated events, known as Monte Carlo (MC). These events are generated according to physics-based models that simulate a particular process (for example $e^+e^- \to B^0\overline{B}^0$). Each particle generated in the simulation decays either in a customized fashion (for example, one B^0 could be required to decay to the signal mode) or according to the known properties of that particle (usually taken from the RPP). The generated particles traverse a detailed model of the detector. Version 4 of the `GEANT` software package is used to simulate the interactions

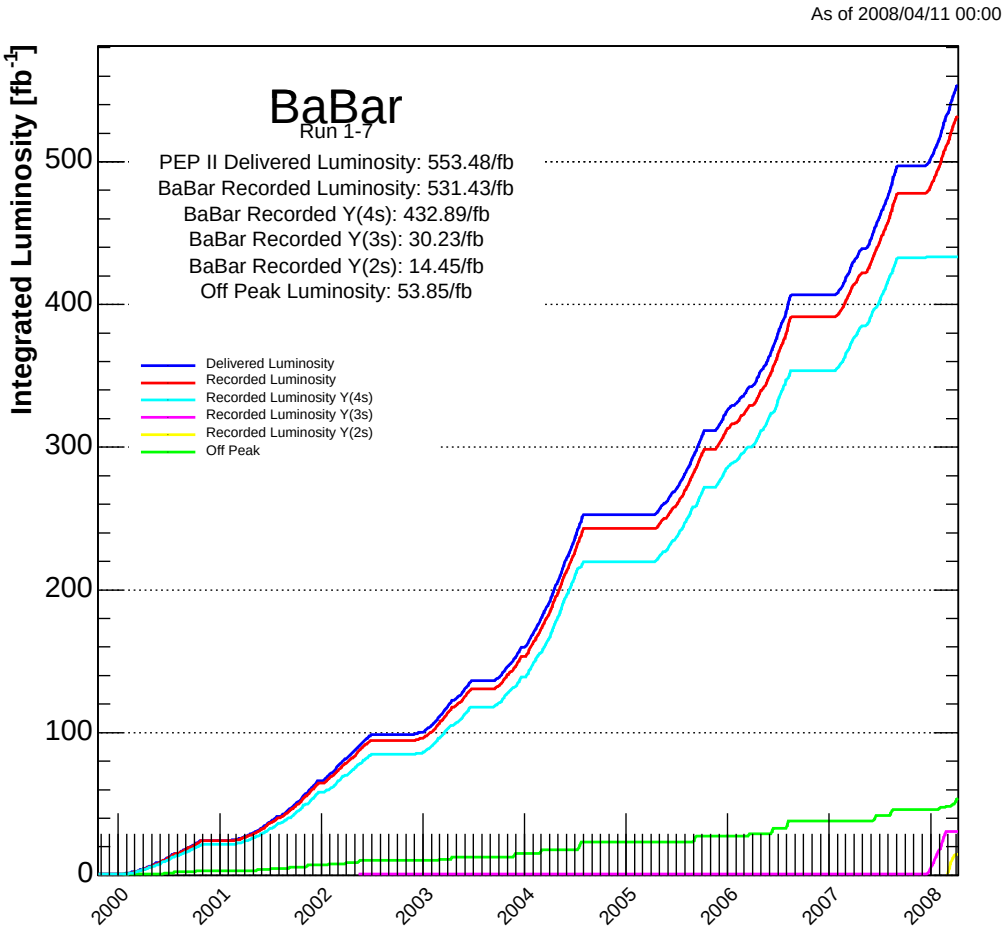

Figure 3.15: Delivered and recorded luminosity as a function of time.

of the particles with the detector material and the responses of the detector subsystems [36]. Real data obtained by reading out the detector at random beam crossings are merged with simulated events in order to add realistic beam backgrounds to the simulation.

We use several MC samples that simulate signal events, where one B^0 (or $\overline{B}^0$) is required to decay to $K^+K^-K^0_S$. A large sample of signal events is generated uniformly in 3-body phase space. This "phase-space MC" is used for many studies. We also use samples of signal events that have been generated according to an approximation of the true distribution of events on the Dalitz plot. These samples are used primarily for fit validation. To study background from B decays, we use samples of "generic $B\overline{B}$" MC, where both B mesons are allowed to decay according to a large table of known B decays, supplemented by hadronization modeled using the software package JETSET [37]. These samples are equivalent to $720.9\,\mathrm{fb}^{-1}$ of $e^+e^- \to B^0\overline{B}^0$ events and $638.2\,\mathrm{fb}^{-1}$ of $e^+e^- \to B^+B^-$ events. We make more minor use of samples consisting of simulated $e^+e^- \to q\overline{q}$ events, where one sample has $q = \{u, d, s\}$ and another has $q = c$.

Chapter 4

Measurement of CP Violation in $B^0 \to K^+K^-K^0$

In this chapter the analysis of the data, leading to measurements of CP violation in the $B^0 \to K^+K^-K^0$ system, is presented. The first sections describe the event selection process for the subdecays $B^0 \to K^+K^-K^0_S$, where the K^0_S decays to either $\pi^+\pi^-$ ($K^+K^-K^0_{S+-}$) or $\pi^0\pi^0$ ($K^+K^-K^0_{S00}$). The later sections describe the fit procedure for the combined analysis of those two subdecays plus $B^0 \to K^+K^-K^0_L$. The event selection for the decays with K^0_L was primarily the work of others, and so is not described in detail here.

This analysis is built on several previous *BABAR* analyses of the same decay mode. For the quasi-two-body decay $B^0 \to \phi K^0$, the branching fraction [39] and CP asymmetries [40, 28] were measured and updated several times as more data was collected. The branching fraction and CP asymmetries in $B^0 \to K^+K^-K^0_S$ were first reported by *BABAR* in 2004 [41]. (The branching fraction measurement was inclusive, while the CP asymmetry measurements excluded ϕK^0_S decays.) The CP asymmetry measurements were updated in 2005 [28]. Many of the analysis techniques described below, in particular the event selection, were developed for these earlier analyses. These decays have also been studied extensively by the Belle experiment [42, 43, 44].

4.1 Event Selection

At 10.58 GeV, the hadronic cross section is dominated by the combined processes $e^+e^- \to q\overline{q}$, where $q = \{u, d, s, c\}$, known as *continuum* events. As listed in Table 4.1, the $b\overline{b}$ cross section is enhanced due to the presence of the $\Upsilon(4S)$ resonance but is still not the dominant process. The first challenge of the analysis is to discriminate between true B meson decays and the background due to these continuum processes. A secondary priority is the efficient selection of true $B^0 \to K^+K^-K^0_S$ decays while eliminating backgrounds originating from other B meson decays.

Table 4.1: Production cross-sections at a CM energy of 10.58 GeV [38]. The cross-section listed for e^+e^- production includes the effect of limited detector acceptance.

Products	Cross-section(nb)
$b\overline{b}$	1.05
$c\overline{c}$	1.30
$s\overline{s}$	0.35
$u\overline{u}$	1.39
$d\overline{d}$	0.35
$\tau^+\tau^-$	0.89
$\mu^+\mu^-$	1.16
e^+e^-	~ 40

Because of the large data sample collected by the *BABAR* detector, it is impractical for every analyst to individually select events from the entire dataset. Therefore, *BABAR* runs a number of simple event selections known as *skims* in a centralized manner. The goal of skimming is to vastly reduce the size of the dataset that an individual analyst must examine, while maintaining nearly 100% efficiency for signal events. This analysis is performed using the output of a skim called `BToCPP`, which selects a group of similar three-body B decays. The output of the skim is 2.7% of the size of the total dataset.

4.1.1 Reconstruction

Events are reconstructed using Release 18 of the *BABAR* software. The standard reconstruction algorithms generate a number of lists for each event, where each list

contains particle candidates that meet certain criteria. These lists are then used to assemble B meson candidates. For charged kaons, we use the `GoodTracksLoose` list. This list selects tracks with $p_T > 100\,\mathrm{MeV}/c$, a maximum momentum of $10\,\mathrm{GeV}/c$, at least 12 hits in the DCH, $|d_0|$ of less than 1.5 cm, and $|z_0| < 10\,\mathrm{cm}$. We also require that candidates pass the `NotAPion` PID selector, which will be described more completely in Sec. 4.1.3.

For $K^+K^-K^0_{S+-}$ decays, K^0_S candidates are taken from the `KsDefault` list. This list is formed by geometrically fitting a pair of charged tracks that have an invariant mass in a $100\,\mathrm{MeV}/c^2$ window around the K^0_S mass. K^0_S candidates that fall in an invariant mass window of $50\,\mathrm{MeV}/c^2$ around the K^0_S mass after the fit are added to the list. B^0 candidates are created by vertexing the charged kaon and K^0_S candidates with a fitting algorithm known as `TreeFitter`. In the fit, the production point of the B^0 candidate is constrained to the beamspot. Most observables used in later stages of the analysis are calculated after this fit is complete. The B^0 candidate is then refit, adding mass constraints to the K^0_S and B^0 candidates. This second fit is used for the calculation of the candidate's position on the Dalitz plot. (The B^0 mass constraint serves to restrict the reconstructed position on the DP to the physically allowed region, simplifying the fitting procedure that will be discussed in later.)

For $K^+K^-K^0_{S00}$ decays, K^0_S candidates are taken from the `KsToPi0Pi0Default` list. Two pairs of photons with invariant masses roughly consistent with a π^0 are combined to form the K^0_S candidate. The B^0 candidate is vertexed as described above, except the K^0_S mass constraint is applied for both fits instead of only the second. As above, the fit is repeated with the addition of a B^0 mass constraint in order to calculate the candidate's DP coordinates.

4.1.2 Kinematic Variables

The most powerful variables for discriminating between signal and background are two nearly uncorrelated kinematic variables, m_{ES} and ΔE, used in many B Factory analyses.

The beam-energy-substituted mass, $m_{\rm ES}$, is defined as

$$m_{\rm ES} \equiv \sqrt{(s/2 + \vec{p}_i \cdot \vec{p}_B)^2/E_i^2 - \vec{p}_B^2}, \tag{4.1}$$

where $\sqrt{s}$ is the CM energy, $(E_i,\ \vec{p}_i)$ is the laboratory four-momentum of the initial e^+e^- system, and $\vec{p}_B$ is the B^0 candidate momentum in the laboratory frame. Conservation of energy is expressed by the other variable, ΔE, defined as

$$\Delta E \equiv E_B - \sqrt{s}/2, \tag{4.2}$$

where E_B is the energy of the B^0 candidate in the CM frame.

Perfectly reconstructed signal events have $m_{\rm ES} = M_B$ and $\Delta E = 0$. For the initial event selection, we require candidates to fall in the window $m_{\rm ES} > 5.20\,{\rm GeV}/c^2$ and $|\Delta E| < 0.20\,{\rm GeV}$. Distributions of these variables are shown for signal MC and data in Fig 4.1. Note that when plotting the data at this stage, we only plot events in the region $5.20 < m_{\rm ES} < 5.26\,{\rm GeV}/c^2$, called the $m_{\rm ES}$ *sideband*. Using this "blind analysis" approach, we avoid looking at the signal region of the data until the analysis procedure has been finalized [45].

The final selection of data used in the DP fits is taken from a smaller *signal region*, defined as $m_{\rm ES} > 5.26\,{\rm GeV}/c^2$ and -0.06 $(-0.12) < \Delta E < 0.06\,{\rm GeV}$ for $K^+K^-K^0_{S+-}$ $(K^+K^-K^0_{S00})$. These tighter boundaries are chosen to reduce contamination of the signal from $B\overline{B}$ backgrounds.

4.1.3 Particle Identification

Particles are identified using ${\rm d}E/{\rm d}x$ measurements from the SVT and DCH, and the Cherenkov angle and number of photons measured in the DIRC. These measurements are used to form a likelihood L_i^{PID} for each particle type i. By making cuts on ratios of these likelihoods, several selectors are created for each particle type with varying efficiencies and fake rates. Three of the kaon selectors are used in this analysis: `NotAPion`, `Loose`, and `Tight`. The `NotAPion` selector requires that the ratio of kaon or proton likelihoods to the pion likelihood be greater than 0.20. The `Loose` selector

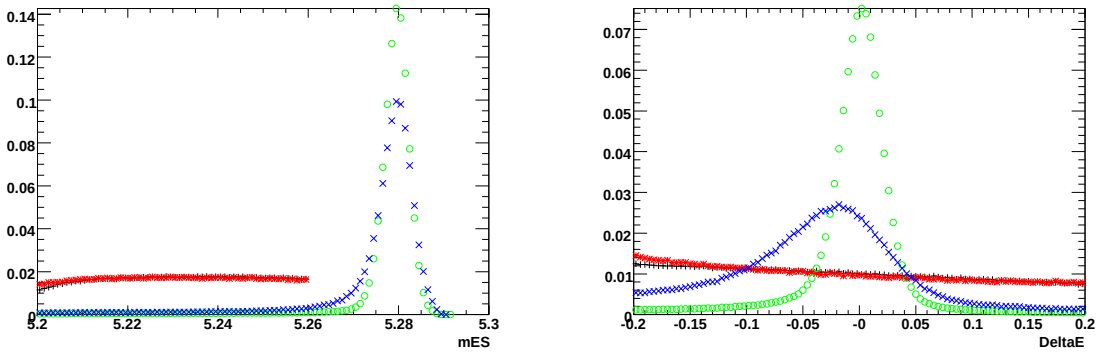

Figure 4.1: Distributions of the kinematic variables (left) $m_{\rm ES}$ and (right) ΔE, before any cuts are applied. Signal MC is shown with green circles (blue crosses) for $K^+K^-K^0_{S+-}$ ($K^+K^-K^0_{S00}$). Data is shown with black ticks (red stars) for $K^+K^-K^0_{S+-}$ ($K^+K^-K^0_{S00}$). As shown in the left plot, a cut is placed on $m_{\rm ES}$ to remove signal events in data from both plots until the analysis procedure is finalized. All distributions are normalized to unit area.

requires $L_K^{PID}/L_\pi^{PID} > 0.8176$ and $L_K^{PID}/L_p^{PID} > 0.018$, and also vetoes any particle consistent with an electron. The `Tight` selection is similar, but the requirements are tightened to $L_K^{PID}/L_\pi^{PID} > 0.9$ and $L_K^{PID}/L_p^{PID} > 0.2$ for tracks with momenta up to 2.5 GeV/c.[1]

Previous iterations of this analysis of inclusive $B^0 \to K^+K^-K^0_S$ decays required both charged kaon candidates to pass the `Tight` selection. This led to a pion misidentification rate of less than 2% [41]. The analyses of $B^0 \to \phi K^0_S$ made less stringent cuts, requiring only that one kaon candidate pass the `Loose` selection and the other pass the `NotAPion` selection [46]. In this analysis, this `NotAPion+Loose` selection is used for events with K^+K^- invariant mass, $m_{K^+K^-}$, less than 1.1 GeV/c^2. In this region, this selection increases the signal efficiency in $K^+K^-K^0_{S+-}$ by 13%, while the increase in $B\overline{B}$ background is negligible as estimated from the generic $B\overline{B}$ MC. The `Tight+Tight` selection is used for events in the rest of the phase space.

If we were to use the `NotAPion+Loose` selection across the whole DP, the number of candidates in generic $B\overline{B}$ MC passing all cuts that have a PID error increases by

[1] For tracks with momenta greater than 2.5 GeV/c, the cuts increase as a function of momentum.

nearly a factor of 5. Therefore we do not make that change.

4.1.4 K^0_S Selection

Several cuts are made on both $K^0_S \to \pi^+\pi^-$ and $K^0_S \to \pi^0\pi^0$ candidates. First, a requirement is placed on the lifetime significance, calculated as the reconstructed lifetime of the K^0_S candidate divided by its uncertainty: $\tau_{K^0_S}/\sigma_{\tau_{K^0_S}} > 3$. Second, we require $\cos\alpha_{K^0_S} > 0.999$, where $\alpha_{K^0_S}$ is the angle between the line connecting the reconstructed B^0 and K^0_S decay vertices and the K^0_S momentum. Finally, we make a cut on the reconstructed dipion invariant mass: $m_{K^0} - 20\,\mathrm{MeV}/c^2 < m_{\pi^+\pi^-}\ (m_{\pi^0\pi^0}) < m_{K^0} + 20\,\mathrm{MeV}/c^2$ ($30\,\mathrm{MeV}/c^2$). Plots of $\cos\alpha_{K^0_S}$ and the lifetime significance for signal and continuum background are shown in Fig. 4.2.

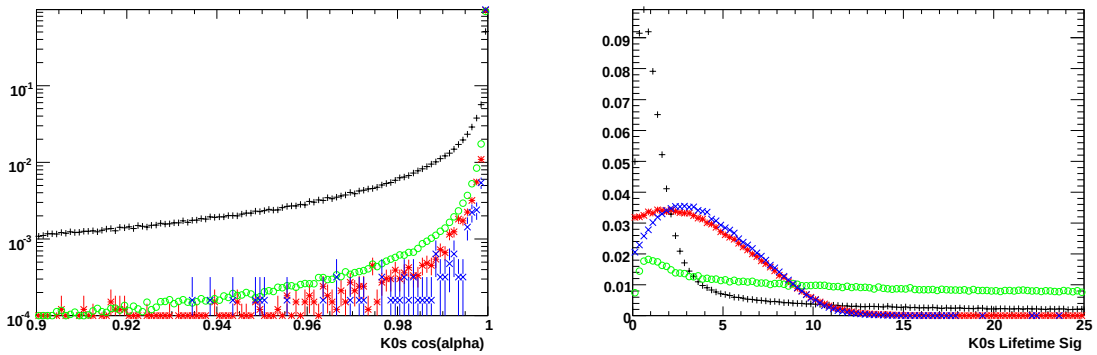

Figure 4.2: Distributions of variables used for K^0_S selection, before any cuts are applied. Signal MC is shown with green circles (blue crosses) for $K^+K^-K^0_{S+-}$ ($K^+K^-K^0_{S00}$). Background, taken from the m_{ES} sideband in onpeak data, is shown with black ticks (red stars) for $K^+K^-K^0_{S+-}$ ($K^+K^-K^0_{S00}$). The left plot shows $\cos\alpha_{K^0_S}$, while the right plots shows the lifetime significance. Distributions are normalized to unit area.

Additional cuts are imposed on each of the four photons used to reconstruct K^0_S candidates in the $K^0_S \to \pi^0\pi^0$ subdecay. The initial selection used to form the `KsToPi0Pi0Default` list required the photon energies E_γ to be greater than 30 MeV. Studies of MC samples indicate that tighter cuts reduce $B\overline{B}$ backgrounds while also reducing signal efficiency; we require $E_\gamma > 50\,\mathrm{MeV}$. We also make a cut on the lateral

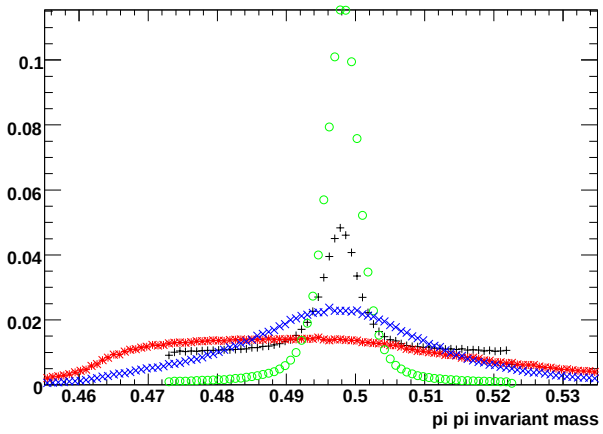

Figure 4.3: Distributions the dipion invariant mass of K^0_S candidates, before any cuts are applied. Signal MC is shown with green circles (blue crosses) for $K^+K^-K^0_{S+-}$ ($K^+K^-K^0_{S00}$). Background, taken from an $m_{\rm ES}$ sideband in onpeak data, is shown with black ticks (red stars) for $K^+K^-K^0_{S+-}$ ($K^+K^-K^0_{S00}$).

moment (LAT), defined as

$$LAT = \frac{\sum_{i=2}^{N_{\rm crystals}} E_i \Delta x_i}{\sum_{i=0}^{N_{\rm crystals}} E_i \Delta x_i}, \tag{4.3}$$

where $N_{\rm crystals}$ is the number of crystals in an EMC cluster, each with energy E_i and ordered from the most energetic to the least. For $i \geq 2$, Δx_i is the distance from the cluster local maximum to crystal i, while $\Delta x_{0,1} = 5\,{\rm cm}$. An EMC bump with $N_{\rm crystals} \leq 2$ has a LAT of zero by definition. Photons tend to have a low LAT value, so we make the loose requirement that $LAT > 0.01$, thus rejecting events with $LAT = 0$ while keeping most others.

The K^0_S selection for $K^+K^-K^0_{S+-}$ was largely inherited from previous iterations of this analysis. For $K^+K^-K^0_{S00}$, we made an attempt to optimize the cuts on ΔE, the K^0_S mass, the minimum photon energy E_γ, and the lateral moment. We varied the cut values for each of these variables over predefined ranges, evaluating the signal significance ($S/\sqrt{S+B}$), self-crossfeed fraction, and $B\overline{B}$ background for each combination of cut values. The amounts of signal and $B\overline{B}$ background were estimated

using the appropriate MC samples, while the amount of $q\overline{q}$ background was estimated using data from the $m_{\rm ES}$ sideband. For $q\overline{q}$ background, the number of events found in the sideband is extrapolated to the number expected in the signal region using the Argus shape discussed in Sec. 4.5.3. The cut values were selected with the goal of maximizing the significance while keeping self-crossfeed and $B\overline{B}$ background as low as possible.

4.1.5 Continuum Suppression

As discussed in Sec. 4.1, the dominant background is from continuum events. Because the $\Upsilon(4S)$ is just above $B\overline{B}$ threshold, $B\overline{B}$ pairs are created nearly at rest in the CM frame, giving their decay products a relatively isotropic distribution. Continuum events are relatively "jetty" in the CM frame. This topological difference is exploited using several variables, all calculated in the CM frame.

The variable θ_T is defined as the angle between the thrust axis of the B^0 candidate's decay products and the thrust axis of all charged and neutral particles in the rest of the event (ROE).[2] As shown in Fig. 4.4a, for continuum events $|\cos\theta_T|$ peaks near 1 while for signal events it is flat. We require $|\cos\theta_T| < 0.9$ as a first step in rejecting continuum background. We also use the angle θ_B between the B^0-momentum direction and the beam axis, as shown in Fig. 4.4b.

Finally, we use the Legendre moments

$$L_0 = \sum_i |\vec{p^*}_i|, \text{ and} \tag{4.4}$$

$$L_2 = \sum_i |\vec{p^*}_i| \frac{3\cos^2\theta_i - 1}{2}, \tag{4.5}$$

where the sums run over the ROE, and θ_i is the angle between the momentum $\vec{p^*}_i$ and the thrust axis of the B^0 candidate. Distributions of these variables are shown in Fig. 4.4.

The four event shape variables shown in Fig. 4.4 are correlated, and so cannot

[2]The thrust axis is defined to be the direction that maximizes the sum of the longitudinal momenta of the particles in question [38].

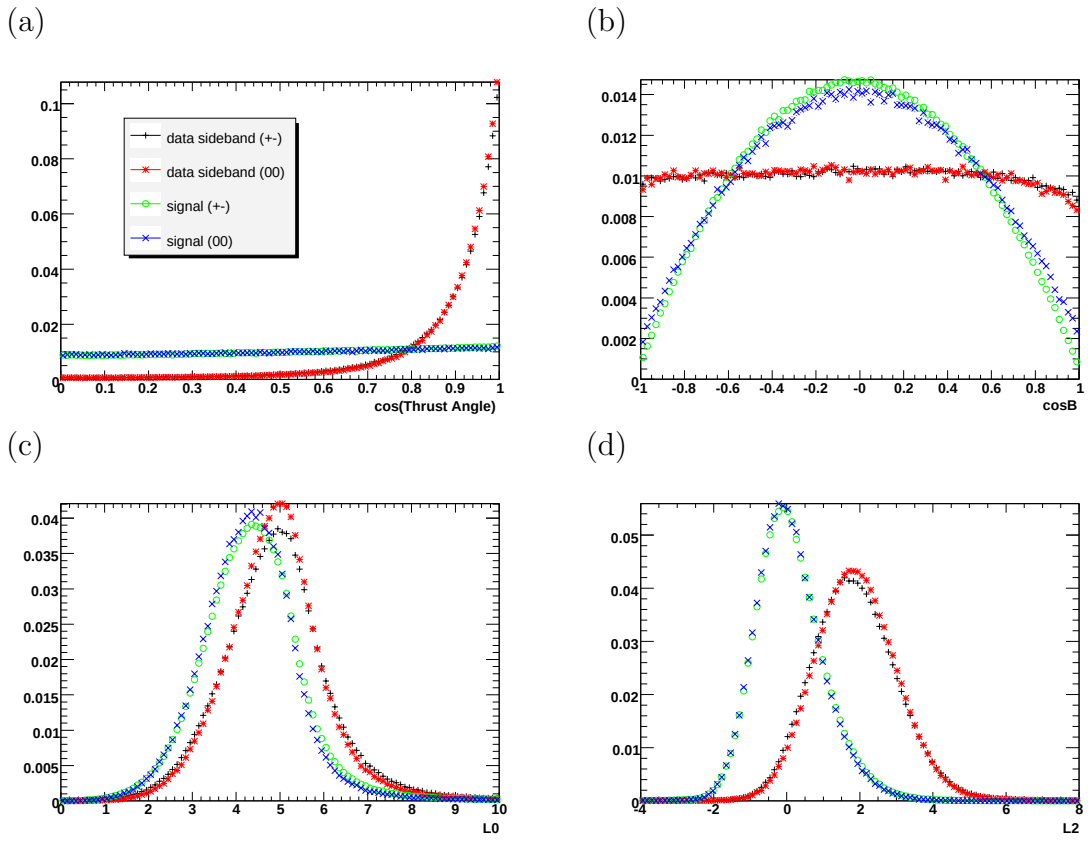

Figure 4.4: Distributions of event shape variables used as inputs to the Fisher discriminant: (a) $|\cos\theta_T|$, (b) $\cos\theta_B$, (c) L_0, and (d) L_2.

be independently included in a likelihood fit. Therefore, we combine them into an optimized linear combination called a Fisher discriminant $\mathcal{F}$ [47], shown in Fig. 4.5. In our initial selection, we make only a loose cut on the Fisher discriminant, requiring $-6 < \mathcal{F} < 4$.

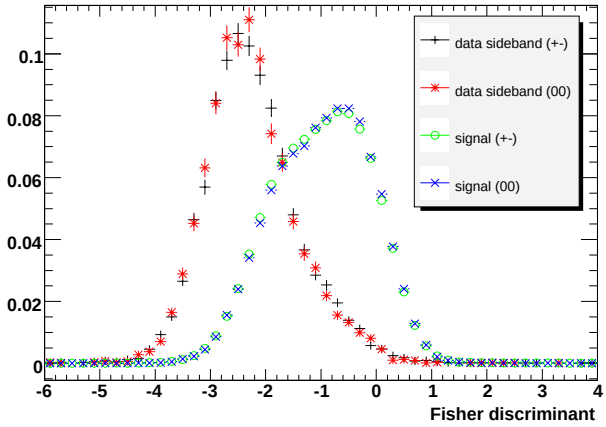

Figure 4.5: Distributions of the Fisher discriminant for signal and continuum background.

4.1.6 Best Candidate Selection

Some events have more than one reconstructed B^0 candidate. If there is more than one K^0_S candidate, then we keep only the B^0 candidates that are formed using the K^0_S candidate with reconstructed mass closest to the actual K^0 mass. If there are more than two charged kaon candidates, then we choose the B^0 candidate whose daughter kaons pass the tightest PID selectors. For the few events that still have multiple B^0 candidates after these choices are made, we choose the candidate with the best vertex probability from the B^0 vertex fit.

The best candidate is selected from those candidates that pass all of the basic selection cuts. There are 1.02 (1.15) candidates per event in the $K^+K^-K^0_{S+-}$ ($K^+K^-K^0_{S00}$) mode.

4.1.7 Signal Efficiency

The selection criteria described in the preceding sections, and the resulting effect on the signal efficiency, are summarized in Table 4.2. Note that the actual average efficiency is higher than the value quoted in the Table because the real signal is concentrated in areas of phase space with higher efficiency. Using MC generated with a more realistic model of the Dalitz plot, the average efficiency is found to be 26.9% (6.6%) in $K^+K^-K^0_{S+-}$ ($K^+K^-K^0_{S00}$).

Table 4.2: Table of signal efficiencies (in %), determined from phase-space signal MC. The best candidate in an event is chosen from candidates that pass the cuts listed above the line. The remaining cuts are applied after the best candidate is selected. The "signal box" is defined as $m_{\rm ES} > 5.26\,{\rm GeV}/c^2$ and -0.06 (-0.12) $< \Delta E < 0.06\,{\rm GeV}$ for $K^+K^-K^0_{S+-}$ ($K^+K^-K^0_{S00}$). The final cut on $\mathcal{F}$ is only applied for some portions of the analysis.

	$K^+K^-K^0_{S+-}$		$K^+K^-K^0_{S00}$	
Cut	Relative eff.	Total eff.	Relative eff.	Total eff.
$m_{\rm ES} > 5.2\,{\rm GeV}/c^2$,				
$\quad\lvert\Delta E\rvert < 0.2\,{\rm GeV}$	48.5	48.5	25.9	25.9
$\cos\theta_T < 0.9$	88.8	43.0	89.5	23.2
$-6 < \mathcal{F}$	99.9	43.0	99.9	23.2
K^0_S cuts	87.7	37.7	52.8	12.2
Photon cuts	N/A	N/A	78.3	9.6
$K^\pm$ PID	69.7	26.3	71.1	6.8
Signal box	93.6	24.6	78.7	5.4
$\mathcal{F} < 4$	99.9	24.6	99.9	5.4
$-20 < \Delta t < 20\,{\rm ps}$,				
$\quad 0.01 < \sigma_{\Delta t} < 2.5\,{\rm ps}$	96.6	23.7	96.9	5.2
$-2.5 < \mathcal{F}$	95.4	22.6	95.6	5.0

4.2 Flavor Tagging

As introduced in Sec. 2.2.2, in order to measure the time-dependent *CP* asymmetry, we must determine several properties of the other, partially reconstructed, neutral B

meson in the event ($B_{\rm tag}$). In particular, we need to measure the difference between the proper decay times of the two mesons, Δt, and determine the flavor (B^0 or $\overline{B}^0$) of the other meson at the time of its decay.

The flavor of the $B_{\rm tag}$ meson is determined using a multivariate neural network (NN) technique [11, 48]. The NN is trained using a large sample of MC events. The output of the NN is broken into seven mutually exclusive *tagging categories*, based on the characteristics of the event used to identify the tag flavor. In order from highest purity to least, the categories are: *Lepton, KaonI, KaonII, KaonPion, Pion, Other,* and *Untagged*. The *Lepton* category indicates the presence of a lepton consistent with a semileptonic B decay, where the sign of the charge of the lepton indicates the flavor of the parent b quark. Similarly, the *KaonI* and *KaonII* categories identify the sign of the charge of a kaon in the event with the flavor of the b quark via the decay chain $b \to c \to s$. The *Pion* category uses the charge of the slow pion from D^* decays to identify the flavor of the decaying B meson. The *KaonPion* category combines properties of the kaon- and pion-based tagging methods. The *Other* category combines the output of various methods, such as tagging using Λ decays or the highest momentum track in the event. Events without a reliable flavor tag are classified as *Untagged*.

The discriminating power of each tagging category i is quantified using an effective tagging efficiency $Q_i = \epsilon_i(1-2w_i)^2$, where ϵ_i is the fraction of events assigned to the category and w_i is the mistag fraction (the fraction of events tagged with the wrong flavor). The difference in mistag fraction between B^0- and $\overline{B}^0$-tagged events is called Δw_i. The values of these parameters are determined in a fit to a data sample of B^0 mesons ($B_{\rm flav}$) decaying to the flavor eigenstates $D^{(*)-}h^+$ ($h^+ = \pi^+, \rho^+, a_1^+$) and $J/\psi K^{*0}$ ($K^{*0} \to K^+\pi^-$).

4.2.1 Δt Reconstruction

The vertex of the $B_{\rm tag}$ decay is reconstructed from all remaining tracks in the event after the reconstruction of the signal candidate B_{CP}. A geometric fit is performed to these tracks, with the constraint that the B^0-$\overline{B}^0$ pair originate in the beamspot.

Table 4.3: Tagging performance parameters determined from the $B_{\rm flav}$ sample.

Category	ϵ (%)	w (%)	Δw (%)	Q (%)
Lepton	8.68 ± 0.08	2.86 ± 0.32	0.1 ± 0.7	7.7 ± 0.1
KaonI	11.00 ± 0.08	5.62 ± 0.34	-0.7 ± 0.8	8.7 ± 0.1
KaonII	17.19 ± 0.10	14.94 ± 0.40	-0.5 ± 0.7	8.5 ± 0.2
KaonPion	13.74 ± 0.09	23.1 ± 0.5	-3.1 ± 0.9	4.0 ± 0.1
Pion	14.30 ± 0.09	32.7 ± 0.6	6.3 ± 0.8	1.7 ± 0.1
Other	9.61 ± 0.08	41.9 ± 0.7	4.8 ± 1.0	0.25 ± 0.04
Total	74.5 ± 0.2			30.8 ± 0.3

The distance along the boost axis between the reconstructed $B_{\rm tag}$ and B_{CP} vertices, Δz, has an RMS resolution of 180 μm. This resolution is dominated by the resolution of the $B_{\rm tag}$ vertex position (the B_{CP} vertex alone has a resolution of approximately 50 μm) and includes contributions from a long tail. When the resolution is parameterized as described below (Eq. 4.7), the narrowest Gaussian distribution has a width of about 100 μm [48].

A good approximation to the expression used to calculate Δt is the relation

$$\Delta z = \beta\gamma c \Delta t, \tag{4.6}$$

where $\beta\gamma \simeq 0.56$ is the boost of the $\Upsilon(4S)$ system in the laboratory. In practice, corrections are applied to account for the non-zero momentum of the B in the $\Upsilon(4S)$ rest frame, and for the 20 mrad angle between the boost direction and the z-axis as defined by the *BABAR* DCH [48].

The Δt resolution is parameterized by a resolution function $\mathcal{R}$ that is the sum of three Gaussian distributions (core, tail, and outlier):

$$\begin{aligned} \mathcal{R} \;=\; & \sum_{k=1}^{2} \frac{f_k}{S_k \sigma_{\Delta t}\sqrt{2\pi}} \exp\left(-\frac{(\delta_t - b_k \sigma_{\Delta t})^2}{2(S_k\sigma_{\Delta t})^2}\right) \\ & + \frac{f_3}{\sigma_3\sqrt{2\pi}} \exp\left(-\frac{\delta_t^2}{2\sigma_3^2}\right), \end{aligned} \tag{4.7}$$

where $\delta_t = \Delta t - \Delta t'$. The core and tail distributions have means and widths proportional to the error on Δt, respectively scaled by bias factors b_k and scale factors S_k. The fractions f_k are constrained so that $f_1 = 1 - f_2 - f_3$. The tail scale factor is fixed to $S_2 = 3$, and the outlier width is fixed to $\sigma_3 = 8\,\text{ps}$. The remaining parameters of the resolution function are determined in a fit to the B_{flav} sample. The results of this fit, used in our fits to the data, are shown in Table 4.4. The core parameters b_1 and S_1 are split by tagging category in the fit. Because the resolution is dominated by the tag-side resolution, the resolution function parameters are independent of the signal decay.

Table 4.4: Values of signal Δt resolution function parameters determined in a fit to the B_{flav} sample.

Parameter	Value
$b_{1,\text{Lepton}}$	-0.042 ± 0.032
$b_{1,\text{KaonI}}$	-0.141 ± 0.031
$b_{1,\text{KaonII}}$	-0.204 ± 0.024
$b_{1,\text{KaonPion}}$	-0.167 ± 0.025
$b_{1,\text{Pion}}$	-0.220 ± 0.025
$b_{1,\text{Other}}$	-0.164 ± 0.031
$b_{1,\text{NoTag}}$	-0.205 ± 0.018
$S_{1,\text{Lepton}}$	1.04 ± 0.05
$S_{1,\text{KaonI}}$	1.05 ± 0.05
$S_{1,\text{KaonII}}$	1.090 ± 0.036
$S_{1,\text{KaonPion}}$	1.090 ± 0.038
$S_{1,\text{Pion}}$	1.108 ± 0.038
$S_{1,\text{Other}}$	1.11 ± 0.05
$S_{1,\text{NoTag}}$	1.111 ± 0.027
f_2	0.093 ± 0.006
b_2	-1.35 ± 0.11
S_2	3
f_3	0.0045 ± 0.0007
σ_3	8 ps

4.3 Maximum Likelihood Method

All results are extracted from unbinned maximum likelihood (ML) fits. The likelihood function $\mathcal{L}$ is

$$\mathcal{L} = \prod_{c} \exp\left(-\sum_{i=1}^{M} n_{i,c}\right) \prod_{j=1}^{N_c} \left[\sum_{i=1}^{M} n_{i,c}\mathcal{P}_{i,c}\left(\vec{x}_j;\vec{\alpha}_{i,c}\right)\right], \tag{4.8}$$

where N_c is the total number of events j in category c, M is the number of signal and background hypotheses i, and $n_{i,c}$ is the number of events in a given hypothesis and category. The probability density function (PDF) $\mathcal{P}_{i,c}$ for each hypothesis depends on the observables $\vec{x}_j$ and the parameters $\vec{\alpha}_{i,c}$.

The PDFs are split twice by category, meaning that the PDFs for different categories can have independent structure and parameters. The first split is by the four ways of detecting the K^0: $K^0_S \to \pi^+\pi^-$, $K^0_S \to \pi^0\pi^0$, K^0_L detected in the EMC, and K^0_L detected in the IFR. Second, the PDFs are split by the seven tagging categories discussed in Sec. 4.2. Therefore, there are $4 \times 7 = 28$ different variations on the PDFs, depending on the categories a given event falls into.

The number of hypotheses M varies depending on the category. Both K^0_S modes have three hypotheses: signal, continuum background, and $B\overline{B}$ background. The K^0_L modes have those plus an extra category of $B\overline{B}$ background, giving a total of four hypotheses.

Each $\mathcal{P}_{i,c}$ is formed as a product of PDFs that describe the observables used in the fit ($m_{\rm ES}$, ΔE, $m_{K^+K^-}$, $\cos\theta_H$, Δt, and sometimes $\mathcal{F}$), with slight variations

depending on the K^0 mode. The PDF structure is

$$\begin{aligned}
\mathcal{P}_{\mathrm{Signal},K^+K^-K^0_S} &= \mathcal{P}(m_{\mathrm{ES}})\mathcal{P}(\Delta E)\mathcal{P}(m_{K^+K^-},\cos\theta_H,\Delta t),\\
\mathcal{P}_{\mathrm{Signal},K^+K^-K^0_L} &= \mathcal{P}(\Delta E)\mathcal{P}(m_{K^+K^-},\cos\theta_H,\Delta t);\\
\mathcal{P}_{q\overline{q},K^+K^-K^0_S} &= \mathcal{P}(m_{\mathrm{ES}})\mathcal{P}(\Delta E)\mathcal{P}(m_{K^+K^-},\cos\theta_H)\mathcal{P}(\Delta t),\\
\mathcal{P}_{q\overline{q},K^+K^-K^0_L} &= \mathcal{P}(\Delta E)\mathcal{P}(m_{K^+K^-},\cos\theta_H)\mathcal{P}(\Delta t);\\
\mathcal{P}_{B\overline{B},K^+K^-K^0_{S+-}} &= \mathcal{P}(m_{\mathrm{ES}})\mathcal{P}(\Delta E)\mathcal{P}(m_{K^+K^-},\cos\theta_H)\mathcal{P}(\Delta t),\\
\mathcal{P}_{B\overline{B},K^+K^-K^0_{S00}} &= \mathcal{P}(m_{\mathrm{ES}},\Delta E)\mathcal{P}(m_{K^+K^-},\cos\theta_H)\mathcal{P}(\Delta t),\\
\mathcal{P}_{B\overline{B},K^+K^-K^0_L} &= \mathcal{P}(\Delta E)\mathcal{P}(m_{K^+K^-},\cos\theta_H)\mathcal{P}(\Delta t);
\end{aligned}$$

where we have suppressed the splitting over tagging categories and the EMC/IFR splitting for the K^0_L mode because these splits do not change the structure of the PDFs. (Instead, only the values of the PDF parameters depend on the category.) For the low-mass fit (Sec. 4.3.1), each PDF listed above is multiplied by an additional PDF: for the K^0_S modes, a PDF that depends on the Fisher discriminant, $\mathcal{P}(\mathcal{F})$; for the K^0_L modes, PDFs that depend on the missing momentum Fisher discriminant and the Legendre moments, $\mathcal{P}(\mathcal{F}_{miss})\mathcal{P}(L_2/L_0)$. Details about the PDFs used for the K^0_L mode can be found in Ref. [50].

The optimal values of the floating parameters are determined by maximizing the function $\mathcal{L}$. In practice, this is done by minimizing the quantity $-\ln\mathcal{L}$, also known as the negative log likelihood (NLL).

4.3.1 Overview of fit procedure

Results are extracted from a sequence of three fits, summarized here.

The first fit is to all selected events. The event yields, isobar coefficients (c_r and φ_r), and one pair of *CP* parameters (b_r and δ_r) are free parameters in the fit. The *CP* parameters are shared for all charmless contributions to the DP model. We refer to this step as the *fit to the whole Dalitz plot*.

In the second fit, all isobar coefficients except those for the $\phi(1020)$ are fixed to the values found in the first fit. In this step, called the *low-mass fit*, we fit only to

the events in the region of the phase space with $m_{K^+K^-} < 1.1\,\mathrm{GeV}/c^2$. Event yields, $\phi(1020)$ isobar coefficients, and *CP* parameters for the $\phi(1020)$ and $f_0(980)$ are free in the fit. Because this fit is to a small region of the phase space, we are able to include the Fisher discriminant as an observable in the fit.

In the final fit, called the *high-mass fit*, all isobar coefficients are fixed to the values found in the fit to the whole DP. This fit is to events with $m_{K^+K^-} > 1.1\,\mathrm{GeV}/c^2$. Similarly to the whole DP fit, the only floating parameters are the event yields and one pair of average *CP* parameters shared by all charmless contributions.

The configuration of *CP* asymmetry parameters in the fits is summarized in Table 4.5.

Table 4.5: Models of direct *CP* asymmetry used in the various fits.

Component	Direct *CP* parameters		
	Whole DP Fit	High-mass fit	Low-mass fit
ϕK^0	$\delta_{K^+K^-K^0}$, $b_{K^+K^-K^0}$	$\delta_{K^+K^-K^0}$, $b_{K^+K^-K^0}$	$\delta_{\phi K^0}$,$b_{\phi K^0}$
$f_0(980)K^0$			$\delta_{f_0K^0}$,$b_{f_0K^0}$
$X_0(1550)K^0$			$\delta_{K^+K^-K^0}$, $b_{K^+K^-K^0}$
$(K^+K^-K^0_S)_{NR}$			
$\chi_{c0}K^0$, D^-K^+, $D_s^-K^+$	No direct *CP* asymmetry		

4.4 Signal Parameterization

This section describes the parameterization of the PDFs used to describe signal events.

4.4.1 Kinematic and Event Shape PDFs

The kinematic variables m_{ES} and ΔE for signal in both $K^+K^-K^0_{S+-}$ and $K^+K^-K^0_{S00}$ are parameterized using the function

$$f(x) = \exp\left(-\frac{(x-x_0)^2}{2\sigma_{L,R}^2 + \alpha_{L,R}(x-x_0)^2}\right), \tag{4.9}$$

where σ_L and α_L are used for $x < x_0$ while σ_R and α_R are used for $x > x_0$ Note that when $\alpha_{L,R} = 0$, this form reduces to a Gaussian distribution with mean x_0. Distributions of signal MC events (generated with an approximation of the final DP model) with fits to the functional form of Eq. 4.9 are shown in Fig. 4.6.

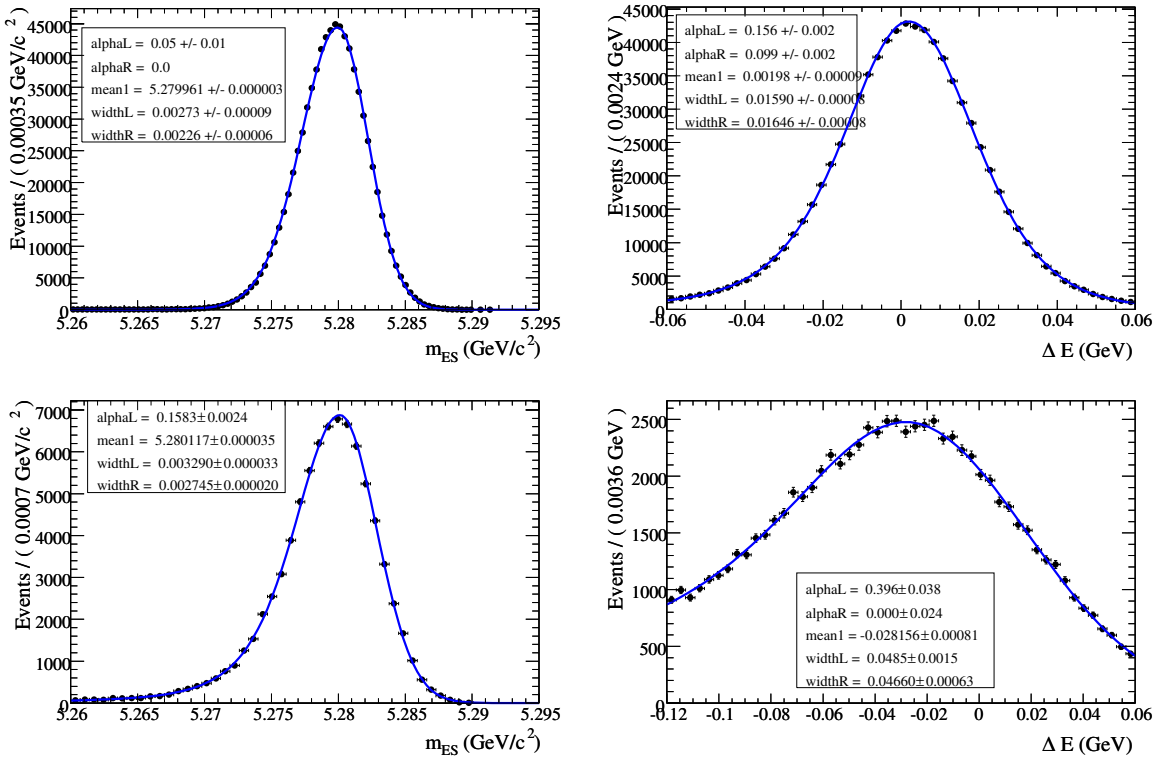

Figure 4.6: Signal PDFs for the kinematic variables for the (top) $K^+K^-K^0_{S+-}$ and (bottom) $K^+K^-K^0_{S00}$ modes, with fits to signal MC events.

The fits to the whole DP and high-mass region cover wide ranges of the phase space. As will be discussed in Sec. 4.5.2, correlations between the Fisher discriminant and the DP in the continuum background prevent us from using the Fisher discriminant in these fits. Therefore, for those fits we apply the cut $\mathcal{F} > -2.5$, as shown in the last line of Table 4.2, and do not include a PDF for $\mathcal{F}$ in the fit. In contrast, the low-mass fit covers only a small slice of phase space, and therefore the correlation between Dalitz plot location and $\mathcal{F}$ can be neglected. This allows us to use all data

in the range $-6 < \mathcal{F} < 4$, and include a PDF for $\mathcal{F}$ in the fit. We parameterize the signal Fisher distributions with the sum of three Gaussian distributions, with the parameters fit separately for each tagging category. Fits to signal MC are shown in Fig. 4.7. The parameters used for these PDFs are listed in Appendix A.1.

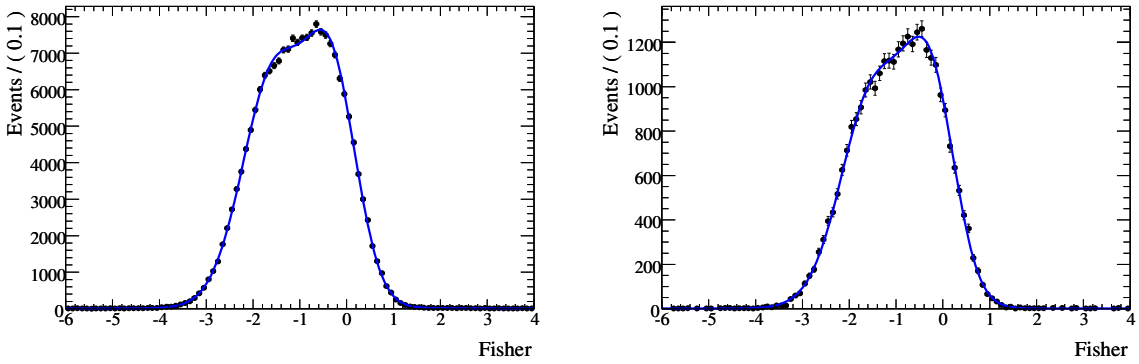

Figure 4.7: Signal PDFs for the Fisher discriminant $\mathcal{F}$, used in the low-mass fit, for (left) $K^+K^-K^0_{S+-}$ and (right) $K^+K^-K^0_{S00}$. The fits are to signal MC events.

4.4.2 Choice of Dalitz Plot Variables

As discussed in Sec. 2.4.2, the decay of a pseudoscalar particle into three pseudoscalar daughter particles can be completely described by two independent variables. The Dalitz plot is traditionally made as a scatter plot with axes given by the squares of invariant masses of daughter pairs. When constructed this way, the Dalitz plot for a pure phase space decay is uniformly occupied within the kinematically allowed two-dimensional space. Two-body resonances are easily identifiable as bands either parallel to an axis or at a 45 degree angle to both axes. However, because of its irregular shape, this construction of the Dalitz plot is often inconvenient when building PDFs.

Instead of the traditional coordinates, we use the *square Dalitz plot*, parameterized in terms of the variables $m_{K^+K^-}$ and $\cos\theta_H$ (also see Sec. 2.4.2). The Jacobian of the

transformation from the traditional coordinates to our variables,

$$dm_{ab}^2\, dm_{ac}^2 = |J|\, dm_{ab}\, d\cos\theta_H, \tag{4.10}$$

is given by

$$|J| = (2m_{ab})(2|\vec{p}||\vec{q}|), \tag{4.11}$$

where $\vec{p}$ ($\vec{q}$) is the K^0 (K^+) momentum in the rest frame of the K^+K^- system.

4.4.3 Signal Efficiency

When fitting to the Dalitz plot distribution, it is critical to account for the variation of the signal efficiency as a function of Dalitz plot location. Using phase space signal MC, we calculate the efficiency $\varepsilon(m_{K^+K^-}, \cos\theta_H)$ of the selection cuts in bins in the square Dalitz plot.

The *BABAR* group responsible for particle identification uses control samples to calculate corrections to the efficiency based on the PID selector used and the momentum and location of each track in the detector. These corrections are shown in Fig. 4.8. The final efficiency maps used in the fits, including the corrections, are shown in Fig. 4.9, both with and without the requirement of $\mathcal{F} > -2.5$.

4.4.4 Dalitz Plot PDF

The PDF describing the Dalitz plot for signal events is formed by combining Eq. 2.20 with the experimental effects of efficiency, tagging dilution, and Δt resolution. The final form of the PDF is:

$$\begin{aligned}
\mathcal{P}_{DP} \;\propto\;& \Big\{ e^{-|\Delta t|/\tau_B} \Big[k(|\mathcal{A}_f|^2 + |\bar{\mathcal{A}}_f|^2) \\
+\;& 2\eta_{CP}\, q_{\rm tag}\, \mathcal{D}\, \mathcal{I}m \left(e^{-2i\beta} \mathcal{A}_f^* \bar{\mathcal{A}}_f \right) \sin\Delta m\Delta t \\
-\;& q_{\rm tag}\, \mathcal{D} \left(|\mathcal{A}_f|^2 - |\bar{\mathcal{A}}_f|^2 \right) \cos\Delta m\Delta t \Big] \Big\} \\
\times\;& |J| \varepsilon(m_{K^+K^-}, \cos\theta_H) \otimes \mathcal{R}(\Delta t, \sigma_{\Delta t}),
\end{aligned} \tag{4.12}$$

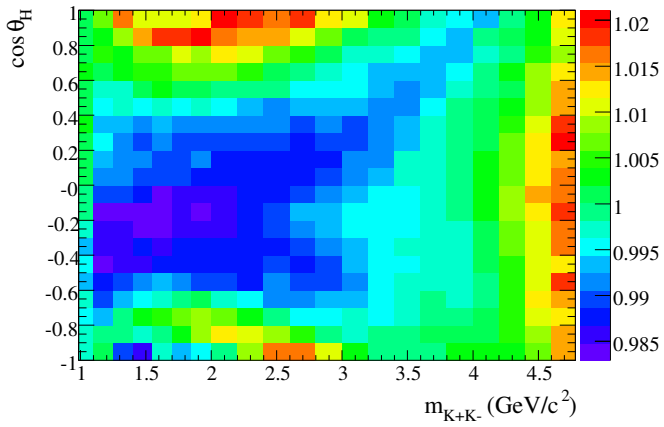

Figure 4.8: Corrections applied to the raw efficiencies to account for differences between data and MC in PID control samples. The plot shown here is for $K^+K^-K^0_{S+-}$. The corrections for $K^+K^-K^0_{S00}$ are similar.

where τ_B is the B^0 lifetime, $q_{\rm tag}$ is 1 (-1) for $B_{\rm tag}$ tagged as a B^0 $(\overline{B}^0)$, η_{CP} is 1 (-1) for K^0_S (K^0_L) decays, $\mathcal{D} = 1 - 2w$ is the dilution, and $k = 1 - q_{\rm tag}\Delta w$. Events in the *Untagged* category are included in the fits with ω fixed to 0.5. Therefore they contribute only to the PDF terms that do not depend on Δt.

4.4.5 Self Crossfeed

Some events, although they contain a true signal decay, are misreconstructed so that one or more of the reconstructed "signal" particles actually comes from the other B meson in the event. These are known as *self crossfeed* (SXF) events. Self crossfeed events can be problematic if they have a different distribution in the Dalitz plot than properly reconstructed signal events, or if they introduce correlations between the Dalitz plot variables and the kinematic variables.

In signal MC samples, we look for events that have been reconstructed and pass the selection criteria but have not been marked as "Truth matched" (TM) by the *BABAR* reconstruction software. (The truth-matching algorithm attempts to determine, for each reconstructed track or neutral cluster in a MC event, the simulated particle to which the reconstructed object corresponds. For instance, when we reconstruct a

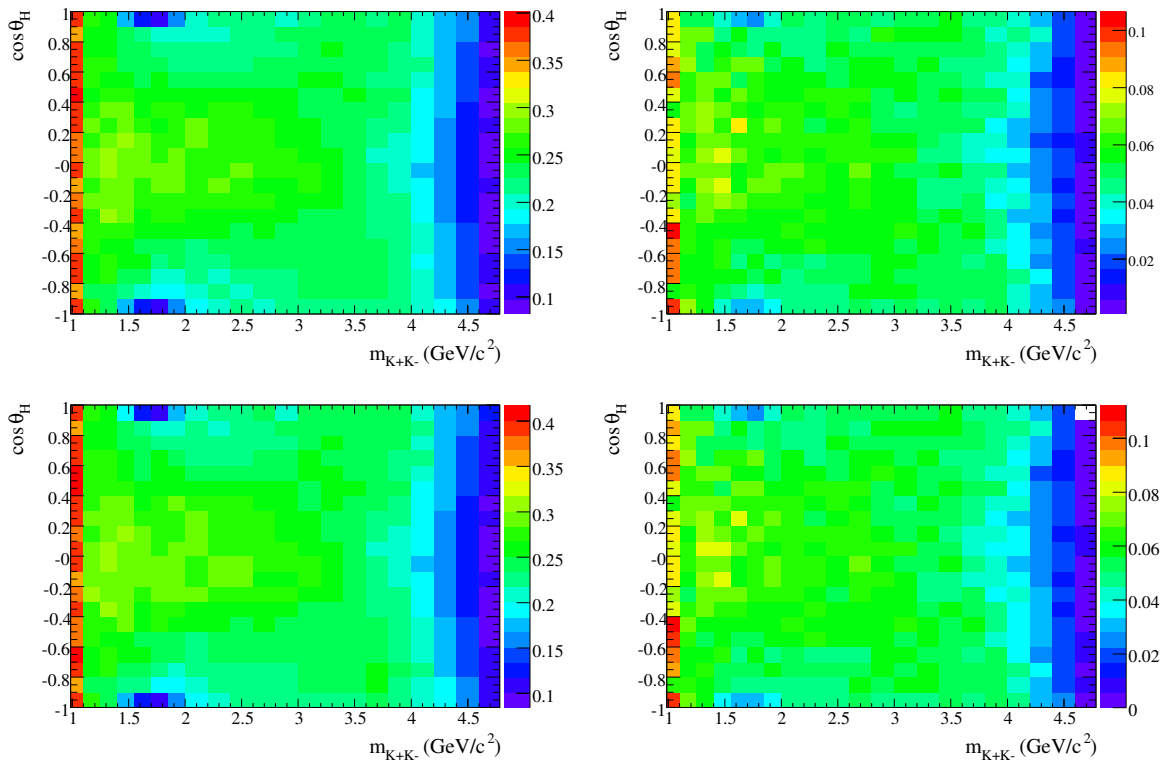

Figure 4.9: Efficiency maps, derived from signal MC, for (left) $K^+K^-K^0_{S+-}$ and (right) $K^+K^-K^0_{S00}$. The top row includes the cut $\mathcal{F} > -2.5$ while the bottom row does not. The efficiency is higher in the leftmost column of bins because the PID requirement is looser for $m_{K^+K^-} < 1.1\,\mathrm{GeV}/c^2$.

track in a MC event as a K^+, if the algorithm can determine that this track did in fact originate from a simulated K^+, then the reconstructed track is marked as "truth matched." If the algorithm determines that this track came from some other particle, for instance a π^+, then the recontructed track is marked as failing to be truth matched. For a composite candidate, the algorithm also checks if the candidate is composed of the correct daughter particles. Truth matching is a non-trivial task, and the algorithm is not perfect. However, because truth matching plays a relatively minor role in this analysis, we use the algorithm nearly as is. We do make an attempt to "recover" $K^0_S \to \pi^+\pi^-$ candidates where one of the pions radiates a photon, which nominally fail the truth-matching algorithm.) Events that fail truth matching can be classified in three categories:

- Radiative events, where the reconstructed K^+, K^-, and K^0_S are from the signal decay, but one of the charged particles on the signal side radiated a photon;
- events with a PID error (usually a pion from the decay of the other B^0 replaces one of the charged kaons in the reconstructed signal decay);
- other events where a decay product from the other B^0 is reconstructed as part of the signal decay, but with no PID error.

Radiative events have slightly broader distributions of $m_{\rm ES}$ and ΔE than normal signal events, but are uniformly distributed across the Dalitz plot as shown in Fig. 4.10. They do not pose a problem for the analysis.

The latter two categories tend to occur primarily in the corners of the Dalitz plot, and so can bias the Dalitz plot fit. These candidates have $m_{\rm ES}$ and ΔE distributions that are very similar to continuum events, and so a restrictive cut in the $m_{\rm ES}$-ΔE plane reduces the prevalence of these events. This is one of the reasons that we restrict the event selection to $m_{\rm ES} > 5.26\,{\rm GeV}/c^2$ and $-0.06(-0.12) < \Delta E < 0.06\,{\rm GeV}$ for $K^+K^-K^0_{S+-}$ ($K^+K^-K^0_{S00}$). After this tight signal region is selected, the fractions of self crossfeed events remaining are given in Table 4.6.

In the $K^+K^-K^0_{S+-}$ mode, the fraction of SXF events is less than 0.4% after the selection criteria. This fraction is small enough that it can be ignored. SXF is much

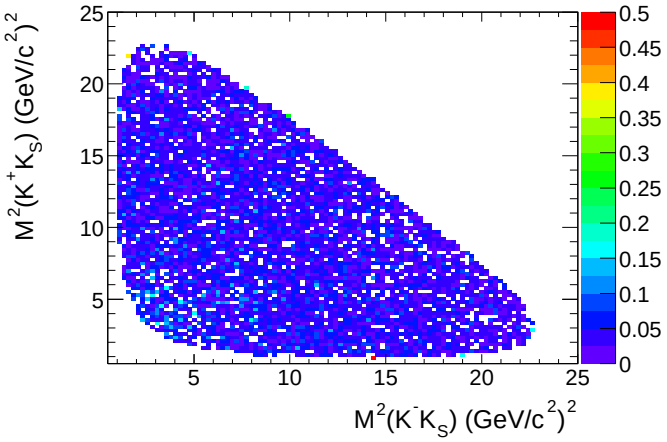

Figure 4.10: Distribution on the Dalitz plot of radiative signal events in $K^+K^-K^0_{s+-}$.

Table 4.6: Fractions of self crossfeed events found in studies of phase space signal MC. All numbers are in percent.

	$K^+K^-K^0_{s+-}$		$K^+K^-K^0_{s00}$	
	Fraction of non-TM	Fraction of all events	Fraction of non-TM	Fraction of all events
Non-truth matched	100	4.6	100	29
Radiative	92	4.3	11	3.2
SXF with PID error	1	0.02	0.1	0.03
Other SXF	7	0.3	89	26

more common in $K^+K^-K^0_{S00}$ because of the ease of forming K^0_S candidates from the wrong combination of photons. As shown in Fig. 4.11, the fraction of self crossfeed events is fairly constant over most of the Dalitz plot, with the exception of high values of $m_{K^+K^-}$. Because this region has relatively little signal, the overall shape is not distorted severely and we do not treat self crossfeed differently from other signal events when we construct the PDFs.

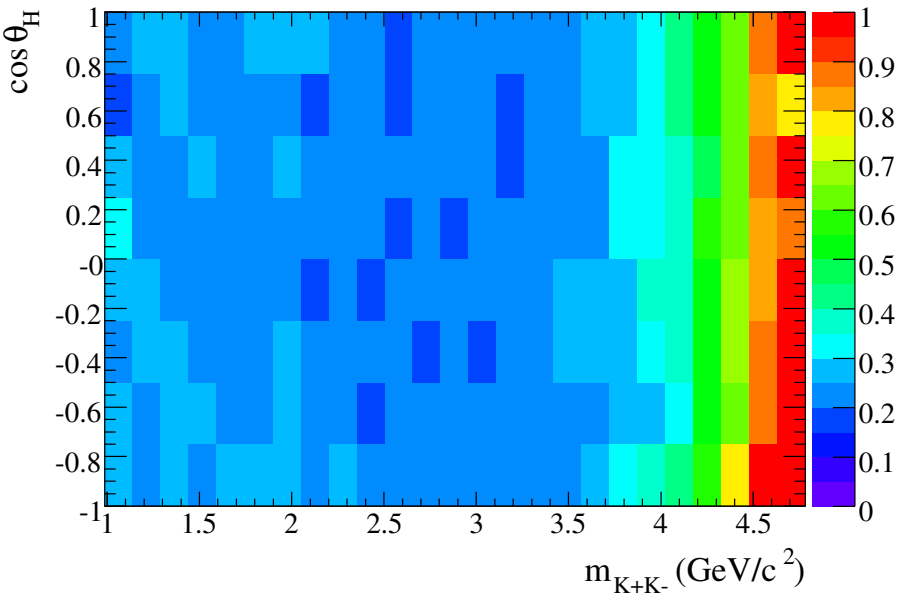

Figure 4.11: For the $K^+K^-K^0_{S00}$ mode, the fraction of reconstructed signal events that are self crossfeed, as a function of position on the square Dalitz plot.

4.4.6 Dalitz Plot Resolution

The Dalitz plot variables $m_{K^+K^-}$ and $\cos\theta_H$ are reconstructed with finite resolution, which can broaden or distort the shape of resonance structures in the data. Also, as noted in Sec 4.1.1, the Dalitz plot variables are calculated after refitting the B^0 candidate with a B mass constraint. This is useful because it ensures that candidates will fall within the kinematically allowed region of the Dalitz plot, but can also introduce biases on the Dalitz plot variable reconstruction.

The resolution is studied using signal MC samples. Because the resonances in our model decay into K^+K^-, we focus on the $m_{K^+K^-}$ resolution and ignore the $\cos\theta_H$ resolution. In bins of the true $m_{K^+K^-}$, we fit a Gaussian shape to the distribution of the difference between the reconstructed and true values of $m_{K^+K^-}$. The means and widths of these Gaussian distributions are plotted in Fig. 4.12.

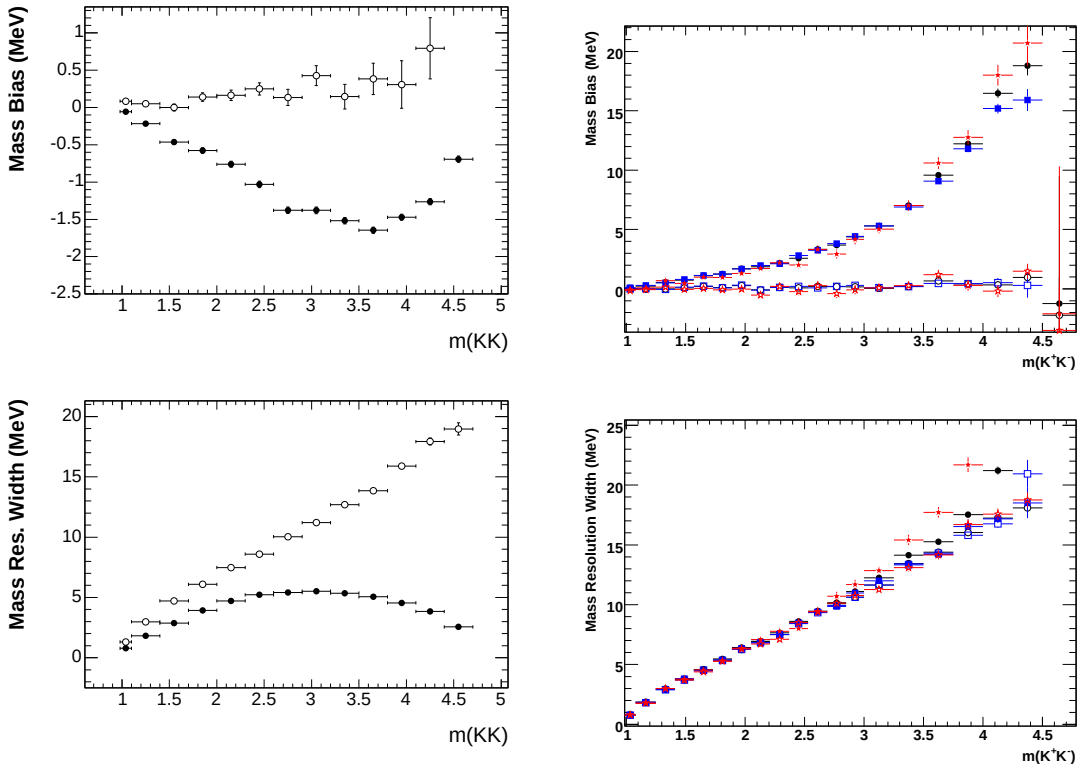

Figure 4.12: $m_{K^+K^-}$ resolution, as measured in MC samples. The top row shows the bias and the bottom row shows the width of the reconstructed $m_{K^+K^-}$. The $K^+K^-K^0_{S+-}$ mode is shown on the left while the $K^+K^-K^0_{S00}$ mode is on the right. In all plots, the filled symbols refer to $m_{K^+K^-}$ reconstructed using a B-mass constraint, which is what is used in the final fit. The open symbols, calculated without a B-mass constraint, are included for comparison. For the $K^+K^-K^0_{S00}$ mode, the black circles show all events, blue squares are for truth-matched events only, and red stars are for self crossfeed events only.

Particularly in the $K^+K^-K^0_{S00}$ mode, the resolution degrades significantly at high $m_{K^+K^-}$. Fortunately the only narrow resonance in that region is the (relatively

unimportant) χ_{c0}. The important ϕ resonance is at $1020\,\mathrm{MeV}/c^2$, where both modes have good resolution. We do not account for resolution in our ML fit. As will be discussed in the section on fit validation, we assign a systematic error that includes a contribution from resolution.

4.4.7 Correlations between observables

In Tables 4.7 and 4.8, we summarize the linear correlations between observables in the ML fit.

Table 4.7: For the $K^+K^-K^0_{S+-}$ mode, the correlations between ML fit observables, determined from phase-space signal MC with selection cuts applied.

Variable	m_{ES}	ΔE	$m_{K^+K^-}$	$\cos\theta_H$	Δt
m_{ES}	1	-0.13	0.001	-0.002	0.03
ΔE		1	-0.03	0.001	-0.0001
$m_{K^+K^-}$			1	-0.0005	-0.0003
$\cos\theta_H$				1	-0.0005

Table 4.8: For the $K^+K^-K^0_{S00}$ mode, the correlations between ML fit observables, determined from phase-space signal MC with selection cuts applied.

Variable	m_{ES}	ΔE	$m_{K^+K^-}$	$\cos\theta_H$	Δt
m_{ES}	1	0.03	-0.05	0.0008	0.008
ΔE		1	-0.009	0.001	-0.004
$m_{K^+K^-}$			1	-0.01	-0.001
$\cos\theta_H$				1	-0.002

4.5 Background Parameterization

Continuum background is primarily studied with onpeak data that falls outside of the signal region in $m_{\rm ES}$ and ΔE. Figure 4.13 shows the layout of these sideband regions on the $m_{\rm ES} - \Delta E$ plane. The use of onpeak data to model the background is useful because it avoids relying on the accuracy of MC simulation. However, it also carries some assumptions about the nature of the sidebands that are discussed in the following sections.

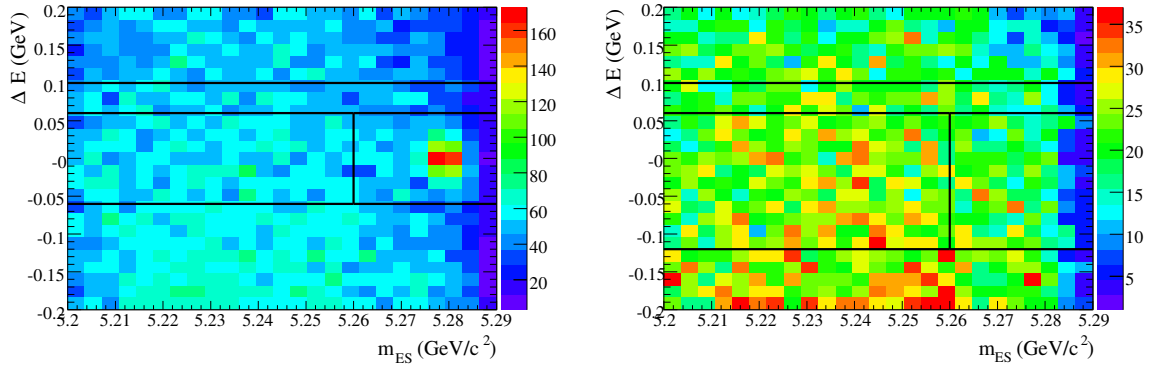

Figure 4.13: The $m_{\rm ES} - \Delta E$ plane showing (right) $K^+K^-K^0_{S+-}$ and (left) $K^+K^-K^0_{S00}$ data events. The box on the right of each plot indicates the signal region. A signal peak is clearly visible in the $K^+K^-K^0_{S+-}$ mode. The box on the left of each plot is the $m_{\rm ES}$ sideband, used for determination of the Dalitz plot background shape. The upper region ($\Delta E > 0.1\,$GeV) of each plot is the ΔE sideband, used for determination of the $m_{\rm ES}$ background shape.

4.5.1 The $m_{\rm ES}$ sideband

Most events in the sideband regions are continuum background. However, there is some contamination from $B\overline{B}$ backgrounds. *Peaking* $B\overline{B}$ background consists of decays such as $B^0 \to K^{*+}K^-K^0$ ($K^{*+} \to K^+\pi^0$) where the π^0 is lost in reconstruction. Because of the lost particle ΔE peaks near $-135\,$MeV for these events, while $m_{\rm ES}$ is distributed in roughly the same manner as signal. The most important reason for restricting the extent of the signal region and the $m_{\rm ES}$ sideband to

$\Delta E > -60\ (-120)$ MeV for $K^+K^-K^0_{S+-}$ ($K^+K^-K^0_{S00}$) is to reduce contamination from peaking background.

Although peaking background is nearly eliminated from the signal region and $m_{\rm ES}$ sideband by the requirement on ΔE, combinatoric $B\overline{B}$ background remains. This class of events originates from $B\overline{B}$ events where decay products from both sides of the event are reconstructed into a $K^+K^-K^0_S$ candidate. We explicitly fit for the yield of these events in the fit, but it is important to recognize that some of the events used to form the continuum background PDFs actually originate from combinatoric $B\overline{B}$ background. Using generic $B\overline{B}$ and $uds + c\bar{c}$ MC samples, we have confirmed that the fraction of $B\overline{B}$ events, relative to the number of continuum events, is roughly the same in the $m_{\rm ES}$ sideband and the signal region. We also use $uds + c\bar{c}$ MC to check that the distribution of events on the Dalitz plot is consistent between the $m_{\rm ES}$ sideband and the signal region, which is important since we use the sideband events to model the background Dalitz plot distribution in the fit to the data. As shown in Fig. 4.14 and Fig 4.15, the distributions are similar to the eye. A 2D Kolmogorov test of the histograms shows in Fig. 4.14 gives a value of 0.47. The χ^2 probability of all three pairs of histograms shown in Fig. 4.15 is 1.

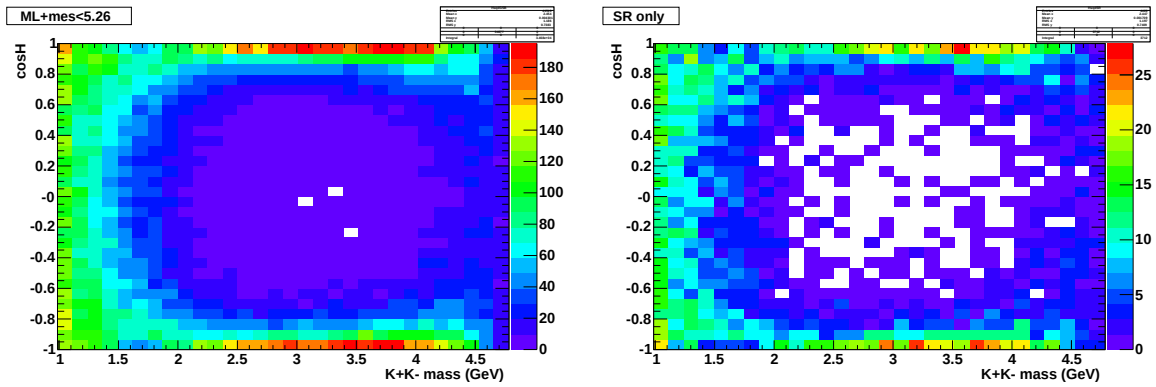

Figure 4.14: Distributions of uds+$c\overline{c}$ MC events for the $K^+K^-K^0_{S+-}$ mode, in (left) the $m_{\rm ES}$ sideband and (right) the signal region.

(A)

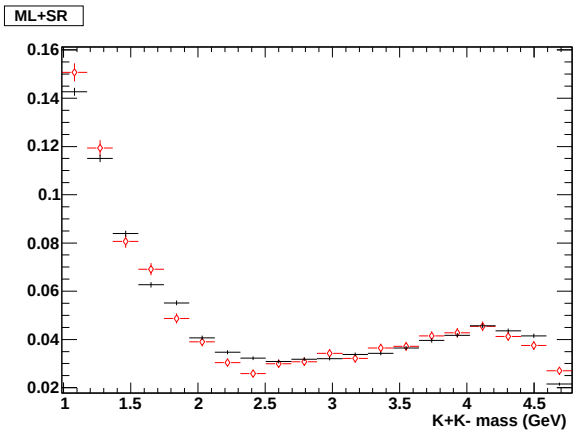

(B)

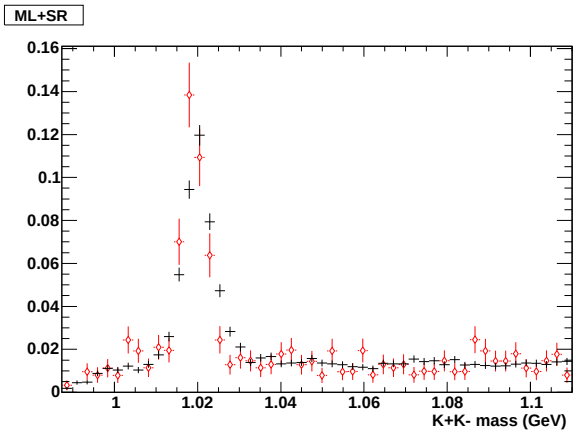

(C)

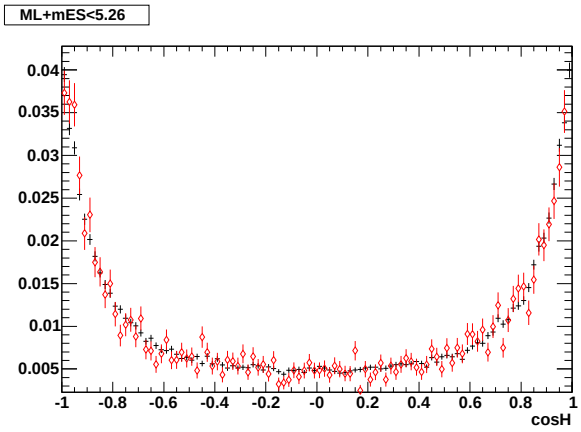

Figure 4.15: For the $K^+K^-K^0_{S+-}$ mode, one-dimensional projections of the Dalitz plot distributions of $uds{+}c\overline{c}$ MC events in the $m_{\rm ES}$ sideband (black points) and signal region (red diamonds). (A) $m_{K^+K^-}$ (B) $m_{K^+K^-}$ (ϕ region) (C) $\cos\theta_H$

4.5.2 Correlations between observables

The observables in a likelihood fit must be uncorrelated, so for a fit that includes the Dalitz plot we must study the correlations between the Dalitz plot and other observables used in the fit.

The fit PDF is split by tagging categories, so we must check whether the background Dalitz plot shape depends significantly on the tagging category. One-dimensional projections of the Dalitz plot distributions of the $m_{\rm ES}$ sideband of onpeak data are shown in 4.16. χ^2 comparisons of the distributions shown in the Figure reveal that differences between the distributions are negligible.

In the center of the Dalitz plot, the momenta of all three daughters are equal in the B^0 rest frame, giving events a more spherical shape. This causes continuum background to have more signal-like values of the Fisher discriminant in the center of the Dalitz plot. To study the correlation of the Fisher discriminant and the DP location, we define a "Dalitz plot distance" variable

$$\Delta_D \equiv \text{minimum}(m_{K^+K^-}, m_{K^+K^0_S}, m_{K^-K^0_S}). \tag{4.13}$$

With this definition, an event at the edge of the Dalitz plot will have $\Delta_D = 0$, while an event at the center will have a high value. As shown in Fig. 4.17, continuum background events show a clear correlation between $\mathcal{F}$ and Δ_D. Therefore, as mentioned earlier, we exclude $\mathcal{F}$ from the ML fits (except for the low-mass fit), and make the cut $\mathcal{F} > -2.5$.

4.5.3 $q\overline{q}$ Background PDFs

The continuum background $m_{\rm ES}$ distribution is parameterized with a threshold function, usually known as the Argus function [49],

$$f(m_{\rm ES}) = m_{\rm ES}\sqrt{1 - {m_{\rm ES}}^2/m_0^2}\exp\left[\xi\left(1 - {m_{\rm ES}}^2/m_0^2\right)\right], \tag{4.14}$$

where m_0 is the endpoint of the $m_{\rm ES}$ distribution (approximately $\sqrt{s}/2$), and ξ is a shape parameter. The distribution is undefined for $m_{\rm ES} > m_0$, so events in this range

(A)

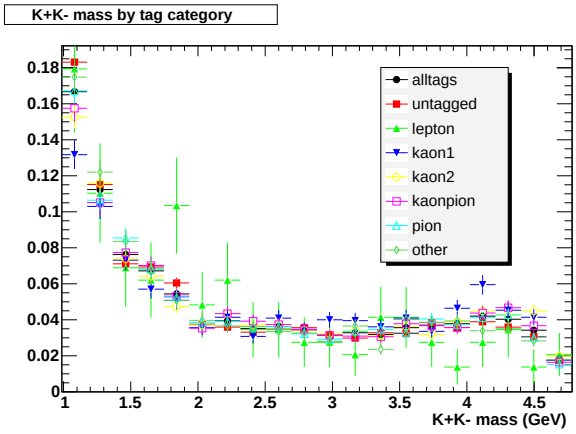

(B)

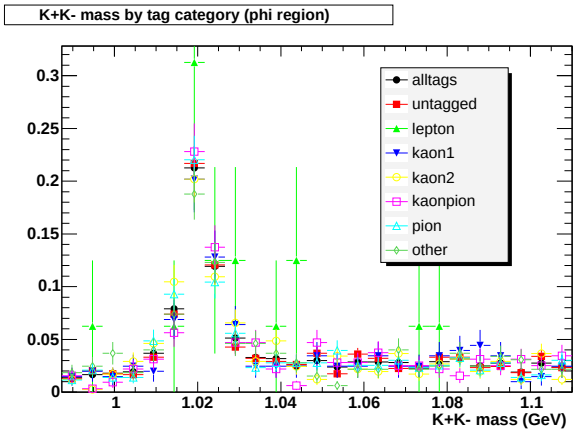

(C)

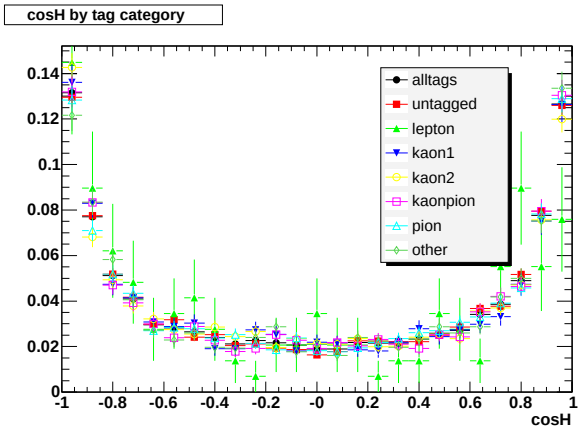

Figure 4.16: Distributions of $m_{\rm ES}$ sideband events from onpeak $K^+K^-K^0_{S+-}$ data, split by tagging category.

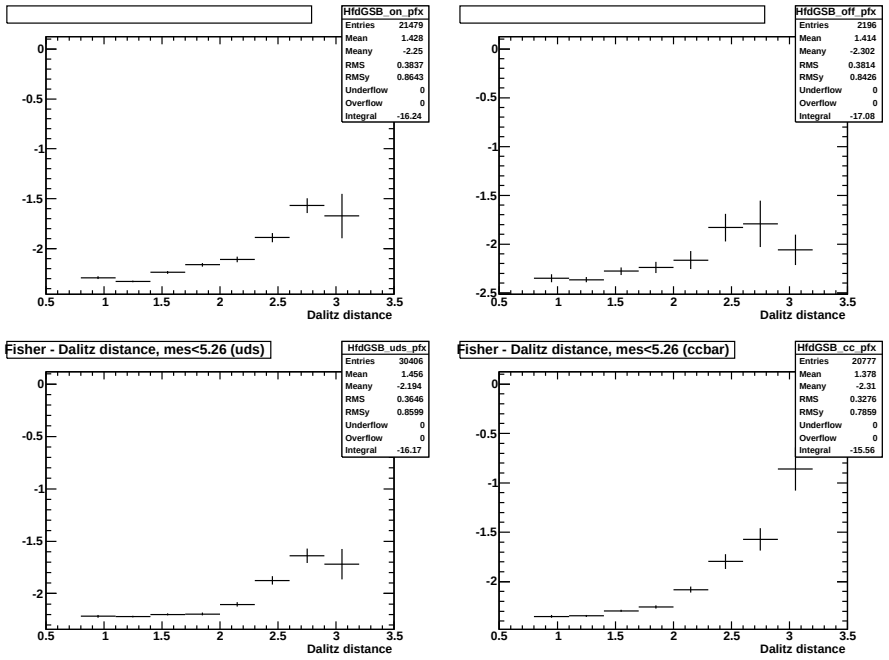

Figure 4.17: The average value of the Fisher discriminant $\mathcal{F}$ as a function of the Dalitz distance Δ_D for $K^+K^-K^0_{S+-}$. Plots are shown for (top left) onpeak data, (top right) offpeak data, (bottom left) *uds* MC, and (bottom right) $c\overline{c}$ MC. All plots are for the $m_{\rm ES}$ sideband region.

are removed from the data sample. The value of ξ is determined separately for each tagging category and for the two K^0_s decay modes, while m_0 is fixed to $5.2895\,\mathrm{GeV}/c^2$ for all events. The m_{ES} PDFs are shown in Fig. 4.18. ΔE is described with a linear PDF, with the slope determined separately for $K^+K^-K^0_{S+-}$ and $K^+K^-K^0_{S00}$. These PDFs are shown in Fig. 4.19. Note that for the ΔE fit, we extend the m_{ES} sideband to include all events in the range $-200 < \Delta E < 200\,\mathrm{MeV}$.

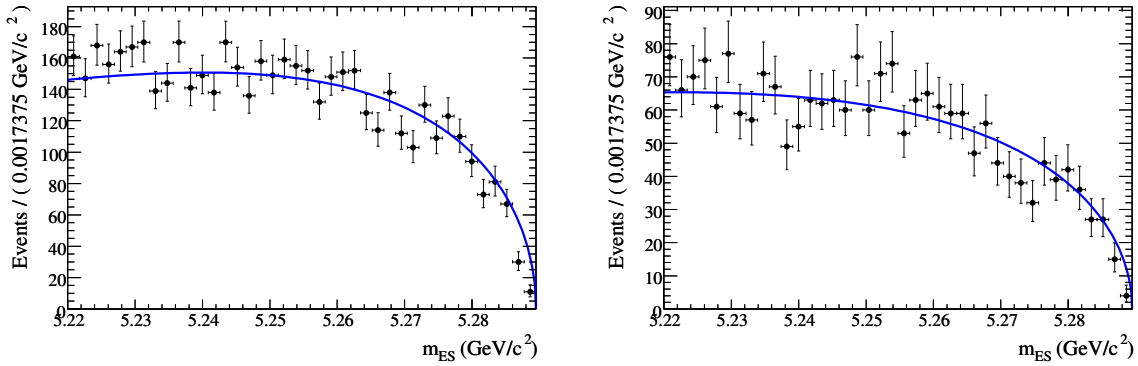

Figure 4.18: m_{ES} PDFs for $q\overline{q}$ background for (left) $K^+K^-K^0_{S+-}$ and (right) $K^+K^-K^0_{S00}$. The points are onpeak data from the ΔE sideband, used in creating the PDFs.

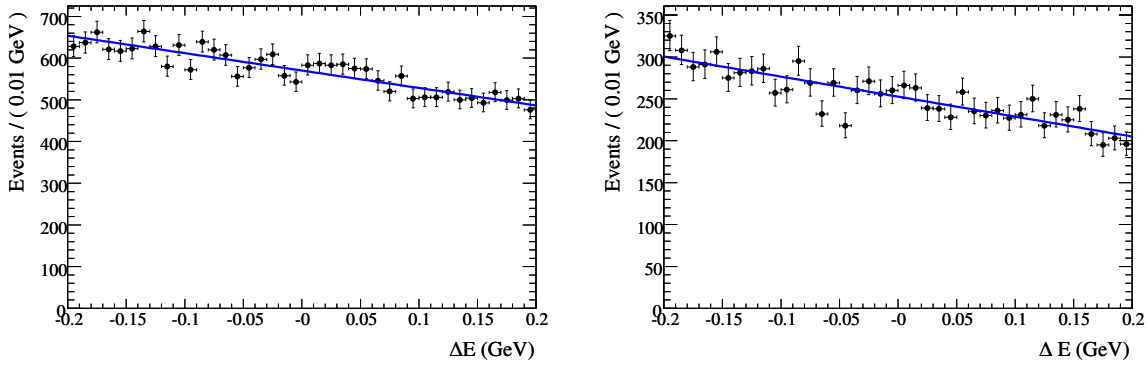

Figure 4.19: ΔE PDFs for $q\overline{q}$ background for (left) $K^+K^-K^0_{S+-}$ and (right) $K^+K^-K^0_{S00}$. The points are onpeak data from the m_{ES} sideband, used in creating the PDFs.

For the low-mass fit, we must also parameterize the shape of the Fisher discriminant distribution. It is described by the sum of two Gaussian distributions, as shown in Fig. 4.20. Only events falling in the low-mass region of the Dalitz plot are used in parameterizing these PDFs.

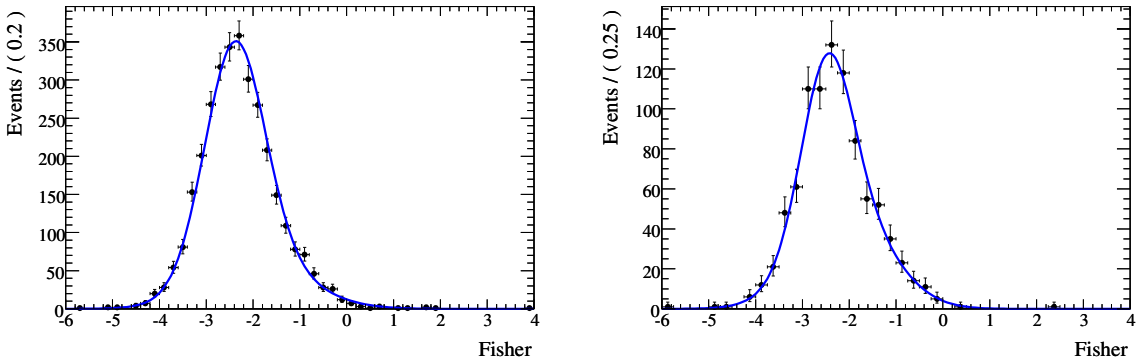

Figure 4.20: Fisher discriminant PDFs for $q\overline{q}$ background for (left) $K^+K^-K^0_{S+-}$ and (right) $K^+K^-K^0_{S00}$. The points are onpeak data from the $m_{\rm ES}$ sideband, used in creating the PDFs.

We assume that the Δt distribution of continuum background events is uncorrelated with the Dalitz plot location. The Δt PDF is parameterized as a sum of "prompt" and "lifetime" contributions, where the latter originates from long-lived D mesons:

$$\mathcal{P}(\Delta t) = \left[f_{\rm prompt}\delta(\delta_t) + (1 - f_{\rm prompt})e^{-|\Delta t|/\tau_{bg}}/4\tau_{bg}\right] \otimes \mathcal{R}_{bg}, \qquad (4.15)$$

where δ is the Dirac δ function. The Δt resolution function $\mathcal{R}_{bg}$ is similar to the signal resolution function given in Eq. 4.7, except the tail Gaussian distribution is omitted. The parameters of the background Δt PDF are determined in fits to the $m_{\rm ES}$ sideband, shown in Fig. 4.21.

The continuum background Dalitz plot distributions are described by two-dimensional histogram PDFs. The binning of these histograms presents a challenge because events are distributed in an irregular fashion, with many events on the left, top, and bottom edges of the square Dalitz plot but very few events in the center. The bins must be fine enough to correctly model narrow structures in the continuum

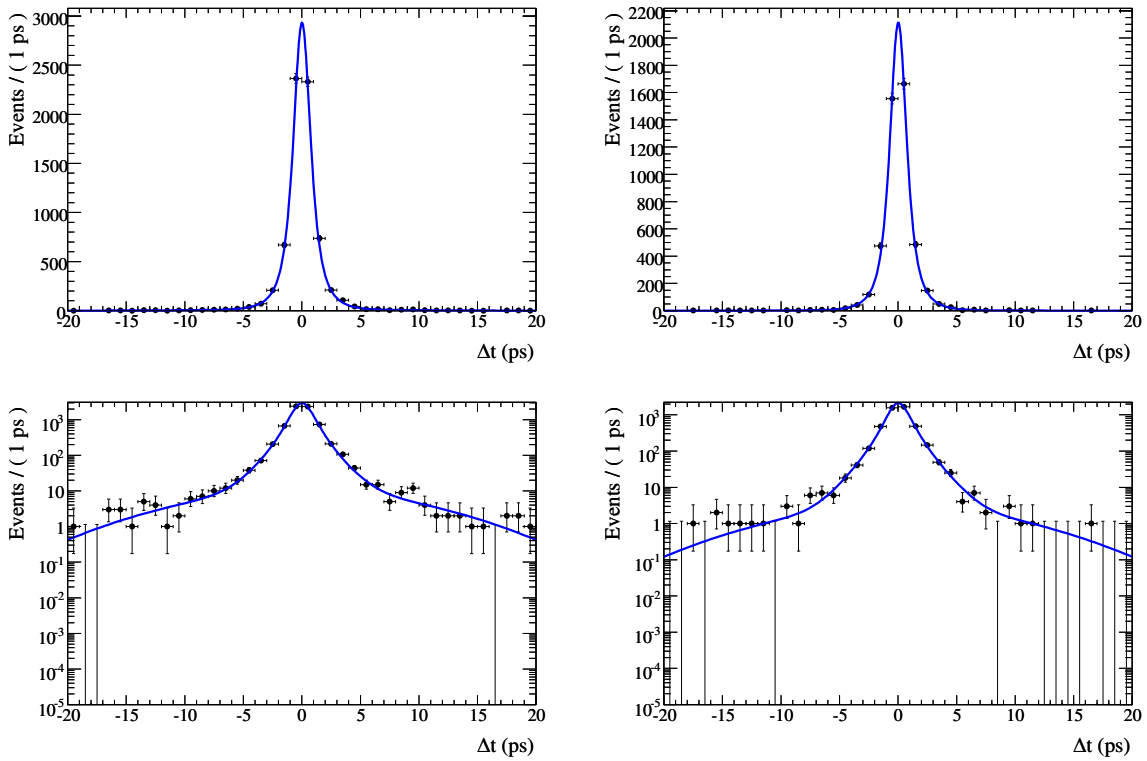

Figure 4.21: Δt PDFs for $q\overline{q}$ background for (left) $K^+K^-K^0_{S+-}$ and (right) $K^+K^-K^0_{S00}$, shown (top) on a linear scale and (bottom) a logarithmic scale. The points are onpeak data from the $m_{\rm ES}$ sideband, used in creating the PDFs.

background (particularly real $\phi \to K^+K^-$ decays). However, coarser binning is necessary in the center of the square Dalitz plot to avoid large statistical fluctuations. To solve these problems, we use a histogram PDF with arbitrary binning, where the edges of every bin can be set independently.[3] The PDFs are shown in Fig. 4.22.

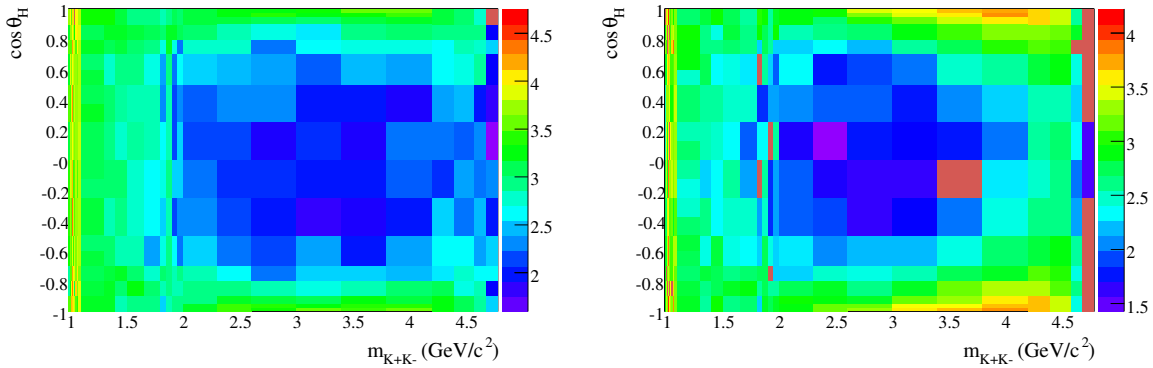

Figure 4.22: Dalitz plot PDFs for $q\overline{q}$ background for (left) $K^+K^-K^0_{S+-}$ and (right) $K^+K^-K^0_{S00}$, shown on a logarithmic scale. Note the extremely fine binning in the $\phi(1020)$ region, and along the top and bottom of the square DP. The PDFs are constructed using onpeak data events from the $m_{\rm ES}$ sideband.

4.5.4 $B\overline{B}$ Background PDFs

As noted earlier, peaking $B\overline{B}$ background originating from $B \to K^+K^-K^0_S h$, where h is a charged or neutral pion, is virtually eliminated by our choice of ΔE selection. In the $K^+K^-K^0_{S+-}$ mode, the remaining $B\overline{B}$ background is shaped very much like continuum background. We model the $m_{\rm ES}$ and ΔE shapes with the Argus function (Eq. 4.14) and a linear PDF, respectively. The parameters of these PDFs are derived from fits to generic $B\overline{B}$ MC, after removing all signal events. The PDFs are shown with $B\overline{B}$ MC events in Fig. 4.23. Due to the limited statistics available in the $B\overline{B}$ MC samples, we are not able to split the PDF parameters by tagging category.

Despite the wider ΔE cut in the $K^+K^-K^0_{S00}$ mode, the peaking $B \to K^+K^-K^0_S h$ background is still negligible. Excluding signal events, we find 38 events in the generic

[3]The PDF is implemented in `RooFit` as `Roo2DArbHistPdf`.

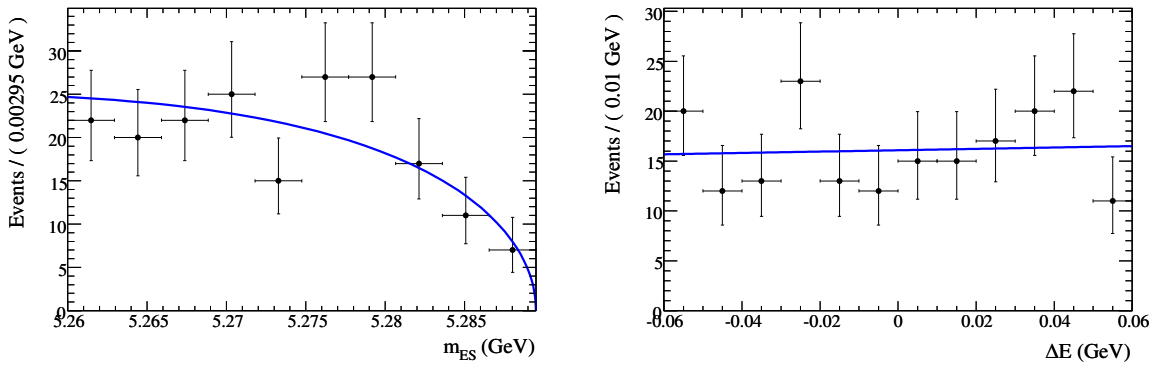

Figure 4.23: Kinematic PDFs for $B\overline{B}$ background for $K^+K^-K^0_{S+-}$, with points from generic $B\overline{B}$ MC.

$B^0\overline{B}^0$ MC sample and 77 events in the generic B^+B^- MC sample that pass all selection cuts. Scaling from the MC to the data luminosity, we expect a $B\overline{B}$ background yield of $38/2.1 + 77/1.8 = 61$ events.[4] The dominant source of these events is misreconstructed $K^0_S \to \pi^0\pi^0$ candidates. We observe a significant correlation between $m_{\rm ES}$ and ΔE in these events, and so we model these variables with a two-dimensional histogram PDF. To make this PDF, we use the $B\overline{B}$ MC events passing the selection cuts in the wide region defined by $5.2 < m_{\rm ES} < 5.3\,{\rm GeV}/c^2$ and $-200 < \Delta E < 200\,{\rm MeV}$. We make a 2D KEYS PDF of $m_{\rm ES}$ and ΔE from these events, which helps to smooth the statistical fluctuations caused by having a small event sample. The KEYS PDF is then used to create a regular 2D histogram PDF, which is used in the fitting. The histogram PDF is shown in Fig. 4.24.

The distribution of $B\overline{B}$ MC events across the tagging categories: { `Lepton, KaonI, KaonII, KaonPion, Pion, Other, Notag` }= {16, 9, 26, 36, 31, 22, 53} in the $K^+K^-K^0_{S+-}$ mode, is consistent with the tagging fractions in the high-statistics $B_{\rm flav}$ sample. Hence, we use the same tagging fractions for the $B\overline{B}$ background as are used for signal events.

[4] A veto is applied to remove events from the generic $B\overline{B}$ MC that are actually signal $B^0 \to K^+K^-K^0_S$ events.

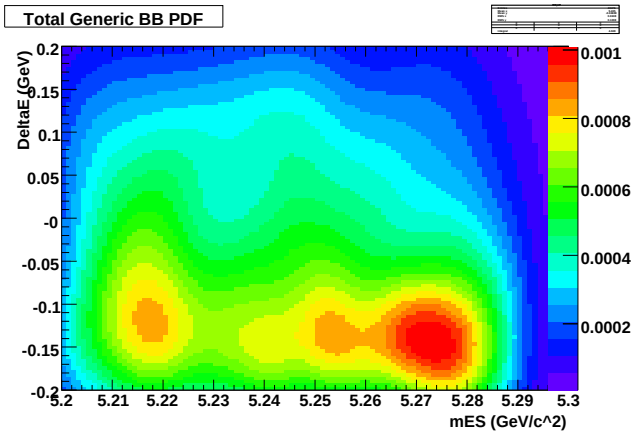

Figure 4.24: Two-dimensional PDF for $m_{\rm ES}$ and ΔE for $B\overline{B}$ background in the $K^+K^-K^0_{S00}$ mode. Note that the PDF describes wider ranges of $m_{\rm ES}$ and ΔE than are actually used in the fit.

For both $K^+K^-K^0_{S+-}$ and $K^+K^-K^0_{S00}$, the Δt resolution function for $B\overline{B}$ background uses a similar parameterization to that used for $q\overline{q}$ background. We multiply Eq. 4.15 by a factor

$$1 + q_{\rm tag} S_{B\overline{B}} \sin\Delta m\Delta t + C_{B\overline{B}} \cos\Delta m\Delta t \tag{4.16}$$

to add the possibility of CP violation in the $B\overline{B}$ background. For the nominal fit, $S_{B\overline{B}}$ and $C_{B\overline{B}}$ are fixed to zero, but we vary them when estimating the systematic errors. The resolution biases and scale factors are fixed to the same values as used for $q\overline{q}$ background, while the lifetime of the long-lived portion is fixed to the B^0 lifetime. The fraction of prompt decays is determined by fitting to the generic $B\overline{B}$ MC. Δt PDFs for $B\overline{B}$ background are shown in Fig. 4.25.

Two-dimensional histogram PDFs are used to describe the $B\overline{B}$ background distribution on the square Dalitz plot. For both $K^+K^-K^0_{S+-}$ and $K^+K^-K^0_{S00}$, we use generic $B\overline{B}$ MC events to fill 2D histograms with arbitrary binning. These histograms are similar to those used for the DP distributions of $q\overline{q}$ events, but with much coarser bins due to the limited statistics of the MC samples. These histogram PDFs are shown in Fig. 4.26.

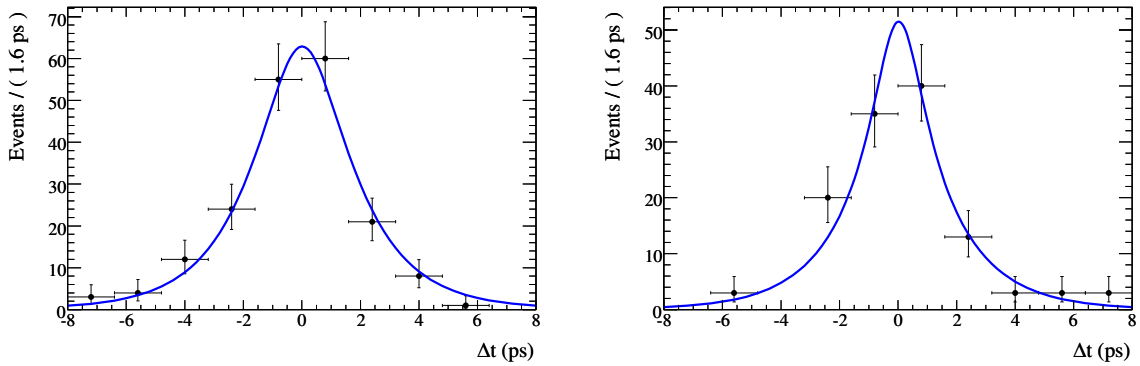

Figure 4.25: Δt PDFs for $B\overline{B}$ background for (left) $K^+K^-K^0_{S+-}$ and (right) $K^+K^-K^0_{S00}$. Points are from generic $B\overline{B}$ MC.

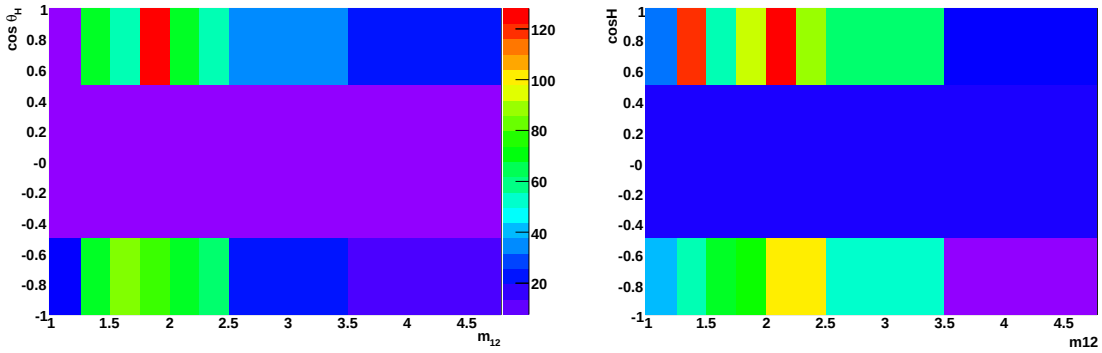

Figure 4.26: Histogram PDFs describing the $B\overline{B}$ background for (left) $K^+K^-K^0_{S+-}$ and (right) $K^+K^-K^0_{S00}$.

4.6 Fit Validation

As described in Sec. 4.3, all results are extracted using a series of ML fits to the data. To check that the fit method is unbiased, we perform several "pure toy Monte Carlo" studies. In this method, the PDFs are used to generate data samples, which are then fit using those same PDFs. For each category, the number of events generated is given by a Poisson distribution around the mean number of events expected for that category. Other parameters (for example, the *CP* asymmetry parameters and isobar coefficients) are set to reasonable values.

Over a large ensemble of trials, the average fit result for each floating parameter should be equal to the value that was generated. A significant deviation from the generated value could indicate a problem with the fit. For each trial we calculate the normalized residual, or *pull*, for each floating variable, where

$$pull \equiv (x_{\rm fit} - x_{\rm generated})/\sigma_{x_{\rm fit}}. \tag{4.17}$$

$\sigma_{x_{\rm fit}}$ is the error returned by the fit on the floating parameter x. With this definition, the distribution of pulls for any floating parameter for an ensemble of toy trials should be a Gaussian shape with unit width and a mean of zero. If the mean is different from zero, then the fit is biased for that parameter. If the width differs from unity, then the error on the parameter is misestimated. The results of our toy studies are presented in Sec. 4.6.1.

We perform a separate check using a so-called "embedded toy" method. The technique is similar to pure toys, but only the background events are generated directly from the PDFs. The signal events are taken from a signal MC sample which is generated with a realistic model of the Dalitz plot shape. Results of embedded toy tests are presented in Sec. 4.6.2.

4.6.1 Pure Toy Tests

Toys are done separately for the fit to the whole DP, the high-mass fit, and the low-mass fit. We also do toys for a fit to the $K^+K^-K^0_{S+-}$ mode alone, and then for a

fit to all modes ($K^+K^-K^0_{S+-}$, $K^+K^-K^0_{S00}$, and $K^+K^-K^0_L$) combined. For the most part, the discussion here will be restricted to the tests of the combined fit.

There are 44 floating parameters in the fit to the whole Dalitz plot: 2 *CP* parameters, 6 pairs of isobar coefficients, 2 non-interfering isobar coefficients, 3 signal yields, 3 $q\overline{q}$ background yields, 3 $B\overline{B}$ background yields, 6 tagging category fractions for $q\overline{q}$ backgrounds for each of the 3 modes, and the EMC fraction for $q\overline{q}$ background events in the K^0_L mode. All fits are done with the `MIGRAD` routine of the `MINUIT` package, with subsequent refinement of the error matrix performed by the `HESSE` algorithm.

The pull distributions for the *CP* asymmetry parameters in the whole DP fit to all $K^+K^-K^0$ modes are shown in Fig. 4.27. 1000 toy fits were performed. We reject any fits (about 20) that do not have a full, accurate covariance matrix. The means and widths of the pull distributions for key floating parameters are listed in Tab. 4.9. Some pull distributions have non-zero means, however the *CP* asymmetry parameters are unaffected by this problem.

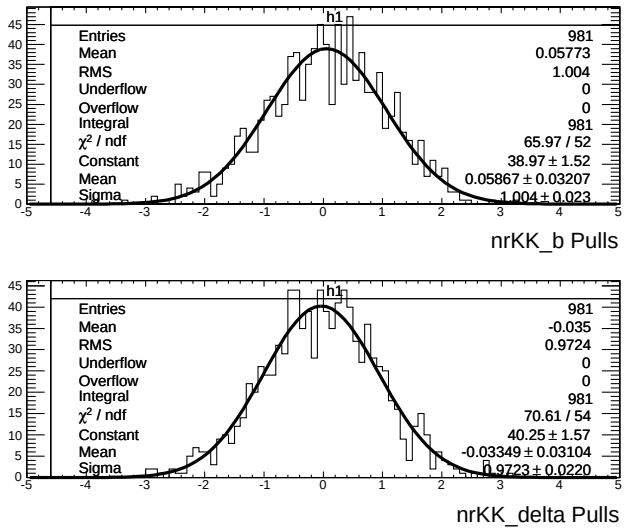

Figure 4.27: Pull distributions for the *CP* asymmetry parameters (top) $b_{K^+K^-K^0}$ and (bottom) $\delta_{K^+K^-K^0}$. The curves are fits to Gaussian distributions.

Toy fits are also useful because they provide an estimate of the statistical errors on the floating parameters. Most of the power in this analysis comes from the

Table 4.9: Results of toys for the whole Dalitz plot fit. The means and widths are derived from fits of Gaussian distributions to the pull results.

Parameter	Mean	Width
$b_{K^+K^-K^0}$	0.06 ± 0.03	1.00 ± 0.02
$\delta_{K^+K^-K^0}$	-0.03 ± 0.03	0.97 ± 0.02
c of ϕ	-0.26 ± 0.03	0.94 ± 0.02
φ of ϕ	0.02 ± 0.03	0.99 ± 0.02
c of $f_0(980)$	-0.07 ± 0.03	0.96 ± 0.02
φ of $f_0(980)$	0.26 ± 0.03	0.96 ± 0.02
c of $X_0(1550)$	0.00 ± 0.03	0.94 ± 0.02
φ of $X_0(1550)$	0.14 ± 0.03	0.97 ± 0.02
c of $NR_{K^+K^0}$	-0.08 ± 0.03	0.92 ± 0.02
φ of $NR_{K^+K^0}$	0.10 ± 0.03	0.97 ± 0.02
c of $NR_{K^-K^0}$	0.10 ± 0.03	0.87 ± 0.02
φ of $NR_{K^-K^0}$	-0.20 ± 0.03	1.03 ± 0.02
c of χ_{c0}	-0.37 ± 0.03	1.02 ± 0.02
φ of χ_{c0}	-0.11 ± 0.04	1.01 ± 0.03
c of D^+	-0.21 ± 0.03	0.92 ± 0.02
c of D_s^+	-0.22 ± 0.03	0.95 ± 0.02
$K^+K^-K^0_{S+-}$ signal yield	-0.02 ± 0.03	0.90 ± 0.02
$K^+K^-K^0_{S+-}$ $q\overline{q}$ yield	-0.08 ± 0.03	0.99 ± 0.02
$K^+K^-K^0_{S+-}$ $B\overline{B}$ yield	-0.02 ± 0.04	1.04 ± 0.03
$K^+K^-K^0_{S00}$ signal yield	-0.03 ± 0.03	0.96 ± 0.02
$K^+K^-K^0_{S00}$ $q\overline{q}$ yield	-0.07 ± 0.03	0.90 ± 0.02
$K^+K^-K^0_{S00}$ $B\overline{B}$ yield	0.00 ± 0.03	0.99 ± 0.03
$K^+K^-K^0_L$ signal yield	-0.12 ± 0.04	1.01 ± 0.03
$K^+K^-K^0_L$ $q\overline{q}$ yield	-0.10 ± 0.03	0.96 ± 0.02
$K^+K^-K^0_L$ $B\overline{B}$ yield	0.20 ± 0.03	0.96 ± 0.02

$K^+K^-K^0_{S+-}$ mode. While the $K^+K^-K^0_{S00}$ and $K^+K^-K^0_L$ modes add signal events, they also add a large amount of background. By comparing the errors on the floating parameters found in toy experiments, we can assess the improvement gained by adding the additional modes. As shown in Tab. 4.10, the additional modes do improve the expected errors.

Table 4.10: Comparison of errors from toy fits to $K^+K^-K^0_{S+-}$ versus toy fits to all $K^+K^-K^0$ ($K^+K^-K^0_{S+-}$, $K^+K^-K^0_{S00}$, and $K^+K^-K^0_L$).

	Mean error	
Parameter	$K^+K^-K^0_{S+-}$	All $K^+K^-K^0$
$b_{K^+K^-K^0}$	0.043	0.040
$\delta_{K^+K^-K^0}$	0.09	0.08
c of ϕ	0.0016	0.0015
φ of ϕ	0.33	0.33
c of $f_0(980)$	0.07	0.06
φ of $f_0(980)$	0.27	0.26
c of $X_0(1550)$	0.026	0.022
φ of $X_0(1550)$	0.24	0.21
c of $NR_{K^+K^0}$	0.09	0.07
φ of $NR_{K^+K^0}$	0.32	0.26
c of $NR_{K^-K^0}$	0.11	0.09
φ of $NR_{K^-K^0}$	0.40	0.32
c of χ_{c0}	0.007	0.006
φ of χ_{c0}	0.6	0.5
c of D^+	0.24	0.20
c of D^+_s	0.22	0.17

Independent toys are used to validate the low- and high-mass fits. As shown in Fig. 4.28, the pull distributions of the *CP* parameters and isobar coefficients in the low-mass fit toys show that the fit is well-behaved. Similar toy results for the *CP* parameters in the high-mass fit are shown in Fig. 4.29.

Fits to pure toys are used to study several additional issues. In the data, we find that the fits often converge to local minima of the likelihood function, thus failing to find the true minimum. This raises a question of whether our model adequately describes the data. To test this question, we perform the low-mass fit to a large pure

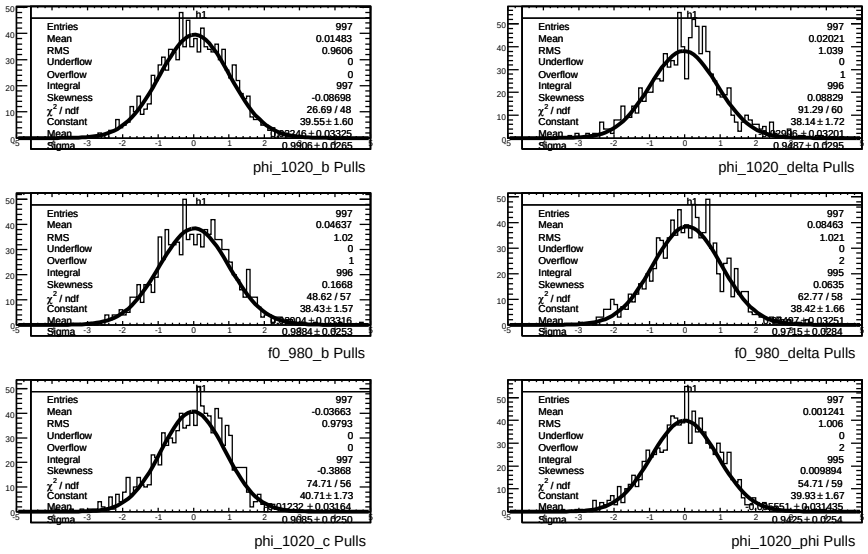

Figure 4.28: Toy results for the low-mass fit to all $K^+K^-K^0$ events: pull distributions for the isobar parameters and *CP* asymmetries.

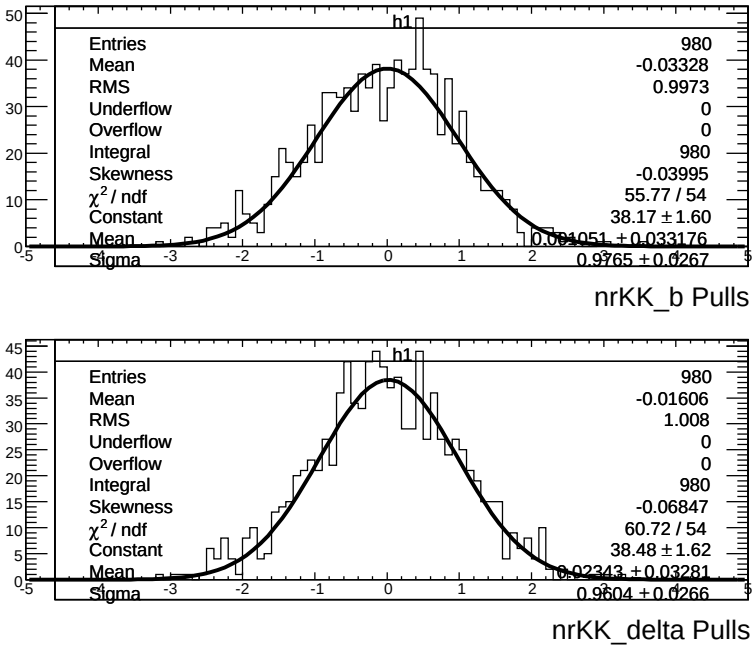

Figure 4.29: Toy results for the high-mass fit to all $K^+K^-K^0$ events: pull distributions for the *CP* asymmetry parameters.

toy sample (where we know that the model describes the data perfectly), generated with artificially enhanced signal purity. We repeat this fit many times, randomizing the initial values of the floating parameters before each fit. We observe similar ambiguities as seen in the data, thus we are able to reject the hypothesis that the ambiguities are created by an inadequate model of the signal on the DP.

We also use pure toy tests to evaluate whether there is a statistical difference between floating the $\phi(1020)$ and $f_0(980)$ isobar coefficients in the low-mass fit. (If these were the only two components in the fit, these two approaches would be mathematically identical.) As expected, we find that it does not matter which set of isobar coefficients is floated.

4.6.2 Embedded Toy Tests

The use of real signal MC events in embedded toys allows us to test for effects that may be neglected in the PDF structure but exist in the actual signal. Correlations between the observables in the fit that are neglected in the PDF construction (and are thus neglected in pure toys) will be accounted for in embedded toys (as long as the correlations are in the signal).

Given the number of signal MC events available, we are able to do 440 embedded toy fits. Pull distributions for the *CP* asymmetry parameters on the whole DP are shown in Fig. 4.30. No biases are observed. Similar plots for the high-mass fit are shown in Fig. 4.31.

Pull distributions for low-mass fit embedded toys are shown in Fig. 4.32. Here we observe significant biases in the *CP* asymmetry parameters. To study this issue, we repeat the embedded toy study, but use the Monte Carlo truth information to determine the Dalitz plot coordinates ($m_{K^+K^-}$ and $\cos\theta_H$) for each event. This provides a test of whether the Dalitz plot resolution (discussed in Sec. 4.4.6), ignored in the fit PDF, is responsible for the biases. As shown in Fig. 4.33, the biases are reduced somewhat in this test. In particular the bias on δ_ϕ is eliminated. From further embedded toy studies using the $K^+K^-K^0_{S+-}$ and $K^+K^-K^0_{S00}$ modes alone, we determine that these biases are largely caused by the poor resolution of the $K^+K^-K^0_L$

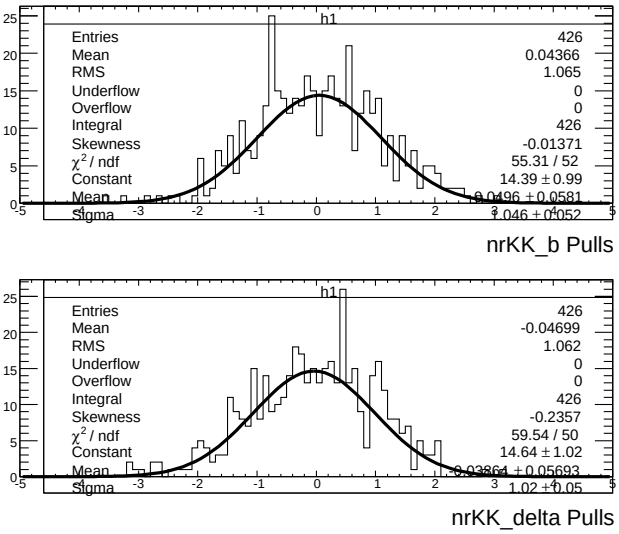

Figure 4.30: Pull distributions for the *CP* asymmetry parameters (top) $b_{K^+K^-K^0}$ and (bottom) $\delta_{K^+K^-K^0}$, derived from embedded toy fits to all $K^+K^-K^0$ modes. The curves are fits to Gaussian distributions.

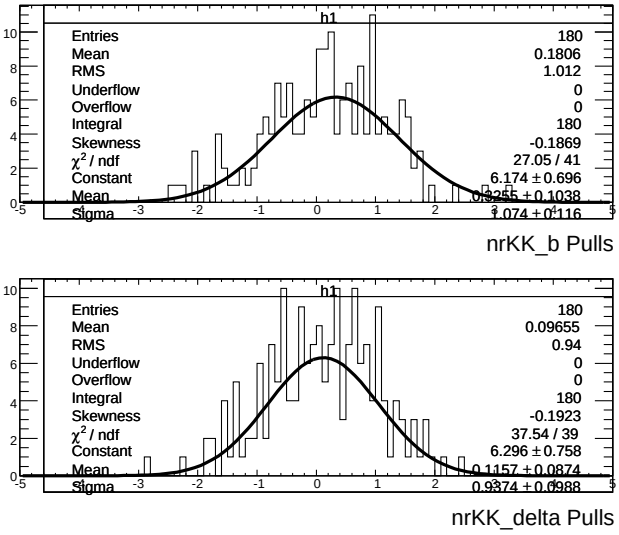

Figure 4.31: Pull distributions for the *CP* asymmetry parameters (top) $b_{K^+K^-K^0}$ and (bottom) $\delta_{K^+K^-K^0}$, derived from embedded toy fits to all $K^+K^-K^0$ modes. The curves are fits to Gaussian distributions.

mode.

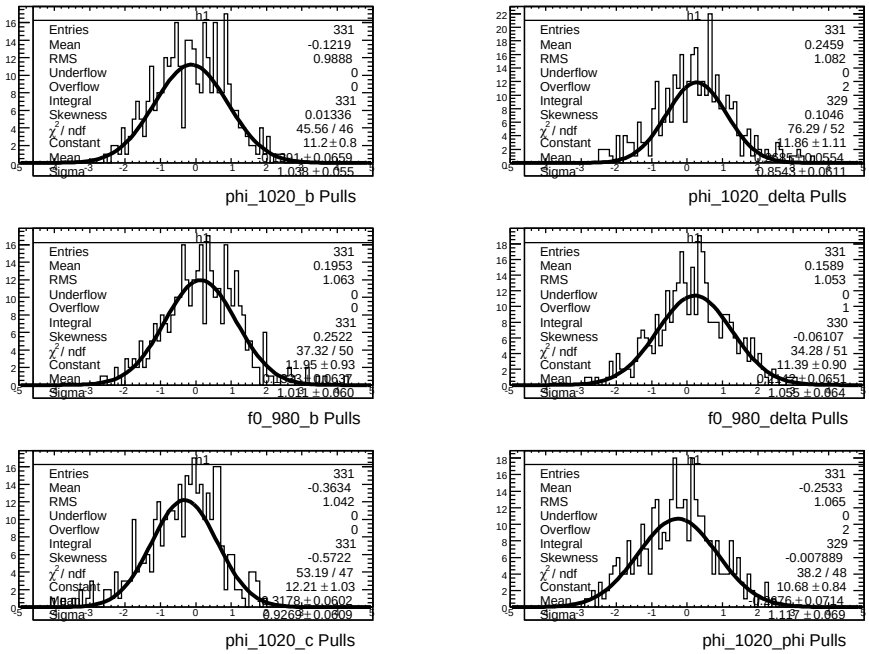

Figure 4.32: Embedded toy results for the low-mass fit to all $K^+K^-K^0$ events: pull distributions for the isobar parameters and *CP* asymmetries.

The biases on the *CP* parameters can be accounted for as a systematic error. Because this error is introduced by adding the $K^+K^-K^0_L$ mode, we must consider the tradeoff between statistical and systematic errors due to adding this mode. As shown in Table 4.11, because the statistical errors are large, the gain in statistical error that we get from adding the additional modes outweighs the increases in systematic error.

We perform a final stage of fit testing called *iterated embedded toys*. The purpose of these tests is to emulate as closely as possible the actual fit sequence used in the fits to data. For a given embedded toy sample, we first perform the whole DP fit. The isobar coefficients determined from that fit are then propagated to the high- and low-mass fits, just as in the fits to the data. This test is particularly important because of the small but significant fit biases observed for some of the isobar coefficients in the validation of the whole DP fit. These biases are not particularly important on their own, but we must be sure that they do not introduce biases in the *CP* parameters

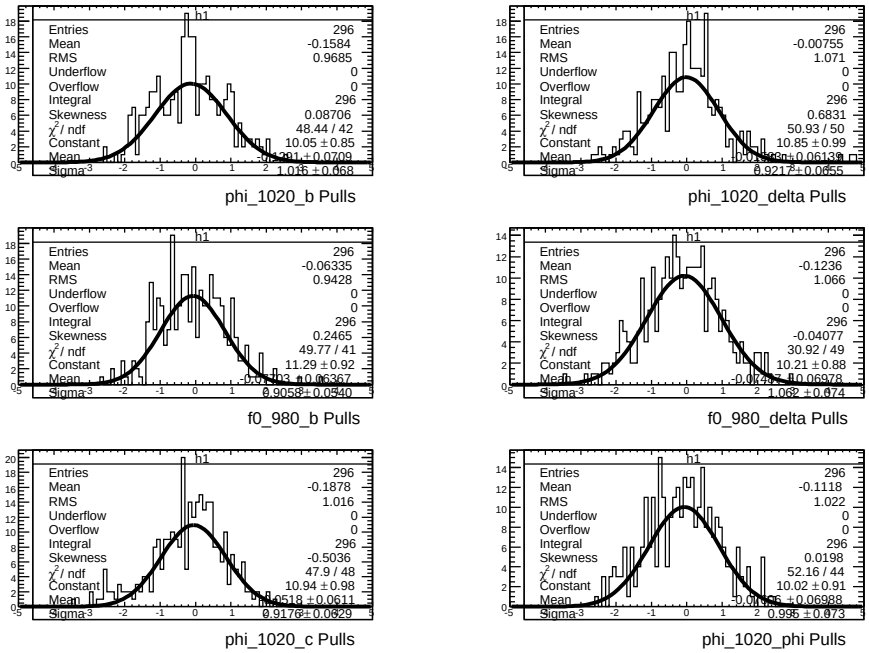

Figure 4.33: Embedded toy results for the low-mass fit to all $K^+K^-K^0$ events, using the MC truth information for the Dalitz plot coordinates. Pull distributions for the isobar parameters and *CP* asymmetries are shown.

Table 4.11: Tradeoff between statistical error and fit bias in the low-mass embedded toy fits. The last row is for fits to data samples with perfect Dalitz plot resolution (MC truth information used to get the Dalitz plot position).

	$\phi(1020)$ b		$\phi(1020)$ δ		$f_0(980)$ b		$f_0(980)$ δ	
	stat	bias	stat	bias	stat	bias	stat	bias
$K^+K^-K^0_{S+-}$	0.11	0.01	0.17	0.02	0.18	0.00	0.19	0.00
$K^+K^-K^0_{S+-}$ w/$K^+K^-K^0_{S00}$	0.10	0.01	0.16	0.02	0.17	0.01	0.18	0.01
All $K^+K^-K^0$	0.09	0.01	0.15	0.06	0.16	0.04	0.17	0.04
All $K^+K^-K^0$ (truth)	0.09	0.02	0.14	0.01	0.16	0.00	0.16	0.01

determined in the subsequent fits.

Because the iterated embedded toys are the most realistic emulation of the actual fit procedure, we use the biases (or lack thereof) observed in these toys to evaluate the corresponding systematic uncertainties. The pull distributions for the *CP* parameters found in iterated embedded toys are shown in Figures 4.34 and 4.35 for the high-mass and low-mass fits, respectively. In Fig. 4.35, the wide width of the pull distribution for the c_ϕ parameter is not fully understood, but since the *CP* violation results do not depend on this parameter we feel this problem can be neglected.

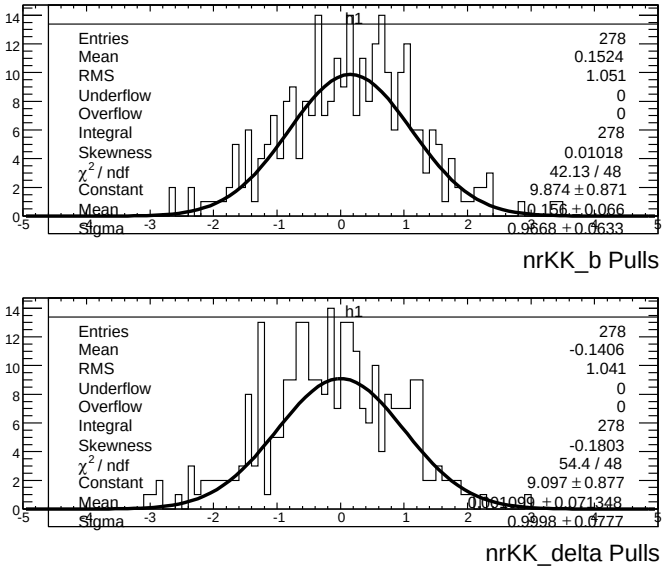

Figure 4.34: Pull distributions for the *CP* parameters, found in iterated embedded toy fits to the high-mass region.

4.7 Fit Results

4.7.1 Fit to the Whole Dalitz Plot

The event selection criteria yield 3266 $K^+K^-K^0_{S+-}$, 1611 $K^+K^-K^0_{S00}$, and 27513 $K^+K^-K^0_L$ candidates in the sample for the whole DP fit. When fitting the data, we

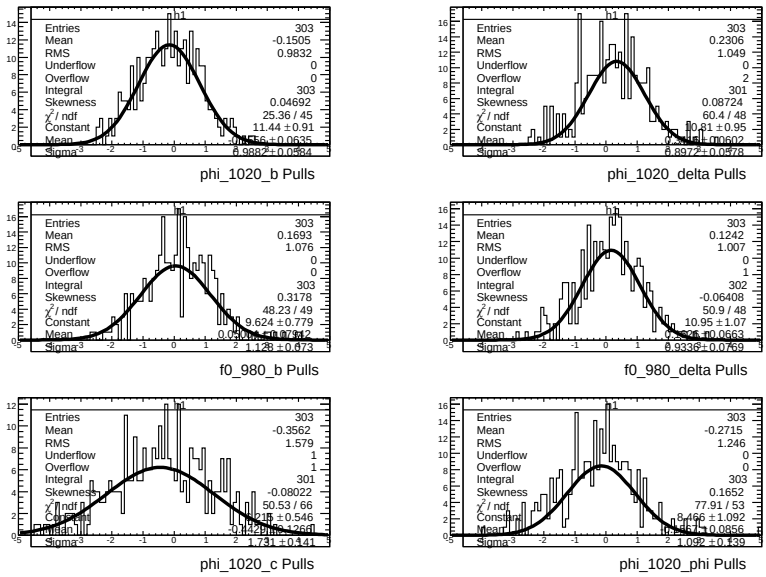

Figure 4.35: Pull distributions for the *CP* parameters and ϕ isobar coefficients, found in iterated embedded toy fits to the low-mass region.

run many fits, each time randomizing the initial values of the isobar coefficients and *CP* parameters within reasonable ranges. Out of 725 fits, 623 converge with a full, accurate covariance matrix from `HESSE`. As shown in Fig. 4.36, there are a number of solutions. However, over a wide range of NLL, the *CP* parameter $\delta_{K^+K^-K^0}$ falls either near the nominal solution or at the trigonometric reflection (near $\pi/2 - \beta$) of that solution.

The best solution, at NLL $= -102004$, is clearly separated from the others. In Fig. 4.37, we show only the results for the *CP* parameters and isobar coefficients for solutions with NLL < -101995. These plots show that the fits which converge to the best NLL have a unique set of isobar and *CP* parameters, with the exception of an ambiguity in the phase of the χ_{c0}. The second best solution is suppressed by 6 units of NLL, corresponding to 3.5σ significance, allowing us to ignore it in the final results.

Event yields for the best solution are listed in Table 4.7.1. Using the average efficiency found in signal MC, these yields translate to branching fraction measurements

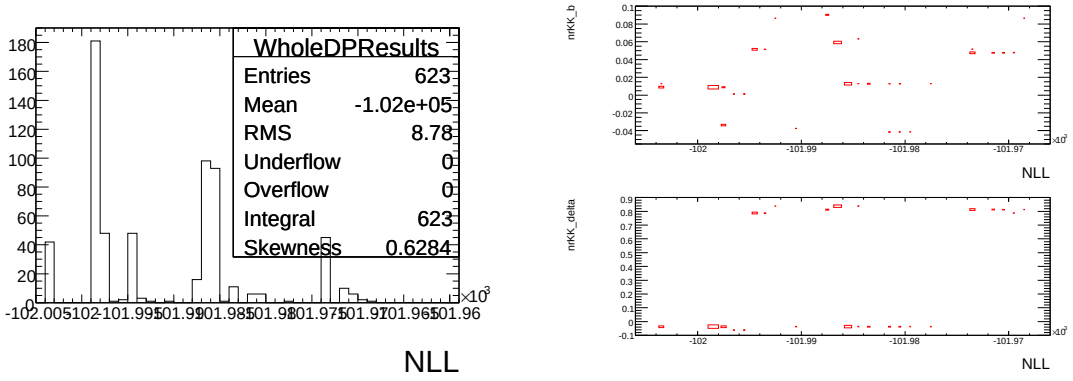

Figure 4.36: (Left) The distribution of NLL for fits to the whole DP with randomized initial parameters; (right) distributions of values of the *CP* parameters (top) $b_{K^+K^-K^0}$ and (bottom) $\delta_{K^+K^-K^0}$ versus the fit NLL.

of $\mathcal{B}(B^0 \to K^+K^-K^0) = (26.6 \pm 1.0) \times 10^{-6}$ for $K^+K^-K^0_{S+-}$, $\mathcal{B}(B^0 \to K^+K^-K^0) = (37.0 \pm 4.4) \times 10^{-6}$ for $K^+K^-K^0_{S00}$, and $\mathcal{B}(B^0 \to K^+K^-K^0) = (34.1 \pm 3.1) \times 10^{-6}$ for $K^+K^-K^0_L$. (Note that the errors quoted on the branching fractions are statistical only. Also, the efficiencies do not include the efficiency corrections used in making the efficiency maps shown in Fig. 4.9.) The first of these measurements is in good agreement with the PDG value of $\mathcal{B}(B^0 \to K^+K^-K^0) = (24.7 \pm 2.3) \times 10^{-6}$, while the latter two are high but still statistically compatible. In $K^+K^-K^0_{S00}$, the $B\overline{B}$ background yield is in agreement with the number of events found in generic $B\overline{B}$ MC.

$m_{\rm ES}$ projections of the data and fit PDF are shown in Fig. 4.38. As binned in these plots, the χ^2 per bin is 1.0 for $K^+K^-K^0_{S+-}$ and 1.3 for $K^+K^-K^0_{S00}$. Similar plots are shown for ΔE in Fig. 4.39. The χ^2 per bin for these plots is 1.0 for $K^+K^-K^0_{S+-}$, 0.7 for $K^+K^-K^0_{S00}$, and 2.8 for $K^+K^-K^0_L$.

We also plot the data using the ${}_s\mathcal{P}$lot technique, an event-weighting method that allows us to plot the data with the individual signal and background PDFs [51]. For $K^+K^-K^0_{S+-}$, these plots are shown in Fig. 4.40. Similar plots are shown for $K^+K^-K^0_{S00}$ in Fig. 4.41. The ${}_s\mathcal{P}$lot technique requires the data be refit with the total PDF modified to remove the PDF for the variable being plotted. It is not

(a)

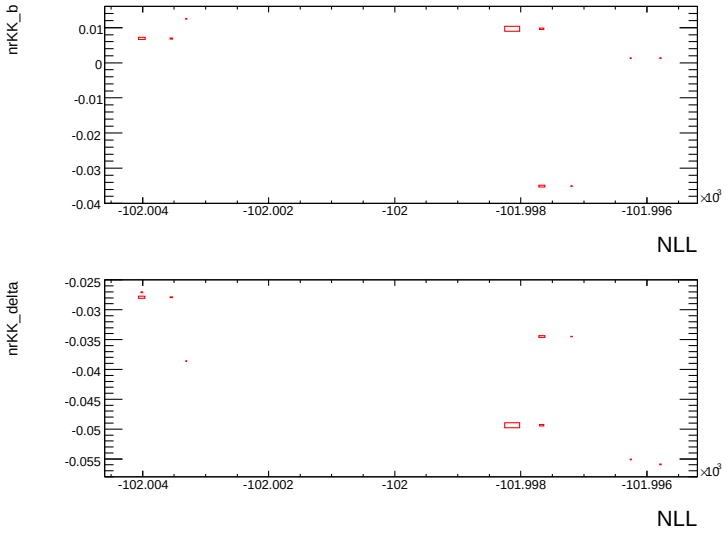

(b)

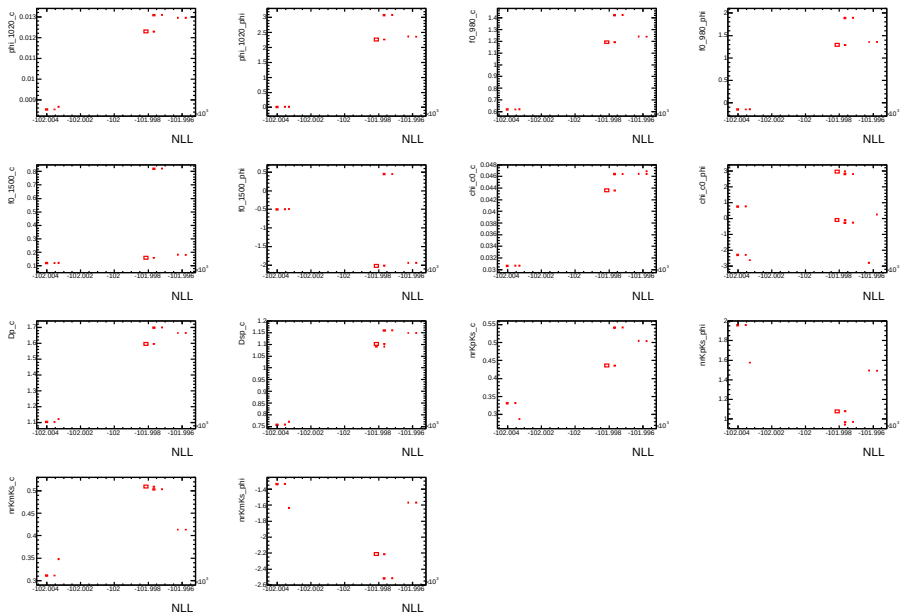

Figure 4.37: Distributions of whole DP fit results (NLL < -101995): (a) *CP* parameters versus NLL, (b) Isobar parameters versus NLL.

Table 4.12: Event yields found in the whole DP fit. Errors are statistical only.

Mode	Parameter	Fitted Value
$K^+K^-K^0_{S+-}$	n_{Signal}	947 ± 37
	$n_{q\overline{q}}$	2235 ± 55
	$f_{q\overline{q},\text{Lepton}}$	0.0022 ± 0.0020
	$f_{q\overline{q},\text{KaonI}}$	0.067 ± 0.006
	$f_{q\overline{q},\text{KaonII}}$	0.144 ± 0.008
	$f_{q\overline{q},\text{KaonPion}}$	0.125 ± 0.008
	$f_{q\overline{q},\text{Pion}}$	0.156 ± 0.008
	$f_{q\overline{q},\text{Other}}$	0.118 ± 0.007
	$n_{B\overline{B}}$	84 ± 25
$K^+K^-K^0_{S00}$	n_{Signal}	144 ± 17
	$n_{q\overline{q}}$	1419 ± 41
	$f_{q\overline{q},\text{Lepton}}$	0.0026 ± 0.0017
	$f_{q\overline{q},\text{KaonI}}$	0.060 ± 0.007
	$f_{q\overline{q},\text{KaonII}}$	0.107 ± 0.009
	$f_{q\overline{q},\text{KaonPion}}$	0.106 ± 0.009
	$f_{q\overline{q},\text{Pion}}$	0.158 ± 0.010
	$f_{q\overline{q},\text{Other}}$	0.139 ± 0.009
	$n_{B\overline{B}}$	49 ± 17
$K^+K^-K^0_L$	n_{Signal}	770 ± 71
	$n_{q\overline{q}}$	24864 ± 198
	$F_{q\overline{q},\text{EMC}}$	0.7304 ± 0.0031
	$f_{q\overline{q},\text{Lepton}}$	0.0099 ± 0.0008
	$f_{q\overline{q},\text{KaonI}}$	0.0591 ± 0.0016
	$f_{q\overline{q},\text{KaonII}}$	0.1386 ± 0.0023
	$f_{q\overline{q},\text{KaonPion}}$	0.1394 ± 0.0023
	$f_{q\overline{q},\text{Pion}}$	0.1675 ± 0.0025
	$f_{q\overline{q},\text{Other}}$	0.1225 ± 0.0022
	$n_{B\overline{B},\text{Peaking}}$	1074 ± 127
	$n_{B\overline{B},\text{Non-peaking}}$	851 (fixed)

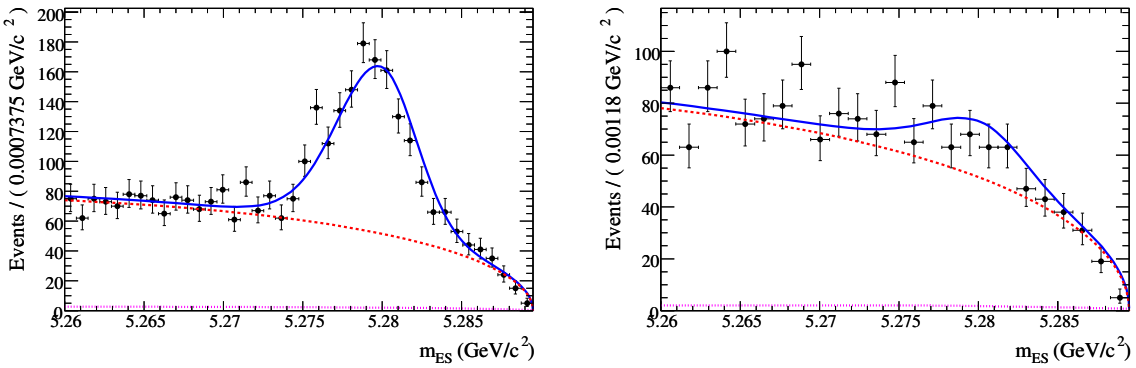

Figure 4.38: $m_{\rm ES}$ projections for the fit to the whole DP in (left) $K^+K^-K^0_{S+-}$ and (right) $K^+K^-K^0_{S00}$. The points are the data. The curves show the PDF projections: solid blue is the total, dashed red is the $q\overline{q}$ background, and dotted magenta is the $B\overline{B}$ background.

feasible to use this technique for ΔE in the $K^+K^-K^0_L$ mode, because ΔE is the only kinematic variable available. Instead we plot the ΔE distribution and PDF after making a cut on the event shape variables (tighter than the cut used for the actual event selection). This tighter cut has 16% efficiency for signal events. The resulting plot is shown in Fig. 4.42.

The isobar coefficients found in the best solution are given in Table 4.7.1. Note that the amplitudes can only be measured relative to each other, so one component must have its amplitude fixed in the fit. We choose to fix the magnitude and phase of the non-resonant K^+K^- component, as shown in the Table. The fit fraction FF_r of an individual resonance r is computed by integrating the lineshape of the resonance over the phase space, and dividing by the integral of the coherent sum of all of the isobars:

$$FF_r \;=\; \frac{2c_r^2\,(1+b_r^2)\int dPS\cdot|f_r|^2}{\int dPS\cdot\Gamma}. \tag{4.18}$$

Because interference is ignored in the numerator of this definition, the sum of the fit fractions will not, in general, be equal to unity.

The best solution for the average *CP* parameters $b_{K^+K^-K^0}$ and $\delta_{K^+K^-K^0}$ are given in Table 4.7.1. These parameters translate to the standard *CP* violation observables

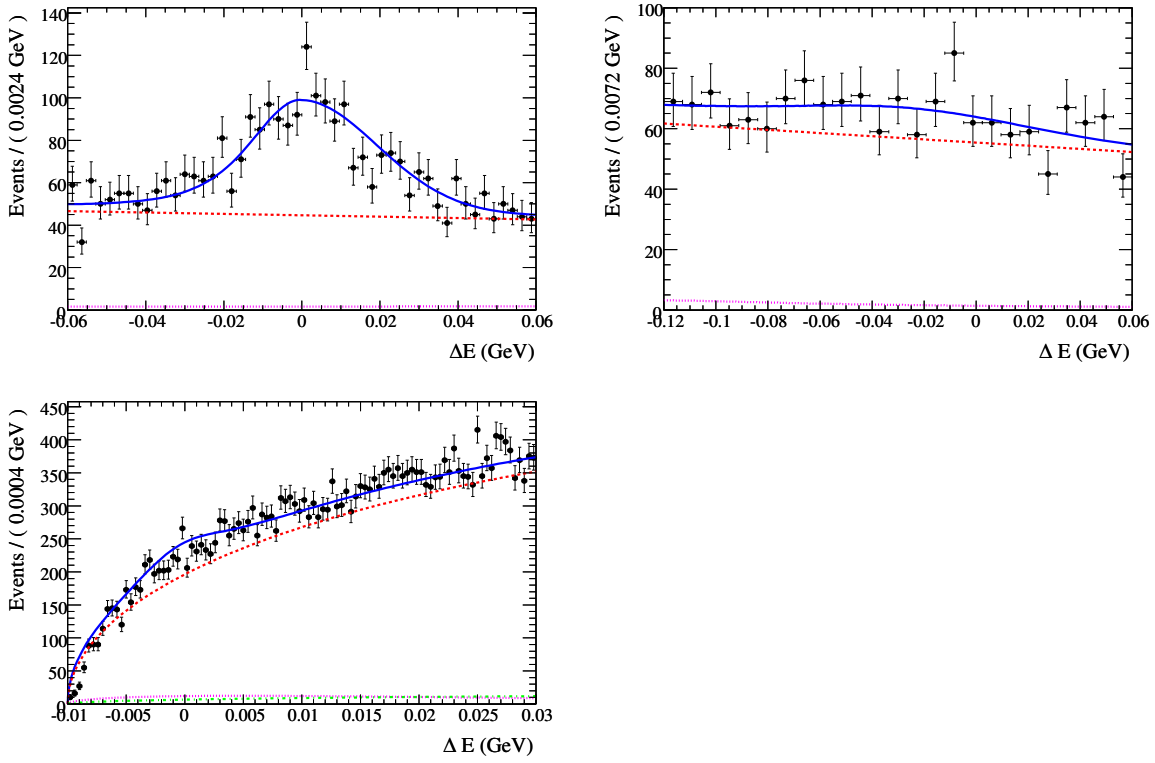

Figure 4.39: ΔE projections for the fit to the whole DP in (top left) $K^+K^-K^0_{S+-}$, (top right) $K^+K^-K^0_{S00}$, and (bottom left) $K^+K^-K^0_L$. The points are the data. The curves show the PDF projections: solid blue is the total, dashed red is the $q\overline{q}$ background, and dotted magenta is the $B\overline{B}$ background. For $K^+K^-K^0_L$ there is an additional $B\overline{B}$ background category (the non-peaking $B\overline{B}$ background), shown in dashed-dotted green.

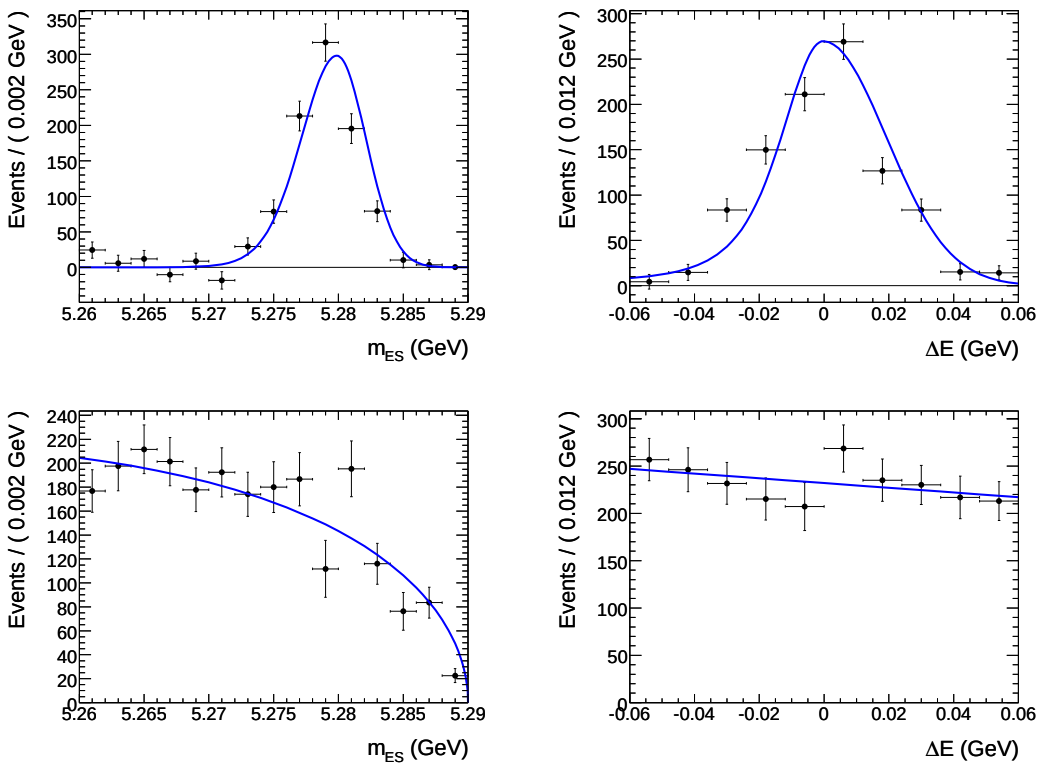

Figure 4.40: Distributions of the kinematic variables (left) $m_{\rm ES}$ and (right) ΔE in the onpeak $K^+K^-K^0_{S+-}$ data. Points are derived using the ${}_s\mathcal{P}$lot method, while the curves are the PDFs used in the fit. The top row shows signal and the bottom row shows $q\overline{q}$ background.

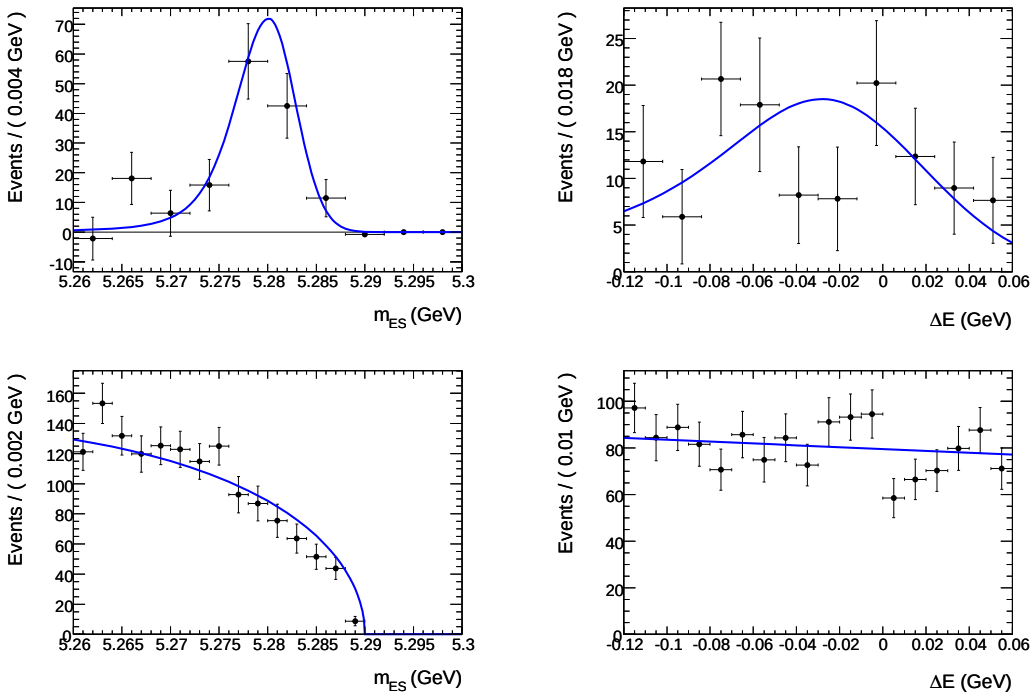

Figure 4.41: Distributions of the kinematic variables (left) $m_{\rm ES}$ and (right) ΔE in the onpeak $K^+K^-K^0_{S00}$ data. Points are derived using the ${}_s\mathcal{P}$lot method, while the curves are the PDFs used in the fit. The top row shows signal and the bottom row shows $q\overline{q}$ background.

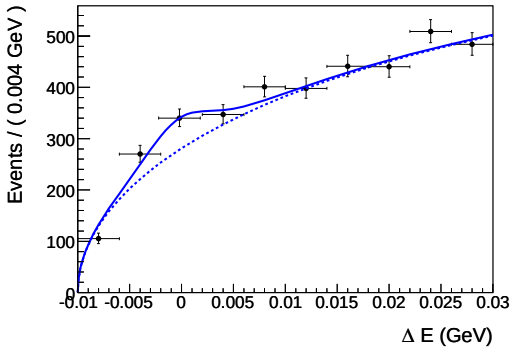

Figure 4.42: Distributions of the kinematic variable ΔE in the onpeak $K^+K^-K^0_L$ data. Points are the data and the curve is the total PDF, including signal and backgrounds. The signal is enhanced with a cut on the event shape variables.

Table 4.13: Isobar coefficients and corresponding fit fractions found in the whole DP fit. Errors are statistical only. Fit fractions for the *NR* components are combined into one fraction. The sum of the fit fractions is 177%.

Parameter	DP Component	Fitted Value	Fit Fraction (%)
c	$NR_{K^+K^-}K^0$	1.0 (fixed)	112 ± 15
φ	$NR_{K^+K^-}K^0$	0.0 (fixed)	
c	$NR_{K^-K^0}K^+$	0.31 ± 0.09	
φ	$NR_{K^-K^0}K^+$	-1.34 ± 0.37	
c	$NR_{K^+K^0}K^-$	0.33 ± 0.07	
φ	$NR_{K^+K^0}K^-$	1.95 ± 0.28	
c	$\phi(1020)K^0$	0.0085 ± 0.0010	12.5 ± 1.3
φ	$\phi(1020)K^0$	-0.02 ± 0.23	
c	$f_0(980)K^0$	0.622 ± 0.045	40 ± 10
φ	$f_0(980)K^0$	-0.14 ± 0.14	
c	$X_0(1550)K^0$	0.114 ± 0.018	4.1 ± 1.3
φ	$X_0(1550)K^0$	-0.47 ± 0.20	
c	$\chi_{c0}K^0$	0.031 ± 0.005	3.0 ± 1.3
φ	$\chi_{c0}K^0$	0.8 ± 0.5 or -2.3 ± 0.5	
c	D^-K^+	1.11 ± 0.15	3.6 ± 1.5
c	$D_s^-K^+$	0.76 ± 0.14	1.8 ± 0.6

by the following relations:

$$\begin{aligned} A_{CP,r} &= -\frac{|c_r|^2 - |\bar{c}_r|^2}{|c_r|^2 + |\bar{c}_r|^2} \\ &= -\frac{2b_r}{1+b_r^2}, \text{ and} \qquad (4.19) \\ \beta_{eff,r} &= \beta + \delta_r, \qquad (4.20) \end{aligned}$$

where $\beta = 0.379$ is the SM value of the CKM angle measured in $b \to c\bar{c}s$ decays. Note that in the whole DP fit and the high-mass fit, the b and δ parameters are shared by all resonances, so we drop the subscript r in those cases.

Using these relations, the whole DP fit finds $A_{CP} = -0.015 \pm 0.077$ and $\beta_{eff} = 0.352 \pm 0.076$. Note that since the phase β_{eff} enters from B^0 mixing as $2\beta_{eff}$, there is an unresolvable ambiguity between solutions at β_{eff} and solutions at $\beta_{eff} + \pi$.

Table 4.14: The values of the *CP* parameters found in the whole DP fit.

Name	Fitted Value
$b_{K^+K^-K^0}$	0.008 ± 0.039
$\delta_{K^+K^-K^0}$	-0.028 ± 0.076

Correlations between the *CP* parameters are about 1%. Correlations between each *CP* parameter and the isobar coefficients are somewhat higher, with a maximum of about 10%. A list of important correlations is given in Table B.

We show in Fig. 4.43 the Δt distributions of the ${}_s\mathcal{P}$lot-weighted signal component for the $K^+K^-K^0_{S+-}$ sample.Events corresponding to B^0- and $\overline{B}^0$- tags are shown, and followed by a plot of the distribution of the time-dependent *CP* asymmetry $\mathcal{A}(\Delta t) = (N_{B^0} - N_{\overline{B}^0}) / (N_{B^0} + N_{\overline{B}^0})$.

To quantify the significance of the measured *CP* violation, we perform a likelihood scan of the β_{eff} parameter. $\delta_{K^+K^-K^0}$ (and thus β_{eff}) is fixed to various values, and at each value a number of fits are done with randomized initial parameters to find the best NLL and the best values of the other floating parameters. The results of this scan are shown in Fig. 4.44. The significance of *CP* violation in the data is calculated as $n_\sigma = \sqrt{2\Delta NLL}$, where ΔNLL is the change in NLL between the best solution

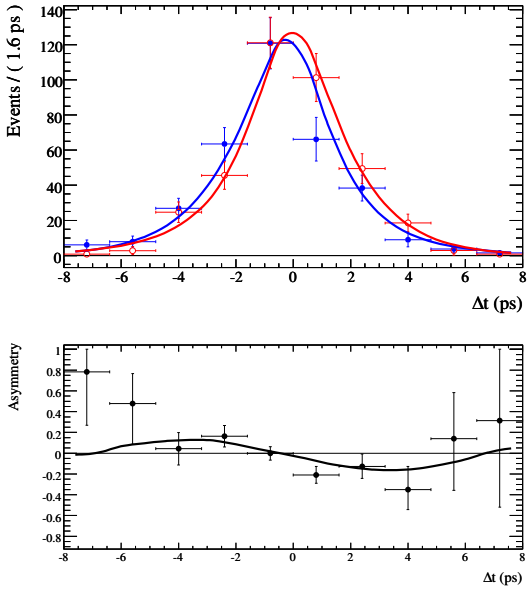

Figure 4.43: (Top) Δt distributions and (bottom) time-dependent CP asymmetry for $K^+K^-K^0_{S+-}$. For the Δt distributions, B^0- ($\overline{B}^0$-) tagged signal-weighted events are shown as filled (open) circles, with the PDF projection in solid blue (dashed red).

and the point where $\beta_{eff} = 0$. Systematic errors are accounted for by convolving the likelihood curve with a Gaussian distribution. The width of this Gaussian is given by the systematic error on β_{eff} (see Sec. 4.8). We find that $\beta_{eff} = 0$ is excluded at 4.8σ (5.1σ), including statistical and systematic errors (statistical errors only).

The local minimum on the right side of Fig. 4.44 (near $\beta_{eff} = 1.2\,\text{rad}$) is caused by the ambiguity $\sin 2\beta_{eff} = \sin 2(\pi/2 - \beta_{eff})$. This ambiguity is broken by terms proportional to $\cos 2\beta_{eff}$, introduced by interference between S- and P-wave contributions to the decay amplitude. (In most measurements of $\sin 2\beta$, the data cannot distinguish between these two solutions.) From the likelihood scan (and from the secondary solutions of the initial fit, some of which land in this local minimum), we find the significance of the nominal solution against the reflection where $\beta_{eff} \to \pi/2 - \beta_{eff}$ to be 4.6σ.

Projections of the DP variables $m_{K^+K^-}$ and $\cos\theta_H$ are shown in Fig. 4.45 and Fig. 4.46, respectively. The PDF projection is normalized to the data independently in each plot. The agreement between the data and the total PDF is good

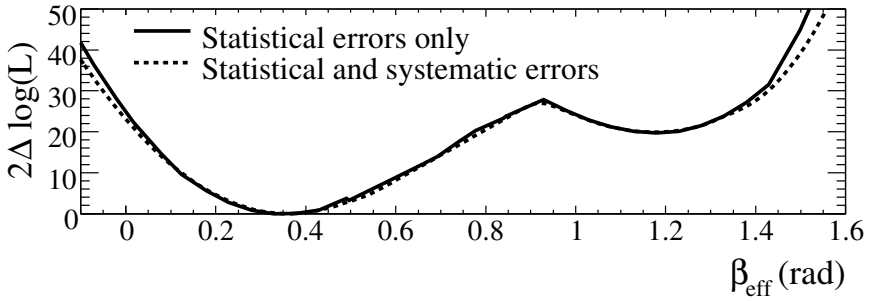

Figure 4.44: The change in twice the negative log likelihood as a function of β_{eff} for the fit to the whole DP.

for $K^+K^-K^0_{S+-}$ and $K^+K^-K^0_{S00}$. For $K^+K^-K^0_L$, there is poor agreement when looking at the whole DP. The situation improves somewhat when looking only at the low-mass region, provided that the normalization is done independently in that region. Signal-weighted distributions of the Dalitz plot variables $m_{K^+K^-}$ and $\cos\theta_H$ are shown for $K^+K^-K^0_{S+-}$ in Fig. 4.47.

The Dalitz plot model for this analysis adds amplitudes for non-resonant contributions that depend on $m^2_{K^+K^0}$ and $m^2_{K^-K^0}$. These terms were not present in our previous analysis [52],[5] nor were they relevant in the Dalitz plot analyses of $B^+ \to K^+K^-K^+$. The shape parameter α_{NR} for these terms is fixed to the value used for the NR term proportional to $m_{K^+K^-}$. To test the statistical significance of these terms, we repeat the fits to data with c_{NR,K^+K^0} and c_{NR,K^-K^0} fixed to zero. In 200 fits with randomized initial parameters, the best NLL is -101990. Comparing with the NLL of the nominal fits, the statistical significance of these terms is: $\sqrt{2 \times (-101990 - (-102004))} = 5.3\sigma$.

4.7.2 Fit to the High-Mass Region

The high-mass fit sample consists of 2384 $K^+K^-K^0_{S+-}$, 1406 $K^+K^-K^0_{S00}$, and 20032 $K^+K^-K^0_L$ events (the same sample as for the whole DP fit, but with $m_{K^+K^-} > 1.1\,\mathrm{GeV}/c^2$). Fixing the isobar coefficients to the best solution found for the whole

[5]Note that in our previous analysis, we tested incorporating these terms into our model, but the magnitudes of the corresponding isobar coefficients were consistent with zero.

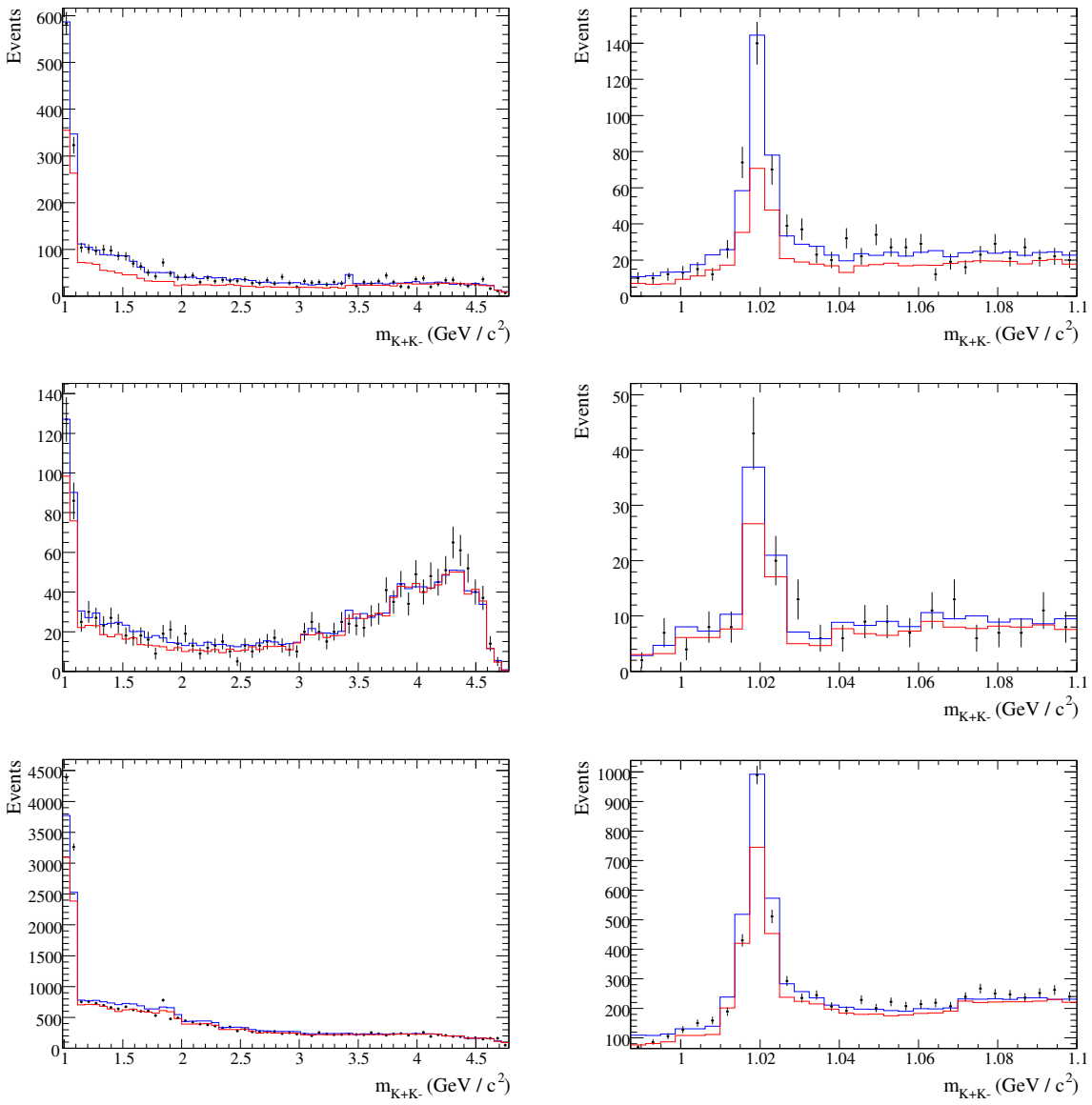

Figure 4.45: Projections of $m_{K^+K^-}$ for the data and the PDF of the whole DP fit result. The plots in the left column show the whole mass range, while the plots on the right zoom into the low-mass region (but still show results of the whole DP fit). Projections are shown for (top) $K^+K^-K^0_{S+-}$, (center) $K^+K^-K^0_{S00}$, and (bottom) $K^+K^-K^0_L$. The blue lines denote the total PDF and the red lines are the $q\overline{q}$ background component of the PDF.

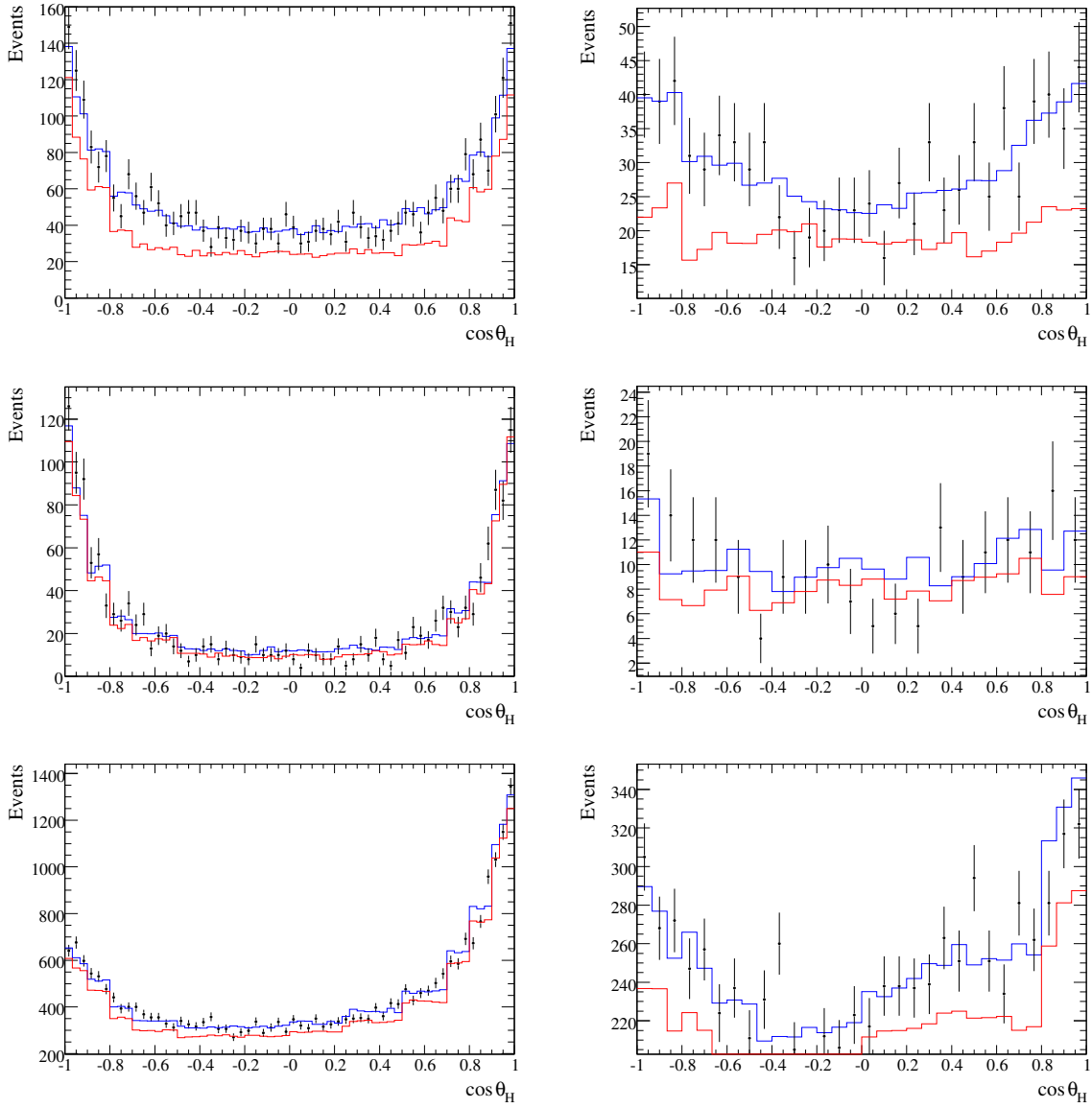

Figure 4.46: Projections of $\cos\theta_H$ for the data and the PDF of the whole DP fit result. The plots in the left column show the whole mass range, while the plots on the right zoom into the low-mass region (but still show results of the whole DP fit). Projections are shown for (top) $K^+K^-K^0_{S+-}$, (center) $K^+K^-K^0_{S00}$, and (bottom) $K^+K^-K^0_L$. The blue lines denote the total PDF and the red lines are the $q\overline{q}$ background component of the PDF.

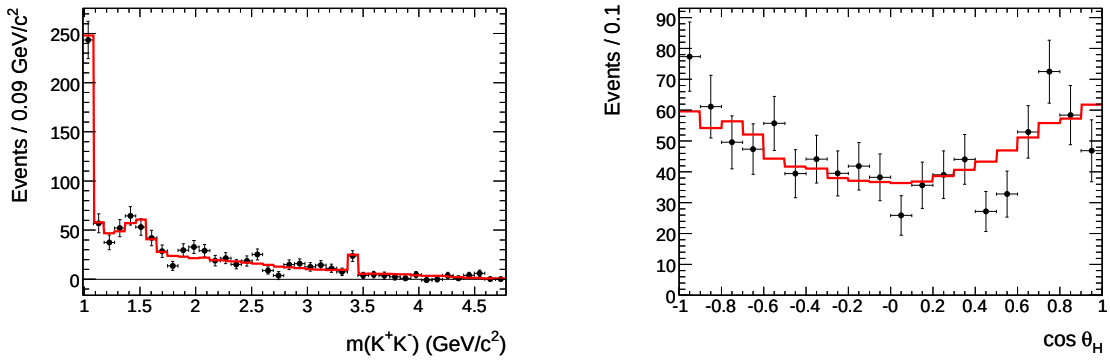

Figure 4.47: ${}_s\mathcal{P}$lots of the Dalitz plot variables (left) $m_{K^+K^-}$ and (right) $\cos\theta_H$ for $K^+K^-K^0_{S+-}$ events. The points are the signal-weighted data events and the histograms are projections of the signal Dalitz plot PDF.

Dalitz plot, we make 200 fits to the high-mass region, floating only the yields and average *CP* parameters. The results are shown in Figure 4.48. There is a clear solution with NLL of -62102.6. The results of the floating parameters for the best solution are given in Table 4.7.2. The correlation between $b_{K^+K^-K^0}$ and $\delta_{K^+K^-K^0}$ is 4%. Correlations between the other parameters and the *CP* parameters are all less than 1%.

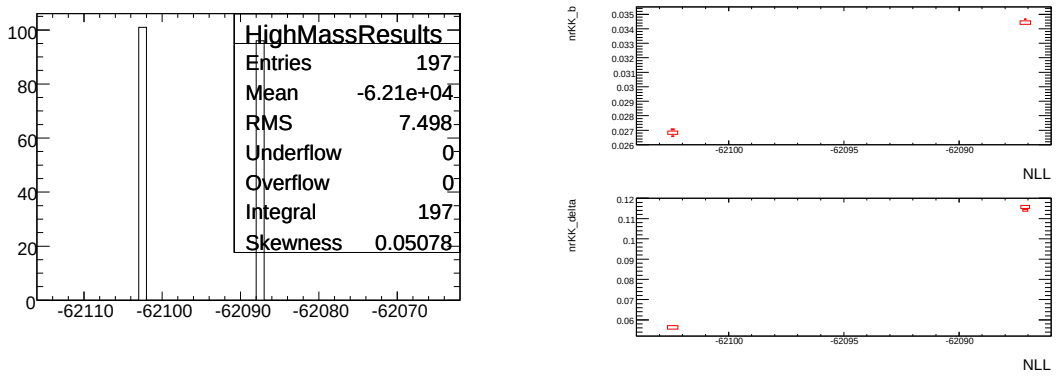

Figure 4.48: (Left) The distribution of NLL for fits to the high-mass region with randomized initial parameters; (right) distributions of values of the *CP* parameters (top) $b_{K^+K^-K^0}$ and (bottom) $\delta_{K^+K^-K^0}$ versus the fit NLL.

The *CP* parameters found by the fit translate to $A_{CP} = -0.05 \pm 0.10$ and $\beta_{\mathit{eff}} =$

Table 4.15: Results of the high-mass fit to the data.

Mode	Parameter	Fitted Value
All	$b_{K^+K^-K^0}$	0.027 ± 0.051
	$\delta_{K^+K^-K^0}$	0.057 ± 0.087
$K^+K^-K^0_{S+-}$	n_{Signal}	673 ± 31
	$n_{q\overline{q}}$	1643 ± 48
	$f_{q\overline{q},\text{Lepton}}$	0.0018 ± 0.0023
	$f_{q\overline{q},\text{KaonI}}$	0.072 ± 0.007
	$f_{q\overline{q},\text{KaonII}}$	0.158 ± 0.010
	$f_{q\overline{q},\text{KaonPion}}$	0.127 ± 0.009
	$f_{q\overline{q},\text{Pion}}$	0.160 ± 0.010
	$f_{q\overline{q},\text{Other}}$	0.115 ± 0.008
	$n_{B\overline{B}}$	68 ± 24
$K^+K^-K^0_{S00}$	n_{Signal}	87 ± 14
	$n_{q\overline{q}}$	1285 ± 39
	$f_{q\overline{q},\text{Lepton}}$	0.0034 ± 0.0020
	$f_{q\overline{q},\text{KaonI}}$	0.060 ± 0.007
	$f_{q\overline{q},\text{KaonII}}$	0.111 ± 0.009
	$f_{q\overline{q},\text{KaonPion}}$	0.107 ± 0.009
	$f_{q\overline{q},\text{Pion}}$	0.162 ± 0.011
	$f_{q\overline{q},\text{Other}}$	0.137 ± 0.010
	$n_{B\overline{B}}$	34 ± 15
$K^+K^-K^0_L$	n_{Signal}	462 ± 56
	$n_{q\overline{q}}$	18680 ± 178
	$F_{q\overline{q},\text{EMC}}$	0.7499 ± 0.0036
	$f_{q\overline{q},\text{Lepton}}$	0.0123 ± 0.0010
	$f_{q\overline{q},\text{KaonI}}$	0.0626 ± 0.0019
	$f_{q\overline{q},\text{KaonII}}$	0.1407 ± 0.0027
	$f_{q\overline{q},\text{KaonPion}}$	0.1377 ± 0.0026
	$f_{q\overline{q},\text{Pion}}$	0.1693 ± 0.0028
	$f_{q\overline{q},\text{Other}}$	0.1224 ± 0.0025
	$n_{B\overline{B}}$	318 ± 119

0.436 ± 0.087. To calculate the significance of *CP* violation in the high-mass region, we repeat the fit, fixing $\beta_{eff} = 0$. In this fit we find NLL of -62087.7, a change of 14.9 units of NLL from the nominal result, corresponding to a significance of 5.5σ for *CP* violation, accounting for statistical errors only. Using the low-side error of the asymmetric systematic uncertainty (see Sec. 4.8), we find the significance of *CP* violation to be 5.1σ. A plot of the tag asymmetry as a function of Δt is shown in Fig. 4.49.

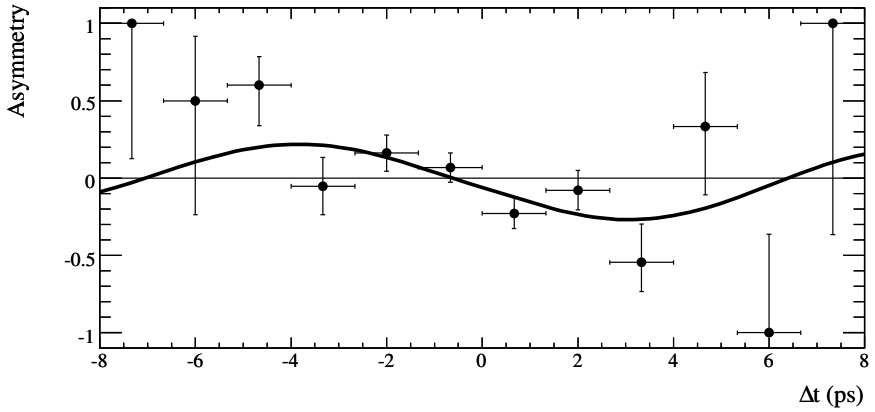

Figure 4.49: The time-dependent *CP* asymmetry in the $K^+K^-K^0_{S+-}$ mode, for the high-mass fit.

4.7.3 Fit to the Low-Mass Region

1359 $K^+K^-K^0_{S+-}$, 348 $K^+K^-K^0_{S00}$, and 7481 $K^+K^-K^0_L$ events with $m_{K^+K^-} < 1.1\,\mathrm{GeV}/c^2$ enter the fit to the low-mass region. (Note that the cut on the Fisher discriminant is looser for this fit than the others, so the sum of the events entering this fit and the high-mass fit does not equal the number of events entering the whole DP fit.) We perform 200 fits to the data, randomizing the initial parameter values for each fit. The event yields found in the fit are given in Table 4.7.3. These yields are consistent between the various solutions discussed below. Also consistent between the various solutions are several shape parameters for the $K^+K^-K^0_L$ $q\overline{q}$ L_2/L_0 distribution which are floated in the low-mass fit.

Table 4.16: Event yields found in the low-mass fit to the data.

Mode	Parameter	Fitted Value
$K^+K^-K^0_{S+-}$	n_{Signal}	282 ± 20
	$n_{q\overline{q}}$	1040 ± 35
	$f_{q\overline{q},\text{Lepton}}$	0.0057 ± 0.0032
	$f_{q\overline{q},\text{KaonI}}$	0.068 ± 0.008
	$f_{q\overline{q},\text{KaonII}}$	0.137 ± 0.011
	$f_{q\overline{q},\text{KaonPion}}$	0.131 ± 0.011
	$f_{q\overline{q},\text{Pion}}$	0.158 ± 0.012
	$f_{q\overline{q},\text{Other}}$	0.128 ± 0.011
	$n_{B\overline{B}}$	37 ± 15
$K^+K^-K^0_{S00}$	n_{Signal}	37 ± 9
	$n_{q\overline{q}}$	274 ± 18
	$f_{q\overline{q},\text{Lepton}}$	0.0000 ± 0.0019
	$f_{q\overline{q},\text{KaonI}}$	0.065 ± 0.016
	$f_{q\overline{q},\text{KaonII}}$	0.120 ± 0.021
	$f_{q\overline{q},\text{KaonPion}}$	0.125 ± 0.021
	$f_{q\overline{q},\text{Pion}}$	0.146 ± 0.022
	$f_{q\overline{q},\text{Other}}$	0.146 ± 0.022
	$n_{B\overline{B}}$	37 ± 9
$K^+K^-K^0_L$	n_{Signal}	266 ± 36
	$n_{q\overline{q}}$	6878 ± 97
	$F_{q\overline{q},\text{EMC}}$	0.657 ± 0.006
	$f_{q\overline{q},\text{Lepton}}$	0.0074 ± 0.0014
	$f_{q\overline{q},\text{KaonI}}$	0.0541 ± 0.0029
	$f_{q\overline{q},\text{KaonII}}$	0.1371 ± 0.0043
	$f_{q\overline{q},\text{KaonPion}}$	0.1442 ± 0.0044
	$f_{q\overline{q},\text{Pion}}$	0.161 ± 0.005
	$f_{q\overline{q},\text{Other}}$	0.1210 ± 0.0041
	$n_{B\overline{B}}$	76 ± 47

In Fig. 4.50, we show the best fit solutions for the *CP* parameters and ϕ isobar coefficients. We find two sets of solutions, separated by $\Delta\text{NLL} \simeq 0.1$. The isobar coefficients for these solutions are listed in Tab. 4.7.3. The solution referred to as "1A" in the table agrees quite closely with the result found in the whole DP fit. The corresponding solutions for the *CP* parameters are given in Tab. 4.7.3. The other components of the Dalitz plot have their *CP* parameters fixed to $A_{CP} = 0$, $\beta_{\mathit{eff}} = 0.370$ [53].

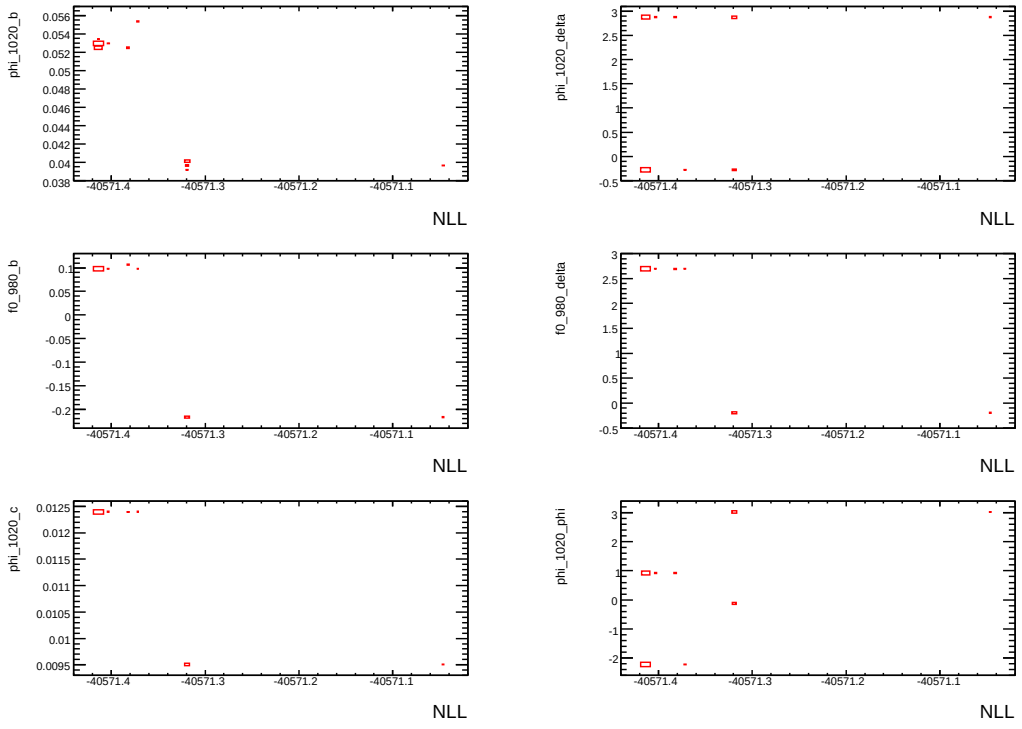

Figure 4.50: Isobar coefficients and *CP* parameters versus NLL for the low-mass fit to all $K^+K^-K^0$ events.

Solutions 1A and 1B have the same likelihood. They differ only by shifts of both φ and β_{eff} for the $\phi(1020)$ by exactly $+\pi$. (Similarly for solutions 2A and 2B.) This is an unresolvable mathematical ambiguity created by terms of the form

$$\pm c_P c_S (1 \pm b_P)(1 \mp b_S) e^{-i(\delta_P + \delta_S \pm \phi_P \mp \phi_S)} (f_P^* f_S)^{(*)}, \tag{4.21}$$

Table 4.17: $\phi(1020)$ isobar coefficients found in the low-mass fit.

	$\phi(1020)$			
#	c_ϕ	φ_ϕ	NLL	number of fits
1A	0.0095 ± 0.0008	-0.07 ± 0.25	-40571.3	13
1B	0.0095 ± 0.0008	3.07 ± 0.25	-40571.3	included with 1A
2A	0.0124 ± 0.0011	-2.16 ± 0.25	-40571.4	57
2B	0.0124 ± 0.0011	0.98 ± 0.25	-40571.4	included with 2A

Table 4.18: *CP* parameters found in the low-mass fit.

	$\phi(1020)$		$f_0(980)$	
#	A_{CP}	β_{eff}	A_{CP}	β_{eff}
1A	-0.08 ± 0.18	0.11 ± 0.14	0.41 ± 0.24	0.14 ± 0.15
1B	-0.08 ± 0.18	3.25 ± 0.14	0.41 ± 0.24	0.14 ± 0.15
2A	-0.11 ± 0.18	0.10 ± 0.13	-0.20 ± 0.31	3.09 ± 0.19
2B	-0.11 ± 0.18	3.24 ± 0.13	-0.20 ± 0.31	3.09 ± 0.19

which enter the interference term of the time-dependent amplitude squared. In all of these terms, the phases appear in the combinations $\delta_P + \phi_P$ or $\delta_P - \phi_P$. So a simultaneous shift by π in both δ_P and ϕ_P has no effect.

Of the four solutions listed in Tab. 4.7.3, only solution 1A has values of β_{eff} for both the ϕ and the f_0 that correspond to the quadrant of the ρ-η plane consistent with the Standard Model. So we choose solution 1A as our nominal solution, while noting that our data cannot exclude the other solutions.

For solution 1A, the correlation coefficients returned by the fitter between key parameters are given in Table 4.7.3.

In Fig. 4.51, we show a two-dimensional scan of the likelihood for the f_0 *CP* parameters. At each point in the scan, fits are repeated with the f_0 *CP* parameters held fixed. Other floating parameters have their initial values randomized before each fit. Multiple fits are done at each point.

Because the low-mass region contains similar contributions from S-wave and P-wave components, the visible time-dependent *CP* asymmetry tends to cancel out. A slight enhancement can be seen if one plots the asymmetry in a tight window around

Table 4.19: Correlations found by the fitter in the low-mass fit.

Name	Correlation with $b_{\phi(1020)}$	$\delta_{\phi(1020)}$	$b_{f_0(980)}$	$\delta_{f_0(980)}$
$b_{\phi(1020)}$	1	−0.06	−0.29	0.13
$\delta_{\phi(1020)}$	−0.06	1	0.45	0.71
$b_{f_0(980)}$	−0.29	0.45	1	0.17
$\delta_{f_0(980)}$	0.13	0.71	0.17	1
$c_{\phi(1020)}$	0.07	0.14	−0.04	0.23
$\varphi_{\phi(1020)}$	−0.11	−0.02	−0.11	−0.14
$n_{\text{Signal},K^+K^-K^0_{S+-}}$	0.00	−0.03	0.01	−0.04
$n_{\text{Signal},K^+K^-K^0_{S00}}$	−0.01	0.00	0.03	0.01
$n_{\text{Signal},K^+K^-K^0_L}$	−0.03	−0.05	−0.10	0.02

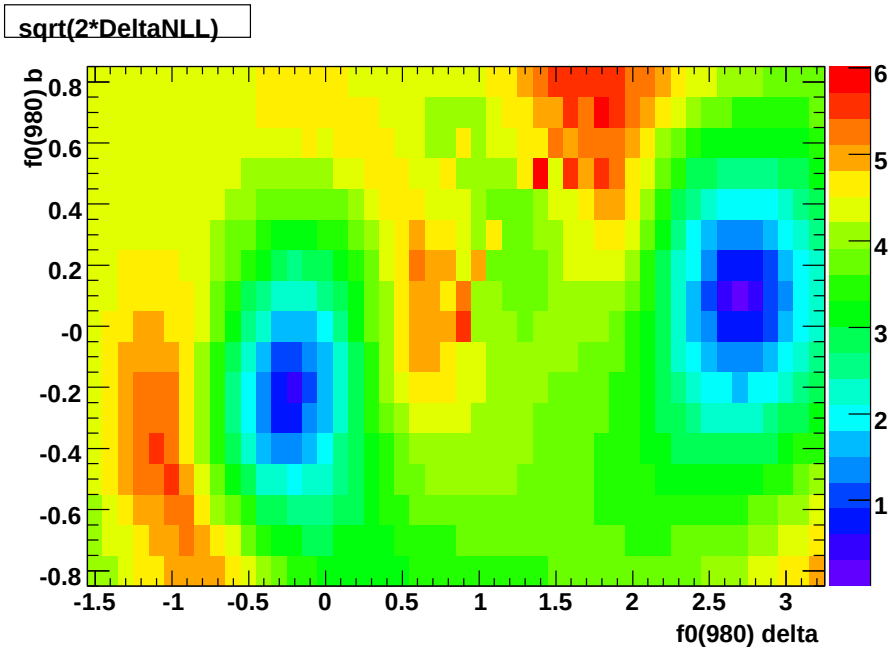

Figure 4.51: Likelihood scan of the $f_0(980)$ *CP* parameters. The color axis is in units of $\sqrt{2\Delta\text{NLL}}$ (σ).

the $\phi(1020)$ mass. These plots are shown in Fig. 4.52.

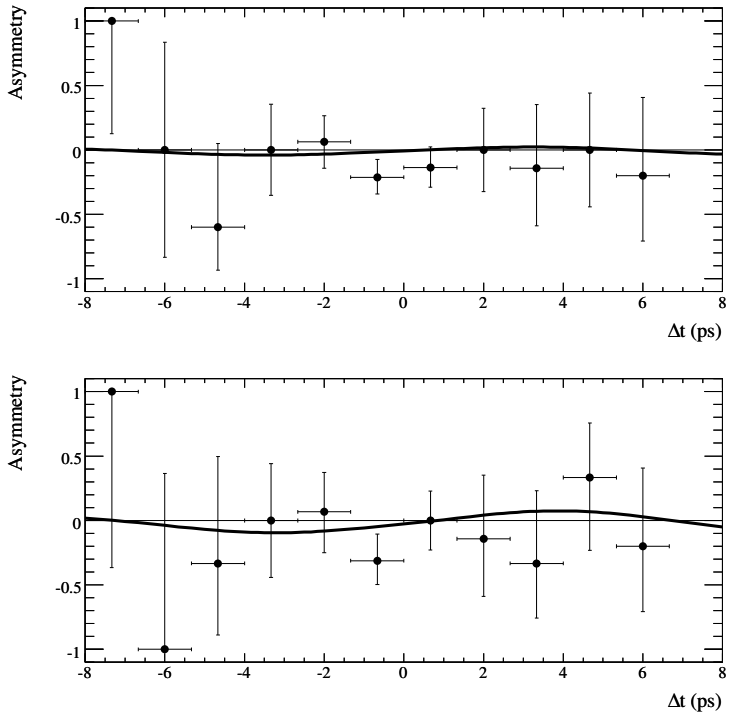

Figure 4.52: *CP* asymmetry of signal-weighted events in (top) the low-mass region, and (bottom) the ϕ region ($1.01 < m_{K^+K^-} < 1.03\,\mathrm{GeV}/c^2$). Both plots show the projection of the low-mass fit result (solution 1A).

4.8 Systematic Uncertainties

In this section, we describe the procedures used to estimate the systematic uncertainties on the measured *CP* asymmetries.

4.8.1 Fit Bias

Fit bias is estimated using the embedded toy fits shown in Sec. 4.6.2. For the low- and high-mass fits, the iterated embedded toys are used. As discussed in that section, this error is dominated by the contribution from the detector resolution, which is not

modeled by the PDF. The bias is defined as the difference between the mean of the distribution of fit values and the generated value.

4.8.2 Fixed PDF Parameters

Most of the parameters used in the PDFs are held fixed in the fits. These parameters are derived from finite and imperfect sources, such as sidebands and Monte Carlo events, and so introduce systematic uncertainty in the results. The procedure for estimating the errors due to these fixed parameters is:

1. Split the fixed PDF parameters into groups of related parameters
2. For a given group of parameters, shift all parameters in the group by $+1\sigma$
3. Repeat the fit to data using the shifted parameters and note the difference Δ_+ from the nominal fit
4. For the same group of parameters, shift all parameters by -1σ from their nominal values
5. Repeat the fit to data using the shifted parameters and note the difference Δ_- from the nominal fit
6. Calculate the systematic uncertainty due to that group of parameters as $(|\Delta_+| + |\Delta_-|)/2$.

The uncertainty σ on a given parameter is taken from the original source used in determining the value of that parameter. The groups used are:

1. Δt: Δt resolution function parameters
2. Tagging: signal tagging category fractions
3. Selection: $m_{\rm ES}$ and ΔE PDF parameters
4. $B\overline{B}$ background: parameters related to $B\overline{B}$ background, most importantly the S and C of the $B\overline{B}$ background, which are nominally zero. We shift them by $\sigma = 0.75$.

5. $B\overline{B}$ background tagging: $B\overline{B}$ background tagging category fractions
6. Fixed $B\overline{B}$ yield in K^0_L
7. Isobar model: the $f_0(980)$ parameters are varied by their errors
8. Isobar model: Mass of the $\phi(1020)$
9. Isobar model: Width of the $\phi(1020)$
10. Isobar model: Mass and Width of the χ_{c0}
11. Isobar model: α_{NR} parameter of the non-resonant components, shifted by $\sigma = 0.02$
12. Isobar model: Mass and Width of the D^- and D_s^- components
13. Isobar model: the $X_0(1550)$ component. Here instead of shifting by the errors, we substitute the mass and width determined by Belle: $m = 1.491$ GeV/c^2, $\Gamma = 0.145$ GeV/c^2 [26]. This is a much larger change than shifting by the errors.

For the low- and high-mass fits, the fits to data with shifted parameters are iterated from the whole DP fit with the parameters shifted in the same fashion.

4.8.3 Isobar coefficients

For the low- and high-mass fits, an additional systematic error is derived from the statistical errors on the isobar coefficients. To estimate this error, we repeat the fit to data many times, each time randomly smearing the isobar coefficients by the covariance matrix from the fit to the whole DP. The widths of the distributions of *CP* parameter results give estimates of the systematic errors introduced by these fixed coefficients. For the δ parameter in the high-mass fit this distribution is rather asymmetric, so we separately find 68% of the area to the left and right of the central value in order to calculate an asymmetric error. For the low-mass fit, this error is very small for the $\phi(1020)$ *CP* parameters because the ϕ isobar coefficients float in the fit.

4.8.4 Other errors

A number of other systematic uncertainties are common to all time-dependent analyses. These include detector effects such as the uncertainty on the beam spot position and possible misalignment of the SVT. We also assign an uncertainty due to the effect of doubly CKM-suppressed decays [54]. Previous iterations of this analysis have found these uncertainties to be similar in size to those estimated for other time-dependent analyses, so we assign the same uncertainties as calculated for the most recent *BABAR* $\sin 2\beta$ analysis [11].

4.8.5 Summary

For each fit, the various systematic uncertainties are added in quadrature to determine the total uncertainty. The systematic uncertainties for the whole DP fit are summarized in Table 4.8.5, and Table 4.8.5 has a similar summary for the high-mass fit. The uncertainties for the low-mass fit are in Tables 4.8.5 and 4.8.5, for the $f_0(980)$ and $\phi(1020)$, respectively.

Table 4.20: Summary of systematic uncertainties on the *CP*-asymmetry parameters $b_{K^+K^-K^0}$ and $\delta_{K^+K^-K^0}$ for the fit to the Whole DP. Translated to A_{CP}, the errors on $b_{K^+K^-K^0}$ correspond to: Model 0.004, Bias 0.003, Other 0.052. This gives a total error on A_{CP} of 0.053.

Category	b			δ		
Fixed Model parameters	Δ_+	Δ_-	Average	Δ_+	Δ_-	Average
$f_0(980)$	0.000	0.000	0.000	0.001	-0.001	0.001
ϕ (Mass)	0.000	0.000	0.000	0.000	0.000	0.000
ϕ (Width)	0.000	0.000	0.000	0.001	-0.001	0.001
χ_{c0}	0.000	0.000	0.000	-0.001	0.001	0.001
α_{NR}	0.000	0.000	0.000	0.008	-0.008	0.008
D^-,D_s^-	0.000	0.000	0.000	-0.001	0.001	0.001
$X_0(1550)$			0.002			0.003
Model Subtotal			0.002			0.009
Fixed PDF parameters						
Δt	-0.007	-0.017	0.012	0.011	-0.019	0.015
Tagging	-0.006	0.005	0.006	0.003	-0.003	0.003
Selection	-0.002	0.002	0.002	-0.002	0.002	0.002
$B\overline{B}$ background	-0.019	0.024	0.021	0.025	0.001	0.013
$B\overline{B}$ background tagging	0.000	0.000	0.000	0.000	0.000	0.000
From charmonium						
Beamspot			0.002			0.006
DCSD			0.007			0.001
"Other" subtotal			0.026			0.021
Fit bias			0.002			0.001
Total			0.026			0.026

Table 4.21: Summary of systematic uncertainties on the *CP*-asymmetry parameters $b_{K^+K^-K^0}$ and $\delta_{K^+K^-K^0}$ for the fit to the high-mass region. Translated to A_{CP}, the errors on $b_{K^+K^-K^0}$ correspond to: Model 0.025, Bias 0.014, Other 0.053. This gives a total error on A_{CP} of 0.060.

Category	b			δ		
Fixed Model parameters	Δ_+	Δ_-	Average	Δ_+	Δ_-	Average
Isobar coefficients	0.013	0.012	0.012	0.050	0.020	$^{+0.050}_{-0.020}$
$f_0(980)$	0.000	0.000	0.000	0.001	-0.001	0.001
ϕ (Mass)	0.000	0.000	0.000	0.000	0.000	0.000
ϕ (Width)	0.000	0.000	0.000	0.000	0.000	0.000
χ_{c0}	0.000	0.000	0.000	-0.002	0.002	0.002
α_{NR}	-0.001	0.001	0.001	0.012	-0.012	0.012
D^-,D_s^-	0.000	0.001	0.000	-0.002	0.002	0.002
$X_0(1550)$			0.003			0.004
Model Subtotal			0.012			$^{+0.051}_{-0.024}$
Fixed PDF parameters						
Δt	-0.003	-0.019	0.011	0.018	-0.015	0.017
Tagging	-0.006	0.006	0.006	0.002	-0.003	0.003
Selection	-0.001	0.001	0.001	0.000	0.001	0.001
$B\overline{B}$ background	-0.019	0.026	0.022	-0.003	0.000	0.002
$B\overline{B}$ background tagging	0.000	0.000	0.000	0.000	0.000	0.000
From charmonium						
Beamspot			0.002			0.006
DCSD			0.007			0.001
"Other" subtotal			0.027			0.018
Fit bias			0.007			0.008
Total			0.030			$^{+0.055}_{-0.031}$

Table 4.22: Summary of systematic uncertainties on the $f_0(980)$ *CP*-asymmetry parameters b and δ for the fit to the low-mass region. Translated to A_{CP}, the errors on b correspond to: Model 0.029, Bias 0.061, Other 0.029. This gives a total error on A_{CP} of 0.074.

Category	b			δ		
Fixed Model parameters	Δ_+	Δ_-	Average	Δ_+	Δ_-	Average
Isobar coefficients	0.016	0.016	0.016	0.023	0.026	0.024
$f_0(980)$	-0.003	0.004	0.003	0.000	-0.006	0.003
ϕ (Mass)	-0.001	0.001	0.001	-0.001	0.002	0.002
ϕ (Width)	0.000	0.000	0.000	0.002	-0.003	0.002
χ_{c0}	0.000	0.000	0.000	0.000	0.001	0.000
α_{NR}	0.000	-0.003	0.001	0.000	0.015	0.008
D^-,D_s^-	-0.001	0.001	0.001	-0.002	0.000	0.001
$X_0(1550)$			0.003			0.031
Model Subtotal			0.017			0.041
Fixed PDF parameters						
Δt	-0.008	-0.021	0.015	0.001	0.029	0.015
Tagging	-0.003	0.004	0.004	0.002	-0.002	0.002
Selection	0.001	-0.001	0.001	-0.002	0.000	0.001
$B\overline{B}$ background	0.002	-0.001	0.002	0.001	0.001	0.001
$B\overline{B}$ background tagging	-0.001	0.000	0.000	0.001	0.000	0.000
From charmonium						
Beamspot			0.002			0.006
DCSD			0.007			0.001
"Other" subtotal			0.017			0.016
Fit bias			0.035			0.031
Total			0.042			0.054

Table 4.23: Summary of systematic uncertainties on the $\phi(1020)$ CP-asymmetry parameters b and δ for the fit to the low-mass region. Translated to A_{CP}, the errors on b correspond to: Model 0.003, Bias 0.028, Other 0.022. This gives a total error on A_{CP} of 0.036.

Category	b			δ		
Fixed Model parameters	Δ_+	Δ_-	Average	Δ_+	Δ_-	Average
Isobar coefficients	0.001	0.001	0.001	0.004	0.005	0.005
$f_0(980)$	-0.002	-0.001	0.001	0.001	-0.005	0.003
ϕ (Mass)	0.000	0.000	0.000	-0.001	0.002	0.001
ϕ (Width)	0.000	0.000	0.000	0.001	-0.001	0.001
χ_{c0}	0.000	0.000	0.000	0.000	0.000	0.000
α_{NR}	0.000	0.000	0.000	0.000	0.000	0.000
D^-,D_s^-	0.000	0.000	0.000	-0.002	0.000	0.001
$X_0(1550)$			0.000			0.001
Model Subtotal			0.001			0.006
Fixed PDF parameters						
Δt	-0.007	0.006	0.007	-0.003	0.004	0.004
Tagging	-0.005	0.005	0.005	0.000	0.000	0.000
Selection	0.001	-0.001	0.001	-0.003	0.001	0.002
$B\overline{B}$ background	0.000	0.000	0.000	0.001	-0.001	0.001
$B\overline{B}$ background tagging	0.000	0.000	0.000	0.000	0.000	0.000
From charmonium						
Beamspot			0.002			0.006
DCSD			0.007			0.001
"Other" subtotal			0.011			0.007
Fit bias			0.014			0.055
Total			0.018			0.055

Chapter 5

Conclusions

Using a time-dependent Dalitz plot analysis, we measure the *CP* violation parameters A_{CP} and β_{eff} for the inclusive decay $B^0 \to K^+K^-K^0$, and separately for the events with $m_{K^+K^-} > 1.1\,\mathrm{GeV}/c^2$. We also measure the *CP* violation parameters for the decays $B^0 \to \phi K^0$ and $B^0 \to f_0(980)K^0$ using events with $m_{K^+K^-} < 1.1\,\mathrm{GeV}/c^2$. These measurements are made combining samples of $K^0_S \to \pi^+\pi^-$, $K^0_S \to \pi^0\pi^0$, and K^0_L events. The results are summarized in Table 5.1, where we give only the primary solution (called 1A in Table 4.7.3) for the low-mass fit.

Table 5.1: The *CP*-asymmetries for $B^0 \to K^+K^-K^0$ for the entire DP, in the high-mass region, and for ϕK^0 and $f_0(980)K^0$ in the low-mass region. The first errors are statistical and the second are systematic.

	A_{CP}	β_{eff}(rad)
Whole DP	$-0.015 \pm 0.077 \pm 0.053$	$0.352 \pm 0.076 \pm 0.026$
High-mass	$-0.054 \pm 0.102 \pm 0.060$	$0.436 \pm 0.087\,^{+0.055}_{-0.031}$
ϕK^0	$-0.08 \pm 0.18 \pm 0.04$	$0.11 \pm 0.14 \pm 0.06$
$f_0 K^0$	$0.41 \pm 0.23 \pm 0.07$	$0.14 \pm 0.15 \pm 0.05$

In the fit to the entire DP, we find that the *CP*-conserving case of $\beta_{eff} = 0$ is excluded at 4.8σ, including statistical and systematic errors. This fit also allows us to exclude the solution for β_{eff} near $\pi/2 - \beta$ at 4.5σ. To date, this is the best single measurement available to establish that $\cos 2\beta > 0$. In the fit to the high-mass region only, we exclude the possibility of $\beta_{eff} = 0$ at 5.1σ including statistical and systematic

errors. This is the first observation of *CP* violation in this decay mode, and the second observation of *CP* violation in penguin-dominated $b \to s$ decays [44, 55].

The results of the fits to the whole DP and the high-mass region are consistent with the SM expectation of $\beta = 0.375 \pm 0.017$ [56], $A_{CP} = 0$. The results for β_{eff} in ϕK^0 and $f_0(980)K^0$ are 1.7σ and 1.5σ less than the SM value, respectively. Note that because these two results are highly correlated, their combined significance is not dramatically greater than for the individual results.

The results presented in this work are published in Ref. [57], and have been compiled by the Heavy Flavor Averaging Group (HFAG) into a summary of *CP* violation results in all $b \to s$ penguin decays. The most recent HFAG compilations are shown in Figures 5.1 and 5.2, and include the measurements made in the low-mass and high-mass fits. Note that the results shown in these figures are translated from the results given in Table 5.1, using the relations

$$\begin{aligned} C &\equiv -A_{CP}, \text{ and} \\ -\eta_f S &\equiv \frac{1-b^2}{1+b^2}\sin(2\beta_{\mathit{eff}}), \end{aligned} \tag{5.1}$$

where η_f is the *CP* eigenvalue of the final state. Our results expressed in these terms are given in Table 5.2. Also, the result presented here for $B^0 \to f_0(980)K^0$ is averaged with the *BABAR* result in $B^0 \to f_0(980)K^0$ with $f_0(980) \to \pi^+\pi^-$ [58].

Table 5.2: The *CP* asymmetry parameters C and $-\eta_f S$ obtained from the main results using Eq. 5.1. Values are shown for $B^0 \to K^+K^-K^0$ on the whole DP, in the high-mass region, and for ϕK^0 and $f_0(980)K^0$ in the low-mass region. The first errors are statistical and the second are systematic.

	C	$-\eta_f S$
Whole DP	$0.015 \pm 0.077 \pm 0.053$	$0.647 \pm 0.116 \pm 0.040$
High-mass	$0.054 \pm 0.102 \pm 0.060$	$0.764 \pm 0.111\,^{+0.071}_{-0.040}$
ϕK^0	$0.08 \pm 0.18 \pm 0.04$	$0.21 \pm 0.26 \pm 0.11$
$f_0 K^0$	$-0.41 \pm 0.23 \pm 0.07$	$0.25 \pm 0.26 \pm 0.10$

We have performed the first time-dependent Dalitz plot analysis of the $B^0 \to$

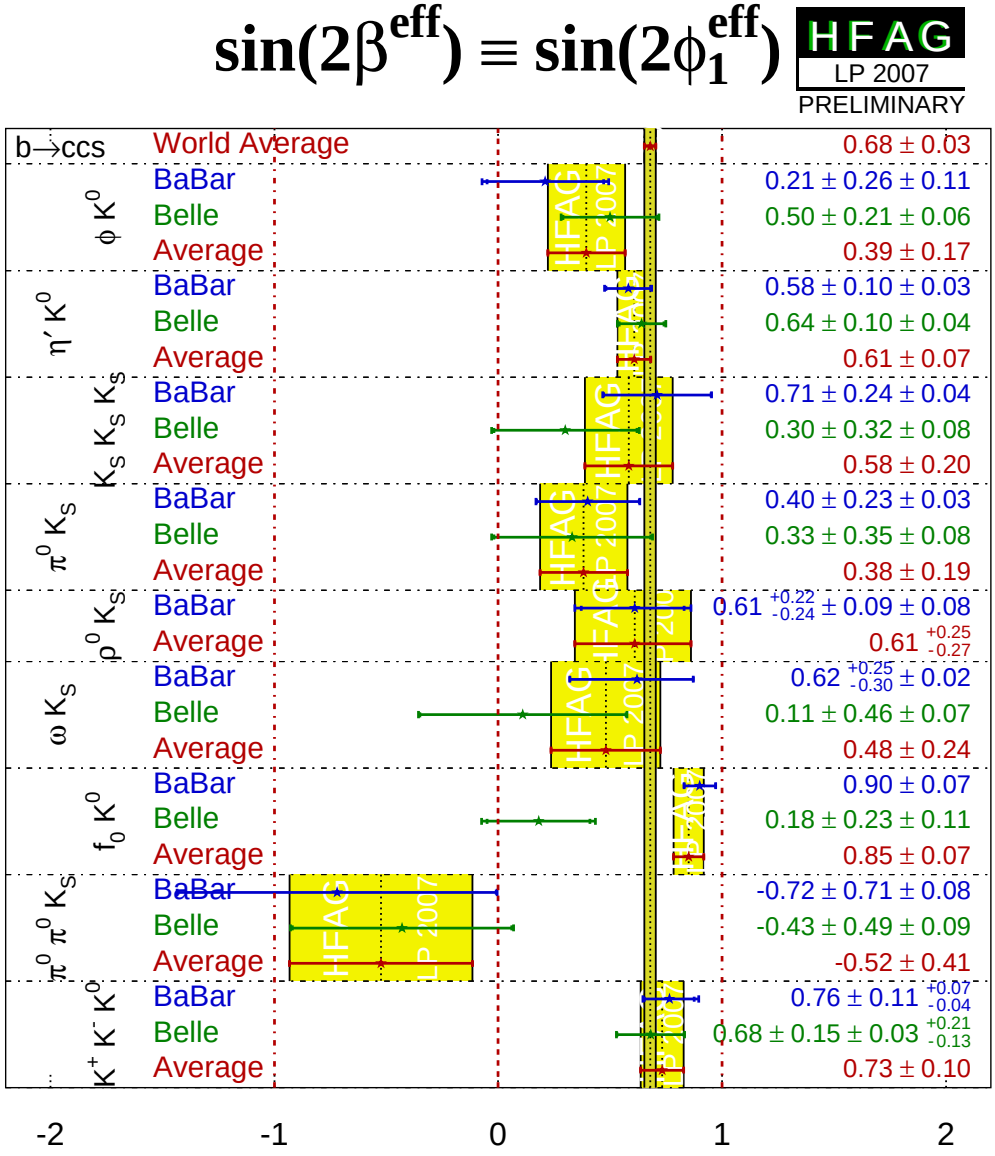

Figure 5.1: Winter 2008 HFAG compilation of $-\eta_f S \approx \sin 2\beta_{eff}$ [56]

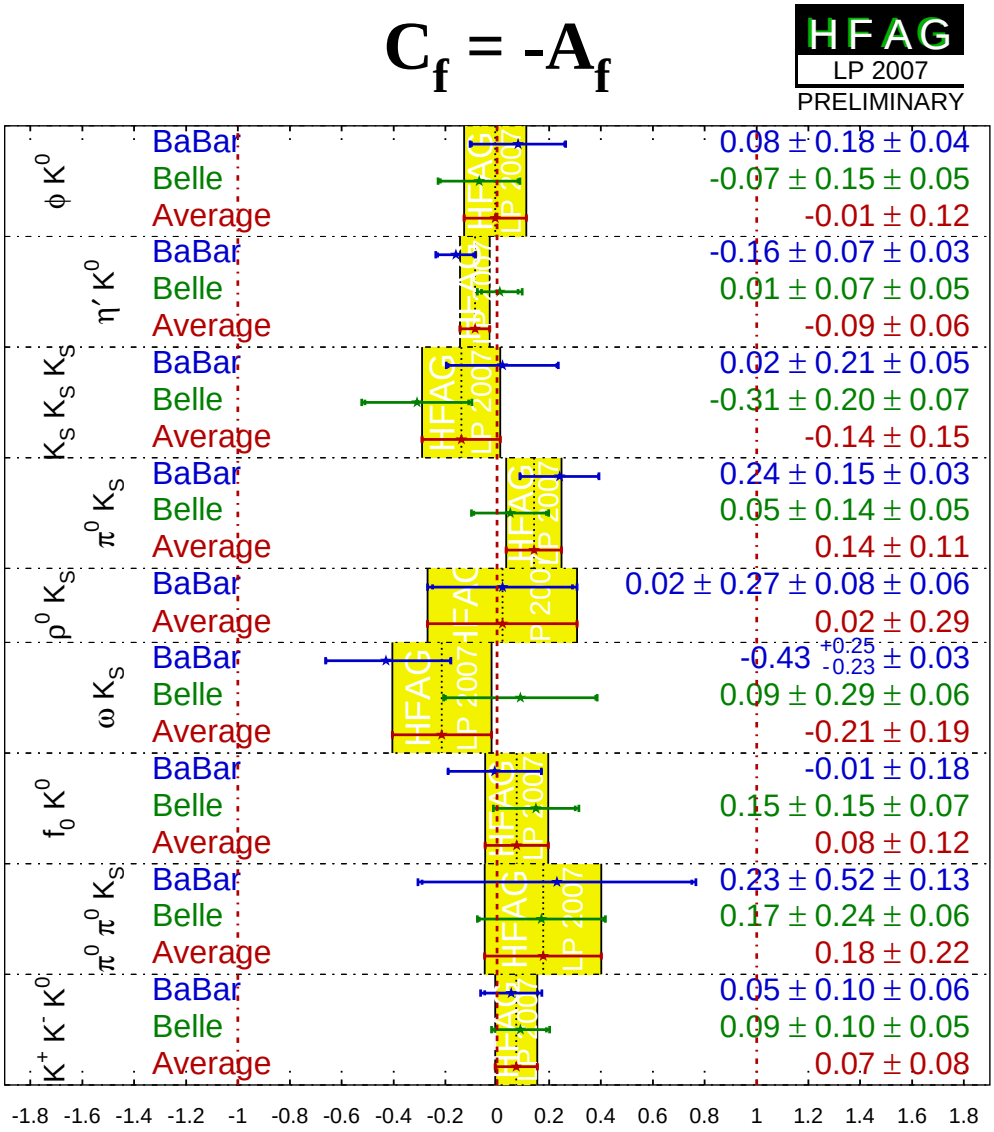

Figure 5.2: Winter 2008 HFAG compilation of $C = -A_{CP}$ [56]

$K^+K^-K^0$ decay mode. The main goal of this analysis was to measure *CP* violation parameters while correctly accounting for both the interference of multiple amplitudes and the mixture of *CP*-even and *CP*-odd contributions in the decay. We have also improved the knowledge of the amplitude structure of this decay, and we expect future work on this mode to expand of that part of the analysis to include quantitative results.

The results presented here were updated in the summer of 2008, using the same technique as described in this thesis, to use the full *BABAR* dataset. The preliminary results with the full dataset are in Ref. [59]. Also in the summer of 2008, the Belle experiment released preliminary measurements of *CP* asymmetries in $B^0 \to K^+K^-K^0$ using a time-dependent Dalitz plot analysis. Those results were extracted from the data using an analysis method similar to that presented here, and are largely compatible with the results shown here [60].

Appendix A

PDF Details

A.1 Fisher discriminant PDF parameters

The signal PDFs used for the Fisher discriminant in the low-mass fit are described in Sec. 4.4.1. Eight parameters are needed to parameterize the sum of three Gaussian distributions, and these parameters are split over the seven tagging categories. Therefore, there are 56 parameters each for $K^+K^-K^0_{S+-}$ and $K^+K^-K^0_{S00}$.

Category	Gaussian 1 Fraction	Gaussian 1 Mean	Gaussian 1 Width	Gaussian 2 Fraction (10^{-3})	Gaussian 2 Mean	Gaussian 2 Width	Gaussian 3 Mean	Gaussian 3 Width
$K^+K^-K^0_{S+-}$								
Untagged	0.44 ± 0.02	-0.38 ± 0.02	0.52 ± 0.01	11 ± 2	-0.77 ± 0.17	2.6 ± 0.3	-1.55 ± 0.02	0.62 ± 0.01
Lepton	0.45 ± 0.02	-0.21 ± 0.02	0.52 ± 0.01	6 ± 2	-0.76 ± 0.36	2.3 ± 0.5	-1.60 ± 0.04	0.72 ± 0.02
KaonI	0.40 ± 0.03	-0.19 ± 0.03	0.56 ± 0.01	11 ± 3	-0.80 ± 0.35	2.8 ± 0.6	-1.57 ± 0.04	0.78 ± 0.02
KaonII	0.42 ± 0.02	-0.30 ± 0.03	0.55 ± 0.01	9 ± 2	-1.1 ± 0.3	3.2 ± 0.7	-1.55 ± 0.03	0.69 ± 0.02
KaonPion	0.43 ± 0.03	-0.34 ± 0.03	0.54 ± 0.01	11 ± 3	-0.77 ± 0.23	2.4 ± 0.4	-1.54 ± 0.04	0.67 ± 0.02
Pion	0.41 ± 0.02	-0.31 ± 0.03	0.52 ± 0.01	12 ± 2	-0.66 ± 0.28	2.8 ± 0.5	-1.52 ± 0.03	0.68 ± 0.02
Other	0.41 ± 0.03	-0.33 ± 0.04	0.53 ± 0.01	13 ± 4	-1.33 ± 0.20	2.23 ± 0.03	-1.53 ± 0.04	0.66 ± 0.02
$K^+K^-K^0_{S00}$								
Untagged	0.57 ± 0.05	-0.46 ± 0.05	0.57 ± 0.02	7 ± 3	-0.6 ± 0.8	3.1 ± 1.5	-1.64 ± 0.07	0.57 ± 0.03
Lepton	0.34 ± 0.04	-0.08 ± 0.03	0.47 ± 0.02	0 ± 0	N/A	N/A	-1.36 ± 0.06	0.82 ± 0.03
KaonI	0.22 ± 0.03	-0.04 ± 0.04	0.47 ± 0.03	0 ± 0	N/A	N/A	-1.22 ± 0.05	0.93 ± 0.02
KaonII	0.48 ± 0.07	-0.32 ± 0.07	0.56 ± 0.03	6 ± 3	-2.7 ± 2.2	3.8 ± 2.5	-1.5 ± 0.1	0.67 ± 0.04
KaonPion	0.35 ± 0.06	-0.22 ± 0.05	0.49 ± 0.03	5 ± 5	-0.3 ± 1.2	2.0 ± 0.7	-1.38 ± 0.09	0.75 ± 0.04
Pion	0.42 ± 0.08	-0.27 ± 0.08	0.54 ± 0.03	5 ± 4	-0.5 ± 1.1	2.6 ± 1.5	-1.5 ± 0.1	0.68 ± 0.04
Other	0.33 ± 0.07	-0.20 ± 0.07	0.47 ± 0.03	10 ± 10	-1.0 ± 0.6	2.1 ± 0.8	-1.39 ± 0.09	0.71 ± 0.04

Table A.1: PDF parameters for the signal Fisher discriminant distribution.

Appendix B

Fit Correlations

For the whole DP fit, correlation coefficients returned by the fitter between the *CP* asymmetry parameters and other important parameters are listed in Table B. Correlations for the low-mass fit were given in Table 4.7.3.

Table B.1: Correlations among notable floating parameters in the whole DP fit.

	Correlation with	
Name	$b_{K^+K^-K^0}$	$\delta_{K^+K^-K^0}$
c_{D^-}	−0.035	−0.005
$c_{D_s^-}$	0.025	−0.001
$c_{\chi_{c0}}$	−0.039	0.002
$\varphi_{\chi_{c0}}$	−0.052	0.015
$c_{X_0(1550)}$	−0.033	0.022
$\varphi_{X_0(1550)}$	−0.062	0.013
$c_{f_0(980)}$	0.007	0.026
$\varphi_{f_0(980)}$	−0.043	−0.011
$n_{\text{Signal},K^+K^-K^0_{S+-}}$	0.004	0.007
$n_{\text{Signal},K^+K^-K^0_{S00}}$	−0.001	0.000
$n_{\text{Signal},K^+K^-K^0_L}$	−0.080	−0.016
$b_{K^+K^-K^0}$	1	0.011
$\delta_{K^+K^-K^0}$	0.011	1
c_{NR,K^-K^0}	0.096	0.029
φ_{NR,K^-K^0}	−0.091	0.047
c_{NR,K^+K^0}	−0.067	0.074
φ_{NR,K^+K^0}	−0.115	0.077
c_ϕ	0.055	0.022
φ_ϕ	−0.021	−0.084

Appendix C

Measurement of Accelerator Parameters

Typically, accelerator physicists learn about the parameters of the accelerator using instruments such as synchrotron light monitors and beam position monitors placed around the ring. While some measurements can made during normal running conditions (at high currents), others are restricted to low current or single beam running. No measurements (aside from basic luminosity measurements) are possible in the interaction region (IR).

Using the CLEO detector, Cinabro *et al.* pioneered a technique to measure the distribution of event vertices at the CESR e^+e^- collider, and extract various parameters of the accelerator beams [61]. A similar approach was used at the Tevatron [62]. Building on these ideas, we have developed methods to use the large amounts of data collected by *BABAR* to measure the beam parameters at the PEP-II IP. In this section we focus on the measurement of the vertical luminous size, and the subsequent extraction of beam parameters.

C.1 Formalism

A complete introduction to the formalism can be found in Ref. [63]. We repeat the key portions of that reference here.

Assuming that the particle bunches follow Gaussian distributions, and that there is no coupling between the transverse dimensions, the particle distribution in a bunch is

$$\begin{aligned}\rho_b(x,y,z,t) &= \frac{N_b}{\sqrt{(2\pi)^3}\sigma_{xb}\sigma_{yb}\sigma_{zb}} \\ &\quad \times \exp\left[-\frac{(x-\bar{x}_b)^2}{2\sigma_{xb}^2} - \frac{(y-\bar{y}_b)^2}{2\sigma_{yb}^2} - \frac{(z-ct)^2}{2\sigma_{zb}^2}\right],\end{aligned} \tag{C.1}$$

where $b = +$ and $b = -$ are associated with the LER and HER, respectively. N_b is the number of particles in the bunch, the σ_{jb} $(j = x, y, z)$ are the transverse and longitudinal stored-beam sizes, and $\bar{x}_b$ and $\bar{y}_b$ are the transverse bunch centroids. The three-dimensional spatial luminosity distribution $\mathcal{L}(x, y, z)$, also known as the *luminous ellipsoid*, is determined by the time-integrated product of the overlapping particle densities of the two colliding beams.

The vertical luminous size is defined by

$$(\sigma_{y\mathcal{L}})^2 = \overline{y^2}_{\mathcal{L}}(z) = \frac{\int y^2 \rho_+ \rho_-}{\int \rho_+ \rho_-}, \tag{C.2}$$

which is related to the stored-beam sizes by

$$\sigma_{y\mathcal{L}} = \left(\frac{1}{{\sigma_{y-}}^2} + \frac{1}{{\sigma_{y+}}^2}\right)^{-1/2}. \tag{C.3}$$

A similar expression holds for $\sigma_{x\mathcal{L}}$. $\sigma_{x\mathcal{L}}$ and $\sigma_{y\mathcal{L}}$ describe the transverse shape of the luminous ellipsoid (sometimes called the *beamspot*). In the limit of perfect detector resolution, they are directly measurable as the transverse Gaussian widths of the distribution of event vertices.

The transverse beam size σ_{ib} is given in terms of the beam parameters by

$$\sigma_{ib}^2(z) = \epsilon_{ib}\beta_{ib}(z), \tag{C.4}$$

where ϵ_{ib} is the *emittance* of the beam and $\beta_{ib}(z)$ is the value of the beam's β function.

The emittance is the amount of phase space occupied by the beam, while the β function is determined by the magnetic optics of the accelerator. The notation β^*_{ib} is used to denote the value of the β function at the IP. ϵ_y and β^*_y are the principle quantities that we hope to measure in this analysis.

C.1.1 The Hourglass Effect

In the vicinity of the IP, the $e^{\pm}$ trajectories are straight lines, and the IP angular spread σ'_{ib} $(i = x, y)$ induces a longitudinal dependence of the transverse beam size:

$$\sigma_{ib}{}^2(z) = \sigma^{*\,2}_{ib} + \sigma'_{ib}{}^2(z - z^w_{ib})^2$$

where z^w_{ib} is the longitudinal position of the optical waist, σ^*_{ib} is the IP spot size, and

$$\sigma'_{ib} = \sqrt{\frac{\epsilon_{ib}}{\beta^*_{ib}}}$$

is the RMS angular divergence. Equivalently,

$$\sigma_{ib}{}^2(z) = \epsilon_{ib}\beta^*_{ib}\left(1 + \frac{(z - z^w_{ib})^2}{\beta^{*\,2}_{ib}}\right). \tag{C.5}$$

This *hourglass effect* is noticeable only when β^*_{ib} is smaller than or comparable to the bunch lengths. In $e^{\pm}$ rings this is typically true in the vertical only: $\sigma_{yb}(z)$ increases with the distance to the waist, while within a few bunch lengths of the IP, the horizontal beam sizes remain essentially constant (except possibly in the presence of strong beam-beam effects).

In an asymmetric collider each beam is free to have its own emittance, β-function, and waist. However, the expression in Eq. C.3 simplifies considerably if we make the assumptions that the vertical β-functions and the location of the vertical waist are

the same for the two beams. With these assumptions, $\sigma_{y\mathcal{L}}(z)$ is given by

$$\sigma_{y\mathcal{L}}(z) = \sqrt{\frac{\epsilon_{y,\mathrm{eff}}\beta_y^*}{2}\left[1+\left(\frac{z-z_y^w}{\beta_y^*}\right)^2\right]} \tag{C.6}$$

$$= \sigma_{y\mathcal{L}}(z=z_y^w)\sqrt{1+\left(\frac{z-z_y^w}{\beta_y^*}\right)^2}, \tag{C.7}$$

where

$$\epsilon_{y,\mathrm{eff}} = 2\frac{\epsilon_{y+}\epsilon_{y-}}{\epsilon_{y+}+\epsilon_{y-}}. \tag{C.8}$$

Our analysis is based on Eq. C.6 — by measuring the left-hand side (the longitudinal dependence of the vertical luminous size), we can extract quantities on the right-hand side (notably β_y^* and $\epsilon_{y,\mathrm{eff}}$).

C.2 Measurement Technique

The measurement of $\sigma_{y\mathcal{L}}(z)$ is clearly non-trivial. The value of $\sigma_{y\mathcal{L}}$ at the waist is expected to be $5\,\mu$m or smaller. This is already small compared to the single-track vertex resolution of roughly $20\,\mu$m. To complicate things further, to extract the beam parameters of interest we must not only measure the average size $\sigma_{y\mathcal{L}}$, but must also measure the change in this size ($\mathcal{O}(1\,\mu\mathrm{m})$) as a function of z.

C.2.1 Event Selection

We use $e^+e^- \to \mu^+\mu^-$ events, which are produced and recorded by the *BABAR* detector at roughly the same rate as $B\overline{B}$ events. The preliminary selection keeps only events with exactly two charged tracks and less than 3 GeV of total energy deposited in the EMC (to reject Bhabha events). We further require that the dimuon invariant mass fall in a $\pm 200\,\mathrm{MeV}/c^2$ range around the beam energy: $10.38 < m_{\mu^+\mu^-} < 10.78\,\mathrm{GeV}/c^2$.

The track fit of each muon is done independently. Each fit returns the five helix parameters of the track as well as an error matrix. These fits are performed in the

BABAR coordinate system, defined by the DCH. To extract the luminous sizes, the reconstructed tracks are then translated and rotated into the coordinate system defined by the luminous ellipsoid as found by the beamspot calibration (the same calibration used for beamspot-constrained vertexing). The error matrices are transformed accordingly.

Key observables are shown in schematic form in Fig. C.1. For each track, the point of closest approach (poca) in the plane transverse to the beam axis is determined as described above. The distances from the pocas to the beam axis, the distance of closest approach (doca), are called d_1 and d_2. Note that d_1 and d_2 are signed quantities, where the sign depends on the direction of the track relative to the direction of the beam axis.[1] Other relevant helix parameters are the azimuthal angles ϕ_1 and ϕ_2, and the polar angles measured from the beam axis θ_1 and θ_2. The z coordinates z_1 and z_2 are defined as the value of z along the corresponding track at the point of closest approach (for z we use the DCH coordinate system, not the coordinates defined by the luminous ellipsoid). The uncertainties on d_1 and d_2 are taken from the error matrices of the track fits, and are called δ_1 and δ_2. In our notation, we always refer to the more forward track in the detector as track 1, while the more backward track is called track 2.

Based on the variables defined above, several additional quantities are defined for each event. We estimate the doca of the overall event using the average doca of the two muons, $d \equiv (d_1 - d_2)/2$. We also define the "miss distance" m as half the distance between the pocas in the x-y plane: $m \equiv (d_1 + d_2)/2$. Note that m is zero for a perfectly reconstructed event. The total error on d is estimated by $\delta \equiv \sqrt{\delta_1^2 + \delta_2^2}/2$, which is mathematically identical to the error on m. We estimate the longitudinal position of the $\mu^+\mu^-$ vertex as a weighted average $z_v \equiv (z_1 \tan\lambda_2 + z_2 \tan\lambda_1)/(\tan\lambda_2 + \tan\lambda_1)$, where the dip angle λ_i is given by $\lambda_i = \pi/2 - \theta_i$. The azimuthal angles for the two tracks are largely interchangeable (up to a minus sign); for most calculations we use ϕ_1 (which we will call ϕ, for simplicity).

The vertex resolution degrades significantly for very forward tracks, so we keep

[1] More precisely, the doca is positive if $-\vec{d} \times \vec{t}$ is in the $+\hat{z}$ direction, where $\vec{d}$ is the vector from the origin to the track and $\vec{t}$ is the tangent to the track direction [64].

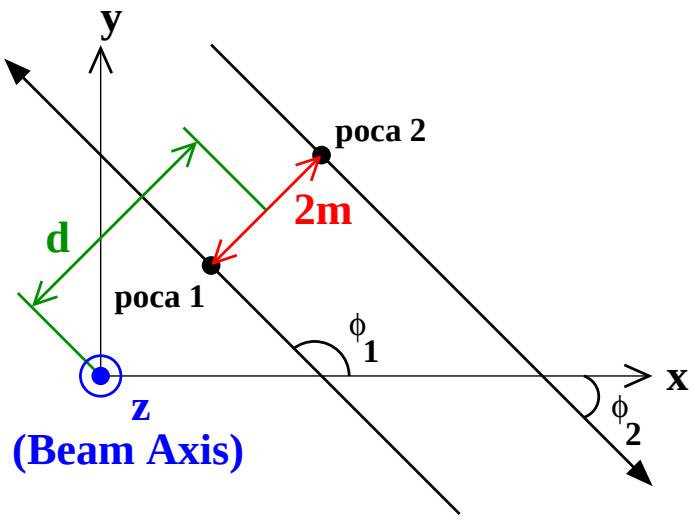

Figure C.1: Schematic view of two reconstructed muon tracks in the transverse plane.

only those events with $\cos\theta_1 < 0.85$. To ensure track quality, we require each track to have at least 20 hits in the DCH and 5 hits in the SVT. We also require that tracks be back-to-back using the selection $\cos(\phi_1 - \phi_2) > -0.99$, although very few events fail this selection. Taking advantage of the accelerator boost, cosmic ray events are eliminated by requiring that $\tan\lambda_1 + \tan\lambda_2 > 0.5$.

Loose cuts are applied to several of the event variables: we require $|d| < 1000\,\mu$m, $|m| < 200\,\mu$m, and $|z_v| < 5\,$cm. We also cut on the event doca error, requiring $2\delta < 35\,\mu$m. The motivation for this cut is given in detail below.

C.2.2 Resolution

At CLEO, the vertex resolution was found to be independent of the vertex position. Therefore the resolution could be treated as a constant factor, added in quadrature with the true luminous region size. Early studies of the vertex resolution at *BABAR* made it clear that the vertex resolution is highly correlated with the trajectories of the tracks in the detector [65]. Therefore, a more sophisticated treatment of the resolution is required.

The correlation between the resolution and the track geometry is shown in

Fig. C.2. The doca error δ varies roughly 40% peak-to-peak in an oscillatory manner as a function of ϕ_1. This variation is partially due to the hexagonal nature of the SVT (see Fig. 3.4); the resolution is best for tracks hitting the SVT modules at near normal incidence, where the measurement is made closest to the IP. However, the structure shown in the figure is mostly caused by the two different readout pitches used in the ϕ-strips of Layers 1 and 2 of the SVT (See Tab. 3.2). Regions with a floating readout strip (known as "skip bonding") have much poorer resolution than those with all strips read out. The effects of the quality of the SVT measurement in Layers 1 and 2 are shown in Fig. C.3.

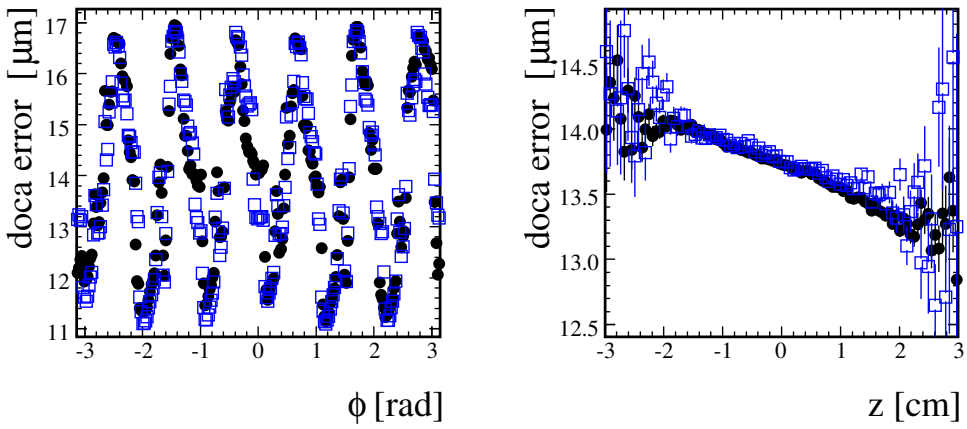

Figure C.2: The doca error δ as a function of (left) the azimuthal angle ϕ_1, and (right) the longitudinal position z_v of the $\mu^+\mu^-$ vertex, for data (black full circles) and for simulation (blue open squares). All selection cuts are applied.

Even more critical for the measurement of $\sigma_{y\mathcal{L}}(z)$ is the dependence of the resolution on z shown in Fig. C.2. The resolution improves by almost 10% for tracks with positive z compared to those with negative z. We found some indication that this variation is also associated with the SVT bonding type (as one moves towards positive z, a higher fraction of tracks hit the areas of the SVT without floating strips). However we were not able to definitively explain this effect.

The overall conclusion from the variations observed in the resolution is that the

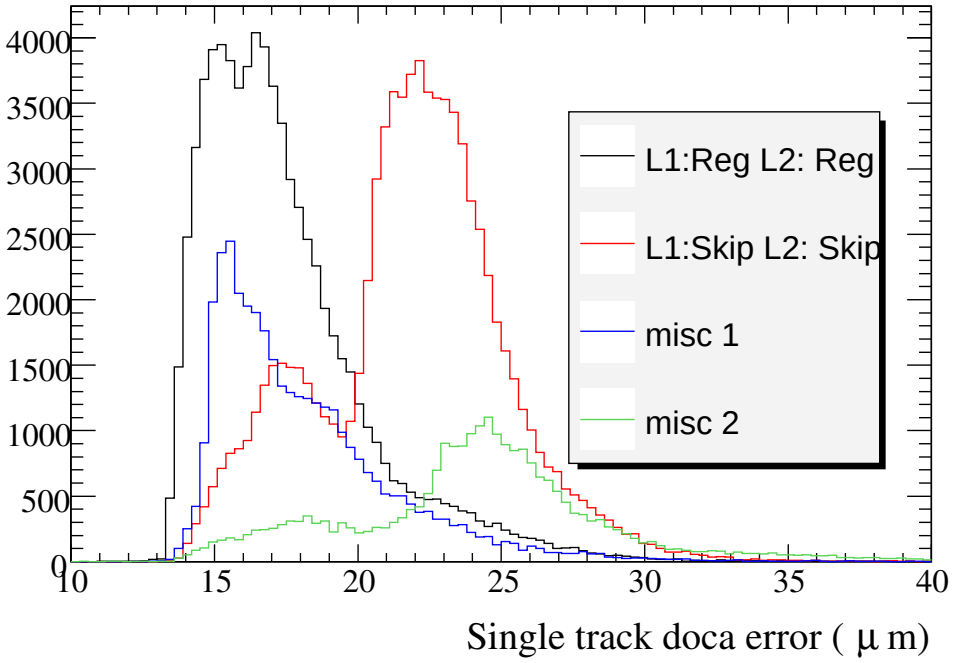

Figure C.3: Distributions of the track doca error (δ_1 and δ_2) in data for various combinations of SVT bonding type in Layers 1 and 2. "Reg" means a hit in an SVT section with all readout strips used; "Skip" means a hit in a section with a floating readout strip. The two "misc" categories are groups of various other possible combinations, including the possibility that the track does not have a hit in a given layer.

resolution is extremely complicated, and needs to be accounted for carefully in any attempt to measure the z-dependence of the luminous size. In the plots shown so far, we have been using the doca error δ as an estimate of the resolution for one given event. For an ensemble of events, the width of the miss-distance distribution provides a direct measurement of the actual resolution in the data. In Fig. C.4, the width of the miss-distance distribution is plotted as a function of δ. There is a linear correlation between the two, indicating that δ is a good measure of the vertex resolution, as expected. However, the slope of the line correlating the two quantities differs significantly from unity, indicating that a scale factor is needed. Also, we find that the shape of the miss distance distribution is not a simple Gaussian distribution.

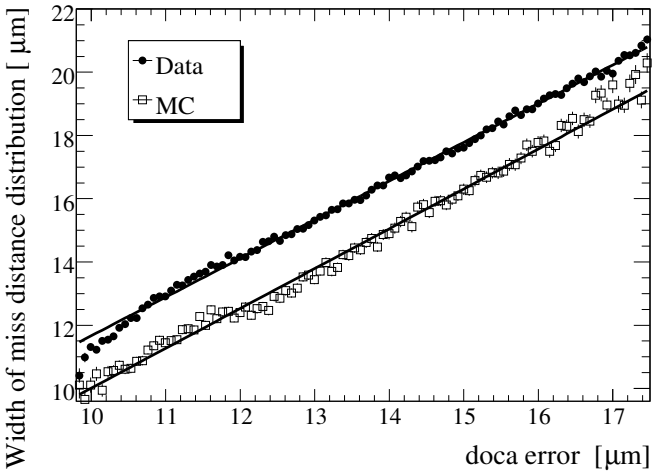

Figure C.4: Width σ_m of the miss-distance distribution, as extracted from Gaussian fits to real (full circles) or simulated (open squares) data, as a function of the doca error δ. The lines are linear fits to the points.

To model the measured resolution, we introduce a resolution function $\mathcal{R}_{\rm doca}$ that incorporates the error estimate δ. $\mathcal{R}_{\rm doca}$ is the sum of three Gaussian distributions G_i:

$$\begin{aligned} \mathcal{R}_{\rm doca}(m) &= f_1 G_1(m;\mu_1(\delta),S_1(\delta)\delta) \\ &+ f_2 G_2(m;\mu_2,S_2\delta) \\ &+ f_3 G_3(m;0,62.5\,\mu{\rm m}). \end{aligned} \tag{C.9}$$

Here the coefficients f_i represent the fraction in each component, and are constrained by $f_3 = 1 - f_2 - f_1$. The distributions have means μ_i, and widths that include scale factors S_i. To test the universality of the core scale factor in this resolution model, we fit the model to data binned in δ, floating only S_1 and fixing other parameters to values determined in a global fit. The results of these fits are shown in Fig. C.5. We see in this plot that the scale factor is not as universal as we hoped, although at least in the data sample shown it is fairly constant over some of the range of δ. We therefore decided to split the core Gaussian parameters (S_1 and μ_1) by δ, fitting for independent values of these parameters for $2\delta < 25\,\mu$m and $2\delta > 25\,\mu$m. Also, we reject events with $2\delta > 35\,\mu$m, as noted in Sec. C.2.1. Using the resolution function modified with these split parameters, we are able to achieve a good fit to the miss distance distribution, as shown in Fig. C.6.

Although this parameterization of the resolution gives a good fit to the overall miss distance distribution, it remains insufficient to fully describe the detector resolution. In particular, the scale factors vary significantly as a function of the position of the tracks in the detector. Therefore, our final resolution model is determined in two steps.

We first determine the fractions f_i by fitting a large event sample (a minimum of one month of data-taking) to the resolution function as described above, including the splitting of the core mean and scale factor.

In the second step, we split the data in bins of the vertex position z_v, azimuthal angle ϕ_1, and polar angle θ_1. In each bin, we refit the miss-distance distribution to Eq. C.9, with the fractions f_i fixed to the values found in the first step and without splitting μ_1 and S_1 by the value of δ. This yields the final scale factors S_i and means μ_i that define the resolution function we will use for extracting the beam parameters.

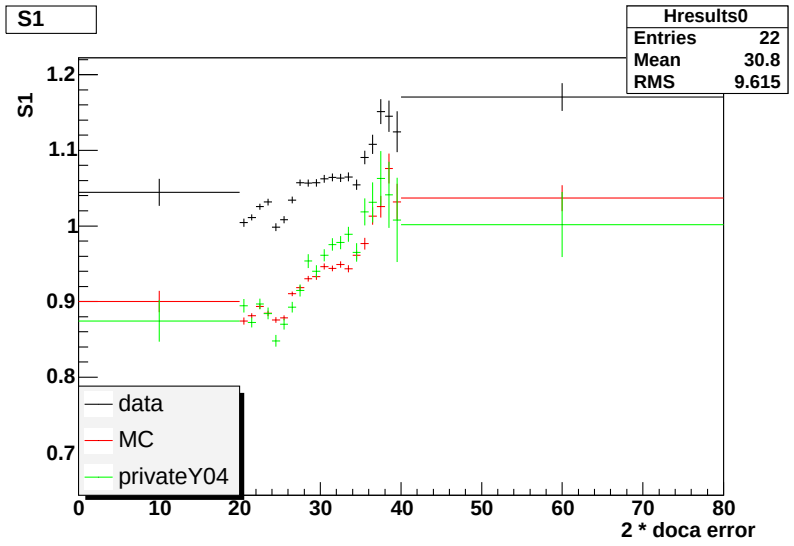

Figure C.5: The core scale factor S_1 found by fitting the resolution function to data samples broken into bins of δ. Black points correspond to a data sample, other points are for two different samples of MC events.

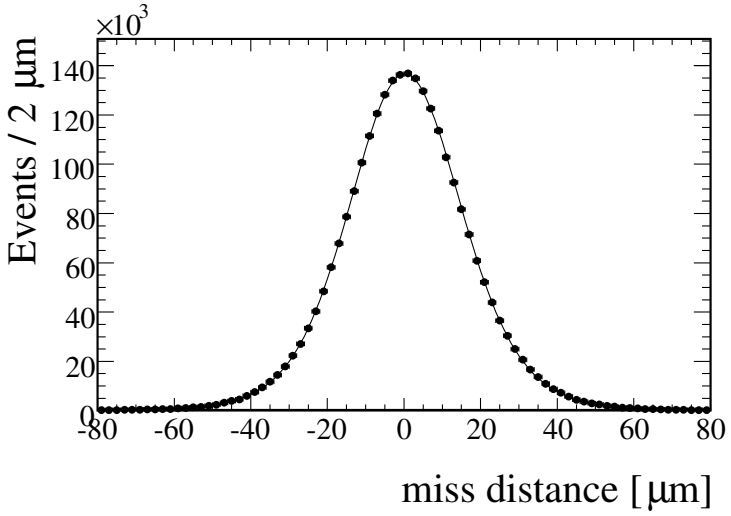

Figure C.6: Distribution of the miss distance m for a typical data sample. The curve is the global fit to the resolution function of Eq. C.9, including splitting the core scale factors as described in the text.

The result of this procedure is shown in Fig. C.7 for the scale factor S_1 of the core Gaussian, and Fig. C.8 for the tail scale factor S_2. Significant variations are seen as a function of ϕ_1, and on close inspection variations across the other detector coordinates are apparent as well. As shown in the figures, we divide the detector into 100 bins of ϕ_1, 3 bins of z_v, and 3 bins of $\cos\theta_1$ for a total of 900 bins.

C.2.3 Fit Procedure

The Gaussian PDF $\mathcal{P}_{\rm doca}$ that describes the doca distribution, neglecting resolution, is given by

$$\mathcal{P}_{\rm doca}(d,\phi,z) = \exp\left(-\frac{1}{2}\frac{\left[d-(y_0(z)\cos\phi_t - x_0\sin\phi_t)\right]^2}{\left[\sigma_{y\mathcal{L}}(z)\cos\phi_t\right]^2+\left[\sigma_{x\mathcal{L}}\sin\phi_t\right]^2}\right), \tag{C.10}$$

where the variable $\phi_t \equiv \phi - t_{xy}$ allows for a global rotation of the luminous ellipsoid around the beam axis by an angle t_{xy}. The constant horizontal size $\sigma_{x\mathcal{L}}$ is a free parameter in the fit, and the vertical size $\sigma_{y\mathcal{L}}(z)$ is given by the expression in Eq. C.7. The parameters x_0 and y_0 account for medium-term drifts of the luminous centroid. Recall that we shift reconstructed tracks into a coordinate system determined by the orientation of the luminous ellipsoid, so in principle x_0 and y_0 should be zero. However, we have found in the data that these parameters are often not zero, so we let them float in the fit. Additionally, we have found that the beamspot calibration does not have the precision to remove the small vertical tilt of the collision axis, so we allow y_0 to depend on z:

$$y_0(z) = y_0(z=0) + (dy_0/dz)z, \tag{C.11}$$

where $y_0(z=0)$ and dy_0/dz are free parameters in the fit.

To extract the IP parameters, we perform an unbinned maximum likelihood fit of the doca distribution to the convolution of the doca PDF and the resolution function, $\mathcal{P}_{\rm doca}(d,\phi,z) \otimes \mathcal{R}_{\rm doca}(d)$. The parameters of $\mathcal{R}_{\rm doca}(d)$ are held fixed to the values determined in the fits to the miss distance distribution described in Sec. C.2.2. There are 8 floating parameters in the fit: x_0, $y_0(z=0)$, dy_0/dz, t_{xy}, z_y^w, $\sigma_{x\mathcal{L}}$, $\sigma_{y\mathcal{L}}(z=z_y^w)$,

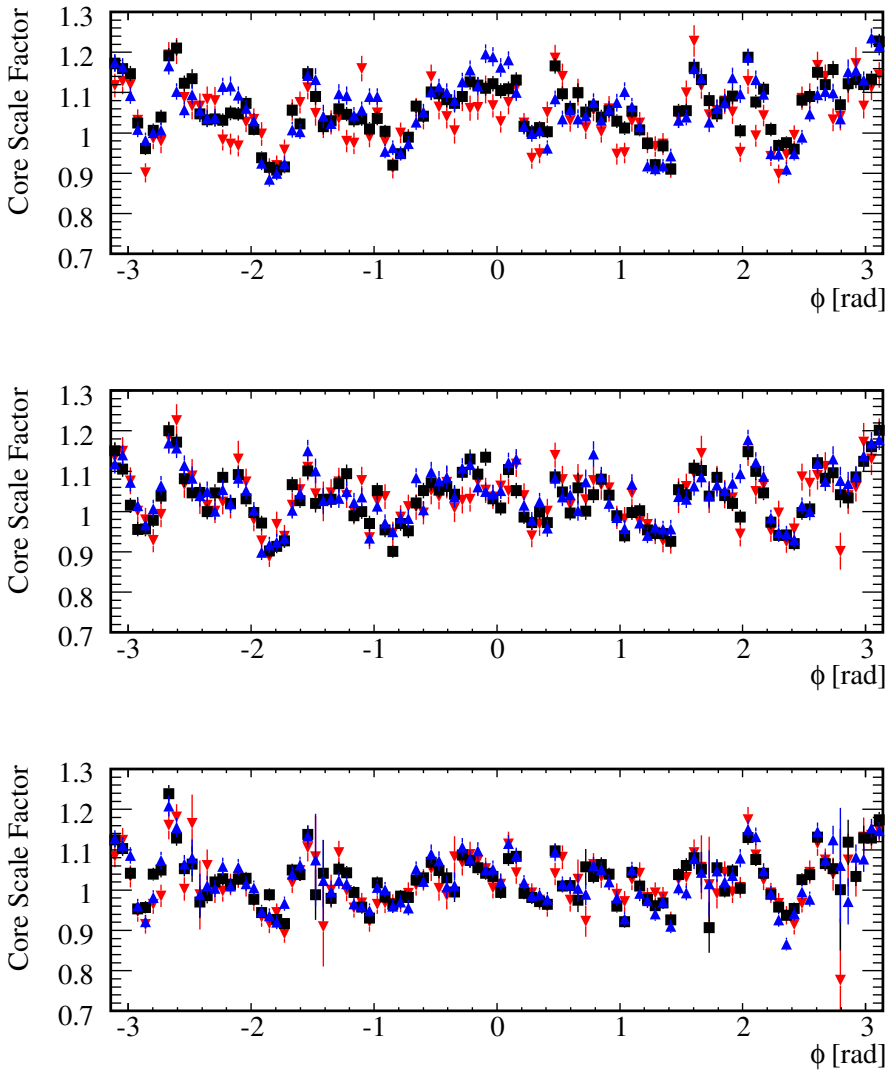

Figure C.7: Scale factor S_1 of the core component of the resolution function as a function of ϕ_1, from fits of Eq. C.9 to a representative data sample. The detector is binned in three bins of $\cos\theta$: $\cos\theta_1 < 0.65$ (top), $0.65 < \cos\theta_1 < 0.75$ (center), $0.75 < \cos\theta_1 < 0.85$ (bottom); and three bins of z_v: negative z_v region (red triangle), central z_v region (black squares), positive z_v region (blue triangles), where z_v is measured in detector coordinates and the exact boundaries of each z_v region depend on the data-taking period.

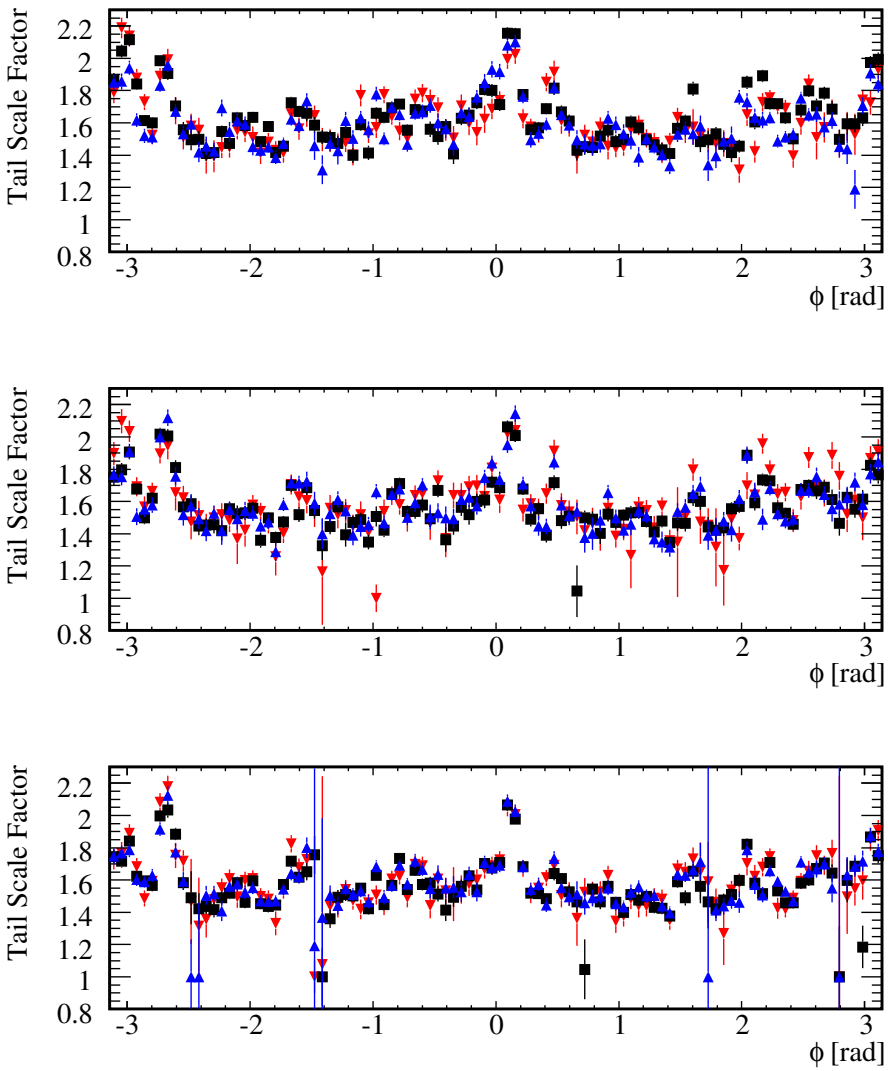

Figure C.8: Scale factor S_2 of the tail component of the resolution function as a function of ϕ_1, from fits of Eq. C.9 to a representative data sample. The detector is binned in three bins of $\cos\theta$: $\cos\theta_1 < 0.65$ (top), $0.65 < \cos\theta_1 < 0.75$ (center), $0.75 < \cos\theta_1 < 0.85$ (bottom); and three bins of z_v: negative z_v region (red triangle), central z_v region (black squares), positive z_v region (blue triangles), where z_v is measured in detector coordinates and the exact boundaries of each z_v region depend on the data-taking period.

and β_y^*.

Figure C.9 shows the measured doca distribution, overlaid with the fit results, for three different cases. A typical data sample is shown on the top; the overall fit result is shown in blue, while the red curve shows the contribution of the resolution to the shape of the distribution. The subset of quasi-vertical muons (center) is primarily sensitive to the horizontal luminous size. The overall fit result for those events is shown in blue, and the contribution to that curve from the horizontal size only, ignoring the vertical size and resolution, appears in green: it totally determines the shape of this distribution. Finally, quasi-horizontal muons (bottom) determine the vertical luminous size. Here the blue curve is defined as in the other two plots, while the magenta curve displays the contribution of the vertical luminous-size size only, ignoring horizontal size and instrumental resolution; the difference between the blue and magenta curves reflects the combined contributions, for these muons, of the resolution and of the horizontal luminous size.

As a check on the self-consistency of the fitting procedure, we refit the data in slices of z. In each slice, we float the $\sigma_{x\mathcal{L}}$ and $\sigma_{y\mathcal{L}}(z = z_y^w)$ parameters, while fixing the others to the results of the global fit. The results of this check are shown in Fig. C.10, where the results of the global fit are shown as curves and the results of the binned fits are shown as points. The vertical hourglass shape is apparent, and the horizontal luminous size is consistent with a constant. The hourglass shape is highly reproducible from one dataset to the next. In some data samples (including the one shown) the horizontal points show a hint of a linear slope or hourglass shape, but this behavior is not consistent when examined over many samples. Both the hourglass effect and the dynamic-β effect could introduce longitudinal variations in the horizontal size, but neither effect is expected to be large enough to be seen clearly in the data. We experimented with fitting for β_x^* but found the results to be unconvincing. (Note that these fits were also unrealistic because they assumed $\beta_{x-}^* = \beta_{x+}^*$, a reasonable assumption for the vertical but not for the horizontal.)

The values of β_y^* and $\sigma_{y\mathcal{L}}$ $(z = z_y^w)$ are highly correlated in the fits. Figure C.11, which shows the error contours for the aforementioned parameters for a typical fit, illustrates this correlation.

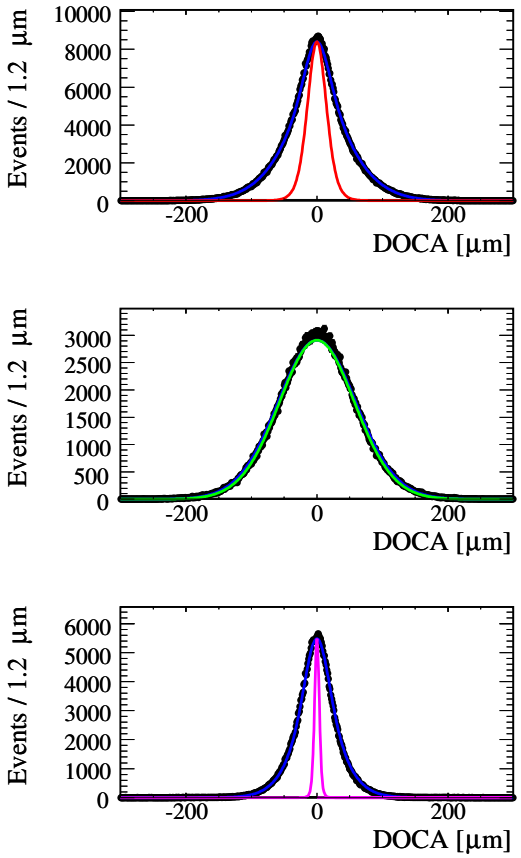

Figure C.9: Measured distribution of d, the distance of closest approach to the beam line, for a typical data sample. Top: all muons; center: quasi-vertical muons ($\pi/4 < |\phi_1| < 3\pi/4$); bottom: quasi-horizontal muons ($|\phi_1| < \pi/4$, $|\phi_1 - \pi| < \pi/4$). The points are the data; the curves are described in the text.

C.2.4 Fit Validation

Initial fit validation is provided by pure toy experiments, where the miss distance and doca distributions are generated using the PDFs. For these tests, the resolution function is generated and fit using the simpler resolution model (no detector bins) used in the first step of the data fitting. Toy results are shown in Fig. C.12. A small (but significant) bias is seen for β_y^*, and the error also appears somewhat underestimated. Other parameters are consistent with no bias (including those not shown here). In both data and toys we notice that the error on β_y^* is highly correlated with the value

of β_y^* determined in the fit. A higher value of β_y^* corresponds to a less noticeable hourglass shape, which translates into a higher error on β_y^*.

Further fit validations are performed using MC samples, which are more useful for testing the complicated resolution modeling used for data. In a first step, ten different simulated data samples were produced, with generated $\sigma_{y\mathcal{L}}$ values ranging from 2 to 20 μm but constant with z (*i.e.* ignoring the hourglass effect). Comparing the "measured" vertical luminous size returned by the fit ($\sigma_{y\mathcal{L}_{\rm fit}}$) to its "true" value ($\sigma_{y\mathcal{L}_{\rm generated}}$) reveals a systematic bias. As shown in Fig. C.13, a simple fit to the function $\sigma_{y\mathcal{L}_{\rm fit}} = \sqrt{\sigma_{y\mathcal{L}_{\rm generated}}{}^2 + \sigma_{y\mathcal{L}_{\rm bias}}{}^2}$ yields $\sigma_{y\mathcal{L}_{\rm bias}} = 2.0 \pm 0.3\,\mu$m. The source of this effect remains unknown, and a z-independent $2\,\mu$m subtraction is applied in quadrature to all subsequent $\sigma_{y\mathcal{L}}$ fit results (including those already shown, such as in Fig. C.10). Although this bias correction is strictly empirical, this approach yields vertical luminous-size measurements that are fairly consistent with those of an independent method (the "Boost" method of Ref. [63]).

In a second step, simulated dimuon samples were generated using realistic emittance values and vertical-hourglass parameters, and analyzed using a procedure identical to that applied to real data. The results of this validation are presented in Table C.1. The fitted values of β_y^* agree with the generated input within statistical errors. The fitted values of $\sigma_{y\mathcal{L}}(z = z_y^w)$ are somewhat high. If we allow the bias correction parameter, nominally fixed to $2\,\mu$m, to float and instead fix $\sigma_{y\mathcal{L}}(z = z_y^w)$ to the generated values, we find that in these samples the fit prefers a bias correction of about $3\,\mu$m, but that β_y^* agrees less well with the generated values (it is too small). Therefore we leave the bias correction set to $2\,\mu$m, but use $1\,\mu$m as the estimated error on the bias correction (as opposed to the smaller error noted above).

The more complicated treatment of the resolution, with resolution function parameters determined independently in bins of detector position, was found to correct biases in fits to MC samples. Using the simpler resolution model with no direct dependence on detector position, we found $t_{xy} = 4.4 \pm 0.9$ mrad (4.9σ off) and $z_y^w = -1.4 \pm 0.2$ cm (2.5σ off) in a fit to Sample 1 of Tab. C.1. These biases seemed to point to inadequate modeling of the resolution, and in fact they disappear when fitting with the more complicated resolution function.

Table C.1: Fit results on simulated event samples. The errors are statistical only.

Parameter	Generated	Fit result
	Sample 1: 1,172,222 events	
$\beta^*_{y+} = \beta^*_{y-}$ (cm)	1.21	1.16 ± 0.13
$\sigma_{y\mathcal{L}}$ $(z = z^w_y)$ (μm)	3.25	3.55 ± 0.17
z^w_y (cm)	-0.9	-0.99 ± 0.08
t_{xy} (mrad)	0	0.33 ± 0.54
$\sigma_{x\mathcal{L}}$ (μm)	75.76	76.26 ± 0.06
	Sample 2: 1,336,813 events	
$\beta^*_{y+} = \beta^*_{y-}$ (cm)	0.80	0.88 ± 0.07
$\sigma_{y\mathcal{L}}$ $(z = z^w_y)$ (μm)	2.64	3.12 ± 0.15
z^w_y (cm)	-0.9	-0.84 ± 0.06
t_{xy} (mrad)	0	0.11 ± 0.51
$\sigma_{x\mathcal{L}}$ (μm)	75.76	76.17 ± 0.06

C.2.5 Systematic Uncertainties

The main source of systematic uncertainty is the $\sim 2\,\mu$m bias correction, which because of the intrinsic correlation between $\sigma_{y\mathcal{L}}$ $(z = z^w_y)$ and β^*_y, affects both of these parameters. We estimate this uncertainty by varying the correction by $\pm 1\,\mu$m and refitting the data.

We use a standard *BABAR* procedure for estimating uncertainties due to possible misalignment of the SVT. Simulated events are reconstructed using a variety of alignment configurations that purposely introduce errors in the alignment. We then repeat fits to these samples to estimate the uncertainty introduced by alignment errors. This method is intended to set an upper limit on the possible error. We find that in the worst case, misalignment increases the measured values of β^*_y by about 20% and of $\sigma_{y\mathcal{L}}$ $(z = z^w_y)$ by about 30%. We found that the effects of misalignment are largely absorbed by the floating x_0 and y_0 parameters in the fit.

Additional systematic errors could be introduced by short-term drifts of the transverse luminous centroid, that would remain unaccounted for by the medium-term average parameters x_0 and y_0. For instance, rapid variations in the actual vertical centroid could, if large enough, bias the $\sigma_{y\mathcal{L}}$ and β^*_y measurement. We have studied

several weeks of data, binned in one-day intervals, and concluded that the transverse centroid motion is typically slow enough and small enough for the associated systematic errors to be neglected.

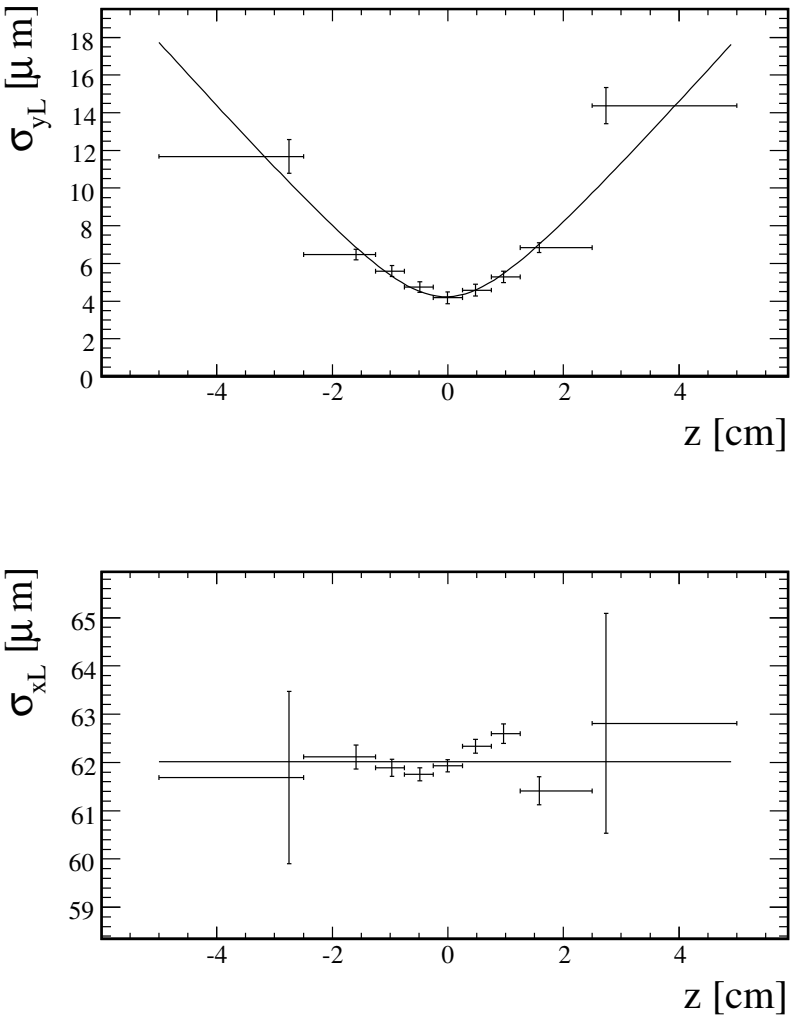

Figure C.10: Measured z-dependence of the vertical (top) and horizontal (bottom) luminous size, extracted from a sample of 8.5×10^5 $e^+e^- \to \mu^+\mu^-$ events collected over ten days in December 2003. The lines show the result of the simultaneous fit to all events; the points with error bars result from fitting the data separately in each z bin.

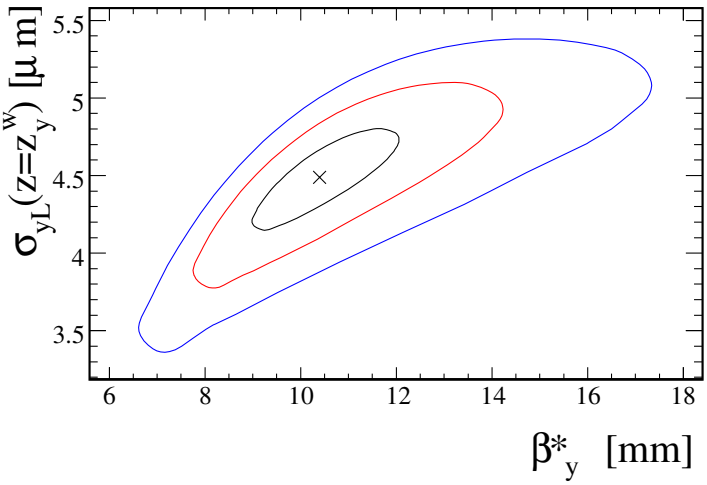

Figure C.11: The inner, center, and outer curves show the boundaries of the 1, 2, and 3 σ regions allowed by the fit around the central value indicated by a cross. These results are from a typical fit to the data. The allowed regions are tilted due to the correlation between β_y^* and $\sigma_{y\mathcal{L}}$ ($z = z_y^w$).

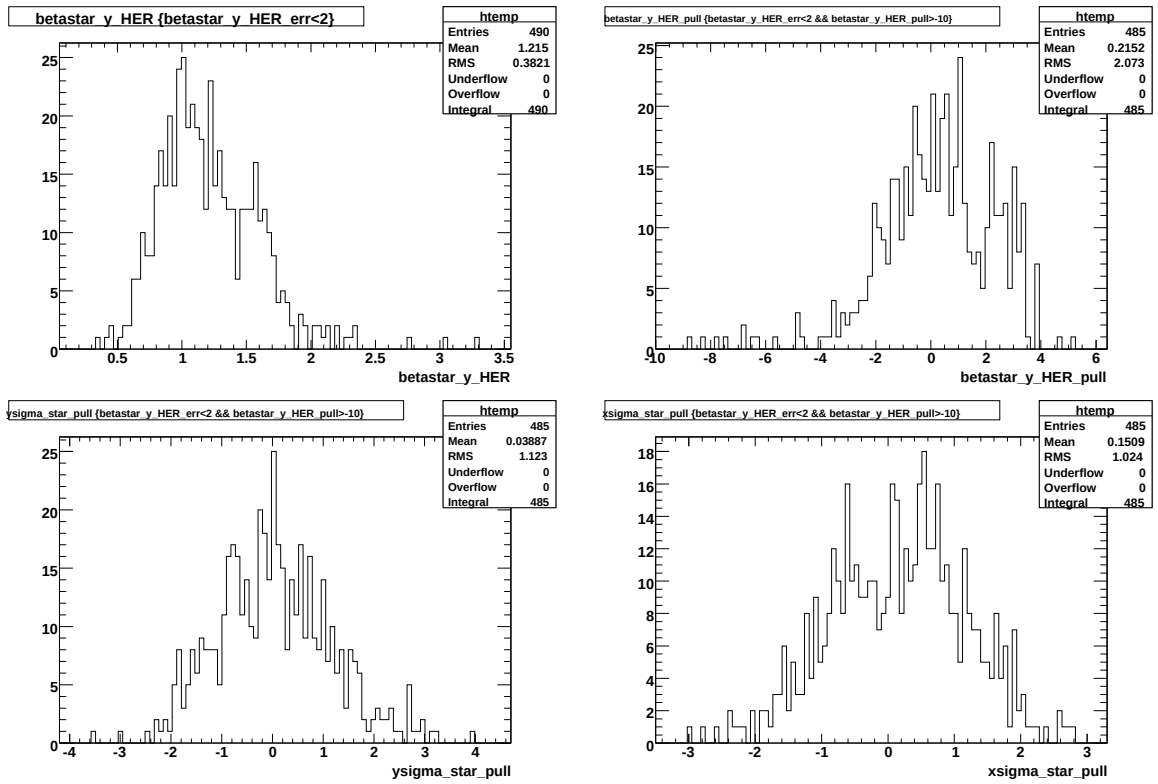

Figure C.12: Results of toy beam parameter fits. The upper left plot shows the distribution of fit values of β_y^*, for a generated value of $\beta_y^* = 1.1\,\mathrm{cm}$. The upper right plot shows the resulting distribution of pulls for β_y^*. The lower plots show pull distributions for (left) $\sigma_{y\mathcal{L}}$ ($z = z_y^w$) and (right) $\sigma_{x\mathcal{L}}$.

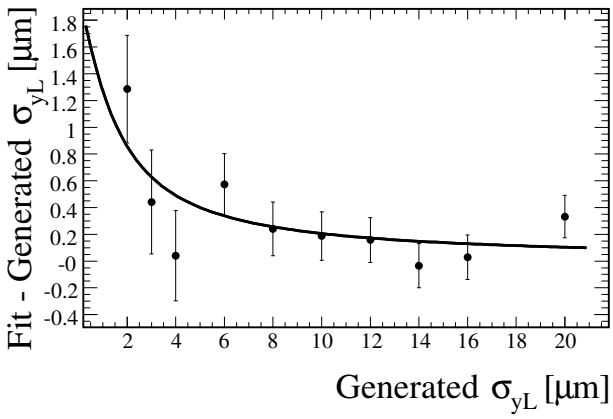

Figure C.13: Difference between the fitted and the generated values of $\sigma_{y\mathcal{L}}$ in simulated event samples generated with no hourglass effect. The curve fitted to the data points provides a parameterization of the measurement bias.

C.3 Fit Results

A complete history of the beam parameters for Runs 1-6 is given in Figures C.14-C.19. Figures C.14, C.15 and C.19 show a second set of error bars for a subset of the points (Run 5). For these points the inner error bar reflects the statistical error while the outer error bar shows the quadrature sum of the statistical and systematic error, where the systematic error is found by varying the bias correction. Other errors are statistical only.

Fig. C.14 includes a set of points reflecting independent measurements of β_y^* performed by accelerator physicists using measurements of the accelerator phase-advance at low current. We find values of β_y^* that agree remarkably well with these measurements. In Ref. [63], we present two additional methods of extracting β_y^* from *BABAR* events. These methods are independent of each other and this method, and have different systematic uncertainties. Both of these methods consistently give somewhat higher values for β_y^* than the method presented here (and thus have worse agreement with the accelerator-based method shown in the Figure). This discrepancy is not fully understood. One possibility is the impact of non-negligible x-y coupling. As discussed in [63], we studied the impact of coupling on all three analyses using simulations, and found that the method shown here was the least sensitive to coupling, while for the "Boost" method coupling increased the measured value of β_y^* by several millimeters. However, the third method (involving the measurement of the longitudinal distribution of luminosity, denoted $d\mathcal{L}/dz$) was only slightly more sensitive to coupling than this method, and found measurements of β_y^* in agreement with the Boost method. Therefore, coupling does not provide a clear explanation for the discrepancies between measurements. Another possibility is that the bias correction in this analysis is overestimated, which would cause this method to underestimate the value of β_y^*. However, reducing the bias correction would increase the discrepancy, discussed below, between this analysis and the Boost method in measurements of $\sigma_{y\mathcal{L}}(z = z_y^w)$. The small bias (around 1 mm) found on β_y^* in pure toys (Fig. C.12) has the wrong sign to account for the disagreement. Measurements of $\sigma_{y\mathcal{L}}(z = z_y^w)$, shown in Fig. C.15, range from 2 to 6 μm. As shown in Ref. [63], these measurements are

consistently higher than those found using the Boost method. A larger bias correction could alleviate this discrepancy, but would worsen the discrepancy in β_y^* noted above. Again, the source of the disagreement is not certain, but could be due to coupling or a combination of factors.

Figure C.16 shows the results for $\sigma_{x\mathcal{L}}$. After a gentle decline over the first two Runs, $\sigma_{x\mathcal{L}}$ decreased notably in the spring of 2003, when the horizontal tunes of both rings were moved close to the half-integer. A horizontal size of about 65 μm, with fluctuations of several microns, was maintained for the rest of the running. The global beamspot tilt t_{xy} is shown in Fig. C.17, and tn location of the optical waist z_y^w is shown in Fig. C.18. The waist position is measured in the detector coordinate system, and is in rough agreement with independent measurements [63].

The effective vertical emittance, shown in Fig. C.19, is extracted by the fit results for β_y^* and $\sigma_{y\mathcal{L}}(z = z_y^w)$. The results range from 2-5 nm rad, approximately consistent with the design goal of 2-3 nm rad. Again, the values found here are consistently larger than those found using the Boost method. This discrepancy could be due to an underestimated bias correction, or the effect of x-y coupling [63].

C.4 Conclusion

Expanding on work done at previous accelerators, we have developed a novel technique for measuring the IP parameters at PEP-II using the *BABAR* detector. A sophisticated treatment of the detector resolution is required in order to measure the vertical size of the luminous region with a detector whose resolution is several times larger. We extract results for nearly the entire history of PEP-II operation. The results are in approximate agreement with independent methods, although some discrepancies remain. These disagreements may be due to residual biases in the measurement techniques, unmodeled accelerator physics effects, or a combination of the two.

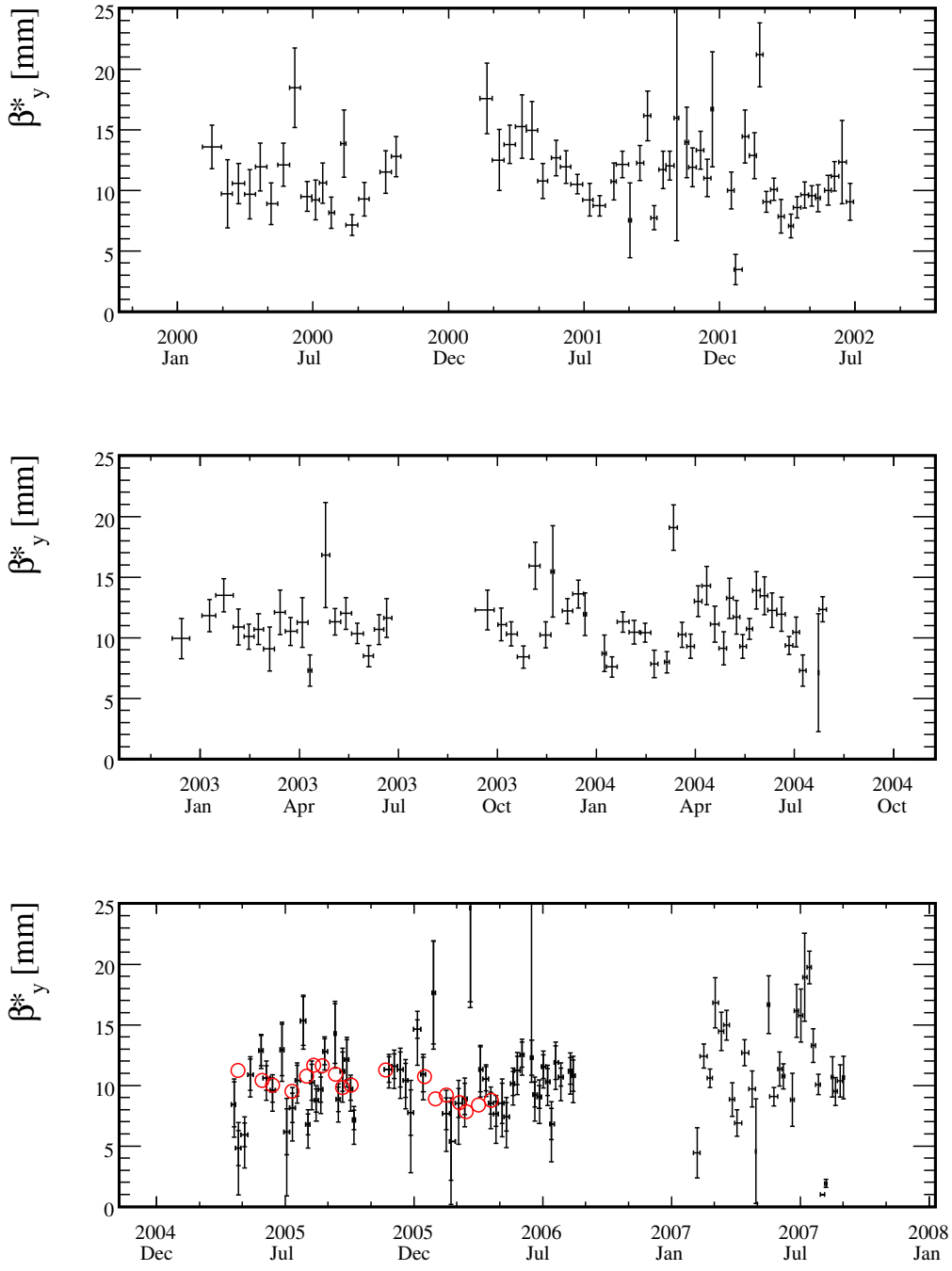

Figure C.14: Fit results for β_y^* for Runs 1-6. Red circles are independent measurements made using the accelerator phase-advance.

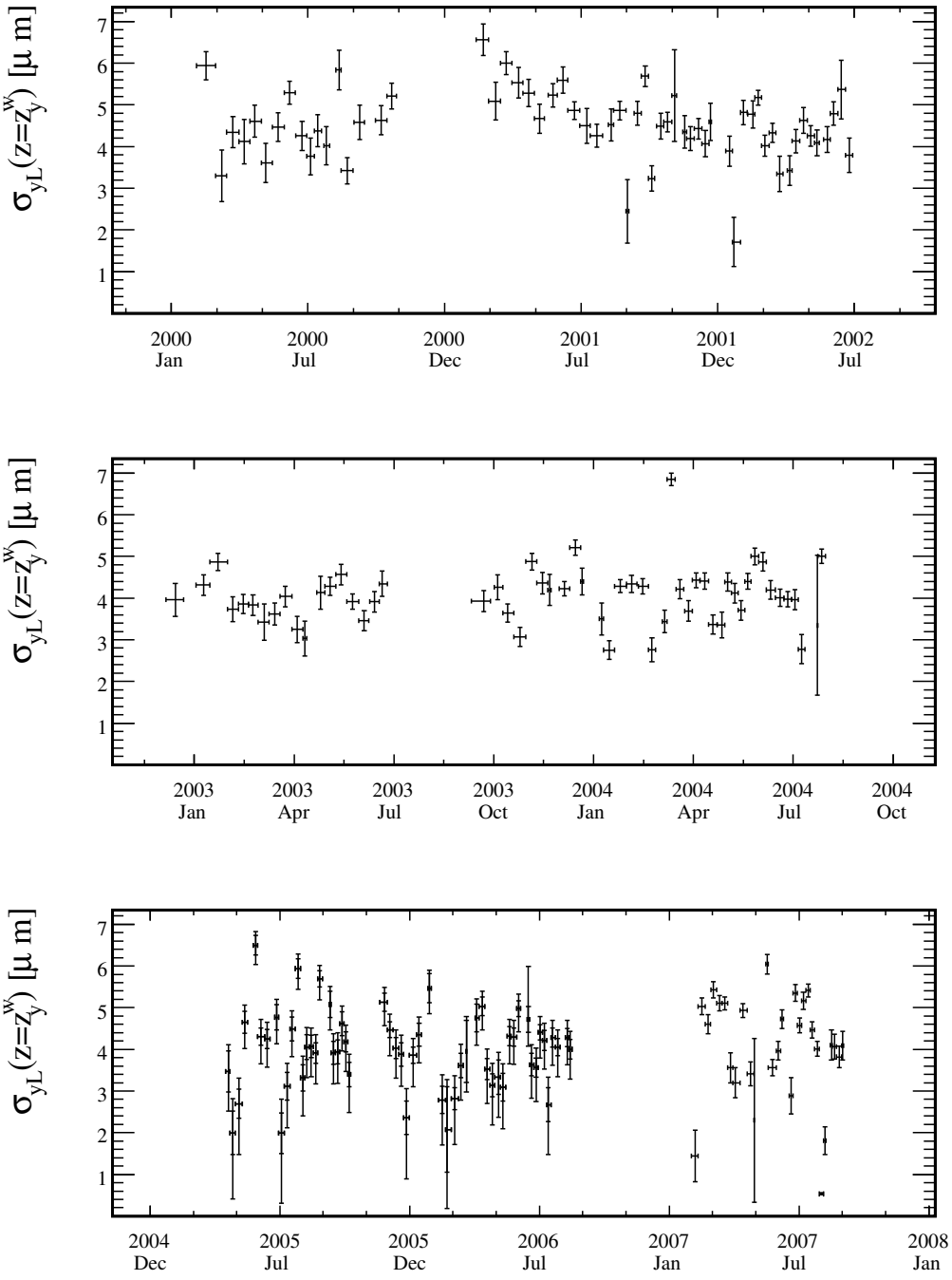

Figure C.15: Fit results for $\sigma_{y\mathcal{L}}(z = z_y^w)$ for Runs 1-6.

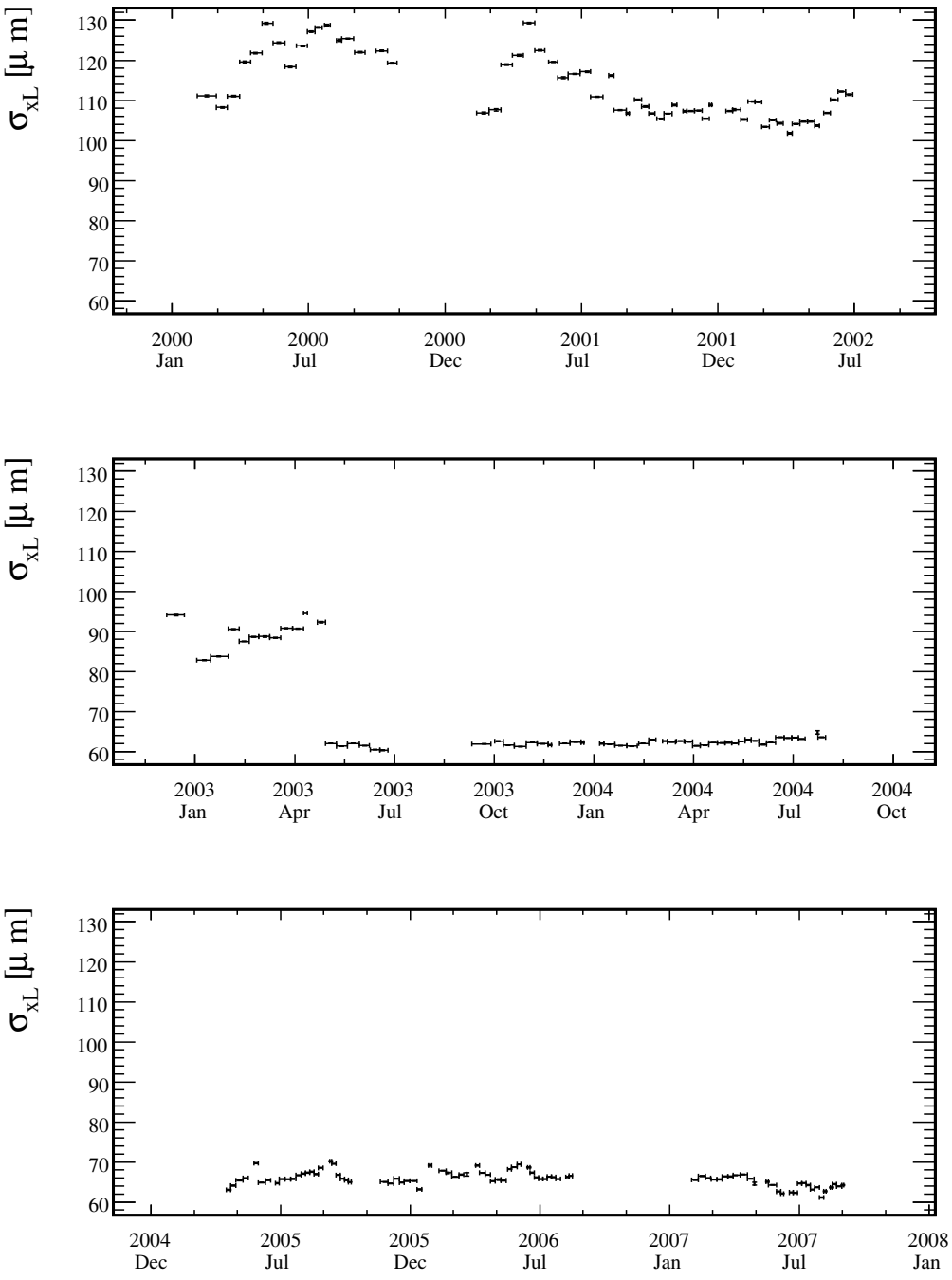

Figure C.16: Fit results for $\sigma_{x\mathcal{L}}$ for Runs 1-6.

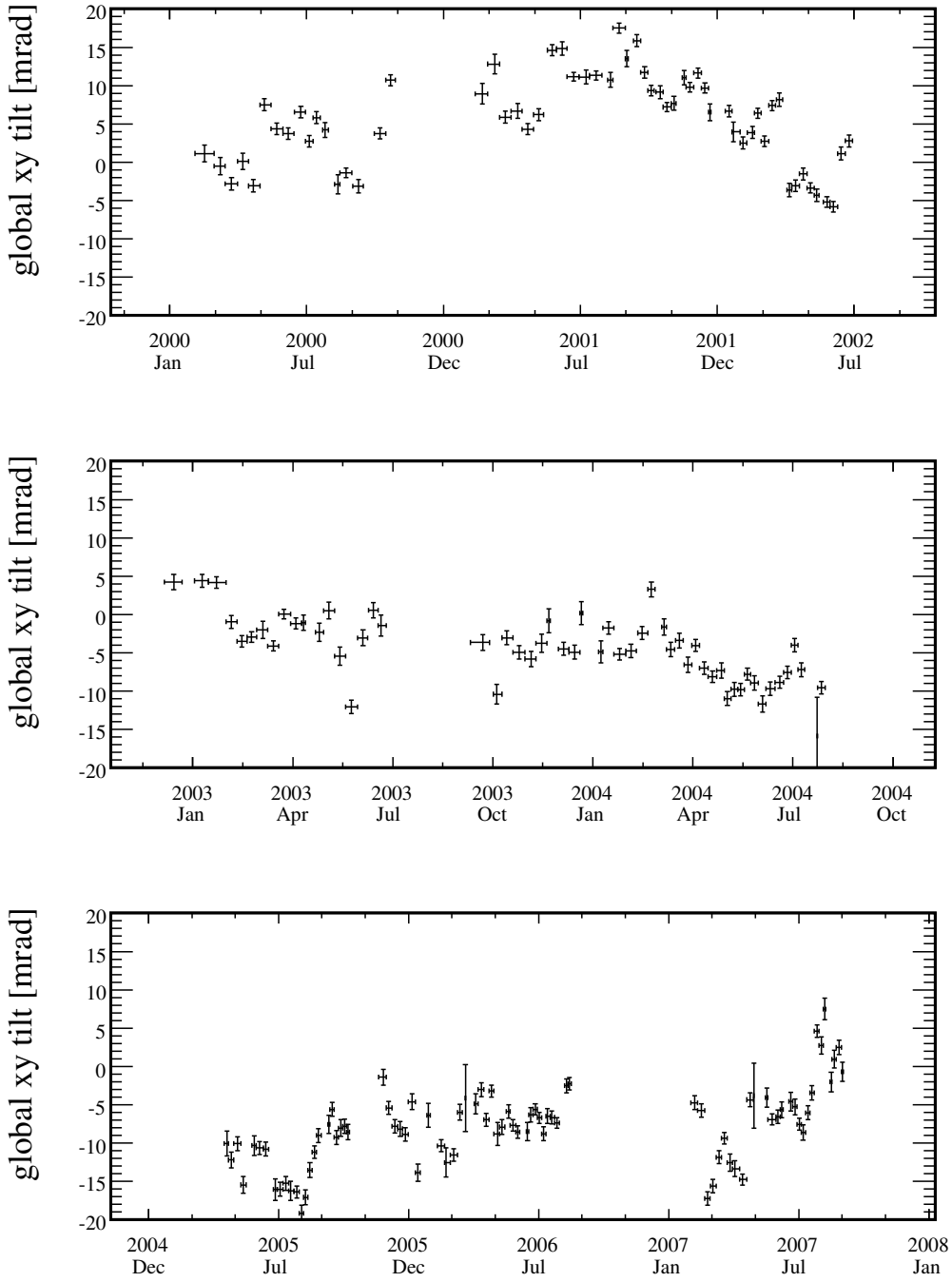

Figure C.17: Fit results for t_{xy} for Runs 1-6.

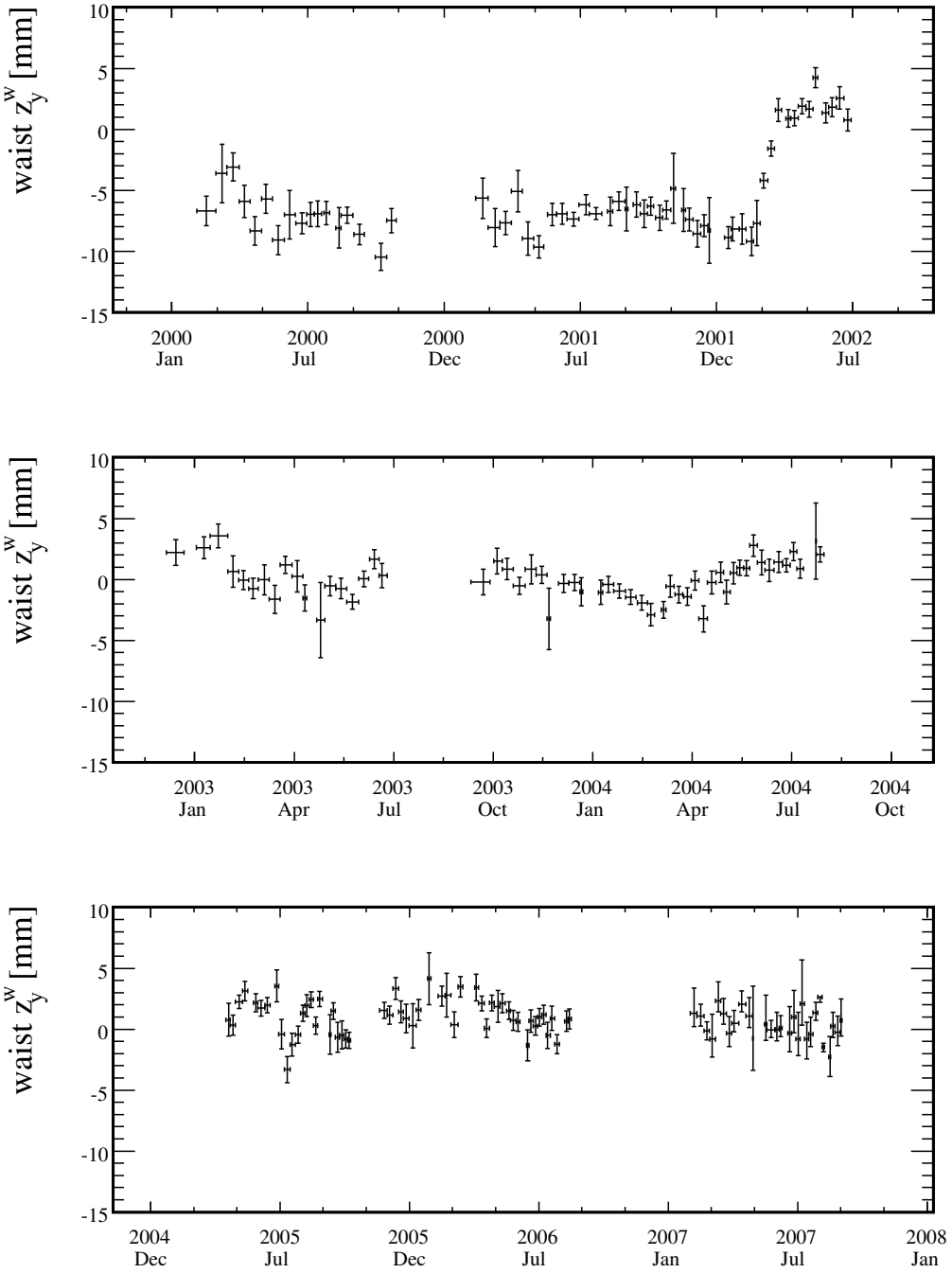

Figure C.18: Fit results for z_y^w for Runs 1-6.

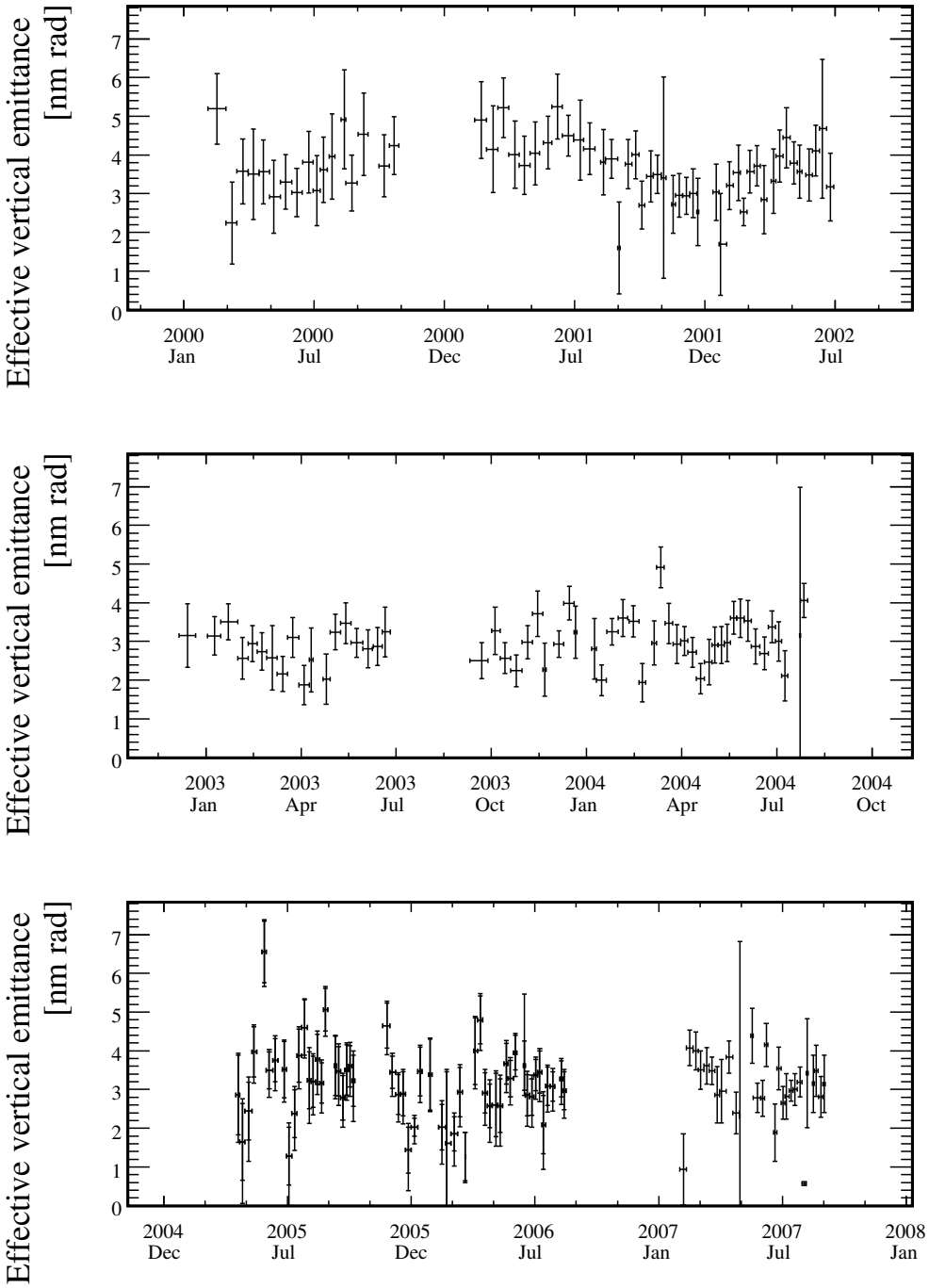

Figure C.19: Results for $\epsilon_{y,\text{eff}}$ for Runs 1-6, extracted from the fit results for β_y^* and $\sigma_{y\mathcal{L}}(z = z_y^w)$.

Bibliography

[1] C. S. Wu, E. Ambler, R. W. Hayward, D. D. Hoppes and R. P. Hudson, Phys. Rev. **105**, 1413 (1957).

[2] T. D. Lee and C. N. Yang, Phys. Rev. **104**, 254 (1956).

[3] J. H. Christenson, J. W. Cronin, V. L. Fitch and R. Turlay, Phys. Rev. Lett. **13**, 138 (1964).

[4] W.-M. Yao *et al.*, J. Phys. G **33**, 1 (2006).

[5] E. Noether, "Invariante Variationsprobleme", *Nachr. d. König. Gesellsch. d. Wiss. zu Göttingen, Math-phys. Klasse,* 235-257 (1918); E. Noether and M. A. Tavel, [arXiv:physics/0503066].

[6] A. D. Sakharov, Pisma Zh. Eksp. Teor. Fiz. **5**, 32 (1967).

[7] M. B. Gavela, P. Hernandez, J. Orloff and O. Pene, Mod. Phys. Lett. A **9**, 795 (1994); M. B. Gavela, P. Hernandez, J. Orloff, O. Pene and C. Quimbay, Nucl. Phys. B **430**, 382 (1994); P. Huet and E. Sather, Phys. Rev. D **51**, 379 (1995).

[8] N. Cabibbo, Phys. Rev. Lett. **10**, 531 (1963).

[9] M. Kobayashi and T. Maskawa, Prog. Theor. Phys. **49**, 652 (1973).

[10] A. Angelopoulos *et al.* [CPLEAR Collaboration], Phys. Lett. B **444**, 43 (1998).

[11] B. Aubert *et al.* [BABAR Collaboration], Phys. Rev. Lett. **99**, 171803 (2007).

[12] G. L. Kane, P. Ko, H. b. Wang, C. Kolda, J. h. Park and L. T. Wang, Phys. Rev. Lett. **90**, 141803 (2003).

[13] Y. Grossman and M. P. Worah, Phys. Lett. B **395**, 241 (1997).

[14] S. J. Lindenbaum and R. M. Sternheimer, Phys. Rev. **105**, 1874 (1957).

[15] C. Zemach, Phys. Rev. **133**, B1201 (1964).

[16] S. Kopp *et al.* [CLEO Collaboration], Phys. Rev. D **63**, 092001 (2001).

[17] J. M. Blatt and V. F. Weisskopf, *Theoretical Nuclear Physics*, (J. Wiley, New York, 1952).

[18] S. M. Flatté, Phys. Lett. B **63**, 224 (1976).

[19] BES Collaboration, M. Ablikim *et al.*, Phys. Lett. B **607**, 243 (2005).

[20] R. R. Akhmetshin *et al.* [CMD-2 Collaboration], Phys. Lett. B **462**, 380 (1999); M. N. Achasov *et al.*, Phys. Lett. B **485**, 349 (2000)A. Aloisio *et al.* [KLOE Collaboration], Phys. Lett. B **537**, 21 (2002).

[21] E. M. Aitala *et al.* [E791 Collaboration], Phys. Rev. Lett. **86**, 765 (2001).

[22] S. Fajfer, R. J. Oakes and T. N. Pham, Phys. Rev. D **60**, 054029 (1999); S. Fajfer, T. N. Pham and A. Prapotnik, Phys. Rev. D **70**, 034033 (2004).

[23] H. Y. Cheng and K. C. Yang, Phys. Rev. D **66**, 054015 (2002).

[24] H. Y. Cheng, C. K. Chua and A. Soni, Phys. Rev. D **72**, 094003 (2005).

[25] H. Y. Cheng, C. K. Chua and A. Soni, Phys. Rev. D **76**, 094006 (2007).

[26] A. Garmash *et al.* [BELLE Collaboration], Phys. Rev. D **71**, 092003 (2005).

[27] B. Aubert *et al.* [BABAR Collaboration], Phys. Rev. D **74**, 032003 (2006).

[28] *BABAR* Collaboration, B. Aubert *et al.*, Phys. Rev. D **71**, 091102 (2005).

[29] M. Beneke, Phys. Lett. B **620**, 143 (2005).

[30] G. Buchalla *et al.*, JHEP **0509**, 074 (2005).

[31] *BABAR* Collaboration, B. Aubert *et al.*, Nucl. Instr. Meth. A **479**, 1 (2002).

[32] "PEP-II: An Asymmetric B Factory," Conceptual Design Report, SLAC-R-418 (1993); U. Wienands, Y. Cai, S. D. Ecklund, J. T. Seeman and M. K. Sullivan, SLAC-PUB-12612 (2007).

[33] M. T .Allen, Ph. D. Dissertation, Stanford University (2007).

[34] D. Piccolo *et al.*, Nucl. Instrum. Meth. **A515**, 322 (2003); F. Anulli *et al.*, Nucl. Instrum. Meth. **A508** 128 (2003).

[35] G. Benelli, K. Honscheid, E.A. Lewis, J.J. Regensburger, D.S. Smith, Nuclear Science Symposium Conference Record, 2005 IEEE , vol.2, pp. 1145-1148, 23-29 Oct. (2005); W. Menges, IEEE Nucl. Sci. Symp. Conf. Rec. **5**, 1470 (2006) [arXiv:physics/0609039].

[36] S. Agostinelli *et al.*, Nucl. Instrum. Meth. **A506**, 250 (2003).

[37] T. Sjostrand, Comput. Phys. Commun. **82**, 74 (1994).

[38] P.F. Harrison, H.R. Quinn, Eds., *The BABAR Physics Book: Physics at an Asymmetric B Factory*, SLAC-R-0504 (1998).

[39] B. Aubert *et al.* [BABAR Collaboration], Phys. Rev. Lett. **87**, 151801 (2001); B. Aubert *et al.* [BABAR Collaboration], Phys. Rev. D **69**, 011102 (2004).

[40] B. Aubert *et al.* [BABAR Collaboration], Phys. Rev. Lett. **93**, 071801 (2004).

[41] B. Aubert *et al.* [BABAR Collaboration], Phys. Rev. Lett. **93**, 181805 (2004).

[42] K. Abe *et al.* [Belle Collaboration], Phys. Rev. Lett. **91**, 261602 (2003).

[43] Belle Collaboration, K.-F. Chen *et al.*, Phys. Rev. D **72**, 012004 (2005).

[44] Belle Collaboration, K.-F. Chen *et al.*, Phys. Rev. Lett. **98**, 031802 (2007).

[45] A. Roodman, *In the Proceedings of PHYSTAT2003: Statistical Problems in Particle Physics, Astrophysics, and Cosmology, Menlo Park, California, 8-11 Sep 2003, pp TUIT001* [arXiv:physics/0312102].

[46] S. Spanier, D. Dujmic, and M. Krishnamurthy, "Measurement of time-dependent *CP* asymmetries in $B \to \phi K^0$," *BABAR* Analysis Document #313; M. Krishnamurthy, G. Ragghianti, and S. Spanier, "Study of *CP* in $B \to \phi K$," *BABAR* Analysis Document #983.

[47] R. A. Fisher, Ann. Eugen. **7**, 179 (1936).

[48] B. Aubert *et al.* [BABAR Collaboration], Phys. Rev. D **66**, 032003 (2002).

[49] H. Albrecht *et al.* [ARGUS Collaboration], Phys. Lett. B **241**, 278 (1990).

[50] G. Cavoto, E. Di Marco, *et al.* "Time Dependent Dalitz Plot Analysis of $B^0 \to K^+K^-K^0_L$ Decays," *BABAR* Analysis Document #1405.

[51] M. Pivk and F. R. Le Diberder, Nucl. Instrum. Meth. A **555**, 356 (2005).

[52] D. Dujmic, J. M. Thompson, and A. Roodman, "An analysis of the Dalitz plot of the decay $B^0 \to K^+K^-K^0_S$," *BABAR* Analysis Document #1160.

[53] The Heavy Flavor Averaging Group, http://www.slac.stanford.edu/xorg/hfag/, ICHEP 2006 Averages.

[54] O. Long *et al.*, Phys. Rev. D **68**, 034010 (2003).

[55] B. Aubert *et al.* [BABAR Collaboration], Phys. Rev. Lett. **98**, 031801 (2007).

[56] The Heavy Flavor Averaging Group, http://www.slac.stanford.edu/xorg/hfag/, Winter 2008 Averages.

[57] B. Aubert *et al.* [BABAR Collaboration], Phys. Rev. Lett. **99**, 161802 (2007).

[58] B. Aubert *et al.* [BABAR Collaboration], arXiv:0708.2097 [hep-ex].

[59] B. Aubert *et al.* [BABAR Collaboration], arXiv:0808.0700 [hep-ex].

[60] J. Dalseno [The Belle Collaboration], arXiv:0810.2628 [hep-ex].

[61] D. Cinabro, K. Korbiak, R. Ehrlich, S. Henderson and N. B. Mistry, Nucl. Instrum. Meth. A **481**, 29 (2002).

[62] J. Slaughter, J. Estrada, K. Genser, A. Jansson, P. Lebrun, J. C. Yun and S. Lai, *Proceedings of the Particle Accelerator Conference (PAC 03), Portland, Oregon, 12-16 May 2003, pp 1763.*

[63] W. Kozanecki, A. J. Bevan, B. F. Viaud, Y. Cai, A. S. Fisher, C. O'Grady, B. Lindquist, A. Roodman, J. M. Thompson, and M. Weaver, *Interaction-point Phase-Space Characterization using Single-Beam and Luminous-Region Measurements at PEP-II*, SLAC-PUB-13383, Submitted to Nucl. Instr. Meth. A.

[64] G. Lynch, S. Schaffner, S. Wagner, G. Raven, F. Wilson, *BABAR Drift Chamber Tracking Conventions*, *BABAR* Note 488 (1999).

[65] G. Schott, Ph. D. Dissertation, Universite Paris VI (2004).